# CAVITY RINGDOWN SPECTROSCOPY OF THE NITRATE AND PEROXY RADICALS

Thesis by

Kana Takematsu

In Partial Fulfillment of the Requirements

for the degree of

Doctor of Philosophy

California Institute of Technology

Pasadena, California

2011

(Defended May 23, 2011)

# ACKNOWLEDGEMENTS

I know that the Ph. D. journey can be difficult, but my years at Caltech have been some of my happiest, and I owe it to the incredible love and support that I have received from my family and Caltech family over the last years. I also would never have begun this journey without the love and support of past teachers and friends. I don't think that I was ever the normal child, but I was always a loved child, and for that I am eternally grateful.

*To my mother, father, and brother:* Thank you for supporting me, not only the past years in school, but throughout my entire life. You always let me be me. I was lucky to be born your daughter and sister, and I will always love you.

*To my advisor Mitchio:* I've learned to become a better scientist and mentor from our work together. Somewhere along the way, you became not only my advisor but my trusted friend. Thank you. I also thank your wife Laurie and the girls Mei-Li and Jinny for their laughter and smiles.

*To my thesis committee, Geoff, Harry, and Rudy:* I couldn't have asked for a merrier trio. You represent to me the spirit of the scientific community: the camaraderie, the knowledge, and the joy. Thank you.

*To my fellow Okumurons:* You were not only my research peers but were my friends and family outside of the lab. To all the current and past lab members, Aaron, Andrew, David, Julie, Andrei, Laurence, Dave, Kathleen, Sigrid, Kathryn, Leah, Thinh, Matt, Aileen, and Nathan, to all the summer students, Jonathan, Heather, Alex, Eric, Matthew, Geoff, and Marcus, and to all the honorary Okumurons, Stan, Xu, Fred, Pin, and Ralph, thank you. Once an Okumuron, always an Okumuron. I'll always be yours.

*To my friends at Caltech:* There never was a girl who felt more loved. I apologize that I can't name everyone here individually, but thanks to the Potluck group, WMW, the floorball team, and the LA Dipoles. I also want to thank Jenelle and Adrienne. I've never had sisters, but you two are the best "older" sisters a girl could ever have. I also want to thank Laurence, who would have made an excellent twin.

*To the various Caltech lab groups and collaborators:* Thanks to the Blake, Barton, Sander, Wennberg, Seinfeld, and Rees groups for all the merriment and equipment. The gas phase and atmospheric communities have both been so kind. Anne, I owe you another Curious George book, and John, I make fun of you way too much. Terry and Ming-Wei, OSU was that much lovelier with your company

*To Caltech staff:* Thanks to Rick, Steve, Mike, and Tom for dealing with both me and the broken equipment, to Steve and Leah for orders, to Terry, Joe, and Ron for deliveries, to Carlette for fellowship work, to Linda, Anne, Agnes, Dian, and Laura for crazy paperwork, and to facilities for gas cylinders. Thanks also to Ernie, who is part of "Caltech staff" for me.

*Finally, to my past teachers and friends:* To my friends in high school and college, I learned from you how to be a better friend. To my teachers at Daniel and Prof. Darryl DesMarteau at Clemson, I learned from you how to be a better mentor. Thank you. To the University of Chicago, you gave me a chance to learn with the fellowship. It meant the world to me. And finally, to Prof. Laurie Butler and the Butler girls, you showed me the joys of research. I never would have begun my journey without you. Thank you.

*P.S. NSF and EPA:* When I started the Ph. D. journey, I didn't even know that students get paid in graduate school. The fellowships gave me the freedom to pursue my dreams. I've made the best of my opportunities at Caltech and I have thoroughly enjoyed the journey. Thank you.

# ABSTRACT

The chemistry of the Earth's atmosphere consists of complex networks of reactions. Photooxidation of volatile organic compounds (VOCs) in the atmosphere initiates free radical formation. These radicals attack other VOCs to form pollutants and secondary organic aerosols. Quantitative understanding of the radicals and reactions is needed for accurate modeling of the atmosphere. Many species are difficult to study due to low concentrations and short lifetimes. Spectroscopic methods in the ultraviolet and visible regions either do not have the sensitivity or the specificity to characterize these reactions. The work here examines the chemistry and physics of atmospheric radicals by using the sensitive and fast spectroscopic technique cavity ringdown spectroscopy (CRDS), to detect transient species in the near-infrared (NIR) region.

The nitrate radical $NO_3$ is a major nighttime oxidant in the troposphere. It is also a classic example of the breakdown of the Born-Oppenheimer approximation. The radical was first observed a century ago in atmospheric measurements. The structures of the three lowest electronic state however are still not well understood. Difficulties arise from the non-adiabatic Jahn Teller and Pseudo-Jahn-Teller effects. In Chapter 3, we examine the electronic-dipole forbidden $\tilde{A} \leftarrow \tilde{X}$ transition of $NO_3$ in the NIR to elucidate the $\tilde{A}$ state of $NO_3$. In Chapter 4, we examine the role of $NO_3$ in atmospheric reactions by detecting the peroxy radical intermediate of the oxidation of 2-butene by $NO_3$.

The chlorine atom Cl is highly reactive and has been historically considered a coastal or marine layer oxidant. Studies now indicate that Cl atoms can play significant roles in urban mainland chemistry. Isoprene and 2-methyl-3-buten-2-ol (MBO232) are two important biogenic VOC

emissions. Isoprene alone is responsible for emissions of 500 Tg C $y^{-1}$. The peroxy radical intermediates of the oxidation of isoprene and MBO232 by Cl have never been detected using absorption spectroscopy. Chapter 5 includes the first preliminary CRD spectra of the $\tilde{A} \leftarrow \tilde{X}$ transition of Cl-isoprenyl and Cl-MBO232 peroxy radials in the NIR. We also outline kinetic experiments to measure the rates of reaction between the Cl-substituted peroxy radicals and nitric oxide (NO) and hydroperoxy radical ($HO_2$) under high and low $NO_x$ conditions in the troposphere.

# TABLE OF CONTENTS

# LIST OF FIGURES AND TABLES

*Number* *Page*

## *Chapter 1*

# INTRODUCTION

*To everyone who was kind and patient enough to show the world to a curious girl, the first chapter is for you.*

### 1.1 The initial conversation

After a seminar on the quantum mechanics of atomic clocks, I asked a visiting scientist how he explained the significance of his work to a stranger on a plane. To my great surprise, he replied, "British maritime history." To my puzzled look, he continued, "When the British ruled the seas, they had the best marine chronometer and could calculate longitudinal coordinates better than anyone else. If we want to lead in the future, we need to be able to know time to the utmost accuracy." His reply was true but far removed from his earlier talk. It captured the essence of science: the pursuit of basic knowledge with the imagination to see the same ideas in the everyday world.

The everyday world my research occupies is the atmosphere of our planet. The Earth's atmosphere can be divided into separate layers, with humans occupying the lowest level, the troposphere. In elementary school, we learned that the Earth's atmosphere consists mostly of nitrogen (78%) and oxygen (21%). What was not taught to us was that it is the minority of the species (often less than 1 part per million) that drives the chemistry of the atmosphere. The reactions of these few species determine whether we have clear skies or smog formation.

The quality of the air we breathe has been tied to both the quality of life and public health.[1-5] The issue is not just an "urban" problem, as winds can transport pollutants on both local and global scales.[6] While many reactions begin in the gas phase, the gas species can react further to form larger complexes until they begin to coagulate or form particles called secondary organic aerosols (SOA). These aerosols absorb or scatter energy from the sun, playing a major factor in determining the Earth's climate.[7] Any regulation on global warming will have to involve understanding of the underlying gas phase chemistry forming these aerosols.

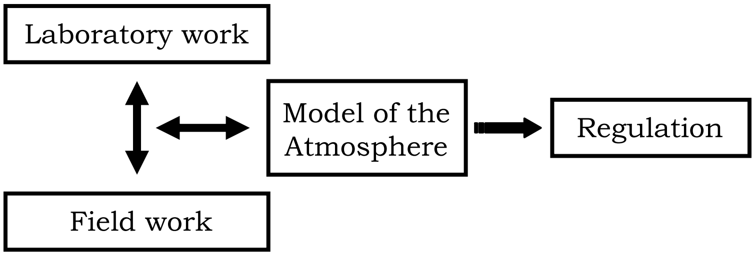

**Figure 1.1.** Diagram of the relationship among different branches of atmospheric chemistry. Parameters obtained in the experimental (laboratory/field) work are used by modelers to describe the chemistry of our atmosphere. The results are used by national and international governing bodies to better regulate the air quality.

There has thus been both scientific and societal interest in accurately modeling the atmosphere of the Earth. The chemistry, however, is very complex with hundreds of reactions going on simultaneously. Considerable field work has been done to identify and measure concentrations of relevant species. *But where do these species come from? How fast do they form? How fast do they react? What do they form?*

Answering these questions requires complementary work in the laboratory, where the complex network of reactions can be isolated into individual reactions (Fig. 1.1). Some experiments focus on re-creating the atmosphere in a more controlled setting. Chamber experiments involve adding known concentrations of gas phase species into a large Teflon bag and measuring product growth over long timescales. While such studies have provided useful data, there are often discrepancies in the measurements. Even a small percentage difference in the yields can lead to large errors in the atmospheric models. Accurate quantification of the parameters is thus critical.

Much of the discrepancy in the chamber experiments could be resolved by studying the reactions on shorter timescales. Due to the transient nature of the initiating species, the oxidation or reaction of the compounds occurs very quickly, ranging from the microsecond to millisecond timescale. The intermediates formed during oxidation can follow multiple pathways, resulting in a large range of products. If we could probe the intermediates directly, we could not only characterize the intermediate, but we could also conduct quantitative kinetic experiments, measuring the rate of reaction between the intermediate and gas species of interest and quantifying product yields of the various pathways.

Our initial conversation on the Earth's atmosphere has brought us to the laboratory to detect specific trace gas intermediates. That is the magic of science. The atmospheric problem is now a chemical physics problem. *How does one detect a species that is transient and exists only in low concentrations? How does one detect a species that has never been detected?* We explore the answers to these questions in the next section.

## 1.2 Detection of transient species

We would like to detect the transient species in a non-invasive manner. Laser spectroscopic methods are ideal, as absorption of low energy photons of light does not change the chemical nature of the species but allows identification, as compounds absorb energies of light characteristic to their molecular rotations, vibrations, and electronic transitions. A spectroscopic method that is fast and sensitive is also necessary, as the species of interest have lifetimes on the microsecond to millisecond timescale and are low in concentration. In our laboratory, we use the laser method cavity ringdown spectroscopy (CRDS).[8,9]

The sensitivity of spectroscopic methods is related directly to the probability of photons interacting with the sample. The earliest atmospheric experiments gained sensitivity by maximizing the pathlength of detection. For example, many people are familiar with current efforts to measure ozone levels in the troposphere. These measurements however have a rich history. In 1881, Hartley measured the ozone absorption of ultraviolet (UV) light by pointing a spectrometer at the sun from mountain tops across Europe.[10] In 1918, a mercury lamp was set in one town and a spectrometer was placed four miles away in another valley to measure ozone levels directly in the troposphere.[11]

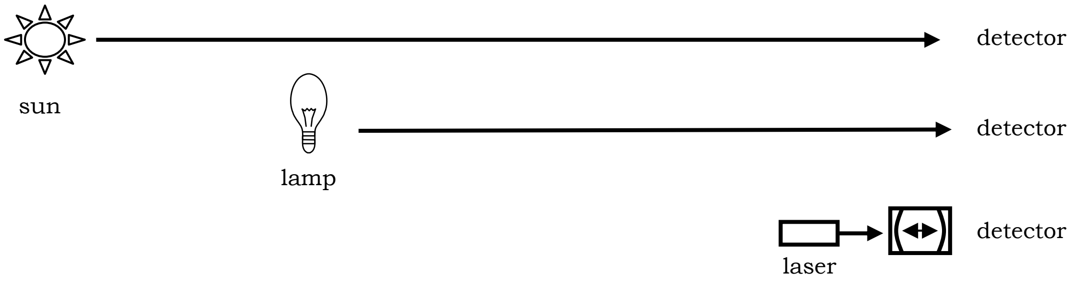

**Figure 1.2.** To achieve enough sensitivity to detect gas phase species in spectroscopic experiments, the detector and light source were historically placed kilometers apart. The optical cavity (shown on the bottom) is only a few centimeters in length. It uses highly reflective mirrors such that the effective pathlength the light propagates is equivalent to a few kilometers.

The measurements were amazing for their time, and there are still measurements being done today in which we point a laser to the sky and record the observations. These situations, however, are not ideal for a laboratory setting. One alternative is to place two highly reflective mirrors at the end of a sample cell. When laser light is injected into the cavity, the laser pulse is reflected back and forth such that the effective pathlength of the cell is equivalent to a few kilometers (Fig. 1.2). This is the underlying idea of CRDS.

CRDS allows for detection of species below 1 part per million. To truly appreciate the sensitivity of the technique, imagine measuring the height of Mt. Everest with a ruler. To match the relative sensitivity of CRDS, the measurement would have to be made with a precision of inches. CRDS also measures samples on the microsecond timescale, as the time of detection is related directly to the time it takes for light to be reflected about the cavity. Thus, CRDS is an ideal technique for directly probing the intermediates of atmospheric reactions.

Choosing the detection wavelength is governed by both the characteristic molecular trait by which we choose the species to be identified and the chemistry which we use to generate the species in the laboratory. The electromagnetic spectrum is shown in Fig. 1.3. Rotational, vibrational, and electronic transitions lie typically in the microwave, infrared (IR), and visible/UV regions, respectively. With commercial availability of sensitive detectors and high power laser sources, many experimental studies have been done in the visible and IR regions. While transitional energies are distinct to the species, many species absorb similar wavelengths of light. Overlapping spectral bands complicates individual identification and quantification of species.

In this work, we detect gas phase species in the near-infrared (NIR) region. Many species do not absorb photons in this region. Most intermediates of atmospheric reactions are highly reactive species called radicals. These radicals tend to have low-lying electronic transitions in the NIR. We run quantum mechanical calculations on the radical structure and electron density to predict the electronic transitional energies. The bands are then detected in the NIR using CRDS.

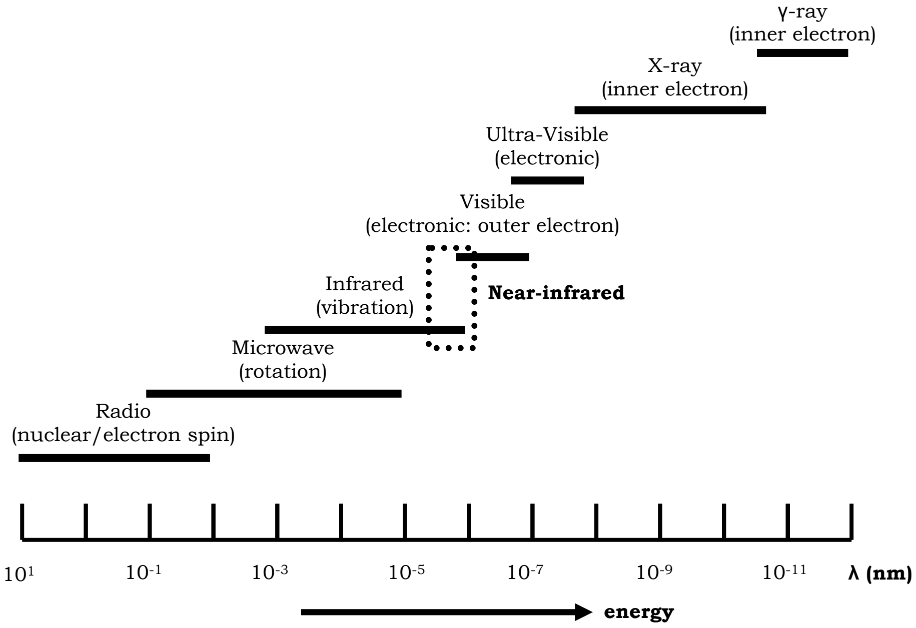

**Figure 1.3.** Diagram of the electromagnetic spectrum. As the wavelength gets shorter, each photon of light has more energy. For each region, the corresponding molecular transition is written in the parentheses. We conduct our experiments in the near-infrared, examining the rovibronic transitions of various gas phase species.

Before we conduct any experiments, the radical species must be generated in the laboratory. Often there are many ways to generate radicals. The ideal chemical method produces a high concentration of radicals with minimal secondary chemistry. Byproducts of the radical formation can have consequences for both detection and kinetic experiments. Products may absorb in the NIR and interfere with detection. They or subsequent products may react with the radical and complicate measurements of the reaction rates. The physical manner in which we produce these radicals must also be considered. Thermal heat, electric discharge, laser photolysis, and chemical reactions are only a few examples of how radicals have been generated in the laboratory. Each approach requires a different set of chemicals and equipment.

The chemical methodology we choose is dependent on the purpose of the experiment. If the goal is to detect and characterize the radical, the method that produces the most abundant radical concentration without spectral interference is chosen. If the goal is to measure the kinetic rate constants, the method that minimizes secondary chemistry is chosen. For kinetic experiments, the physical method of radical production has to also allow for time resolution, as it is critical to measure the precise moment the radical is formed and begins to react with other gas species.

The ultimate goal of all experiments is to reproduce the most atmosphere-like conditions in the laboratory such that measurements made in the laboratory can be directly input to the atmospheric model. Many of the ideas behind the chemical methodologies originate from chemical reactions in the atmosphere. Thus, we now discuss the chemistry of the atmosphere.

### 1.3 The chemistry of the atmosphere: the role of the peroxy radical

The majority of atmospheric reactions are initiated by the sun. Stable compounds absorb solar energy and break apart into reactive species called radicals. These radicals attack other compounds to generate new species. The new species can continue to react in the gas phase or form SOA. Transport of species from different geographic locations and different atmospheric layers plays an important role in the atmosphere.[12] We focus on the chemical reactions in this work. Only a brief overview of the chemistry is given here, as there are excellent books written on this subject.[13,14]

Many of the compounds involved in the reactions are volatile organic compounds (VOCs).[15,16] VOCs include hydrocarbon and oxygenated species from both biogenic and anthropogenic sources. Global biogenic VOC emissions contribute more than 1150 Tg (C) $yr^{-1}$, while anthropogenic VOC emissions contribute 100 Tg (C) $yr^{-1}$.[17] In urban areas, anthropogenic sources still dominate.

The largest biogenic non-methane VOC emission is isoprene (Fig 1.4). Isoprene is naturally released by deciduous trees and contributes ~500 Tg (C) $yr^{-1}$.[14] With two double bonds and multiple attack sites, isoprene is very reactive and can form a variety of products from oxidation by atmospheric radicals. The majority of anthropogenic VOC emissions are hydrocarbons from car exhaust and petrochemical plants. A breakdown of non-methane VOCs in an urban city such as Los Angeles showed VOC contributions from alkane (40-45%), alkene (10%), aromatic hydrocarbons (20%), oxygenated species (10-15%), and a small percentage of yet to be identified VOCs.[18]

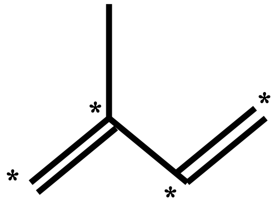

**Figure 1.4.** Isoprene is the most abundant non-methane VOC in the atmosphere. Upon oxidation, various products are formed. The asterisk (*) labels the various oxidation sites of isoprene.

The fate of VOCs in the troposphere is tied directly to the formation of the peroxy radical intermediate.[19] The hydroxyl radical (OH) and ozone ($O_3$) are formed during the day:

OH source: $O_3 + h\nu\ (\lambda<336\text{ nm}) \rightarrow O(^1D) + O_2$ (1.1)

$O(^1D) + H_2O \rightarrow 2OH$ (1.2)

$O_3$ source: $NO_2 + h\nu\ (\lambda<420\text{ nm}) \rightarrow NO + O(^3P)$ (1.3)

$O(^3P) + O_2 \rightarrow O_3$ (1.4)

The radical (X = OH, $O_3$) can abstract either a H-atom or react with the VOC to form an alkyl radical (R). In the presence of oxygen, the alkyl radical is immediately converted to a peroxy radical.

$\text{VOC} + X \rightarrow R$ (1.5)

$R + O_2 \rightarrow ROO$ (peroxy radical) (1.6)

Peroxy radicals can follow many chemical pathways after formation (Fig 1.5). They can react with other peroxy radicals to form carbonyl compounds (RHO), hydroperoxides (ROOH), and alcohols (ROH). They can also react with nitric oxide (NO) to form alkoxy radicals (RO), which can initiate their own complex network of reactions.[20,21] The chemistry of the troposphere is often categorized into two domains: low and high $NO_x$ conditions, in which $NO_x$ includes compounds NO, $NO_2$, and $NO_3$. In rural environments with low $NO_x$ conditions, the peroxy-peroxy reaction pathways dominate. In urban environments with high $NO_x$ conditions, the peroxy-NO reaction pathways dominate.

The significance of peroxy radicals can also be understood by their relation to other atmospheric networks. One of the most important questions in tropospheric chemistry is whether we can accurately model ozone concentrations. There is a tendency in popular literature to use the misleading terminologies "good" and "bad" ozone. The "good/bad" refers not to the chemical composition of ozone ($O_3$) but to the different roles ozone plays in the atmosphere. In the stratosphere, ozone absorbs harmful UV rays. In the troposphere, ozone or inhalation of ozone is adverse to human health.[22-25]

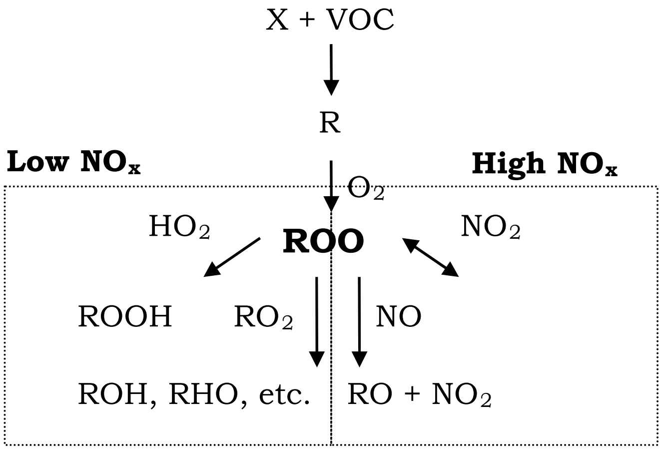

**Figure 1.5.** Schematic of the formation and subsequent chemistry of peroxy radicals. The peroxy radical can follow multiple pathways. Observed products can be grouped under low and high NO$_x$ conditions. Measurement of the kinetic rate constants of the various species with ROO is critical for accurate modeling of the atmosphere.

In a polluted high NO$_x$ environment, peroxy radicals react with NO to form alkoxy radicals and nitrogen dioxide ($NO_2$):

$$RO_2 + NO \rightarrow RO + NO_2 \tag{1.7}$$

$NO_2$ can be photolyzed to form ozone (reactions 1.3-1.4). Thus, the two networks are connected. Peroxy radicals indirectly lead to ozone formation, while ozone-initiated oxidation of VOCs leads to peroxy radical formation. There has thus been much effort to characterize the peroxy radicals and their chemistry in the atmosphere. The simplest peroxy radicals include the hydroperoxyl ($HO_2$), methyl peroxy ($CH_3O_2$), and ethyl peroxy ($C_2H_5O_2$) radicals. Rate constants for these radicals with $HO_2$ and NO have been measured to model low and high $NO_x$ conditions, respectively.[26,27]

In some cases, the radical can directly add to the VOC to form a substituted peroxy radical:

$$\mathrm{VOC} + \mathrm{X} \rightarrow \mathrm{RX} \quad (1.8)$$

$$\mathrm{RX} + \mathrm{O_2} \rightarrow \mathrm{RXOO^{\cdot}} \text{ (substituted peroxy radical)} \quad (1.9)$$

The substituted peroxy radicals can undergo similar reactions with NO and other peroxy radicals. There is, however, considerably less work on the kinetics and detection of substituted intermediates. Questions have risen with respect to the mechanism and yields of these addition reactions. *Does the radical addition lead to formation of substituted peroxy radical or is the adduct in quasi-equilibrium with the reactants? Are there new reaction pathways that need to be considered? Does the substituent on the peroxy radical affect its reactivity with other peroxy radicals and NO?* These issues need to be resolved to gain a full picture of the peroxy and substituted peroxy radical chemistry in the atmosphere.

We have thus far mentioned VOC oxidation by OH and ozone. Along the marine coast, halogens (I, Br, Cl) also influence the chemistry of the atmosphere. Halogens are very reactive, and it is only their general low abundance in the atmosphere that limits their importance to non-coastal environments. Recent reports however may change this picture, as relatively high levels of nitryl chloride ($ClNO_2$) have been reported inland.[19,28,29] $ClNO_2$ can photolyze to form both Cl atoms and $NO_2$. We have already discussed the impact of $NO_2$ on ozone levels. Cl-initiated oxidation of VOCs must also be well-characterized.

At nighttime, there are no longer photolytic sources for OH, ozone, or Cl. Instead, another radical, the nitrate radical ($NO_3$), dominates the nighttime chemistry. $NO_3$ is very reactive and oxidizes VOCs as rapidly as other atmospheric radicals. During the daytime, however, $NO_3$ is destroyed by sunlight:

$$NO_3 + h\nu\ (\lambda < 700\ \text{nm}) \rightarrow NO + O_2 \qquad (1.10\ \text{a})$$

$$NO_3 + h\nu\ (\lambda < 580\ \text{nm}) \rightarrow NO_2 + O \qquad (1.10\ \text{b})$$

At nighttime, $NO_3$ becomes the most abundant oxidant in the troposphere. The reaction rates of $NO_3$ with various VOCs have been measured.[30,31] $NO_3$-substituted peroxy radicals, however, have never been detected in the gas phase.

$NO_3$ also has a rich history with other scientific communities and has proven to be an equally interesting and challenging problem in itself. We discuss in the next section how the nitrate radical has entertained experimentalists and theorists alike in the physical chemistry community.

## 1.4 A puzzle for many: the nitrate radical

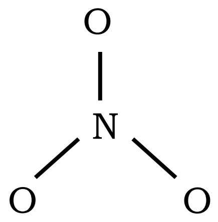

**Figure 1.6.** Picture of the $NO_3$ radical. This deceivingly simple radical has proven to be a spectroscopic and theoretical puzzle for over a century.

Spectroscopic signatures of $NO_3$ were obtained in the visible region as early as 1880.[32] Consisting of only four atoms, $NO_3$ appeared to be a simple system to calculate its electronic structures (Fig. 1.6). Modeling the states of $NO_3$ is particularly important for accurate simulations of $NO_3$ oxidation of VOCs.

The Born-Oppenheimer (BO) approximation is often invoked to simplify quantum mechanical calculations. The approximation states that as electrons are very light in mass compared to nuclei in a compound, they should be able to instantaneously adjust to positional changes in the nuclei to minimize the overall energy of the compound. Mathematically, the wavefunction describing the electronic and nuclear motion of a molecular system can be separated into two functions. For $NO_3$, however, this approximation is no longer valid. Thus, the quantum calculations becomes very challenging, and new theoretical approaches must be developed.

To test and push the development of accurate quantum models, quantitative features of the electronic states of $NO_3$ must be measured for comparison. $NO_3$ has been detected in the visible region; however it has been difficult to retrieve structural information from these spectra. Considerably less work has been done on $NO_3$ in the NIR region. We therefore use CRDS to probe $NO_3$ in the NIR region to elucidate the non-adiabatic effects of $NO_3$.

## 1.5 Summary

We began with a simple conversation on the composition of the Earth's atmosphere and how it was the minority of the gas species that drives the chemistry of the atmosphere. The effect of air quality on public health and the role of aerosols in climate change make modeling the atmosphere both a scientific and societal issue. In order to model the atmosphere accurately, the complex network of reactions has to be studied in the controlled setting of a laboratory. We use the fast and sensitive spectroscopic method CRDS to study the intermediates of VOC oxidation and measure their kinetic rate constants with other atmospheric species.

In particular, we are interested in the tropospheric peroxy and nitrate radicals. The *peroxy radical* is formed upon VOC oxidation and can follow many chemical pathways. Subsequent products have large consequences for the atmosphere, including ozone and smog formation. The *nitrate radical* is the primary initiator of VOC oxidation at night and can form substituted peroxy radicals. Although a small radical, $NO_3$ is proving very difficult to simulate, and more data is needed to better understand its non-adiabatic effects.

In the next chapter, we discuss the method of CRDS in more technical terms and provide details of our apparatus. In Chapter 3, we describe the non-adiabatic effects of $NO_3$ and the information we learned from the $NO_3$ spectra obtained in the NIR region. In Chapter 4, we discuss detection of the $NO_3$ substituted peroxy radicals in the NIR region using CRDS. Finally, in Chapter 5, we outline preliminary efforts to detect and conduct kinetic experiments on Cl-substituted peroxy radicals.

## 1.6 References

(1) Elliott, P.; Wartenberg, D. *Environmental Health Perspectives* **2004**, *112*, 998.

(2) Landrigan, P. J.; Kimmel, C. A.; Correa, A.; Eskenazi, B. *Environmental Health Perspectives* **2004**, *112*, 257.

(3) Samet, J. M.; Dearry, A.; Eggleston, P. A.; Ford, J.; Froines, J.; Gelobter, M.; Gong, H.; Kinney, P. L.; Leikauf, G. D.; Lipsett, M.; Lwebuga-Mukasa, J. S.; Mannino, D.; McDonnell, W.; Morandi, M.T.; Neas, L. M.; Porras, C.; Prasad, S.; Redd, S.; Schwab, M.; Servin, T.; Shepard, P.; Spengler, J. D.; Sugerman-Brozan, J.; Targ, N.; Wallace, D.; Wallace, R.; White, R. H.; Woodruff, T.; Amer Lung, A. *Environmental Health Perspectives* **2001**, *109*, 357.

(4) Ebi, K. L.; McGregor, G. *Environmental Health Perspectives* **2008**, 1*16*, 1449.

(5) Jacob, D. J.; Winner, D. A. *Atmospheric Environment* **2009**, *43*, 51.

(6) Peters, L. K.; Berkowitz, C. M.; Carmichael, G. R.; Easter, R. C.; Fairweather, G.; Ghan, S. J.; Hales, J. M.; Leung, L. R.; Pennell, W. R.; Potra, F. A.; Saylor, R. D.; Tsang, T. T. *Atmospheric Environment* **1995**, *29*, 189.

(7) *Contribution of Working Group I to the Fourth Assessment Report of the Intergovernmental Panel on Climate Change, 2007.* Solomon, S., D. Qin, M. Manning, Z. Chen, M. Marquis, K.B. Averyt, M. Tignor and H.L. Miller Ed.; Cambridge University Press; New York, NY, 2007.

(8) Scherer, J. J.; Paul, J. B.; Okeefe, A.; Saykally, R. J. *Chem. Rev.* **1997**, *97*, 25.

(9) Brown, S. S.; Stark, H.; Ravishankara, A. R. *Appl. Phys. B-Lasers Opt.* **2002**, *75*, 173.

(10) Hartley, W. N. *Journal of the Chemical Society, Transactions* **1881**, *39*, 111.

(11) Strutt, R. J. *Proc. R. Soc. Lond. Ser. A - Contain. Pap. Math. Phys. Character* **1918**, *94*, 260.

(12) Jacob, D. J. *Introduction to Atmospheric Chemistry*; Princeton University Press, 1999.

(13) Seinfeld, J. H.; Pandis, S. N. *Atmospheric Chemistry and Physics*; Wiley-Interscience, 1997.

(14) Finlayson-Pitts, B. J.; Pitts, J. N. *Chemistry of the Upper and Lower Atmosphere: Theory, Experiments, and Applications*; Academic Press, 1999.

(15) Atkinson, R.; Arey, J. *Accounts of Chemical Research* **1998**, *31*, 574.

(16) Atkinson, R.; Arey, J. *Chemical Reviews* **2003**, *103*, 4605.

(17) Guenther, A.; Hewitt, C. N.; Erickson, D.; Fall, R.; Geron, C.; Graedel, T.; Harley, P.; Klinger, L.; Lerdau, M.; McKay, W. A.; Pierce, T.; Scholes, B.; Steinbrecher, R.; Tallamraju, R.; Taylor, J.; Zimmerman, P. *J. Geophys. Res. - Atmos.* **1995**, *100*, 8873.

(18) Lurmann, F. W.; Main, H. H. Sacramento, CA, 1992.

(19) Thornton, J. A.; Kercher, J. P.; Riedel, T. P.; Wagner, N. L.; Cozic, J.; Holloway, J. S.; Dube, W. P.; Wolfe, G. M.; Quinn, P. K.; Middlebrook, A. M.; Alexander, B.; Brown, S. S. *Nature* **2010**, *464*, 271.

(20) Atkinson, R. *Journal of Physical and Chemical Reference Data* **1997**, *26*, 215.

(21) Atkinson, R. *Atmospheric Environment* **2000**, *34*, 2063.

(22) Bernstein, J. A.; Alexis, N.; Barnes, C.; Bernstein, I. L.; Nel, A.; Peden, D.; Diaz-Sanchez, D.; Tarlo, S. M.; Williams, P. B. *Journal of Allergy and Clinical Immunology* **2004**, *114*, 1116.

(23) Leikauf, G. D. *Environmental Health Perspectives* **2002**, *110*, 505.

(24) Uysal, N.; Schapira, R. M. *Current Opinion in Pulmonary Medicine* **2003**, *9*, 144.

(25) Wigle, D. T.; Arbuckle, T. E.; Walker, M.; Wade, M. G.; Liu, S. L.; Krewski, D. *Journal of Toxicology and Environmental Health-Part B- Critical Reviews* **2007**, *10*, 3.

(26) Sander, S. P.; Friedl, R. R.; Golden, D. M.; Kurylo, M.; Moortgat, G. K.; Wine, P. H.; Ravishankara, A. R.; Kolb, C. E.; Molina, M. J.; Finlayson-Pitts, B. J.; Huie, R. E.; Orkin, V. L. *Chemical Kinetics and Photochemical Data for Use in Atmospheric Studies, Evaluation Number 15*, 2006.

(27) Atkinson, R.; Baulch, D. L.; Cox, R. A.; Crowley, J. N.; Hampson, R. F.; Hynes, R. G.; Jenkin, M. E.; Rossi, M. J.; Troe, J. *Atmos. Chem. Phys.* **2004**, *4*, 1461.

(28) Simon, H.; Kimura, Y.; McGaughey, G.; Allen, D. T.; Brown, S. S.; Coffman, D.; Dibb, J.; Osthoff, H. D.; Quinn, P.; Roberts, J. M.; Yarwood, G.; Kemball-Cook, S.; Byun, D.; Lee, D. *Atmospheric Environment* **2010**, *44*, 5476.

(29) Simon, H.; Kimura, Y.; McGaughey, G.; Allen, D. T.; Brown, S. S.; Osthoff, H. D.; Roberts, J. M.; Byun, D.; Lee, D. *J. Geophys. Res.- Atmos.* **2009**, *114*.

(30) Wayne, R. P.; Barnes, I.; Biggs, P.; Burrows, J. P.; Canosamas, C. E.; Hjorth, J.; Lebras, G.; Moortgat, G. K.; Perner, D.; Poulet, G.; Restelli, G.; Sidebottom, H. *Atmospheric Environment Part A. - General Topics* **1991**, *25*, 1.

(31) Atkinson, R. *Journal of Physical and Chemical Reference Data* **1991**, *20*, 459.

(32) Chappuis, J. *Ann. d. l''ecole Norm. Sup.* **1882**, 159.

## *Chapter 2*

# CAVITY RINGDOWN SPECTROSCOPY AND THE APPARATUS

## 2.1 Introduction to cavity ringdown spectroscopy

Detection of trace species in the gas phase is of interest to many scientific communities, including analytical and spectroscopic chemists. Applications range widely, from quantification of intermediates in the atmosphere to medical diagnosis to detection of dangerous explosives for national security.[1-8] A variety of methods have been developed to study radicals, including photoacoustic spectroscopy,[9-11] laser-induced fluorescence (LIF),[12,13] and photoionization experiments.[14,15] We focus on optical cavity techniques in this chapter.

Traditional absorption spectroscopic experiments consist of a sample cell, laser source, and detector. The Beer-Lambert Law states that:

$$I = I_0 e^{-\sigma N L} \qquad (2.1\ \text{a})$$

where $I$ = the intensity of light transmitted through the sample cell, $I_0$ = the intensity of the incident light, $\sigma$ = the absorption cross section of the sample, $N$ = the concentration of the species, and $L$ = the pathlength of the absorbing sample. If the absorption cross section for a sample is known, the concentration of the species can be quantified. Difficulties arise when the cross section is small. The sensitivity of the technique could be vastly increased if the pathlength ($L$) is increased.

The method is also vulnerable to fluctuations in the laser intensity. If the cross section is small, the Beer-Lambert Law can be approximated as:

$$I = I_0 e^{-\sigma NL} \sim I_0(1-\sigma NL) \tag{2.1 b}$$

With simple algebra, the equation is rewritten as:

$$\sigma NL = \frac{\Delta I}{I_0} \tag{2.1 c}$$

If $\Delta I$ is a small quantity, noise from laser fluctuations masks any measured absorption signal. The ultrasensitive optical cavity technique, cavity ringdown spectroscopy (CRDS), addresses both pathlength and laser power issues directly.

CRDS has been reviewed in the literature.[6,7,16-19] We give a brief history and outline of the technique here. CRDS was developed in the early 1980s during experiments to measure the reflectivity of mirrors. These methods were quickly adapted to spectroscopic experiments.[18] Two highly reflective mirrors ($R$ > 99.99%) are placed at the end of a sample cell ($L$) to form an optical cavity. This arrangement immediately addresses the issue of pathlength, as the sample cell of a few centimeters becomes equivalent to a pathlength of several kilometers. The overall sensitivity of the system is increased by $10^3$-$10^4$ orders of magnitude.

A pulsed CRDS experiment illustrates the insensitivity of CRDS to fluctuations in the laser power (Fig. 2.1). A laser pulse with coherence less than $L$ is injected into the empty cavity. When the pulse hits the surface of the mirror before the detector, >99.99% of the light is reflected back toward the first mirror. Some light ($T = 1 - R$) however is transmitted to the detector. The pulse travels to the first mirror and loses intensity from transmission and mirror diffraction losses before it is reflected back to the other mirror. The transmitted light to the detector is less than the previous measurement. This process repeats until the detector can no longer measure the low intensity of the pulse. The pattern of the collected signal is a "ringdown."

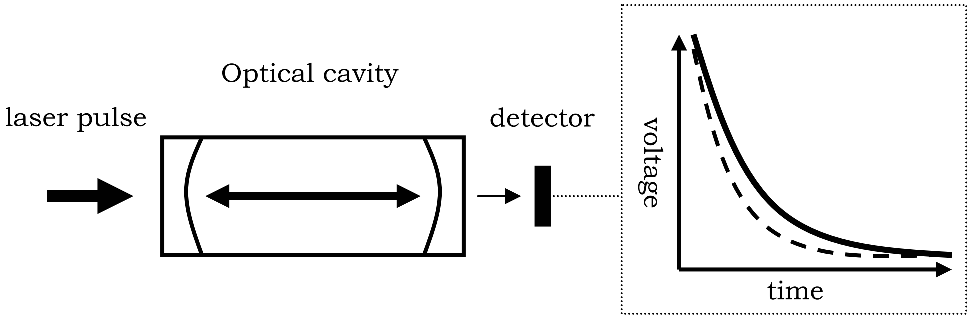

**Figure 2.1.** Schematic of a laser pulse injected into an optical cavity ($L$) for a pulsed CRDS experiment. The detector records signal from an empty cavity (bold line) and an absorber cavity (dashed line). The decay is much faster with the absorber cavity. By comparing the rates of decay, the absorption coefficient for the absorber can be extracted.

The losses in the empty cavity are described mathematically as:

$$\text{total loss} = \frac{\#\ \text{reflections}}{\text{trip}} \times \frac{\text{loss from transmission}}{\text{reflection}} \times \#\ \text{trips} \tag{2.2}$$

$$= 2 \times (1-R) \times \frac{tc}{2L}$$

Following Beer-Lambert's law, we write for the empty cavity

$$I(t) = I_0 e^{-(1-R)\frac{tc}{L}} \tag{2.3}$$

and define a time constant or ringdown time $\tau_{vac}$:

$$\tau_{vac} = \frac{L}{c(1-R)} \tag{2.4}$$

If an absorbing species is added to the cavity, then the total loss includes contribution from the sample absorbance:

$$\begin{aligned} \text{total loss} &= \frac{\text{\# reflections}}{\text{trip}} \times \frac{\text{loss from transmission + absorbance}}{\text{reflection}} \times \text{\# trips} \\ &= 2 \times [(1-R)+\sigma NL'] \times \frac{tc}{2L} \end{aligned} \tag{2.5}$$

where $L'$ = the absorbance pathlength, which does not necessarily have to equal the pathlength of the optical cavity ($L$), e.g., the distance between the two reflective mirrors.

We then write for the absorbance cavity:

$$I(t) = I_0 e^{-\{(1-R)+\sigma NL'\}\frac{tc}{L}} \tag{2.6}$$

and ringdown time $\tau_{abs}$:

$$\tau_{abs} = \frac{L}{c\{(1-R)+\sigma NL'\}} \tag{2.7}$$

The difference between the inverse of the absorber and vacuum ringdown times is directly related to the absorption coefficient $\alpha$ of the sample:

$$\alpha = \sigma N = \frac{L}{cL'}\left(\frac{1}{\tau_{abs}} - \frac{1}{\tau_{vac}}\right) \tag{2.8 a}$$

By comparing the rates of decay of a cavity with and without an absorber, the absorption coefficient of the sample can be measured. CRDS therefore does not suffer from fluctuations in the laser power, as the measurements are independent of intensity.

Current research on CRDS is focused on increasing the quality or *Q*-factor of the cavity. The *Q*-factor refers to the ratio of energy stored in the cavity versus the energy that is lost. Many groups have focused on coupling the laser to the modes of the cavity for efficient energy transfer. The sensitivities of CRDS and its variants have been reported to be on the order of $10^{-6}$ to $10^{-14}$ per pass.[19-34] The sensitivity of our pulsed CRDS apparatus is on the order of $10^{-6}$ to $10^{-8}$ per pass. Details on the calculation of our sensitivity are in Appendix 2.1.

The absorption coefficient is wavelength dependent. In expression 2.7 for the ringdown constant, both the reflectivity of the mirrors ($R$) and the absorption cross section of the sample ($\sigma$) is wavelength dependent. For spectroscopic experiments, both absorbance and vacuum (background) ringdowns must be collected at each spectral wavelength of interest. There are also other experimental factors to be considered for spectroscopic studies.

Lasers in spectroscopic measurements should be chosen such that their line widths are narrower than the width of the absorption of interest (Fig. 2.2). If a laser interacts with multiple absorption lines, the resulting signal has multi-exponential components. While absorption coefficients can be extracted,[35,36] the analysis is more involved. The absorption cross section of the sample of interest also cannot be too large. Otherwise, the signal decays so rapidly that the detector cannot collect an adequate number of data points for exponential fit of the decay. Zalicki and Zare calculated that the absorbance has to be less than $0.1(1-R)$ for accurate quantification.[35] Thus, CRDS is ideal for spectroscopic studies of trace gas species with relatively small absorption cross sections.

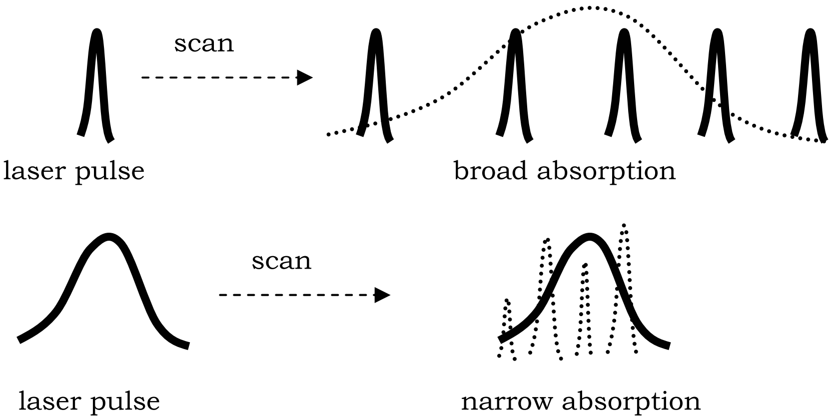

**Figure 2.2.** Illustrations of a laser (bold line) scanning over broad and narrow absorption lines (dotted lines). When the line width of the laser pulse is wider than the absorption lines, problems occur with the analysis, as multiple absorption lines interact with the laser, each with a different exponential decay constant.

For a 50-cm cell and mirrors $R = 0.9999$, the ringdown constant for an empty cavity is 16.7 μs. If we generate $10^{14}$ radicals with cross sections $\sigma = 10^{-20}$ cm$^2$, the ringdown constant becomes 11.1 μs. Thus, detection and kinetic measurements can be conducted on the microsecond timescale. We utilize both the sensitivity and fast time response of CRDS to probe trace atmospheric radicals in the near-infrared (NIR) region. We discuss in the next section the advantages of NIR detection and how we generate NIR light in our laboratory.

## 2.2 The Raman cell as a near-infrared source

While many tunable sources in the visible region are commercially available, there have historically been fewer options in the IR and even fewer options in the NIR regions. One of the main spectroscopic advantages of conducting experiments in the NIR region is less spectral interference. NIR transitions include vibrational overtones and low-lying electronic transitions of radicals. The strengths of these transitions are orders of magnitude weaker than the line strengths in the visible region. Absorption by background species such as water is therefore significantly reduced. There is a trade-off as the radical of interest also has weaker absorption cross sections in the NIR region; however a sensitive technique such as CRDS can overcome these problems. The NIR has provided a new spectral window for many molecular species.[37-42]

Research on new IR sources has exploded in the past two decades. Advances include development of quantum cascade lasers, laser diodes, fiber optics, supercontinuum sources, and difference frequency generation in various crystals.[43-50] The expense and simplicity of the sources vary widely. For laboratories that already utilize tunable visible sources, one simple and economic method to generate tunable NIR light is addition of a Raman cell to the apparatus. The underlying physics is discussed here, along with details of the Raman cell.

The Raman cell consists of a 2-m long metal cell with two silver-coated mirrors at each end. The mirrors have holes in their centers to allow passage of light in and out of the cell. The entrance port of the Raman cell includes an additional "pick-off" mirror attached to the mirror mount. The silver mirrors and pick-off mirror can be aligned in a multipass configuration. We generally operate in a 3-pass configuration, with 200 psi hydrogen in the Raman cell. Specific alignment procedures, along with photos of the cell, can be found in Appendix 2.2. Blueprints of the Raman cell have previously been published in a senior member's thesis.[51]

**Raman scattering**

Stokes: $E = h\nu - \Delta E_{stokes}$

Anti-Stokes: $E = h\nu + \Delta E_{stokes}$

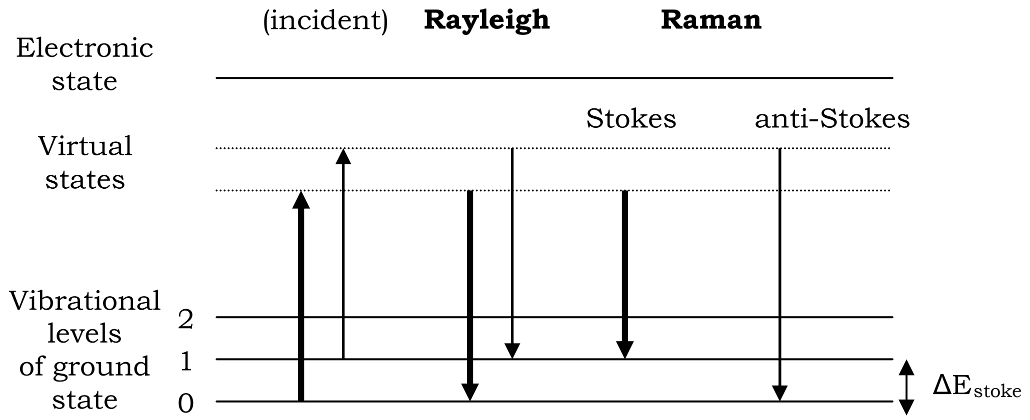

**Figure 2.3.** Diagram of the Rayleigh and Raman scattering upon interaction of the hydrogen molecules with incident light in the Raman cell. The majority of the light is Rayleigh scattered. Some light however is Raman-shifted to longer (Stokes shift) and shorter (anti-Stokes shift) wavelengths.

A diagram of the interaction between the hydrogen molecules and incident light is shown in Fig. 2.3. At room temperature, the majority of the hydrogen molecules occupy the ground electronic state. When light enters the cell, the molecules are excited to the virtual states. The virtual states are not electronic states; thus, these are not electronic transitions. Most of the hydrogen molecules relax back to the ground state, emitting photons of the same wavelength. This is Rayleigh scattering.

Some molecules, however, relax to the excited vibrational states rather than the ground state of hydrogen and emit photons of longer wavelengths (lower energy). This is Raman scattering, with the shift in the photon energy called the Stokes shift. The most intense band results from the first order Stokes shift, in which hydrogen molecules relax to the first vibrational state. The second most intense band results from second order Stokes shift, in which hydrogen molecules relax to the second vibrational state.

At room temperature, there are some hydrogen molecules that already occupy vibrational levels of the ground state. Upon interaction with light, the same scattering phenomena occur. Some of the excited hydrogen molecules can relax to the ground state and emit photons of shorter wavelengths (higher energy). This shift in energy is called anti-Stokes shift. Due to Boltzmann weighting, the intensity of the anti-Stokes-bands is less than the Stokes bands.

The value of the Stokes shift is species dependent, as it relates to the vibrational level of the species. The Stokes shifts for several gases have been reported in the literature, including methane (2916 $cm^{-1}$) and hydrogen (4155 $cm^{-1}$).[52,53] We use hydrogen in our Raman cell. In a typical experiment, the incident light is in the visible region (e.g., $\lambda = 640$ nm at 10 mJ/pulse). The first and second order Stokes outputs (<1 mJ/pulse) are then 872 nm (11470 $cm^{-1}$) and 1367 nm (7315 $cm^{-1}$), respectively. As we use a tunable dye laser to generate visible light, the incident light can easily be tuned to generate tunable NIR light for the CRDS experiments.

## 2.3 The pulsed CRDS apparatus

We use pulsed CRDS to study vibronic transitions of atmospheric species in the NIR region. A diagram of the apparatus is shown in Fig. 2.4. A Nd:YAG laser (Continuum NY61, 532 nm at 100-150 mJ/pulse) is fired at 5/20 Hz to pump a tunable dye laser (Continuum TDL51, $\Gamma = 0.15$ $cm^{-1}$), generating 10-15 mJ/pulse of visible light. Before entering the Raman cell ($P_{H2} = 200$ psi), the beam is propagated by various optics to reduce hot spots and obtain a Gaussian or TM00 mode beam profile. Telescope lens are used to adjust the beam diameter such that the laser pulse does not harm the silver mirrors of the Raman cell. The beam however is focused inside the Raman cell for optimum NIR conversion.

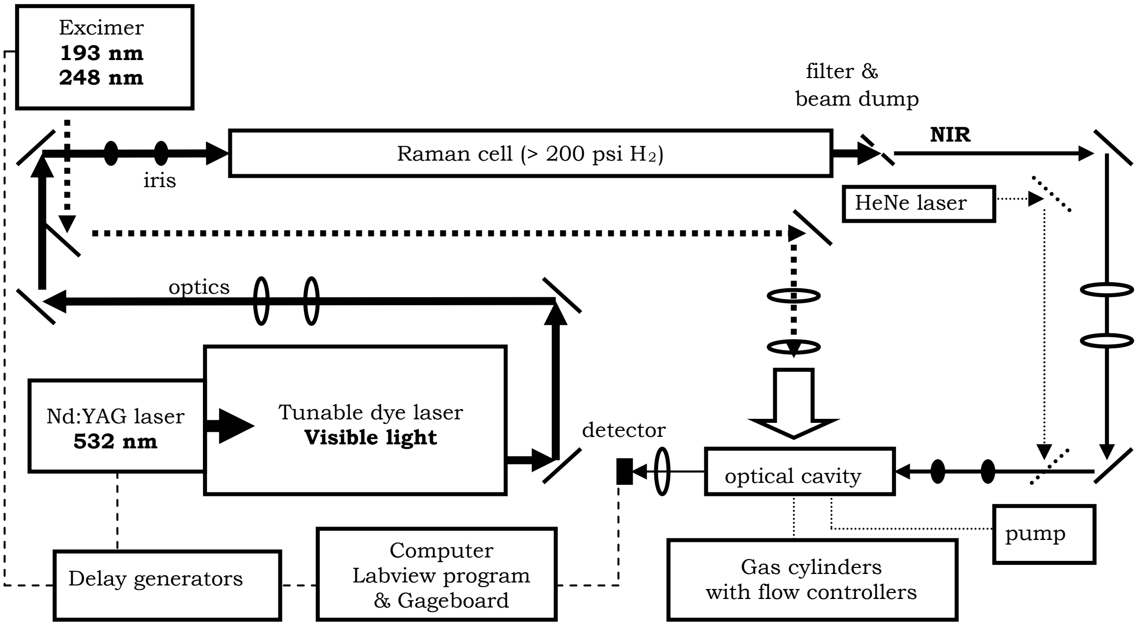

**Figure 2.4.** Schematics of our pulsed CRDS apparatus. The HeNe laser is used for alignment of the optical cavity. Each of the components are discussed in the Chapter 2 appendix. The sensitivity of the apparatus ranges from $\alpha = 10^{-6}$ to $10^{-8}$ per pass, depending on the CRD mirror and ringdown cell utilized in the optical cavity.

Upon exit of the Raman cell, a silicon filter is used to isolate the NIR light of interest (< 1 mJ/pulse). The NIR light is directed toward the optical cavity, with another set of telescope lens to re-focus the beam. After the laser pulse enters the optical cavity, NIR signal is focused with a 10-mm focal lens and collected by a 1-mm diameter InGaAs photodiode with a built-in transimpedance amplifier (Thorlabs PDA 400). Each decay is recorded by a transient digitizer computer board (Gage Compuscope 14100), operating at 20 MHz sampling rate. Five to twenty waveforms are collected before being averaged and fit with an exponential curve in our Labview data collection and analysis program. An overview of the

Labview program is provided in Appendix 2.3.1. The sensitivity of our apparatus ranges from $10^{-6}$ to $10^{-8}$ per pass.

The optical cavity is shown in Fig. 2.5. The optical cavity has been designed to simply alignment while maximizing flexibility. Two metal flanges with CRD mirrors mounts (Newport) are attached to Pyrex couplers that connect directly to the ringdown cell. Windows on the flanges allow NIR light to enter the cell. They also maintain the pressure of the cell. The flanges include gas ports such that helium/nitrogen purge gases can be flowed during the experiments to protect the CRD mirrors. Blueprints of the flanges have been previously published.[51]

We use a variety of Pyrex and stainless steel ringdown cells for our experiments. The choice of ringdown cell depends highly on the nature of the experiment. Most ringdown cells have multiple ports for chemical gas input and pressure readout. As we conduct most experiments under flow conditions, we also connect our ringdown cell to the mechanical vacuum pump. To minimize wall-reactions, many of the cells are coated with Fluoropel. There are various types of Fluoropel. Some are UV-sensitive; others do not adhere to stainless steel. The appropriate Fluoropel sample should be used to coat the ringdown cell for each experiment.

The volumes of the ringdown cells can also largely vary. While it is advantageous to have larger concentrations of radicals for CRDS detection, the mechanical pump has a limited pumping rate. For large volumes, the flow rates of the gases are reduced, increasing the residence time of the reacting species inside the cell. Some radicals have long lifetimes (~ms) and can be studied under long residence time conditions. In other cases, especially for the kinetic experiments, a small volume cell must be used. Diagrams of the ringdown cells and a list of our CRD mirrors are available in Appendix 2.3.2. The alignment of the optical cavity is also discussed in the appendix.

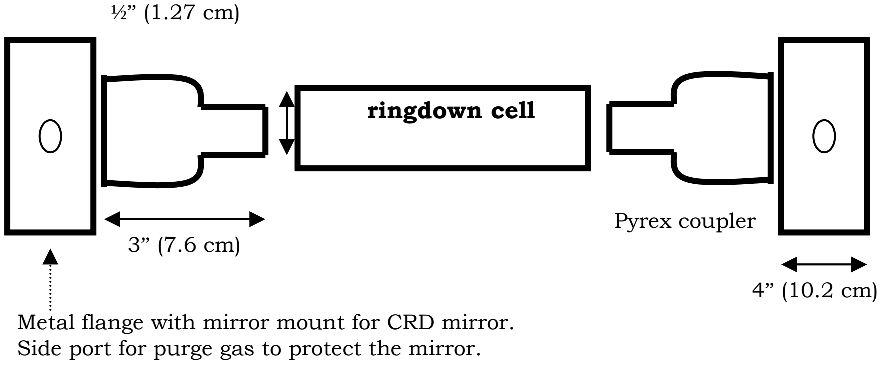

**Figure 2.5.** Diagram of the CRD optical cavity used in our laboratory. The ringdown cell can be easily decoupled from the apparatus such that we can switch in and out the desired cell. The metal flanges holding the CRD mirrors can also be removed without disturbing the ringdown cell such that we can clean or switch the CRD mirrors between experiments.

We conduct experiments over a large wavelength region of interest. Due to the simplicity of the Raman cell, scanning across a large wavelength region mostly involves changing the dyes of the dye laser and the CRD mirrors of the optical cavity. For each dye change, the dye laser is realigned and optimized for power. The position of the dye laser wavelength is also recalibrated. We use a combination of optogalvanic spectroscopy and CRDS for calibration. Details are available in Appendix 2.3.3. The recipes for the various laser dyes covering the 580-670 nm region are also provided in the appendix.

In general, the Nd:YAG and dye lasers used in the apparatus are very durable and, with basic maintenance, can be used for a long time in the laboratory. We provide notes on the general maintenance of the lasers in Appendix 2.3.4. We also utilize a third laser for many of the kinetic experiments, the fluorine excimer laser. The fluorine excimer laser (Lambda Physick LPF 220, 193/248 nm: 60-150 mJ/pulse) generates high energy UV pulses to initiate radical formation. We control the timing between the firing of the fluorine excimer and Nd:YAG (probe) lasers such that time-resolved measurements can be made. The timing conditions are discussed in Appendix 2.3.5.

The shape and size of the excimer beam are controlled by two optical lens, an UV fused silica plano-convex cylindrical lens (Thorlabs F-500mm) and an UV plano-concave lens (Edmund Optics 50.8 mm x 100 FL). The excimer beam is focused 0.5~1-cm wide and stretched to match the dimensions of the quartz window of the ringdown cell. Measurements of the excimer power are made at both the exit of the laser and directly before the ringdown cell. This is especially critical in the case of 193-nm light, as absorption by oxygen greatly decreases the power of light over a long distance. We use a beam blocker, in conjunction with a power detector, to check that the excimer beam profile is uniform.

Photolytic chemical systems are also used to characterize the excimer laser source. We align the UV lenses to maximize radical production. If the reactant concentrations and the photolysis rates are known, we can quantify the amount of radical formation and directly calculate the energy of the excimer pulse inside the ringdown cell. Specific details are given in Chapter 5. Discussion on the chemical methods and modeled kinetics of nitrate and substituted peroxy radicals are reserved until their respective chapters.

## 2.4 Summary

In this chapter, we discussed the chemical physics behind CRDS and provided details of the pulsed CRDS apparatus used in our experimetns. The advantages of spectroscopic studies in the NIR region were also outlined. The appendix for Chapter 2 contains a detailed account of the lasers and computer programs used in our laboratory. Appendix 2.4 is particularly recommended for persons interested in working in the laboratory, as it reviews many lab safety issues.

As we better understand the CRDS apparatus, we discuss in the next chapters the different chemical systems and radicals probed by the apparatus. In Chapter 1, we showed that the understanding of the Earth's atmosphere involves elucidation of both the chemical physics and kinetics of a radical. We begin in the next chapter with a chemical physics perspective. The problem however maintains a firm root in atmospheric chemistry, as we focus on analysis of the most important nighttime oxidant in the troposphere, the nitrate radical.

## 2.5 References

(1) Fiddler, M. N.; Begashaw, I.; Mickens, M. A.; Collingwood, M. S.; Assefa, Z.; Bililign, S. *Sensors* **2009**, *9*, 10447.

(2) Nakaema, W. M.; Hao, Z. Q.; Rohwetter, P.; Woste, L.; Stelmaszczyk, K. *Sensors* **2011**, *11*, 1620.

(3) Wang, C. J.; Sahay, P. *Sensors* **2009**, *9*, 8230.

(4) Senesac, L.; Thundat, T. G. *Mater. Today* **2008**, *11*, 28.

(5) Wallin, S.; Pettersson, A.; Ostmark, H.; Hobro, A. *Anal. Bioanal. Chem.* **2009**, *395*, 259.

(6) Friedrichs, G. *Zeitschrift Fur Physikalische Chemie-International Journal of Research in Physical Chemistry & Chemical Physics* **2008**, *222*, 31.

(7) Wheeler, M. D.; Newman, S. M.; Orr-Ewing, A. J.; Ashfold, M.N. R. *Journal of the Chemical Society-Faraday Transactions* **1998**, *94*, 337.

(8) Ball, S. M.; Jones, R. L. *Chemical Reviews* **2003**, *103*, 5239.

(9) Zoltan, B.; Andrea, P.; Gabor, S. *Applied Spectroscopy Reviews* **2011**, *46*, 1.

(10) Foster, N. S.; Autrey, S. T.; Amonette, J. E.; Small, J. R.; Small, E. W. *American Laboratory* **1999**, *31*, 96S.

(11) Bertrand, L. G. *Journal of the Optical Society of America a-Optics Image Science and Vision* **1985**, *2*, P6.

(12) Daily, J. W. *Progress in Energy and Combustion Science* **1997**, *23*, 133.

(13) Kohsehoinghaus, K. *Progress in Energy and Combustion Science* **1994**, *20*, 203.

(14) Zimmermann, R.; Welthagen, W.; Groger, T. *Journal of Chromatography A* **2008**, *1184*, 296.

(15) Ledingham, K. W. D.; Singhal, R. P. *International Journal of Mass Spectrometry and Ion Processes* **1997**, *163*, 149.

(16) Brown, S. S.; Stark, H.; Ravishankara, A. R. *Applied Physics B-Lasers and Optics* **2002**, *75*, 173.

(17) *Cavity Ringdown Spectroscopy: An Ultratrace-Absorption Measurement Technique*; Busch, K. W.; Busch, M. A., Eds.; Oxford University Press, 1999.

(18) Scherer, J. J.; Paul, J. B.; Okeefe, A.; Saykally, R. J. *Chemical Reviews* **1997**, *97*, 25.

(19) Berden, G.; Peeters, R.; Meijer, G. *International Reviews in Physical Chemistry* **2000**, *19*, 565.

(20) Foltynowicz, A.; Ma, W. G.; Axner, O. *Optics Express* **2008**, *16*, 14689.

(21) Engel, G. S.; Drisdell, W. S.; Keutsch, F. N.; Moyer, E. J.; Anderson, J. G. *Applied Optics* **2006**, *45*, 9221.

(22) O'Keefe, A.; Scherer, J. J.; Paul, J. B. *Chemical Physics Letters* **1999**, *307*, 343.

(23) Berden, G.; Peeters, R.; Meijer, G. *Chemical Physics Letters* **1999**, *307*, 131.

(24) Peeters, R.; Berden, G.; Meijer, G. *American Laboratory* **2001**, *33*, 60.

(25) Foltynowicz, A.; Schmidt, F. M.; Ma, W.; Axner, O. *Applied Physics B - Lasers and Optics* **2008**, *92*, 313.

(26) Schmidt, F. M.; Foltynowicz, A.; Ma, W. G.; Lock, T.; Axner, O. *Optics Express* **2007**, *15*, 10822.

(27) van Leeuwen, N. J.; Wilson, A. C. *Journal of the Optical Society of America B-Optical Physics* **2004**, *21*, 1713.

(28) Hall, J. L.; Ye, J.; Diddams, S. A.; Ma, L. S.; Cundiff, S. T.; Jones, D. J. *Ieee Journal of Quantum Electronics* **2001**, *37,* 1482.

(29) Ye, J.; Hall, J. L. *Physical Review A* **2000**, *61*.

(30) Ye, J.; Hall, J. L.; Diddams, S. A. *Optics Letters* **2000**, *25*, 1675.

(31) Yoon, T. H.; Ye, J.; Hall, J. L.; Chartier, J. M. *Applied Physics B-Lasers and Optics* **2001**, *72*, 221.

(32) Ma, L. S.; Ye, J.; Dube, P.; Hall, J. L. *Journal of the Optical Society of America B-Optical Physics* **1999**, *16*, 2255.

(33) Havey, D. K.; Long, D. A.; Okumura, M.; Miller, C. E.; Hodges, J. T. *Chemical Physics Letters* **2009**, *483*, 49.

(34) Long, D. A.; Havey, D. K.; Okumura, M.; Miller, C. E.; Hodges, J. T. *Physical Review A* **2010**, *81*.

(35) Zalicki, P.; Zare, R. N. *Journal of Chemical Physics* **1995**, *102*, 2708.

(36) Mollner, A., *Ph. D. Thesis*, California Institute of Technology, 2007.

(37) Donaldson, D. J.; Tuck, A. F.; Vaida, V. *Chemical Reviews* **2003**, *103*, 4717.

(38) Vaida, V. *Journal of Physical Chemistry A* **2009**, *113*, 5.

(39) Sharp, E. N.; Rupper, P.; Miller, T. A. *Physical Chemistry Chemical Physics* **2008**, *10,* 3955.

(40) Liu, Z. W.; Xu, Y.; Yang, X. F.; Zhu, A. M.; Zhao, G. L.; Wang, W. G. *Journal of Physics D - Applied Physics* **2008**, *41*.

(41) Enami, S.; Yamanaka, T.; Hashimoto, S.; Kawasaki, M.; Aloisio, S.; Tachikawa, H. *Journal of Chemical Physics* **2006**, *125*.

(42) Hirota, E.; Ishiwata, T.; Kawaguchi, K.; Fujitake, M.; Ohashi, N.; Tanaka, I. *Journal of Chemical Physics* **1997**, *107*, 2829.

(43) Angel, S. M.; Carrabba, M.; Cooney, T. F. *Spectroc. Acta Pt. A-Molec. Biomolec. Spectr.* **1995**, *51*, 1779.

(44) Curl, R. F.; Capasso, F.; Gmachl, C.; Kosterev, A. A.; McManus, B.; Lewicki, R.; Pusharsky, M.; Wysocki, G.; Tittel, F. K. *Chemical Physics Letters* **2010**, *487*, 1.

(45) Fischer, C.; Sigrist, M. W. In *Solid-State Mid-Infrared Laser Sources*; Springer-Verlag Berlin: Berlin, 2003; Vol. 89, p 97.

(46) Gmachl, C.; Capasso, F.; Sivco, D. L.; Cho, A. Y. *Reports on Progress in Physics* **2001**, *64*, 1533.

(47) Hugi, A.; Maulini, R.; Faist, J. *Semiconductor Science and Technology* **2010**, *25*.

(48) Richter, D.; Fried, A.; Weibring, P. *Laser & Photonics Reviews* **2009**, *3*, 343.

(49) van Helden, J. H.; Hancock, G.; Peverall, R.; Ritchie, G. A. D. *Journal of Physics D - Applied Physics* **2011**, *44*.

(50) Yin, S.; Ruffin, P.; Brantley, C.; Edwards, E.; Yang, C. E.; Luo, C. In *Photonic Fiber and Crystal Devices: Advances in Materials and Innovations in Device Applications Iv*; Yin, S., Guo, R., Eds. 2010; Vol. 7781.

(51) Deev, A., California Institute of Technology, 2005.

(52) Rabinowitz, P.; Perry, B. N.; Levinos, N. *IEEE Journal of Quantum Electronics* **1986**, *22*, 797.

(53) Aniolek, K. W.; Miller, D. L.; Cernansky, N. P.; Owens, K. G. *Applied Spectroscopy* **1997**, *51*, 820.

# Appendix for Chapter 2

## Appendix 2.1 Calculation of the sensitivity

In section 2.1, we wrote an expression for the absorption coefficient (2.8a). We rewrite the equation here in terms of absorbance as:

$$A = \sigma N L' = \frac{L}{c}\left(\frac{1}{\tau_{abs}} - \frac{1}{\tau_{vac}}\right) = \frac{L}{c} \times \frac{\Delta\tau}{\tau_{vac}} \times \frac{1}{\tau_{abs}} \qquad (2.8\ \text{b})$$

At the beginning of our experiments, we collect ten ringdown signals and calculate both the standard deviation and average of the ringdown constants. Depending on the alignment of the optical cavity, values for $\Delta\tau/\tau$ range from 0.1-0.7 %. The distance between the CRD mirrors is determined by the length of the ringdown cell ($L$ = 40-70 cm); the reflectivity of our mirrors ($R$) range from 0.9995-0.9999%. A diagram of the ringdown cells and a list of CRD mirrors are provided in Appendix 2.3.2.

Suppose $L$ = 70 cm, $\Delta\tau/\tau$ = 0.4%, and $1/\tau$ = 67000 (corresponding to a ringdown time of 15 µs). The sensitivity or minimum absorbance is:

$$\begin{aligned} A = \frac{70}{3 \times 10^{10}} \times \frac{0.4}{100} \times 67000 &= 6.3 \times 10^{-7} \text{ minimum absorbance/pass} \\ &= 0.63 \text{ ppm/pass} \end{aligned} \qquad (\text{A-2.1})$$

Sensitivity is often reported as the value for which the observed absorption has a signal-to-noise ratio (S/N) = 3 or 5. The calculated $A_{min}$ is multiplied by the desired S/N accordingly.

The sensitivity can also be reported to take into account the length of the sample cell and the number of ringdown signals averaged for data analysis:

$$\frac{A}{L} = 8.9 \times 10^{-9} \text{ min absorbance/cm}$$

$$\frac{A}{L} \times \sqrt{\frac{\text{\# avg ringdowns}}{\text{repetition rate of laser}}} = \frac{A}{L} \times \sqrt{\frac{10}{5\text{ Hz}}} = 1.26 \times 10^{-8} \text{min absorbance/cm/Hz}^{\frac{1}{2}}$$

(A-2.2 a-b)

Thus, special attention should be given to the units for comparison of sensitivities of different apparatuses.

## Appendix 2.2 Photos and alignment of the Raman cell

This section provides instructions on how to align the Raman cell with a HeNe laser. The HeNe light is guided into the Raman cell through the entrance port and is reflected back and forth in the cell *n* number of times before exiting the cell. Alignment is easier once the components of the Raman cell are understood.

The Raman cell in our apparatus consists of a 2-m stainless steel tube with mirror/flange attachments at each end. Blueprints of the Raman cell have been published.[1] A basic diagram of the Raman cell is shown in Fig. A-2.1. The viewport consists of a window connected to a metal piece (copper gasket seal). The metal piece lowers a contraption with two small mirrors into the Raman cell. The contraption is high enough that it does not interfere with the passing light beam. The mirrors are angled such that the entrance and exit of the Raman cell can be viewed from inside the cell.

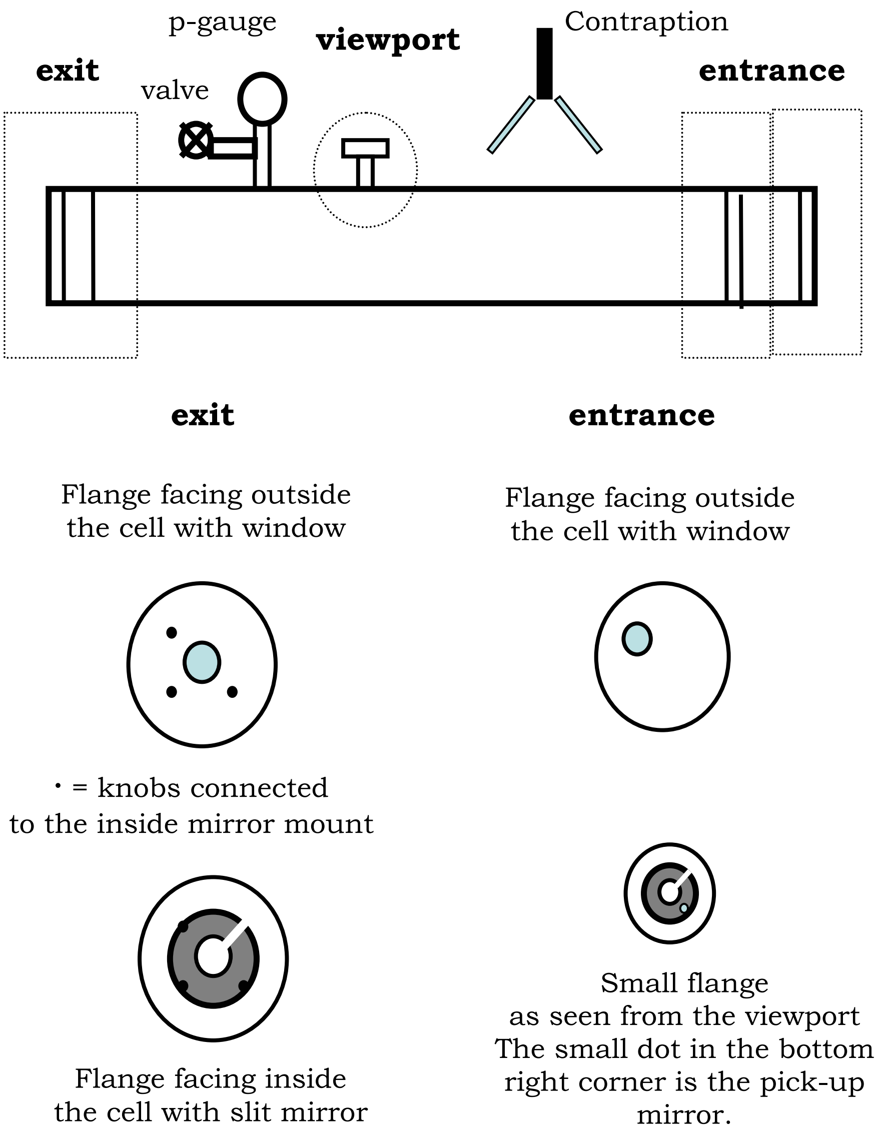

**Figure A-2.1** Diagram of the 2-m stainless steel Raman cell used in the laboratory. Individual components are highlighted, including the exit and entrance flanges and the viewport.

The metal flange that bolts to the exit side of the cell (o-ring seal) has attachments on both sides of the flange. A small flange holding a BK7 window (o-ring seal) is attached to the center of the flange surface facing outside the cell. A mirror mount holding a modified 3-inch diameter silver-coated mirror is attached to the flange surface facing inside the cell.

The knobs to the mirror mount are bored through the flange such that adjustments can be made from outside the cell.

The metal flange that bolts to the entrance side of the cell (o-ring seal) has a BK7 window (o-ring seal) located in the upper left corner of the flange surface facing outside the cell. Removal of the flange reveals a small flange inside the cell, directly attached to the stainless steel tube by four long screws. A tiny mirror mount for the "pick-up" mirror is located at the bottom of the screws. A larger mirror mount, supporting a 3-inch slit silver-coated mirror identical to the one on the exit flange, is on small flange itself (Fig. A-2.2).

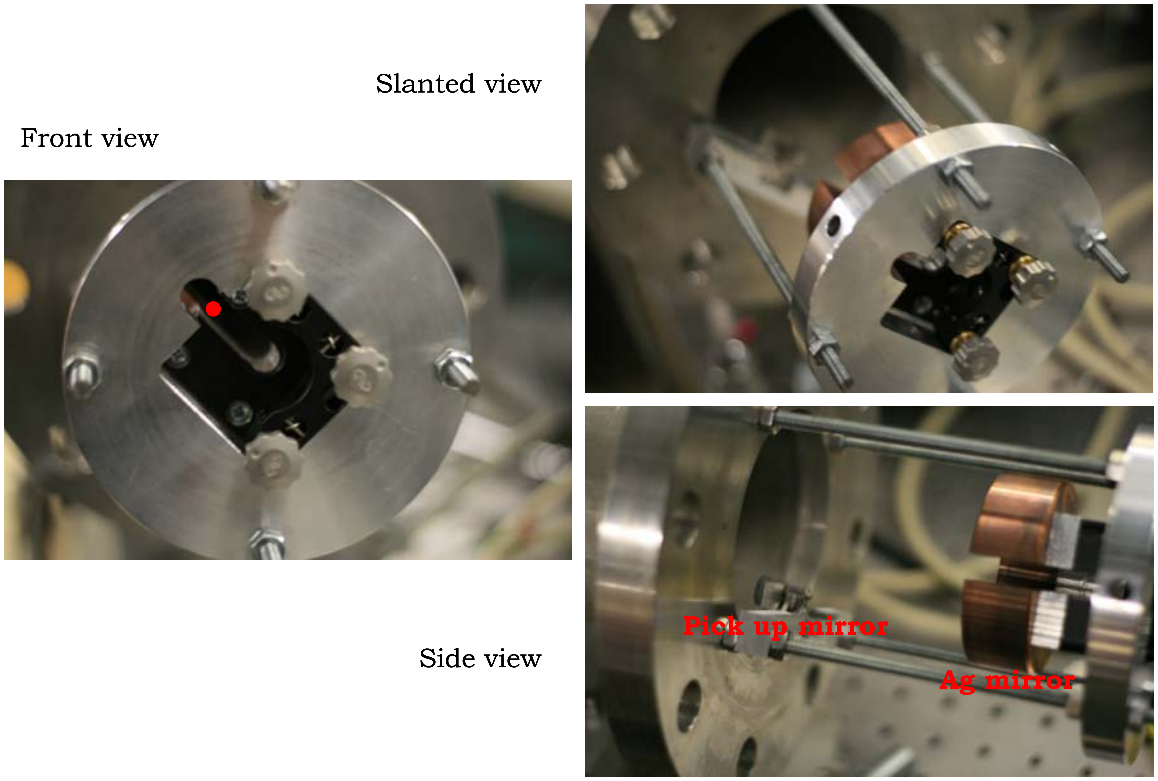

**Figure A-2.2.** Photos of the small flange on the entrance side of the Raman cell. The photo of the front view of the small flange shows a circular shape cutout. One would assume that the cutout is centered with the window on the entrance flange. Closer examination however shows that there is a slight misalignment of the two pieces and the "center" of the window is the marked red spot in the photograph.

Alignment of the Raman cell is recommended for two people. The procedure is as follows:

1. Remove the entrance and exit flanges. Use two mirrors to guide a HeNe laser beam directly through the cell, preferably traveling through the marked spot (Fig. A-2.2). As the cell is 2-m long, the HeNe beam tends to hit the inner walls. Vertical alignment of the HeNe beam is recommended before horizontal alignment. The two mirrors will be called the "HeNe mirrors" in the following instructions.

2. Re-attach the exit flange. To minimize leaks, grease the o-rings with Apiezon L. From the viewport, check to see whether the beam is hitting the silver mirror mounted to the exit flange. Adjust the HeNe mirrors accordingly. Arrange two irises to mark the HeNe beam pathway. From this point on, do NOT touch the HeNe mirrors.

3. There are two mirrors mounted on the entrance side, the pick-up mirror and the silver coated mirror. The Raman cell can be aligned like a Herriot cell for n(odd) passes. The beam is reflected by the silver-coated mirrors on the exit and entrance sides until the last pass, in which the beam hits the pick up mirror and is guided outside the Raman cell through a window. Difficulty in the alignment differs greatly on the choice of configuration.

For conversion to second order Stokes, a 3-pass configuration is sufficient. Simply, adjust the mirror mount on the exit flange such that the HeNe beam is directed towards the pick-up mirror. This can be observed through the viewport. For a 3-pass configuration, the silver-coated mirror on the entrance port never has to be touched.

4. Adjust the pick-up mirror mount such that the beam is traveling through the center of the window on the exit side. The HeNe beam should be visible outside the Raman cell. Put the entrance flange back on the Raman cell.

5. Once HeNe alignment is completed, pump down the cell and do a leak test of the Raman cell. Water from the air can contaminate the cell. If the cell is not leaking, fill the cell with hydrogen gas (~200 psi). Replace the HeNe laser with the laser of interest and align with the same irises. Minor adjustments may have to be made, but Stokes and anti-Stokes outputs, in addition to the origin laser beam (Rayleigh-scattered light), should be observed from the exit of the Raman cell.

In the CRD experiments, visible light from the dye laser is injected into the Raman cell. The conversion efficiency of the visible light to NIR light is inversely proportional to the diameter of the beam. The silver mirrors are however easily damaged by focused light. Telescope lens (- and + focal lens) can be arranged such that the laser beam is large entering the cell but focuses in the middle of the cell. While the alignment can be done with a HeNe laser, re-check the focal point with the dye laser output before directing the dye laser light into the cell.

## Appendix 2.3 Details of the pulsed CRDS apparatus

### A-2.3.1 Overview of the Labview programs

Our data collection and analysis programs are written in Labview version 8.5. The current programs are outlined here. Codes for the programs can be found on the Okumura acquisition computer, under folder "Noyes 105 Data Programs."

The main data collection program is called "mainprogram_excimer2.vi." The front panel is shown in Fig. A-2.3. Each Boolean option opens a subprogram that carries out the selected function. The "Diagnostic" option opens the "readboard.vi" subprogram to collect and analyze ringdown signals. The "Move the dye laser" option opens the "movedyelaser2_dr.vi" subprogram to change the wavelength of the dye laser and thus the wavelength of the NIR light used in the CRDS experiments. The "Excimer on and off" option controls firing of the excimer laser. Finally, the "Scan region" option utilizes all listed subprograms to collect CRD spectra.

The "readboard.vi" subprogram works directly with the digitizer board (Gage CompuScope 14100) installed on the acquisition computer to collect decay signals from the detector of our CRDS apparatus. The subprogram serves as an interface to the digital oscilloscope such that the voltage scale and sampling rate can be adjusted. Data collection begins when the program receives a trigger TTL pulse from delay generator (BNC 555). The delay generator controls firing of all lasers in the CRDS apparatus (Appendix 2.3.5). The ringdown signal is collected and fit to an exponential decay. Both the ringdown constant and its inverse are reported. The number of acquisitions can also be adjusted in the subprogram.

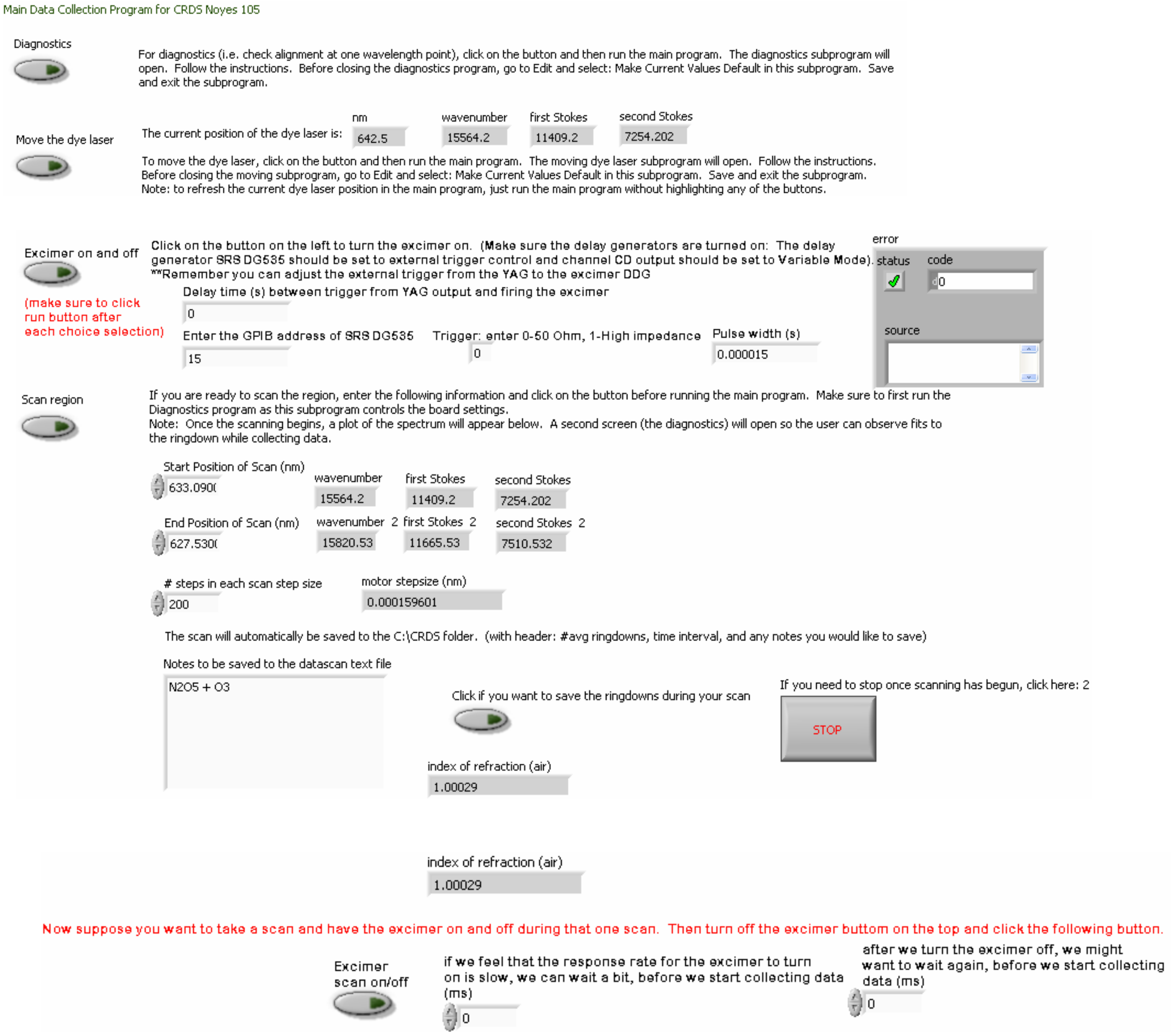

Main Data Collection Program for CRDS Noyes 105

Diagnostics

For diagnostics (i.e. check alignment at one wavelength point), click on the button and then run the main program. The diagnostics subprogram will open. Follow the instructions. Before closing the diagnostics program, go to Edit and select: Make Current Values Default in this subprogram. Save and exit the subprogram.

Move the dye laser

The current position of the dye laser is: nm 642.5 wavenumber 15564.2 first Stokes 11409.2 second Stokes 7254.202

To move the dye laser, click on the button and then run the main program. The moving dye laser subprogram will open. Follow the instructions. Before closing the moving subprogram, go to Edit and select: Make Current Values Default in this subprogram. Save and exit the subprogram. Note: to refresh the current dye laser position in the main program, just run the main program without highlighting any of the buttons.

Excimer on and off

(make sure to click run button after each choice selection)

Click on the button on the left to turn the excimer on. (Make sure the delay generators are turned on: The delay generator SRS DG535 should be set to external trigger control and channel CD output should be set to Variable Mode). **Remember you can adjust the external trigger from the YAG to the excimer DDG

Delay time (s) between trigger from YAG output and firing the excimer: 0

Enter the GPIB address of SRS DG535: 15

Trigger: enter 0-50 Ohm, 1-High impedance: 0

Pulse width (s): 0.000015

error

status ✓

code 0

source

Scan region

If you are ready to scan the region, enter the following information and click on the button before running the main program. Make sure to first run the Diagnostics program as this subprogram controls the board settings. Note: Once the scanning begins, a plot of the spectrum will appear below. A second screen (the diagnostics) will open so the user can observe fits to the ringdown while collecting data.

Start Position of Scan (nm): 633.090( wavenumber 15564.2 first Stokes 11409.2 second Stokes 7254.202

End Position of Scan (nm): 627.530( wavenumber 2 15820.53 first Stokes 2 11665.53 second Stokes 2 7510.532

# steps in each scan step size: 200

motor stepsize (nm): 0.000159601

The scan will automatically be saved to the C:\CRDS folder. (with header: #avg ringdowns, time interval, and any notes you would like to save)

Notes to be saved to the datascan text file: N2O5 + O3

Click if you want to save the ringdowns during your scan

If you need to stop once scanning has begun, click here: 2

index of refraction (air): 1.00029

index of refraction (air): 1.00029

Now suppose you want to take a scan and have the excimer on and off during that one scan. Then turn off the excimer buttom on the top and click the following button.

Excimer scan on/off

if we feel that the response rate for the excimer to turn on is slow, we can wait a bit, before we start collecting data (ms): 0

after we turn the excimer off, we might want to wait again, before we start collecting data (ms): 0

**Figure A-2.3.** A snapshot of the front panel of the main data collection program "mainprogram_excimer2.vi" Spectra with the excimer on and off are plotted below the panel, such that the user can observe the spectra as data is collected

The subprogram "movedyelaser2_dr.vi" controls the position of the dye laser through DAQ card (NI USB-6008). The DAQ card sends a TTL pulse to a step motor connected to the grating of the dye laser. The step motor rotates counter or counterclockwise, according to high or low voltage input from the computer. Given two dye laser positions (nm), the subprogram calculates how many TTL pulses need to be sent to the step motor to adjust the grating of the dye laser accordingly. Details of the circuit connecting the DAQ card to the dye laser step motor are available in Appendix 2.3.4.

Collection of CRD spectra is more involved. Before any scan, the settings in "readboard.vi" should be selected and saved in the file. The gage board settings cannot be changed once the scan is started. To collect a spectrum with the excimer continuously on, the front panel options "scan region" and the "excimer on and off" should be highlighted simultaneously. To collect a spectrum with the excimer off, the "excimer on and off" button should not be highlighted. The beginning and end wavelengths of the scan and the step size of the scan are manually entered in the front panel. The wavelengths refer to the position of the dye laser. Thus, for scans in the NIR region, the appropriate wavelengths in the visible must be selected. For example, to scan the 7000-7100 $\text{cm}^{-1}$ range, the difference in indexes of refraction for air and vacuum must be taken into account (Appendix 2.3.3) before calculating the corresponding wavelengths of light in the visible, 653.4-648.7 nm.

$$\begin{gathered} 7000-7100\ \text{cm}^{-1} \xrightarrow{\text{correct index of refraction}} 6995-7105\ \text{cm}^{-1} \\ \frac{10^7}{6995+2*4155(\text{Stokes})} = 653.4\ \text{nm} \\ \frac{10^7}{7105+2*4155(\text{Stokes})} = 648.7\ \text{nm} \end{gathered} \tag{A-2.3}$$

The step size of the scan refers to the number of TTL pulses that are sent to the step motor before data collection. The "motor stepsize" on the front panel provides the effective nm-wavelength scale for one TTL pulse.

The program automatically saves a text file with all the wavelengths and inverse ringdown time constants at each scanning point. The averaged ringdown signals for each scanning point can also be saved in separate text files by selecting "Click if you want to save the ringdowns during your scan" on the front panel. Once all the options have been selected or entered, the main program can be run. The program will ask the user to check the gage board settings and scanning range before initiating the scan.

The main program calls the "movedyelaser2_dr.vi" to move the position of the dye laser to the starting wavelength of the scan. The "readboard.vi" collects and fits the ringdown signals. The "corrected" dye laser position (see Appendix 2.3.3) and inverse ringdown constant are plotted on the main screen. The "movedyelaser2_dr.vi" then moves the dye laser by the user-selected step size. The process repeats until the end of the scanning range. If the scan has to be stopped during the middle of the experiment, the "Stop" Boolean button, and not the "Stop" of the "mainprogram_excimer_2.vi," should be selected.

To collect simultaneous spectra during a photolysis experiment for excimer on and off, select the "excimer scan on/off" button located at the bottom of the front panel. The Boolean "Excimer on and off" button should not be selected. Instructions for other inputs remain the same. Once the scan is started, the main program uses an additional subprogram to control the firing of the excimer laser. Specific details of the external control of the excimer are reserved until Appendix 2.3.5. To briefly summarize, the computer controls a delay generator connected to the excimer such that the excimer fires at a specified time before the ringdown signal is collected by the detector. At each scanning wavelength, the main program turns the excimer on and collects the ringdown signals using "readboard.vi." After the averaged ringdown signal has been collected, the computer turns off the excimer and repeats the collection of ringdown signals.

We mainly use the previous program for data collection. When we switch laser dyes, we use the Labview program "Calibration of the dye laser.vi" to calibrate the position of the dye laser in the visible region. Specifics of the calibration procedure are provided in Appendix 2.3.3 The program has a very similar format to the main data collection program. The main difference is that the program collects optogalvanic spectra rather than CRD spectra. Thus, the "readboard.vi" is replaced by "optogalvanic.vi", which analyzes optogalvanic signals by integrating the areas beneath the signals.

Smaller subprograms are stored in the "Noyes 105 Data Programs" folder. Most do simple calculations such as determination of the residence time given the voltage of the flow meters. One program compares CRD background spectra with a reference water spectrum to calculate the concentration of water in the cell. Labview significantly eases the daily operation of the apparatus; thus future lab members should continue to update and add to the current collection of programs and subprograms.

### A-2.3.2 Components of the optical cavity

A diagram of the optical cavity was shown in Fig. 2.5. We use a variety of ringdown cells in our laboratory. For long residence time experiments, we use long multi-port Pyrex cells (Fig. A-2.4). For photolysis experiments, we use stainless steel cells with quartz windows of various sizes (Fig. A-2.5). We also use multiple CRD mirrors to scan different regions of interest. A list of the current CRD mirrors in the laboratory is provided in Table A-2.1. 1" Teflon adapters are used to mount smaller diameter (0.8 ") mirrors into our 1" Newport mirror mounts.

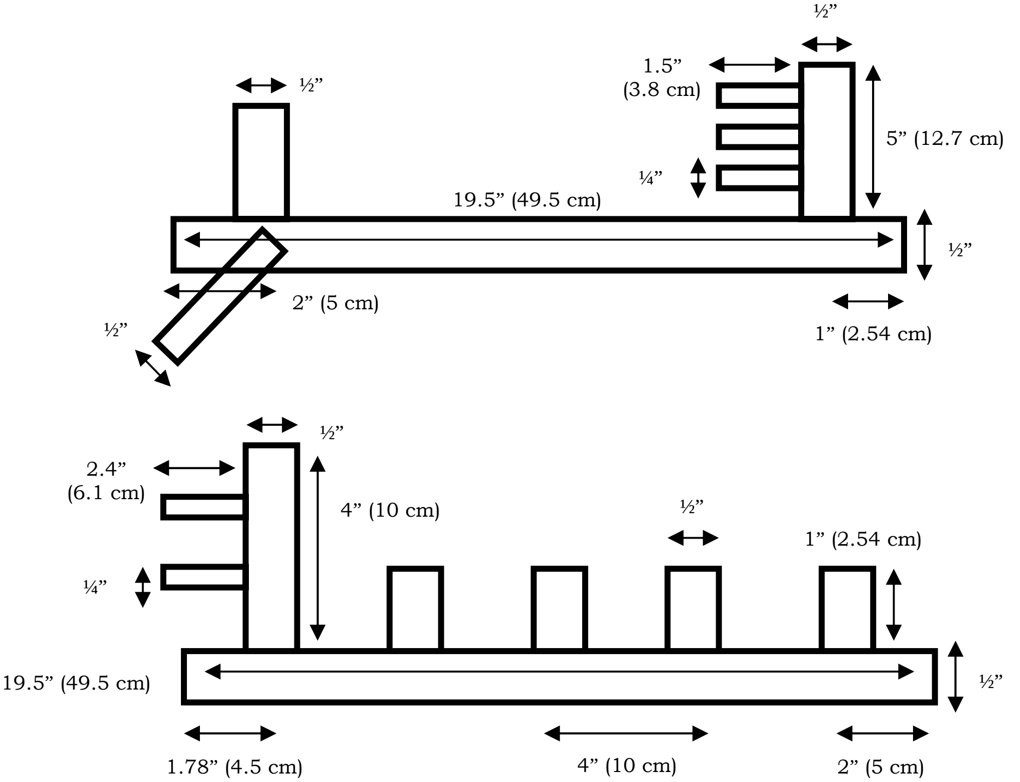

**Figure A-2.4.** Schematic of Pyrex cells used for long residence time CRD experiments.

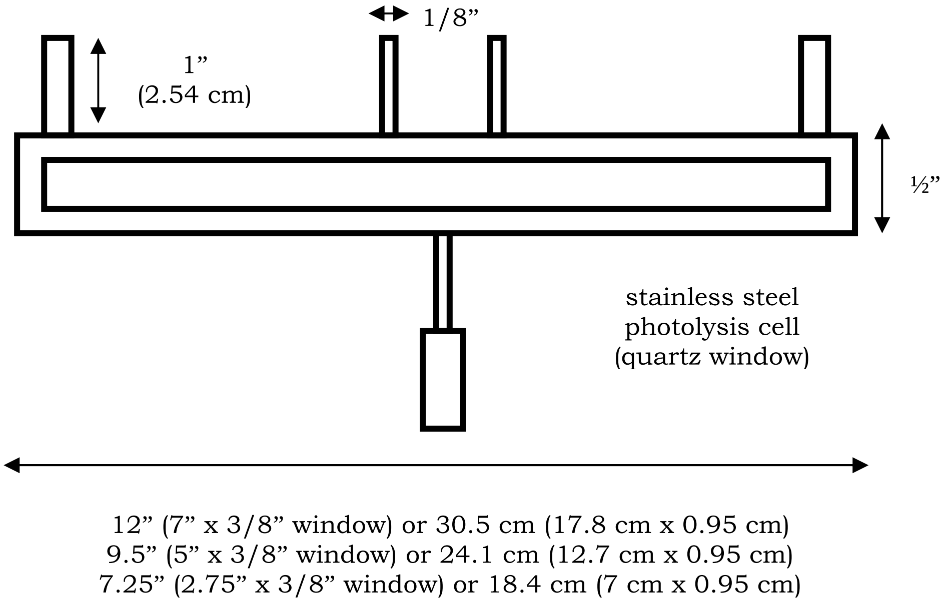

**Figure A-2.5.** Schematic of stainless steel cells with quartz windows used for CRD photolysis experiments

| Company | Center | Reflectivity | Diameter |
|---|---|---|---|
| LGR | 490 nm | 99.995 % | 0.8" |
| Newport | 623 nm | 99.97 % | 1" |
| Nova Wave | 690 nm | 99.9975 % | 1" |
| LGR | 950 nm | 99.99 % | 0.8" |
| Newport | 1060 nm/9434 $cm^{-1}$ | 99.97 % | 1" |
| LGR | 1200 nm/8333 $cm^{-1}$ | 99.99 % | 0.8" |
| LGR | 1315 nm/7600 $cm^{-1}$ | 99.985 % | 1" |
| LGR | 1330 nm/7519 $cm^{-1}$ | 99.99 % | 1" |
| Layertec | 1390 nm/7194 $cm^{-1}$ | 99.99 % | 1" |
| ATF | 1390 nm/7194 $cm^{-1}$ | n/a | 1" |
| LGR | 1400 nm/7143 $cm^{-1}$ | 99.995 % | 1" |
| Nova Wave | 1550 nm/ 6452 $cm^{-1}$ | 99.9975 % | 1" |
| Newport | 1550 nm/6452 $cm^{-1}$ | 99.97 % | 1" |
| LGR | 2800 nm/3571 $cm^{-1}$ | 99.98 % | 0.8" |
| LGR | 2900 nm/3448 $cm^{-1}$ | 99.96 % | 0.8" |
| LGR | 3200 nm/3125 $cm^{-1}$ | 99.94 % | 0.8" |
| LGR | 3300 nm/3030 $cm^{-1}$ | 99.98 % | 0.8" |

**Table A-2.1.** List of CRD mirrors in the laboratory. The experiments in this work utilize the CRD mirrors in the NIR region (6400 - 8600 $cm^{-1}$).

On-axis alignment of the optical cavity is done with a HeNe laser (Fig. 2.4). The procedure is listed below:

1. Turn on the HeNe laser. A second mirror is inserted before the optical cavity along the path of the NIR beam. Mount the ringdown cell (Fig. 2.5) but wait to put on the metal flanges with the CRD mirrors.

2. If the irises have already been set to define a straight path through the ringdown cell, use the two mirrors to align the HeNe beam through the irises. Otherwise, align the beam such that the HeNe goes through the center of the ringdown cell. Fix the irises. Do not touch the HeNe laser beyond this point.

3. The detector (Thorlabs PDA 400) is mounted to a two-dimensional micrometer translational stage. Although the detector consists of an InGaAs photodiode, it can still detect light from the HeNe laser. Insert a focal lens between the detector and exit of the ringdown cell such that the beam focuses before or after the surface of the photodiode. Adjust the vertical and horizontal positions of the detector to maximize the HeNe signal on an oscilloscope.

4. The CRD mirrors should be cleaned before alignment. The "drag-drop" method with methanol works well for most NIR CRD mirrors. On the side of the ringdown cell closest to the detector, mount the metal flange with the first CRD mirror. The reflective or coated surface should face inward. Part of the HeNe beam will be reflected. Use the mirror mount on the flange to direct the HeNe beam through the irises. Run the purge gas slowly to protect the CRD mirror from water in the air.

5. Mount the second flange with the second CRD mirror on the cell. Turn off the purge gas. Although the HeNe beam is hitting the non-coated side of the mirror, part of the beam will be reflected. Use the mirror mounts to direct the HeNe beam through the irises.

6. After both mirrors have been mounted, evacuate the cell. Turn off the HeNe laser and remove any mirrors blocking the pathway of the NIR light. Turn on the Nd:YAG and dye laser. Use an NIR card and a set of mirrors to align the NIR beam through the same irises. A ringdown signal should be observed on the oscilloscope. Adjustments can be made to the mirrors along the NIR pathway to achieve a good ringdown signal, i.e., a ringdown signal with a single exponential decay. The positions of the CRD mirrors can also change upon pressure change. Minor corrections can be made by adjusting the CRD mirror mounts. The Labview

"readboard.vi" program is used to analyze the ringdown signals on the computer.

### A.2.3.3 Calibration of the spectra

Calibration of NIR spectra involves two stages. First, the position of the dye laser is calibrated in the visible region using an optogalvanic spectroscopy apparatus. Second, the exact Stokes shift of the hydrogen gas is determined for calibration in the NIR region using our pulsed CRDS apparatus. We begin our discussion with the first stage of calibration.

There are three parameters of interest in the Labview data collection program with respect to the calibration of the wavelength of the dye laser:

1) the current dye laser wavelength (nm), which is stored in a file: "dyelaserposition.txt"
2) the step size of the dye laser motor (nm/TTL pulse), which is stored in a file: "stepsize.txt"
3) the index of refraction, which is stored in a file: "indexofrefraction.txt"

The first two parameters calibrate the wavelength of the dye laser output, as the beam is propagated through the air. We use the optogalvanic apparatus to adjust the two parameters.

Optogalvanic spectroscopy has been reviewed by Barbieri and Beverini.[2,3] The methodology is quick, inexpensive, and spectrally precise. The approach can be better understood by examining a diagram of the apparatus (Fig. A-2.6). In principle, any gas can be used. We use neon (Ne) gas due to the high number of atomic lines in the visible region and the NIST database of the Ne line positions.[4] The diagram shows a circuit with a simple $0.40 neon lamp. The signal-to-noise (S/N) can be vastly improved by using a hollow cathode tube filled with neon. The basic components and underlying science of the apparatus remain the same.

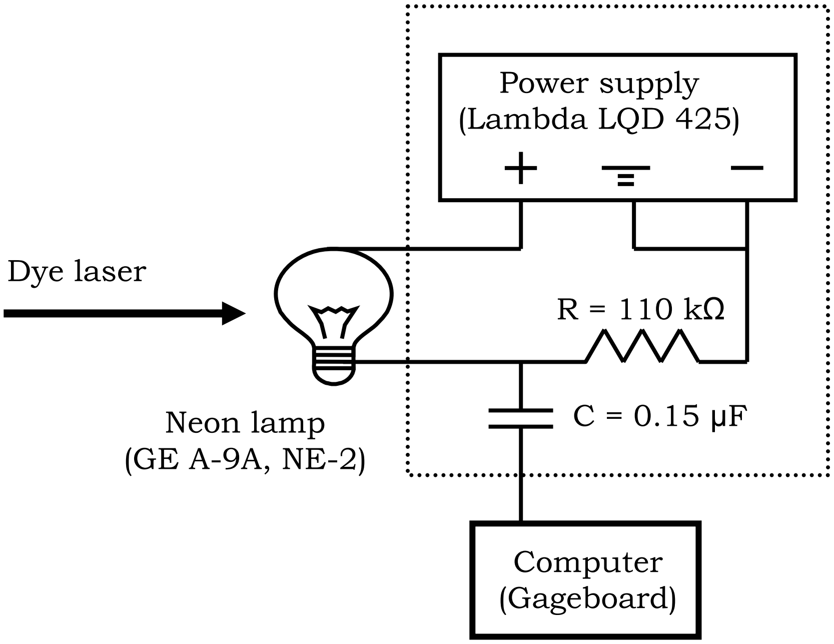

**Figure A-2.6.** Diagram of a basic optogalvanic apparatus that can be made from a cheap neon lamp. For better S/N, the neon lamp is replaced with a hollow cathode tube filled with neon and another homemade optogalvanic circuit (dashed square). The essential components of the two apparatuses remain the same.

The power supply provides current to the lamp. The Ne lamp begins to glow orange, as the gas is discharged. When light is shined on the neon discharge, populations of the excited and ground state neon atoms are affected. These effects are observed externally by changes in the conductivity of the lamp in the circuit. The change in the current can be measured directly by probing the voltage across the resistor (*R*). The change becomes more pronounced when the light is resonant with an atomic transition of neon. Cartoon depictions of the signal are shown in Fig. A-2.7.

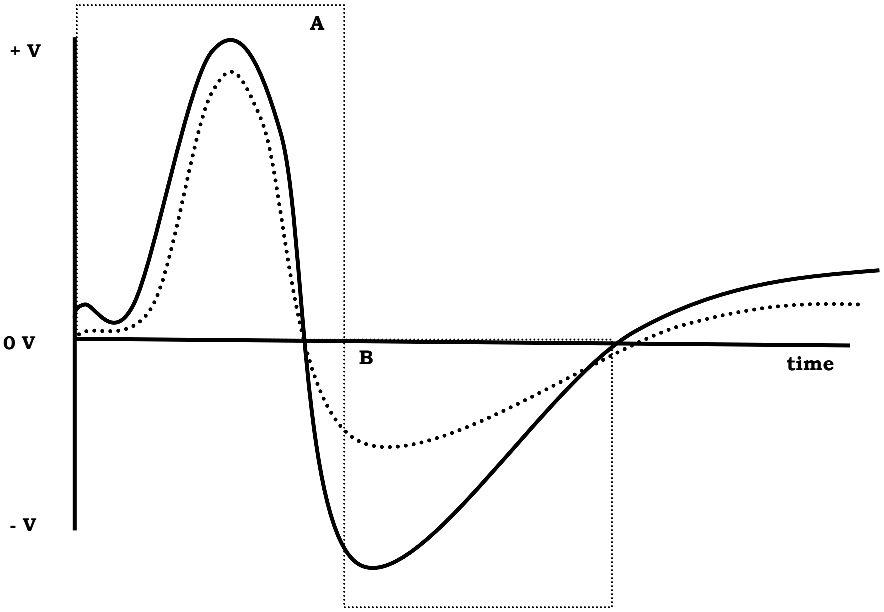

**Figure A-2.7.** Carton depictions of the voltage readout from an optogalvanic apparatus when the light is resonant (dark line) and non-resonant (dotted line) with a neon transition. The area underneath the voltage signal can be positive or negative depending on the sampling window. Sampling window A results in a positive sum or peak while sampling window B results in a negative sum or peak. Sampling window B results in a better S/N peak.

Elucidation of the time response is beyond the scope of this work. We instead probe the circuit for large changes in the voltage to identify the neon transitions. As the Ne transitions are known to high accuracy, the signals can be used to calibrate the dye laser position. We therefore use the Labview program "Calibration of the dye laser.vi" to scan the dye laser and collect signal from the optogalvanic apparatus at each scanning point.

The optogalvanic signal is processed in the Labview subprogram "optogalvanic.vi" using a simple box integrator. The area underneath the voltage signal is calculated and plotted against the wavelength. Areas underneath negative voltage signal is considered "negative." Depending on the shape of the signal and sampling window, the resultant sums can be positive or negative (Fig A-2.7). The peak position, however, should not change. To maximize the S/N of the peak, the sampling window should be chosen to contain the largest absolute change in the voltage signal. Optogalvanic spectra collected in various visible regions are shown in Fig. A-2.8. Recipes for the laser dyes used in the dye laser for each scan are listed in Table A-2.2.

| **Laser Dye** | **Wavelength Range** | **Oscillator & Amplifier** |
|---|---|---|
| Oxazine 720 | 664 - 672 nm | 117.5 mg/0.87 L & 69.3 mg/0.82 L |
| DCM | 620 - 653 nm | 22 mg/0.9 L & 158.3 mg/0.9 L |
| Rhodamine perchlorate 640 | 608 - 622 nm | 192 mg/0.9 L & 101 mg/0.9 L |
| Rh 640 | 603 - 613 nm | 143 mg/1.0 L & 19.0 mg/1.0 L |
| Rh 610 + Rh 640 | 594 - 610 nm | 19.2 mg Rh640 + 34.1 mg Rh 610/0.9 L<br>& 9.6 mg Rh 640 + 16.8 mg Rh610/0.9L |
| Rhodamine chloride 610 | 583 - 597 nm | 96 mg/0.9 L & 33.7 mg/0.9 L |

**Table A-2.2.** List of the dye laser recipes used in the experiments. The solvent for all mixtures is high grade methanol (water < 0.1%).

**Ox 720 laser dye**

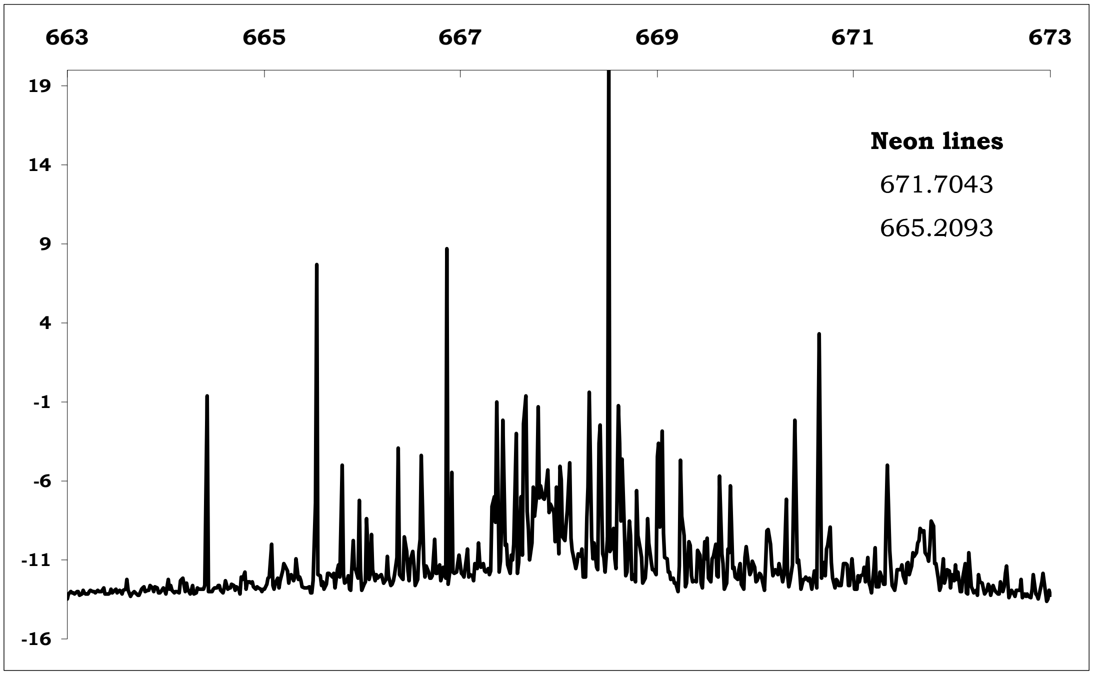

**DCM laser dye**

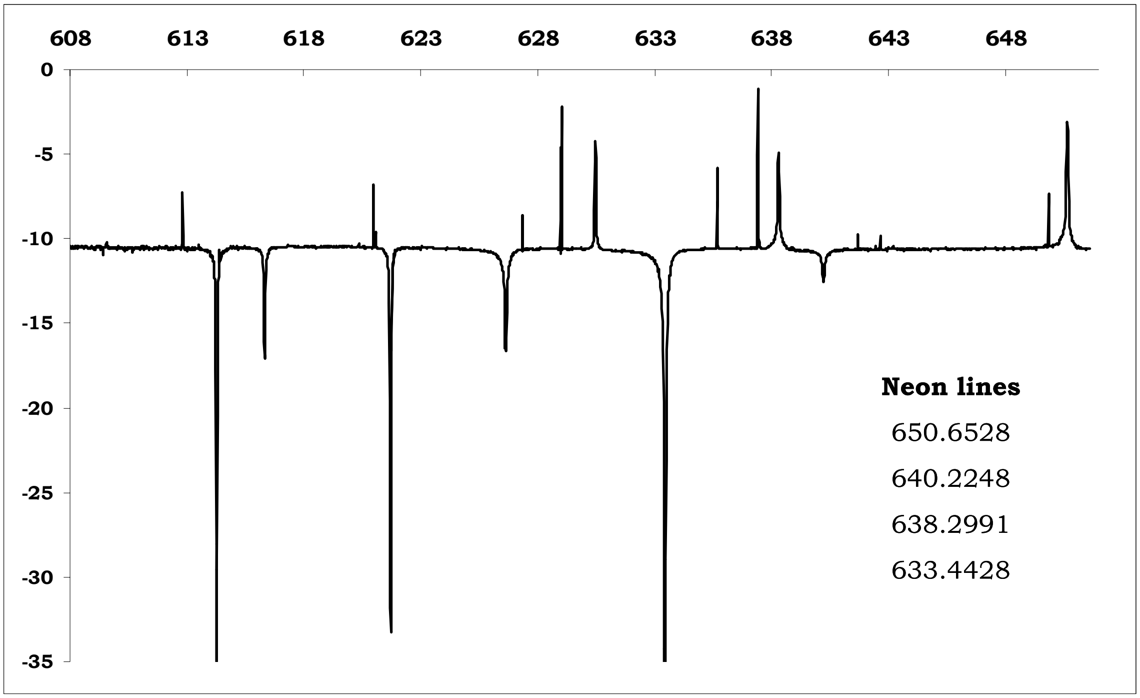

**Rh 640 laser dye**

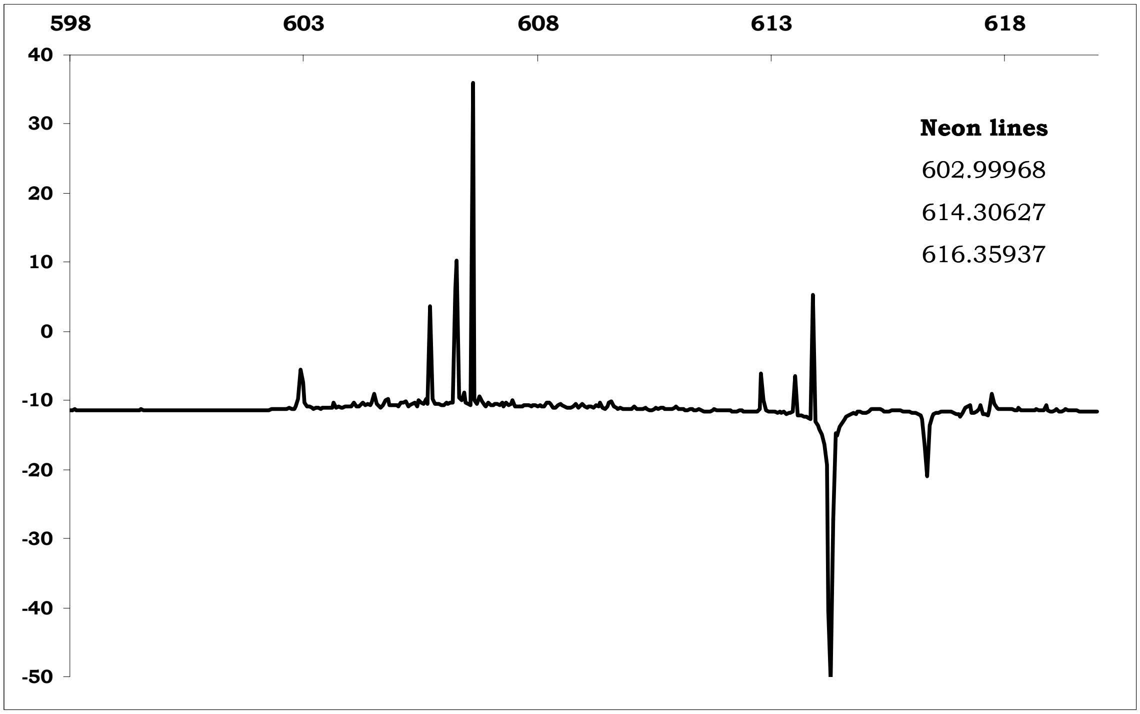

**Rh 610 + Rh 640 laser dye**

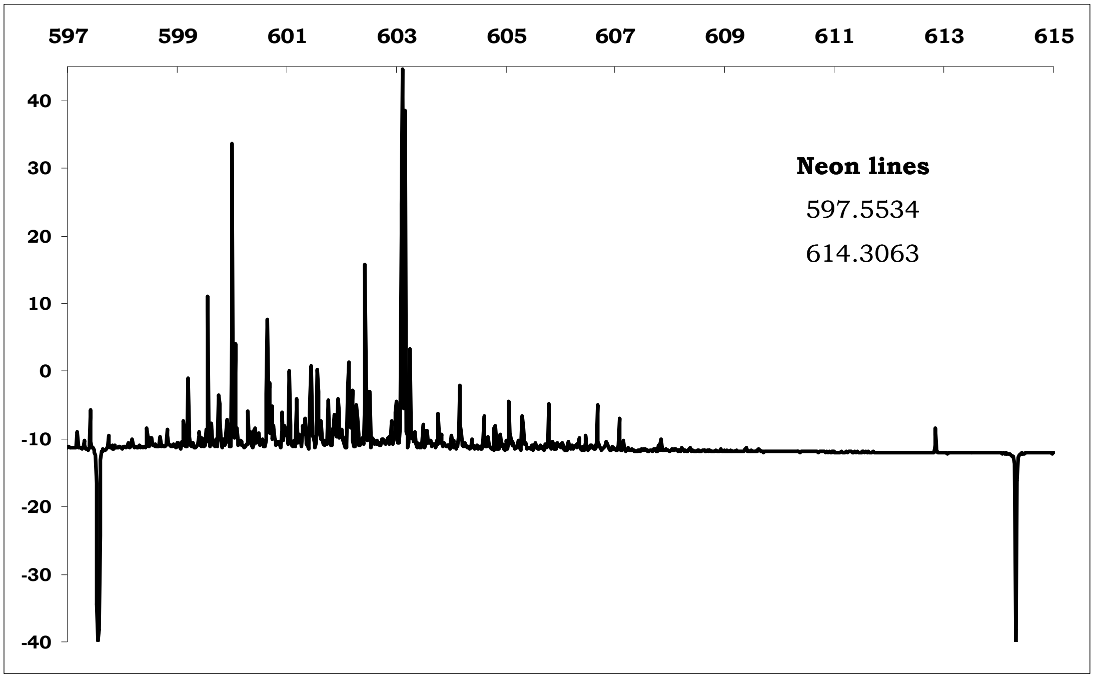

**Rh 610 laser dye**

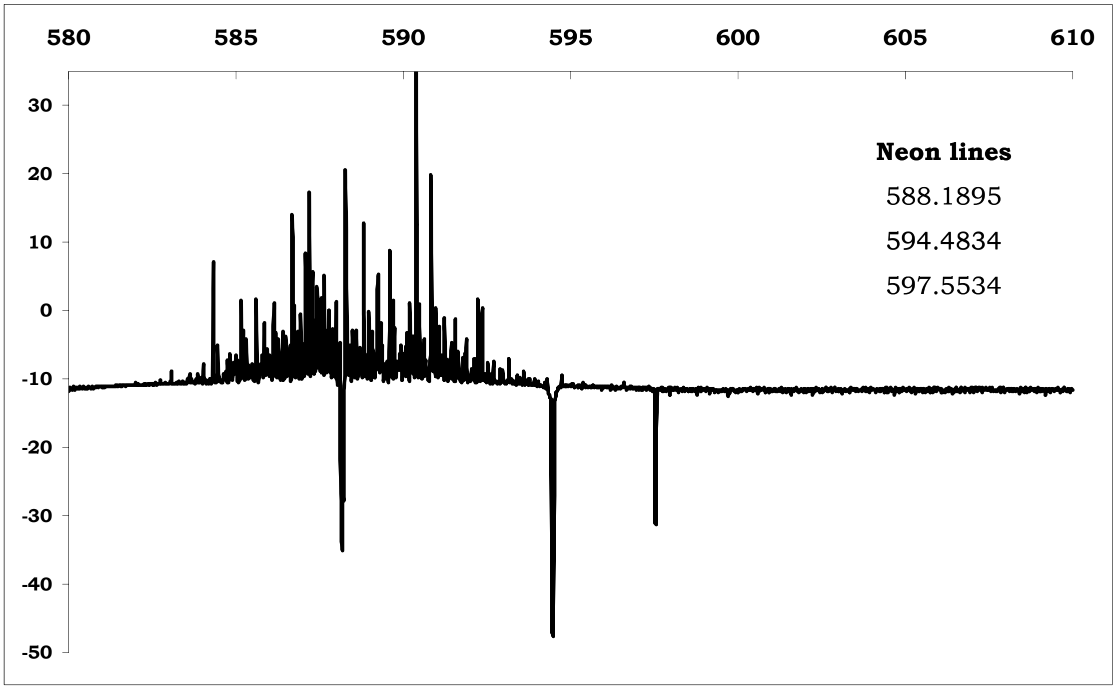

**Figure A-2.8.** Optogalvanic spectra collected in the visible regions using different laser dyes. The frequency axes and the neon lines are all in units of nm. The y-axis is arbitrary, as depending on the alignment, the relative intensities of the bands change. The line positions however are unaffected.

Each peak in the optogalvanic spectra can be fit with a Gaussian line shape to calculate the center of the peak:

$$y = Ae^{-\frac{(x-b)^2}{2c^2}} \tag{A-2.4}$$

where $A$ = amplitude of the peak, $b$ = center of the peak, and $c$ = width of the peak. The centers of the peak are compared to the Ne lines from the NIST database. Ideally, we analyze three peaks evenly spaced across the scanning range; however, as long as the lines are far apart, the analysis works well with even two lines. If there is a systematic difference between the data and NIST frequencies, we move the laser to the peak of interest and adjust the parameter "current dye laser position" to the equivalent NIST frequency. If the differences are not systematic, we adjust, in addition, the parameter controlling the step size of the motor. We first move the laser to the peak of interest and correct the "current dye laser position" as before; we then adjust the "step size of the motor" by:

$$\textit{new step size} = \frac{|\textit{NIST peak 1 - NIST peak 2}|}{\frac{|\textit{data peak 1 - data peak 2}|}{\textit{current step size}}} \tag{A-2.5}$$

The parameters described above involve corrections to the dye laser output as it propagates through the air. Many of our experiments, however, are done under vacuum. We must take into account the difference between the indexes of refraction of air ($n_{air} \neq 1$) and vacuum ($n_{vac}$ = 1).

$$\lambda_{vac}\upsilon = c \rightarrow \frac{\lambda_{vac}\upsilon}{n_{air}} = \frac{c}{n_{air}} \rightarrow \lambda_{dye}\upsilon = \frac{c}{n_{air}} \tag{A-2.6}$$

In the Labview program "Calibration of the dye laser.vi," we process all positions based on the wavelength of the dye laser $\lambda_{dye}$. For vacuum experiments, we switch to the "mainprogram_excimer2.vi." The program multiplies the wavelength by $n_{air}$ and reports the "dye laser" positions as the corrected value. The value of $n_{air}$ depends on the relative water composition of the air (1.00029 ~ 1.00033). Our current parameter for the index of refraction is set to 1.0029.

The best calibration method involves obtaining a reference spectrum in the experimental apparatus under similar temperature and pressure conditions. This is the second stage of our calibration process. Most of the pulsed CRDS experiments are conducted in the NIR region (7000-8700 $cm^{-1}$). Water lines are therefore used for calibration. The "mainprogram_excimer2.vi" program records the "corrected" dye laser position and the inverse of the ringdown constants for each wavelength position during a CRD scan. To convert the frequency-axis (nm) to wavenumbers ($cm^{-1}$) in the NIR region, the "corrected" dye laser positions are converted to wavenumbers in an Excel spreadsheet. The second order Stokes shift is then manually subtracted from the frequencies. We compare our CRD spectrum of water to the PNNL database[5] or Hitran[6] to determine the Stokes shift. The absolute lines positions are known to < 0.1 $cm^{-1}$. In our experiments, the Stokes shift of hydrogen ranges from 4155.15-4155.30 $cm^{-1}$.

### A.2.3.4 Laser maintenance

The Continuum manuals for both the Nd:YAG and dye lasers (NY61 and TDL 51 respectively) and the Laser Physik manual for the excimer laser (LPF 220) review the physical phenomena leading to light generation in great detail and provide protocols for laser alignment and maintenance.

We outline here only the issues that are not discussed in the manuals but are still needed for operation of the lasers.

*NY61 Nd:YAG laser*

The laser head consists of three major components: the housing, the flow tube, and the YAG rods. While most laser housings consist of silver or gold cavities, the NY61 cavity consists of an aluminum housing, packed with barium sulfate powder. The packing is directly related to the efficiency of the YAG power and needs to be replaced every 5-10 years. If the rubber silicone o-rings fail and water contaminates the powder, the packing needs to be replaced immediately. The flow tube is made of 5% Samarium-doped quartz. It not only absorbs UV light but also fluoresces pink light to contribute to the overall YAG power (~10-15%). Over time, the quartz material gets baked by the UV light and also needs to be replaced. In Fig. A-2.9, a photo of a damaged flow cell is shown. Finally, the YAG rods need to be polished and recoated every 5-10 years for peak laser performance.

For problems with low laser power, the protocols in the laser manual on laser alignment or replacement of the flashlamps should be first followed. If the efficiency of the laser power continues to decrease and there is no obvious damage to the optics, the laser head should be resent to the manufacturer (Continuum) or another laser refurbishing company (e.g. Kentek) for evaluation.

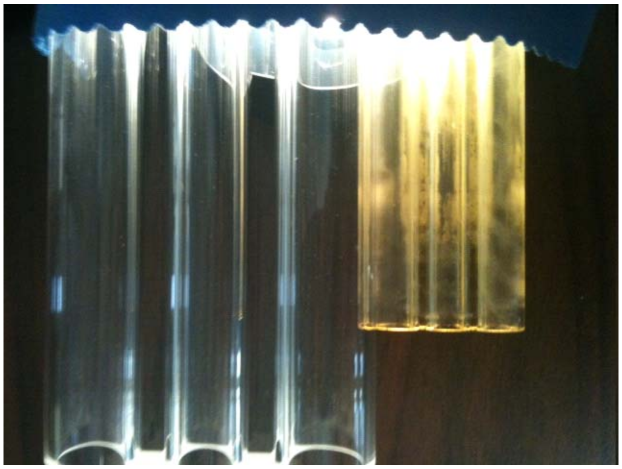

**Figure A-2.9.** Photo of the three-bore flow cell of the laser head of the NY 61 Nd:YAG laser. The material on the left is not made out of the 5% Samarium-doped quartz. However, it illustrates how translucent the material should be. The flow cell on the right has been used in a laser head for extended time. While the flow cell is still intact, the quartz has been baked such that the material has a cloudy appearance.

The Nd:YAG laser also has problems with the control unit (CU601). The laser program crashes after the flashlamp count exceeds a billion counts. The program must be reset, or the laser cannot be fired.

To reset the program, we follow the below procedure:

1. Open switch #8 on the red dip switch component located on the mother board (#503-9900) inside the CU.

2. Reset the key switch to start the countdown display.

3. In the service mode, use the "Parameter Select" button to cycle through each parameter. Set each parameter to the following: Pulse div min = 0, Pulse div max = 11, Rep rate min = half the operating rep rate = 10 Hz, and Rep rate max = operating rep rate = 20 Hz.

4. Reset switch #8 to the closed position and reset the key switch to restart the CU.

While this protocol allows operation of the Nd:YAG laser, the laser can only be externally triggered. TTL pulses must be sent to the control unit to trigger the firing of the flashlamp and Q-switch. For the flashlamp, the signal can be either a positive or negative-going 5V TTL pulse (width 10 μs); for the Q-switch, the signal must be a negative-going 5V TTL pulse (width 10 μs). These signals are supplied by a delay generator. Exact details are available in Appendix 2.3.5. A homemade box connected to a 5V power supply is used as an interface between the delay generator outputs and the inputs for the control unit box, a BNC cable for "ext Q-switch" and a blue 9-pin connector for "externals." A switchbox has also been added to the Q-switch input BNC cable. This is useful for "single shot" procedures for alignment of the Nd:YAG laser.

*TDL 51 dye laser*

External control of the step motor connected to the grating of the dye laser is crucial for experimental scans. The step motor needs a 5V TTL pulse to rotate and a 5/0 V line voltage to determine the direction of rotation. In our laboratory, we use a DAQ card (NI USB 6008) to provide both signals to the step motor. There are two connections to the dye laser, one 25-pin connector for movement of the dye laser and one 15-pin connector for safety interlock of the dye laser. We interface the DAQ card to these connectors via a 37-pin connector and circuit box.

In a senior lab member's notebook, we found a printout of an unidentified connector that sounded very similar to the input of our dye laser step motor (Fig. A-2.10). From the printout, we made a homemade box to interface the DAQ card with the dye laser connection (Fig. A-2.11).

The essential connections for movement of the step motor are pins 34-37, or on the DAQ card, lines P0.3, P0.2, A00, and P0.0, respectively. Outputs from the pins are connected to a TTL integrated component (IC) SN74128N (NOR 50Ω line driver). A subprogram of the Labview program "movedyelaser2_dr.vi" controls the DAQ card such that outputs of the pins can switch from 0 to 5 V rapidly. The outputs of pin 36 (0/5 V) and pin 37 (0 V) work together to create a TTL pulse, while the outputs of pin 34 (0V) and pin 35 (0/5 V) work together to determine the direction of rotation. When pin 35 is 0 V, the IC output is 5 V and the step motor rotates such that the wavelength of the dye laser grows shorter. When pin 35 is 5 V, the IC output is 0 V and the step motor rotates such that the wavelength of the dye laser grows longer.

Only two of the pins, 31 and 33, are currently connected to the 15-pin connector of the dye laser. They both provide 5 V lines to the dye laser and behave as safety interlocks. If the step motor moves the grating of the dye laser to the edge, the dye laser shuts down the motor such that the grating is not damaged. The computer program can receive signals from the dye laser stating whether the grating is at the edge or not. These safety connections are currently not set up, as we have never moved the motor beyond the grating range.

**J1-indexer connector**

**Pin #1_Step + :** This input causes the motor to be incremented one microstep for each pulse it receives. This pulse or pulse train input must be TTL (0 to 5 VDC @ 20 ma) level and have a minimum of one µs pulse width. There is no maximum pulse width. Velocity of the motor will be proportional to the frequency of the input pulse train, and distance will be in equal (in µs) to the number of pulses received. This input is optically isolated. Return is Step- (J1 pin 2)

**Pin # 2_Step - :** This input provides a return for the Step + input. This input it optically isolated and should not be connected to logic ground (J1 pin 8 and J2 pin 8)

**Pin # 3_Dir + :** The state of this input determines the direction the motor will move when step pulses are received on the Step + input. This is a TTL level input with a logic high (5 V @ 20 ma) corresponding to CW motion of the motor and a logic low (O V) corresponding to CCW motion. This input must be defined 80 µs before a step pulse is received and must remain in that state for the duration of the move. This input is optically isolated. Return is Dir- (J1 pin 4).

**Pin #4_Dir - :** This input provides a return for the Dir + input. This input is optically isolated and should not be connected to logic ground (J1 pin 8 and J2 pin 8)

**Pin #5_Res Sel C:** The state of this input along with the state of J1 pins 6 and 7 determines the resolution of the DB Drive. The state of this input is read only at power-up. Changes in state to this input is read only at power-up. Changes in state to this input after power-up will have not effect.

**Pin #6_Res Sel B:** The state of this input along with the state of J1 pins 5 and 7 determines the resolution of the DB Drive. The state of this input is read only at power-up. Changes in state to this input is read only at power-up. Changes in state to this input after power-up will have not effect.

**Pin #7_Res Sel A:** The state of this input along with the state of J1 pins 5 and 6 determines the resolution of the DB Drive. The state of this input is read only at power-up. Changes in state to this input is read only at power-up. Changes in state to this input after power-up will have not effect.

**Pin #8_Logic Gnd:** This input provides a ground for configuring the state of the resolution select inputs. This is internally connected to the logic ground input on J2 pin 8. This input should never be connected to earth ground.

**Figure A-2.10.** Description of a connector to the step motor of the dye laser.

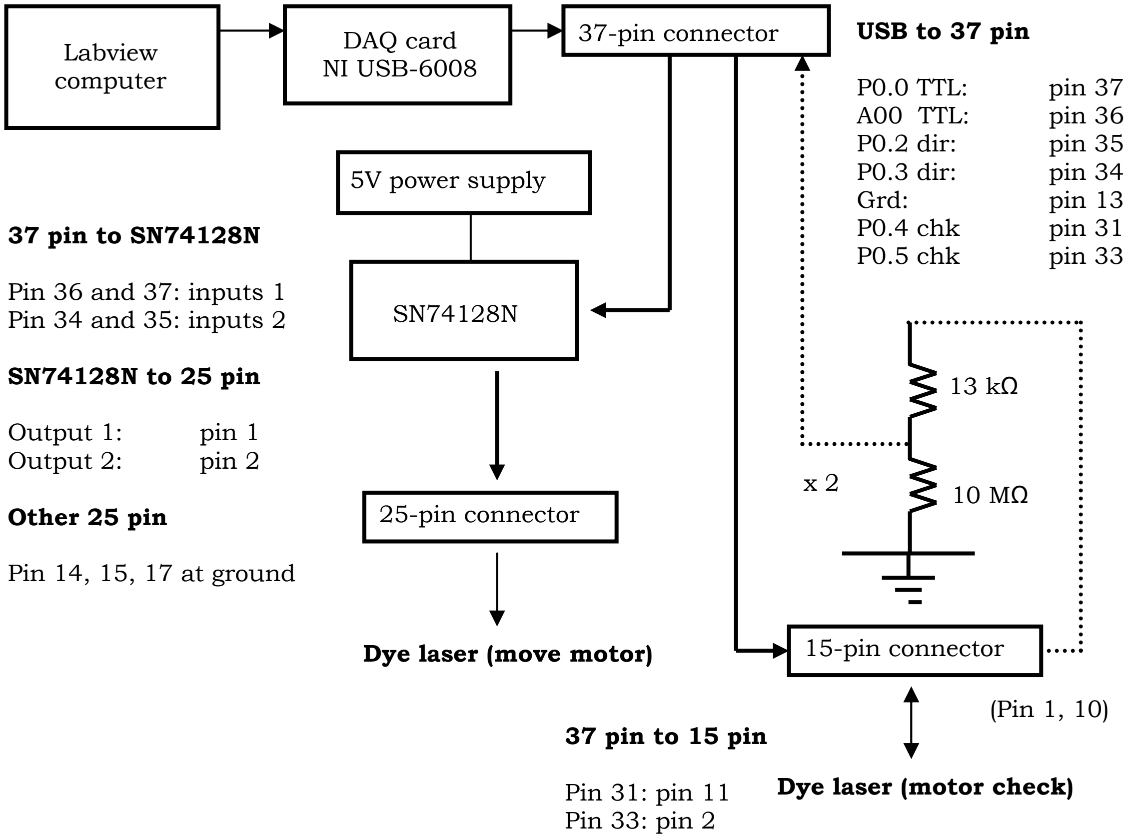

**Figure A-2.11.** Schematics of the connections between the dye laser and DAQ card/computer. The dotted lines are currently not connected. The 25-pin connector is for moving the step motor of the dye laser. The 15-pin connector is for safety checks of the step motor and dye laser grating.

### *LPF 200 Fluorine excimer*

The excimer can be operated at multiple wavelengths, as long as the gas mixture is fluorine-based. The internal program for the excimer laser however can only fill the chamber with the 193-nm gas mixture recipe. To operate the laser at other wavelengths, the fill must be done manually. The following protocol is used:

1. Close all gas cylinder valves. Purge each gas line connected to the excimer three times.

2. Do not touch the halogen line. Remove all other lines and cap off all gas ports on the excimer.

3. Select "New Fill" and execute. The chamber should pump down to ~30 mbar. The program then tries to fill the chamber with gas from the gas ports. However, as all the ports are closed and the halogen cylinder is closed, an error message appears. Push the "break" button.

4. Open the fluorine cylinder. Push F7 to inject a fixed amount of halogen into the chamber. Repeat to fill the chamber with X mbar of gas. The overall pressure reads: "30 + X" mbar. If necessary, the injection can be interrupted by pushing the "break" button. Close the fluorine cylinder when finished.

5. All other gases must be added via the inert gas port. They can be added in any order, although it is recommended that the rare gas and then inert gas are added. Connect the cylinder of interest to the inert gas port. Purge the line three times. Then open the cylinder of interest. Push F6 to inject a fixed amount of the gas into the chamber. Repeat as necessary. If needed, the injection can be interrupted with the "break" button. Close the cylinder. Purge the lines three times before removal. Add all gases accordingly.

We have mostly used 193-nm and 248-nm fills. For operation of the excimer at 193 nm, the gas mixture consists of 100 mbar fluorine, 150 mbar argon, and 2750 mbar neon, while for operation of the excimer at

248 nm, the gas mixture consists of 80 mbar fluorine, 100 mbar krypton, and 2870 mbar neon.

### A.2.3.5 Delay generators for control of the laser firing

Controlling the timing between the firing of the Nd:YAG and excimer lasers is critical for kinetic experiments. We also need to trigger the Labview program "readboard.vi" to collect the ringdown signal at the appropriate time. We achieve these conditions by using two delay generators (Fig. A-2.12). The flashlamps of the NY 61 Nd:YAG laser are specified for 20 Hz rep rate. If we run the experiments at 20 Hz, the triggering of the Nd:YAG, excimer, and data collection program is straightforward (Fig. A-2.13). The first delay generator is internally operated at 20 Hz. Channel A controls the firing of the flashlamp of the Nd:YAG laser. This channel defines the zero of the timing control. Channel B controls firing of the Q-switch. The output of the Nd:YAG laser is optimized by adjusting the time delay for channel B (~280 μs). Channel C triggers the data collection on the computer. The time delay for Channel C is relatively close to the Q-switch firing (Channel B). We collect a few data points before the NIR light reaches the detector to get a better measurement of the baseline.

Finally, Channel D is used to trigger the excimer. There are two separate issues that need to be discussed. First, we need to control when the excimer fires with respect to the Nd:YAG or probe laser. Second, we want to be able to turn the excimer laser on and off during the same experimental scan. With respect to the first issue, the excimer laser light travels a different path to the ringdown cell than the Nd:YAG laser. To define the zero of the kinetic measurements, we measure the exact time that the two laser pulses overlap in the ringdown cell. This is done by observing the NIR CRD signal. The excimer laser causes a small spike in the ringdown signal. The delay time of Channel D (*x*) can be adjusted such that the spike lies on the rise of the CRD signal. This defines the zero point of the kinetics experiments. For example, to do a 10 μs delay experiment, the Channel D delay time is adjusted to "*x*-10" μs. As channel A defines the zero of the timing control, the delay time of Channel A can be set to 10 ms. We can then fire the excimer <10 ms before the NIR pulse reaches the cell to probe the sample of interest.

With respect to the second issue, channel D triggers the second delay generator to send a TTL pulse to the excimer. The excimer only fires upon receiving a TTL pulse with amplitude >3 V and width >15 μs. We therefore also connect the second delay generator to the computer. A subprogram of Labview program "Excimer on and off" is used to rapidly change the amplitude of the TTL pulse from 1 or 4 V to turn the excimer off and on respectively during the course of a scan.

Operating the laser at 20 Hz allows the maximum number of ringdown signals to be collected per second by the CRDS apparatus for averaging. There are however situations in which the gases reside in the ringdown cell for over 50 ms. In the kinetic experiments, we often operate at 5 Hz to guarantee that all gases have been flushed from the ringdown cell before the next excimer pulse initiates chemistry. Triggering all the equipment becomes more difficult, as the Nd:YAG flashlamp must still operate at 20 Hz. We therefore use a combination of TTL ICs to achieve these settings: SN7414 (inverter) and SN7407 (driver) for the excimer channel and SN7400 (NAND) and SN7407 (driver) for the Q-Switch channel. The driver IC is an open-collector. Open-collector devices sink currents in their logic 0 state; thus, an external pull-up resistor is needed to hold the signal line high until the device sinks enough current to pull the line back low. In the circuit, we add a resistor between the common voltage and output of the ICs. In Fig. A-2.14, we show the schematic of the pulses used to operate the Nd:YAG flashlamp and excimer lasers at 5 Hz.

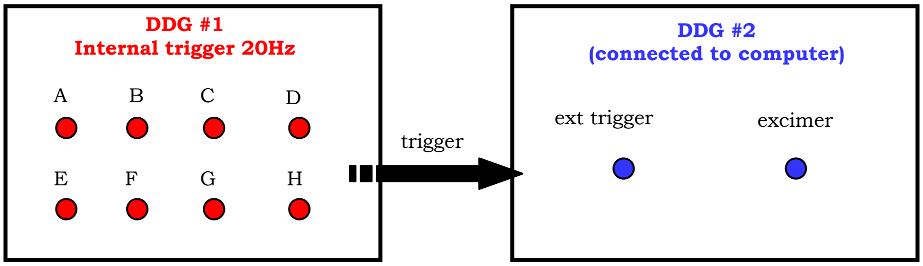

**Figure A-2.12.** Timing of the lasers and data collection program is controlled by two delay generators. The first delay generator is operated at 20 Hz. The second delay generator is externally triggered by an output from the first delay generator.

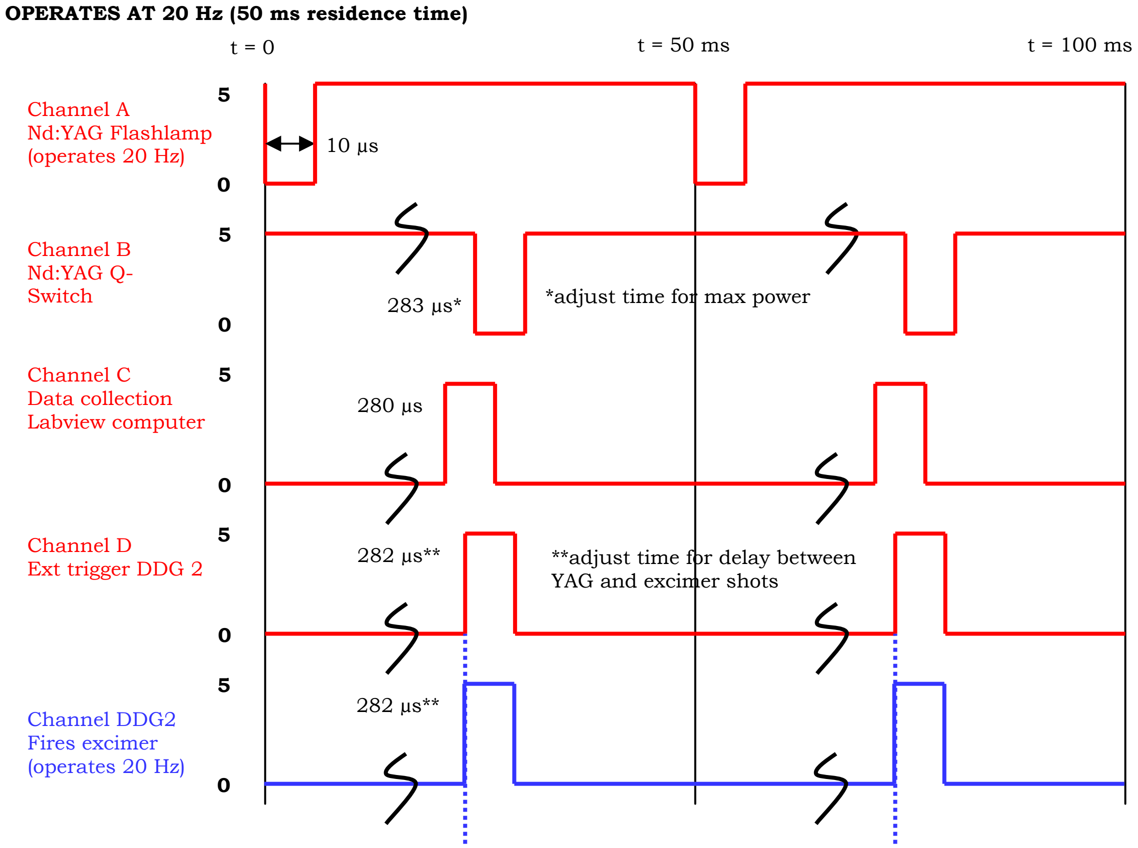

**Figure A-2.13.** Schematic of the outputs from different channels of the delay generators for experiments at 20 Hz rep rate or 50 ms residence time.

**a.**

**OPERATES AT 5 Hz (200 ms residence time)**

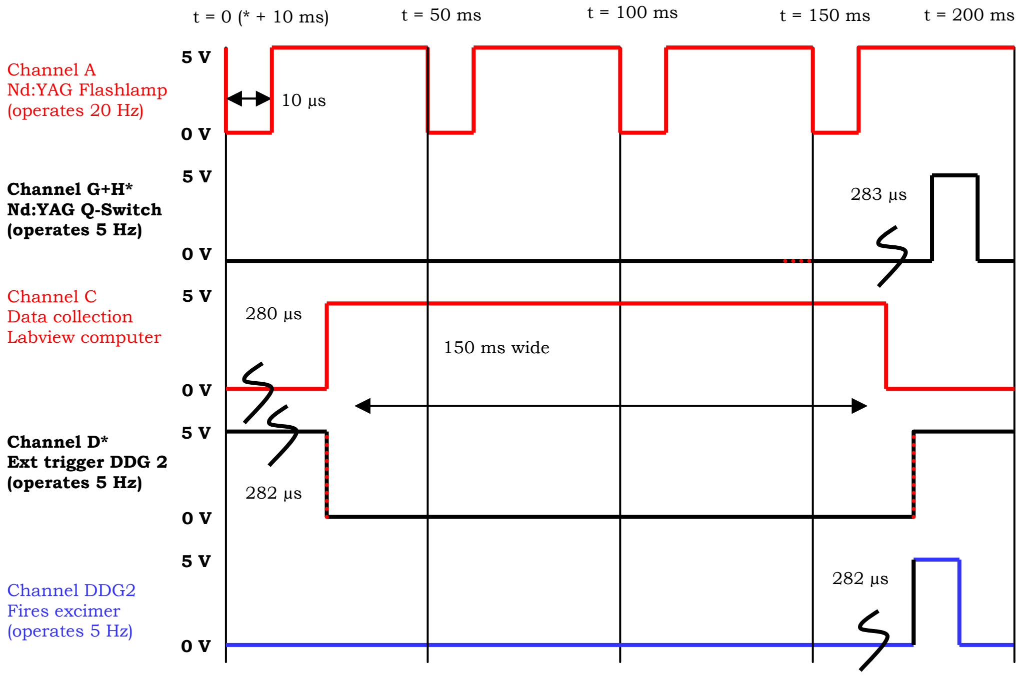

**b.**

**Q-switch for Nd:YAG at 5 Hz**

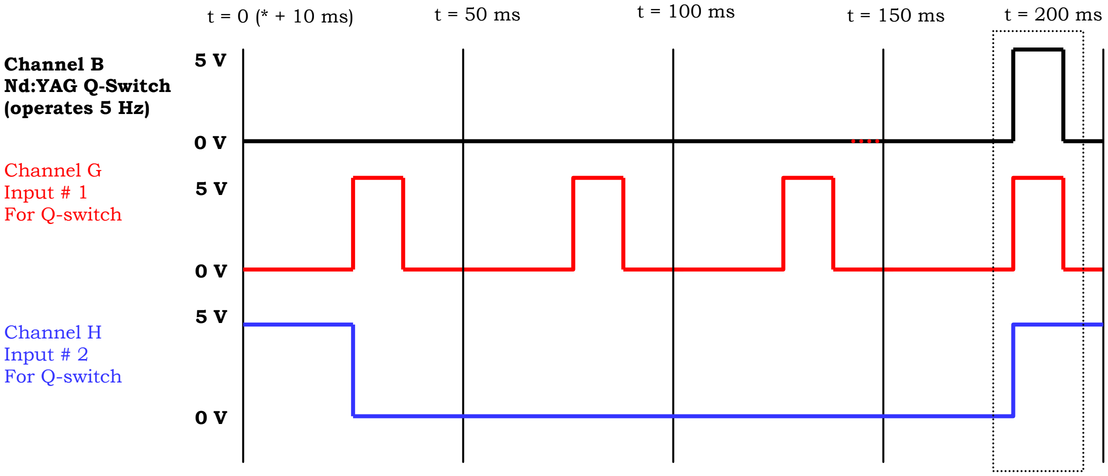

**Figure A-2.14.** Schematic of the different channel outputs for the delay generators for operation at 5 Hz rep rate or 200 ms residence time. Schematic (a) summarizes all the channels. The Q-switch and excimer channels (black) go through an TTL IC component before they are connected to the dye laser or second delay generator, respectively. The circuit for channel D (excimer) is straightforward as the original TTL pulse is just inverted. The circuit for the Q-switch is more complicated, as it involves two channels G and H, which go through the NAND TTL IC. The original G and H inputs are shown in figure (b). Note that the delay time for channel A , and thus all other channels, can be adjusted by 10 ms to provide a larger time window for the kinetic experiments.

## Appendix 2.4 Lab safety and procedures

My advisor once gave a laboratory safety seminar to the first year graduate students in chemistry. After a graphic description of laser light striking the eyeball, one of the students remarked, "I don't want to work in a dangerous lab. I'm going to join an inorganic chemistry group." We are always asked by incoming students and undergraduates how dangerous our laboratory is. Compared to many areas of research, our area of research is very safe. We use less hazardous chemicals and solvents. The laser dyes are mutagenic, but we do not handle them often, and when we do handle them, we wear protective gloves. It is more the nature of the danger that is unfamiliar to most incoming students. Thus, we include here a brief overview of the safety issues in our laboratory. There are many topics not discussed here, e.g., emergency eye wash, showers, fire escape, etc. Every person working in the laboratory should review general safety protocols with the safety officer and other lab members.

### *Lasers*

Lasers are very safe when used correctly. The power and wavelength of the laser should be known by the user before operation. Goggles are wavelength-specific and should be chosen to minimize eye exposure to the most intense wavelengths of laser light. The laser pathway should be well-defined and not designed at eyelevel. If any metal construction is involved, the reflected and scattered light should be contained. Communication is the best protection for persons sharing a laboratory with a laser. Be aware when a laser is being fired in the laboratory.

*Gas samples*

Gas samples are like any other chemical. Some are toxic; others are harmless. The Material-Safety-Datasheets (MSDS) for gases should be checked before any experiment. Some gases can only be transported by specific materials. The material of the line, Swagelok pieces, and o-rings in the connectors should all be checked. When using toxic gases, it is also important to leak check the gas lines before opening the cylinder. There are several ways to leak check a system, including a helium leak detector, methanol/acetone vapor check, and Snoop spray. While many of the gases are invisible and have no smell, some toxic gases such as ozone and halogen have distinct sharp odors. If there is a leak, close the gas cylinder immediately and evacuate the area.

Gases are usually transported to the laboratory in large cylinders. Every cylinder has a CGA number. The CGA number of the pressure regulator should always match the CGA number of the cylinder. For safety reasons, pressure regulators associated with toxic or flammable species are reverse-threaded and have notches on the input. Sometimes we purchase small lecture bottles of gas and make our own high pressure gas cylinder mixture (Fig. A-2.15). Areas exposed to high pressure (>1 atm) are made of metal. Electronics such as low pressure readouts are also protected.

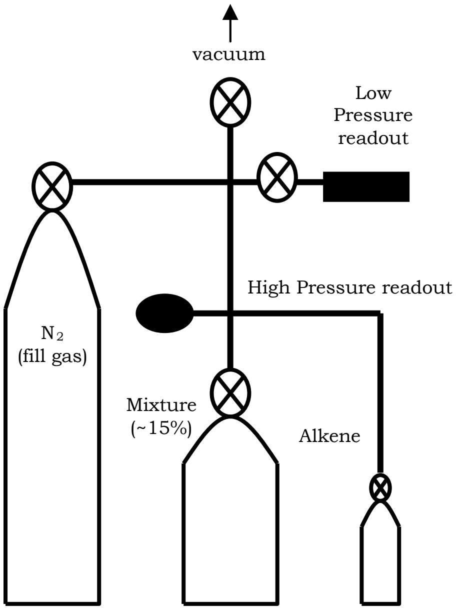

**Figure A-2.15.** Schematic of the preparation of the alkene/$N_2$ cylinder at high pressure. All connected lines and the mixture cylinder are evacuated. After the vacuum line is closed, the valves to the mixture cylinder, alkene lecture bottle, and low pressure readout are opened. After the desired amount of alkene is injected into the mixture cylinder, the valve to the mixture cylinder is closed. The remaining alkene in the line is recollected by placing a liquid nitrogen bath on the alkene lecture bottle. After valves to the alkene lecture bottle and low pressure readout are closed, the valve to the nitrogen (fill gas) cylinder is opened. The valve to the mixing cylinder is slowly opened and filled to the desired total pressure.

### *Baths and liquid nitrogen*

Solid and liquid samples are also used in the experiments. We utilize different temperature baths for the samples (Table A-2.3). The MSDS of the sample should always be checked before choosing the appropriate bath, as there is always a possibility that the container holding the sample may break. We also use baths on the gas lines to remove water and on the vacuum trap to prevent reactive or corrosive species from reaching the mechanical vacuum pump.

Liquid nitrogen is the most common bath used in the laboratory. We use it on the helium purge lines for the CRDS experiments. Nitrogen gas lines are often utilized for atmospheric experiments. Liquid nitrogen should not be used on those lines. Instead, a dry ice/acetone bath or a sieve trap should be used to remove water contaminants. Similar considerations should be made for the bath of the vacuum trap.

If ozone is used in the experiment, a heated trap, filled with copper scrubs, should be added, in addition to a bath, to the vacuum line. Concentrated ozone can cause explosions. The combination of heat and copper eliminates excess ozone. Trapped ozone gives a violet-colored glow. If ozone becomes trapped, stop the ozone source and let the trap warm up slowly, with plenty of head volume. Due to similar concerns, care should be taken to not condense flammable hydrocarbons and oxygen in the same trap.

| **Bath** | **Temperature** |
|---|---|
| Liquid nitrogen | < -196 °C |
| Methanol in Neslab ULT 80 Chiller | 25 °C ~-70°C |
| Dry ice/acetone | -60 °C |
| Salt water/liquid nitrogen | -10 ~-20°C |
| Ice bath | 0 °C |

**Table A-2.3.** Common baths used in our laboratory.

Liquid nitrogen is also used to store samples in bubblers overnight. The bubbler must be leak tight. If there is a leak, air can enter the bubbler and condense. When the bubbler is removed from the liquid nitrogen, the condensed air is immediately warmed and becomes a gas again. As there is not enough head volume for the extra gas, the bubbler explodes. To avoid this problem, flow helium gas through the bubbler to remove all head gas and fill the bubbler with helium (>1 am) before liquid nitrogen storage. The freezing point of helium is below the temperature of liquid nitrogen. Thus, even if there is a minor leak, the helium should leak out of the bubbler before any air enters the bubbler. A relatively tall liquid nitrogen storage dewar is used for storage such that the valves of the bubbler (usually made of Teflon) remain above the liquid nitrogen level and do not contract from the cold temperatures.

Before an experimental run, the bubbler is evacuated while it is under liquid nitrogen in the hood. When the bubbler or sample is removed from the liquid nitrogen dewar, we check the bubbler for liquid. If any liquid is observed in the sample, the bubbler is quickly lowered back into the liquid nitrogen. Helium gas is then run over the sample to slowly warm up the liquid. Similar precautions should be taken with freeze-pump-thaw liquid procedures. The bubbler should not be filled with too much liquid, as the inner glass tube of the bubbler can break upon rapid liquid contraction and expansion.

### *High voltages*

The main danger in a physical chemistry laboratory is the high voltage equipment. Before taking apart any equipment, make sure that the power has been turned off, and the equipment has been unplugged. Many lasers such as the Nd:YAG laser involve high capacitor banks. Even if the equipment is turned off, the capacitors take time to discharge. For emergencies, be aware of the main circuit breaker for the laboratory, so all power can be turned off immediately.

## Appendix 2.5 References

(1) Deev, A., *Ph. D. Thesis*. California Institute of Technology, **2005**.

(2) Barbieri, B.; Beverini, N.; Galli, M.; Inguscio, M.; Strumia, F. *Nuovo Cimento Della Societa Italiana Di Fisica D - Condensed Matter Atomic Molecular and Chemical Physics Fluids Plasmas Biophysics* **1984**, *4*, 172.

(3) Barbieri, B.; Beverini, N.; Sasso, A. *Reviews of Modern Physics* **1990**, *62,* 603.

(4) Ralchenko, Y.; Kramida, A. E.; Reader, J.; Team, N. A. *NIST Atomic Spectra Database (v. 4.0),* **2010**.

(5) Sharpe, S. W.; Johnson, T. J.; Sams, R. L.; Chu, P. M.; Rhoderick, G. C.; Johnson, P. A. *Applied Spectroscopy* **2004**, *58*, 1452.

(6) Rothman, L. S.; Gordon, I. E.; Barbe, A.; Benner, D. C.; Bernath, P. E.; Birk, M.; Boudon, V.; Brown, L. R.; Campargue, A.; Champion, J. P.; Chance, K.; Coudert, L. H.; Dana, V.; Devi, V. M.; Fally, S.; Flaud, J. M.; Gamache, R. R.; Goldman, A.; Jacquemart, D.; Kleiner, I.; Lacome, N.; Lafferty, W. J.; Mandin, J. Y.; Massie, S. T.; Mikhailenko, S. N.; Miller, C. E.; Moazzen-Ahmadi, N.; Naumenko, O. V.; Nikitin, A. V.; Orphal, J.; Perevalov, V. I.; Perrin, A.; Predoi-Cross, A.; Rinsland, C. P.; Rotger, M.; Simeckova, M.; Smith, M. A. H.; Sung, K.; Tashkun, S. A.; Tennyson, J.; Toth, R. A.; Vandaele, A. C.; Vander Auwera, J. *Journal of Quantitative Spectroscopy & Radiative Transfer* **2009**, *110*, 533.

## *Chapter 3*

# THE $\tilde{A} \leftarrow \tilde{X}$ TRANSTION OF THE NITRATE RADICAL ($NO_3$): ELUCIDATION OF THE NON-ADIABATIC EFFECTS

## 3.1 Introduction to the chemical physics problem of $NO_3$

The nitrate radical $NO_3$ is an important nighttime oxidant, playing key roles in both gas phase and aerosol chemistry.[1-3] As we focus on the atmospheric role of $NO_3$ in Chapter 4, we discuss here the chemical physics problem of $NO_3$. Spectra of $NO_3$ were observed in the visible region as early as 1882.[4] In 1953, Walsh analyzed the molecular bonding orbitals of $NO_3$ and found that the radical favored a planar $D_{3h}$ configuration in the ground state: $...(4e')^4(1e'')^4(1a_2')^1$ (Fig. 3.1).[5] With only four atoms and apparent $D_{3h}$ symmetry, $NO_3$ appeared to be a simple system to study. After a century of extensive theoretical and experimental effort, the "simple" open-shell radical $NO_3$ however continues to provoke more questions than answers today.

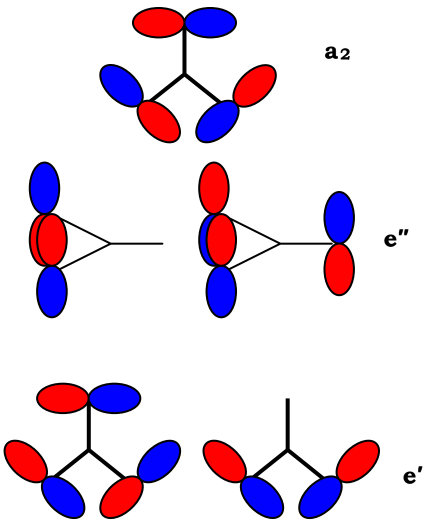

**Figure 3.1.** Diagram of the molecular bonding orbitals of $NO_3$

The non-adiabatic effects of $NO_3$, specifically the Jahn Teller (JT) and pseudo-JT (PJT) effects, complicate study of the radical. The Born-Oppenheimer (BO) approximation, or the separation of nuclear and electronic motions, is commonly invoked to simplify solutions to the Schrödinger equation. The JT effect is a classic example of the breakdown of the BO approximation. The theorem states that a molecule in a degenerate electronic orbital state distorts to a lower symmetry to remove the degeneracy.[6] The PJT effect extends the theorem to molecules whose electronic states are nearly degenerate.[7,8] Both JT and PJT effects have been reviewed in the literature.[9,10] We also provide a more detailed description in Appendix 3.1

Most dynamic studies probe the asymptotic behaviors of reactions to learn about the non-adiabatic effects. In the JT studies, the bound molecules are spectroscopically probed such that the distortion can be observed directly. Various chemical systems have been shown to undergo JT distortion, including the cyclopentadienyl radical $C_5H_5$, the benzene cation $C_6H_6^+$, the silver trimer $Ag_3$, and the methoxy radical $CH_3O$.[9] $NO_3$ provides a unique opportunity to study both JT and PJT effects in the same chemical system.

The three lowest electronic states of $NO_3$ are the $\tilde{X}^2A_2'$, $\tilde{A}^2E''$, and $\tilde{B}^2E'$ states. Spaced approximately an eV apart, the two upper electronic states are JT active, and all three are pseudo-JT coupled (Fig. 3.2). The extent of the strength of these vibronic interactions in $NO_3$ has been heavily debated.[11-14] Of the three electronic states, the ground state $\tilde{X}^2A_2'$ has been the most studied (Table 3.1).[12,13,15-24] Most groups have agreed on assignment of $D_{3h}$ symmetry to the ground state.

Study of the $\tilde{A}^2E''$ and $\tilde{B}^2E'$ excited states has been more challenging. Both states are JT active. While the symmetric stretch and out-of-plane (oop) umbrella modes, $\upsilon_1''(a_1')$ and $\upsilon_2''(a_1'')$ , are non-degenerate, the antisymmetric stretch and antisymmetric in-plane bending modes, $\upsilon_3''(e')$ and $\upsilon_4''(e')$, are degenerate. Study of the JT effect in the excited states therefore becomes a bimodal JT problem. To further complicate matters, the $\tilde{A} \leftarrow \tilde{X}$ transition is electric-dipole forbidden. Therefore, studies of the excited states of $NO_3$ have historically been restricted to studies of the $\tilde{B}$ state.

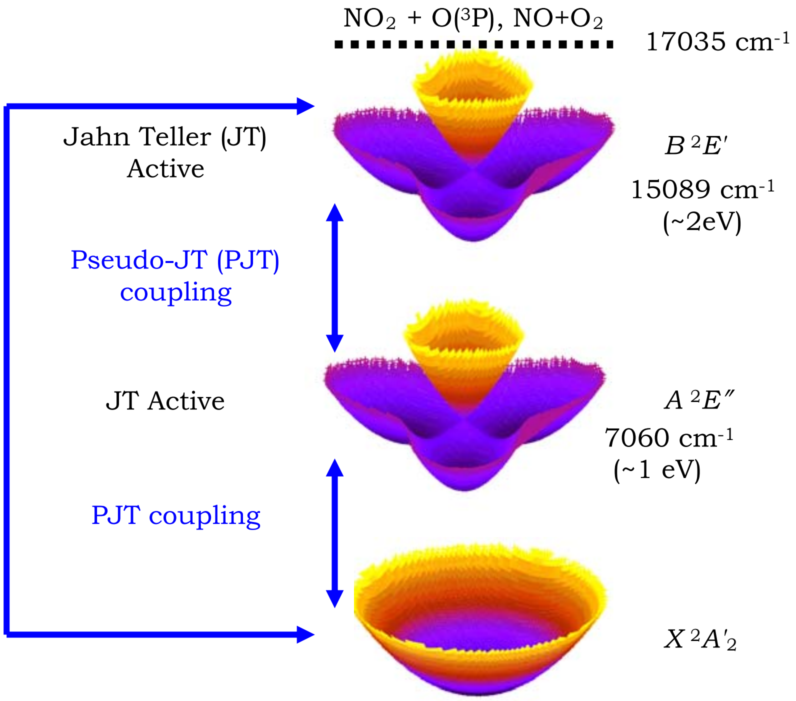

**Figure 3.2.** Schematic of the three lowest electronic states of $NO_3$

Jones and Wulf first assigned the $\tilde{B} \leftarrow \tilde{X}$ transition of $NO_3$ in 1937.[25] The transition is very strong, with $\sigma_{662\ nm} = 2.2 \times 10^{-17}$ $cm^2$.[18-20] Atmospheric groups have used these bands to quantify $NO_3$ concentrations at ambient conditions in the troposphere.[26-30] The $\tilde{B} \leftarrow \tilde{X}$ bands however are not ideal for spectroscopic studies, as the bands are greatly broadened by strong vibronic interactions. Efforts to resolve the bands using jet cooling have proven difficult.[31] Structural details of the $\tilde{B}$ state are not readily available.

In this work, we turn to the dark $\tilde{A}$ state of $NO_3$ to shed light on the non-adiabatic effects of $NO_3$. While the $\tilde{A} \leftarrow \tilde{X}$ transition is dipole forbidden, there are still ways to study the dark excited $\tilde{A}$ state. In the next section, we discuss the relatively brief experimental and theoretical history of the $\tilde{A}$ state and outline our specific goals for studying the $\tilde{A}$ state of $NO_3$.

**Recent theoretical studies of the ground state frequencies**

| | Frequency | Method | Reference |
|---|---|---|---|
| $\upsilon_1''(a_1')$ | 1051.2 | LVC | Stanton, JCP 2007 |
| | 1150 | EOMIP-CCSD//DZP | Crawford & Stanton, JCP 2000 |
| | 1140.6 | MR-SDCI//DZP | Eisfeld & Morokuma JCP 2000 |
| | 1083.5 | MR-SDCI + Davidson/AVTZ-f | Eisfeld & Morokuma JCP 2001 |
| | 1133 | EOMIP-CCSD//TZ2P | Wladyslawski & Nooijen 2002 |
| $\upsilon_2''(a_2'')$ | 796 | EOMIP-CCSD//DZP | Crawford & Stanton, JCP 2000 |
| | 756.8 | MR-SDCI//DZP | Eisfeld & Morokuma JCP 2000 |
| | 773.0 | MR-SDCI + Davidson//AVTZ-f | Eisfeld & Morokuma JCP 2001 |
| | 814 | EOMIP-CCSD//TZ2P | Wladyslawski & Nooijen 2002 |
| $\upsilon_3''(e')$ | 994.3 | LVC | Stanton, JCP 2007 |
| | 1146 | EOMIP-CCSD//DZP | Crawford & Stanton, JCP 2000 |
| | 1439.2 | MR-SDCI//DZP | Eisfeld & Morokuma JCP 2000 |
| | 1376.5 | MR-SDCI + Davidson//AVTZ-f | Eisfeld & Morokuma JCP 2001 |
| | 1113 | EOMIP-CCSD//TZ2P | Wladyslawski & Nooijen 2002 |
| $\upsilon_4''(e')$ | 361 | LVC | Stanton, JCP 2007 |
| | 246 | EOMIP-CCSD//DZP | Crawford & Stanton, JCP 2000 |
| | 173.5 | MR-SDCI//DZP | Eisfeld & Morokuma JCP 2000 |
| | 272.9 | MR-SDCI + Davidson//AVTZ-f | Eisfeld & Morokuma JCP 2001 |
| | 249 | EOMIP-CCSD//TZ2P | Wladyslawski & Nooijen 2002 |

**Previous experimental studies of the ground state frequencies**

| | Frequency | Method | Reference |
|---|---|---|---|
| $\upsilon_1''(a_1')$ | 1060 | LIF | Ishiwata JPC 1983 |
| | 1050/931 | LIF | Nelson JPC 1983** |
| | 1053 | LIF | Kim JCP 1992 |
| $\upsilon_2''(a_2'')$ | 753 | LIF | Kim JCP 1992 |
| | 762 | FTIR | Friedl & Sander JPC 1987 |
| | 763.1 | Ne matrix | Jacox & Thompson JCP 2008 |
| $\upsilon_3''(e')$ | 1480 | LIF | Ishiwata JPC 1983 |
| | 1489/1166 | LIF | Nelson JPC 1983** |
| | 1500 | LIF | Kim JCP 1992 |
| | 1492.393 | IR diode | Kawaguchi JCP 1990 (analysis) |
| | 1000-1100 | Ne matrix | Jacox & Thompson JCP 2008 |
| $\upsilon_4''(e')$ | 365 | CRDS | Deev JCP 2005* |
| | 380 | LIF | Ishiwata JPC 1983 |
| | 360/418 | LIF | Nelson JPC 1983** |
| | 368 | LIF | Kim JCP 1992 |
| | 365.6 | Ne matrix | Jacox & Thompson JCP 2008 |
| | 365.48419 | FTIR | Kawaguchi, J. Mol. Spec. 2011 (submit) |

*used origin 7064 cm$^{-1}$

**assumed ground state in $C_{2v}$ symmetry

**Table 3.1.** The upper table lists the most recent theoretical values of the ground state frequencies of $NO_3$. The lower table lists experimental values. Most groups have agreed that the ground state has $D_{3h}$ symmetry. The most significant experimental disparity is in the value of the $\upsilon_3''(e')$ frequency.

## 3.2 The dark $\tilde{A}$ state of $NO_3$

The $\tilde{A}$ state of $NO_3$ was observed for the first time twenty years ago in a low resolution anion photoelectron spectrum (PES) of the nitrate anion $NO_3^-$. The origin of the $\tilde{A}$ state was estimated to be in the near-infared (NIR) region at $T_0(\tilde{A})$ = 7000(100) cm$^{-1}$.[32] Hirota *et al.* and Kawaguchi *et al.* recognized that the $\tilde{A}$ state could also be studied using spectroscopic absorption methods in the NIR via Herzberg-Teller selection rules (Fig. 3.3).[33,34] The HT selection rules state that a transition is allowed only if the product of the electric dipole transition moment and the initial and final vibronic states contain the totally symmetric representation of the molecular system's point group.

For $NO_3$, the origin of the $\tilde{A} \leftarrow \tilde{X}$ transition is electric dipole forbidden:

$$0_0^0 : a_1' \notin A_2' \otimes \{\mu_{\|}(a_2'') \oplus \mu_{\perp}(e')\} \otimes E'' \,. \tag{3.1}$$

However, vibronic bands of the $\tilde{A} \leftarrow \tilde{X}$ transition such as the parallel and perpendicular bands, $4_0^1$ and $2_0^1$ respectively, are HT allowed:

$$4_0^1 : a_1' \in A_2' \otimes \mu_{\|}(a_2'') \otimes \{E'' \otimes \upsilon_4'(e')\} = A_2' \otimes \mu_{\|}(a_2'') \otimes \{a_1'' \oplus \cancel{a_2''} \oplus \cancel{e''}\} \tag{3.2}$$

$$2_0^1 : a_1' \in A_2' \otimes \mu_{\perp}(e') \otimes \{E'' \otimes \upsilon_2'(a_2'')\} = A_2' \otimes \mu_{\perp}(e') \otimes \{e'\} \,. \tag{3.3}$$

Hirota *et al.* and Kawaguchi *et al.* collected rotationally resolved spectra of the $4_0^1$ and $2_0^1$ bands using diode laser and Fourier transform infrared (FTIR) spectroscopy respectively. Both the upper and lower rotational constants were assigned for the $4_0^1$ band.

Our group and Jacox and Thompson followed with surveys of the $\tilde{A} \leftarrow \tilde{X}$ vibronic bands in the 5000-9000 cm$^{-1}$ region using cavity ringdown spectroscopy (CRDS) of $NO_3$ in the gas phase and FTIR spectroscopy of $NO_3$ in the matrix, respectively.[24,35,36] Multiple vibronic bands were observed and assigned in the spectra. Appendix 3.2 provides a more detailed overview of the previous CRDS survey.

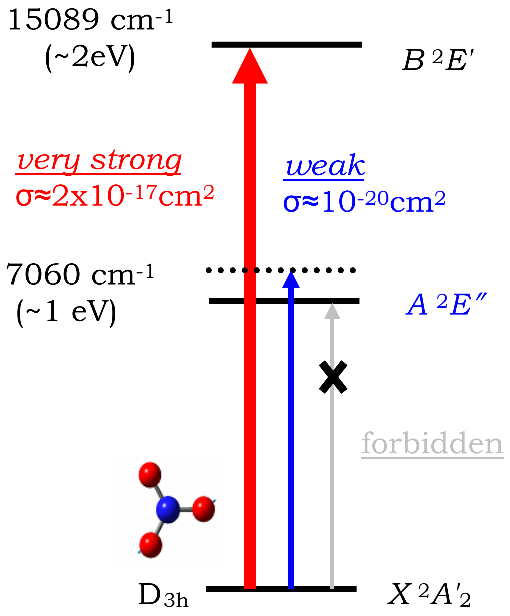

**Figure 3.3.** Schematics of the transitions to the excited electronic states of $NO_3$. While the absorption cross section for the $\tilde{B} \leftarrow \tilde{X}$ transition is quite strong, much of the structural information about $NO_3$ is learned from the weak $\tilde{A} \leftarrow \tilde{X}$ transition of $NO_3$, as spectra of the $\tilde{A} \leftarrow \tilde{X}$ transitions can be rotationally resolved.

Theoretical work on the $\tilde{A}$ state has increased only in the last decade. Multi-reference configuration interaction (MRCI) calculations by Eisfeld *et al.* predict a large JT distortion in the $\tilde{A}$ state, with $C_{2v}$ minimum $B_1$ (depth 2000 cm$^{-1}$) and transition state $A_2$ (pseudorotation barrier 1000 cm$^{-1}$).[16] The calculated JT stabilization energies are much larger in magnitude than the spin-orbit couplings (~50-150 cm$^{-1}$) of similar-sized

JT systems, such as the methoxy radical.[37-39] In many $NO_3$ models, the spin-orbit coupling is thus ignored.

Improvements to the *ab initio* models initially involved incorporation of higher order JT terms.[16,40,41] The growing experimental evidence for strong PJT effects in $NO_3$ led many groups to use the linear multimode vibronic coupling (LVC) model developed by Koppel, Domcke, and Cederbaum.[42] To date, Faraji *et al.* have used the model to simulate Weaver's anion PE spectrum,[43] while Stanton has used the model to simulate band intensities of our previously published CRD spectrum.[44,45] As theoretical models of the $\tilde{A}$ state continue to evolve, we need more experimental benchmarks on the $\tilde{A}$ state of $NO_3$.

The vibrational frequencies of the $\tilde{A}$ state would provide a first means to test the accuracy of the theoretical models. While many $\tilde{A} \leftarrow \tilde{X}$ bands were assigned in the previous CRD and matrix studies, vibrational frequencies of the $\tilde{A}$ state were not able to be definitively determined due to the lack of an assignment of the origin band. Values were instead inferred from spacing between combination bands. Identification of the origin band would lead to absolute fundamental frequencies of the $\tilde{A}$ state of $NO_3$.

The origin of the $\tilde{A} \leftarrow \tilde{X}$ transition of $NO_3$ however has yet to be observed in the gas phase. While the transition is electric dipole forbidden, in principle, we should be able to observe the origin directly via magnetic dipole selection rules. Magnetic transitions are very weak, typically $10^{-5}$ the strength of electric transitions.[46] Only a handful of such studies have been done on polyatomic molecules, including oxygen and formaldehyde.[47-50] We would need a very sensitive technique to observe the origin band of $NO_3$.

Previous experiments have also provided only a qualitative gauge of the JT strength in the $\tilde{A}$ state. The importance of the JT effect in $NO_3$ was apparent in the first PES experiment when Weaver *et al.* observed a strong progression by the Franck-Condon (FC) forbidden $\upsilon_4'$ frequency in the $\tilde{A}$ state that could only be explained by strong vibronic coupling among the three lowest electronic states of $NO_3$.[32] In our previous CRD survey, we observed a series of irregularly spaced $4_0^n$ ($n$ = 1-4) bands. The rotational contours of the bands were fit with symmetric top models; however, the irregular progression of the bands supported small to moderate JT activity along the $Q_4$ coordinate. We also observed surprisingly similar strength absorptions by the parallel $4_0^1$ and perpendicular $2_0^1$ bands. The intensity borrowing mechanisms for the respective bands highlighted the strong vibronic coupling among the three lowest electronic states of $NO_3$ (Appendix 3.2).[44]

The matrix isolation survey supported our gas phase observations. In addition to $^{14}NO_3$, Jacox and Thompson also examined isotopologues of $NO_3$ that reduced the symmetry of the radical to $C_{2v}$. They observed additional satellites and shoulders to absorption features that were attributed to matrix effects. They however did not observe any apparent splitting in the vibronic bands from reduced symmetry.

A quantitative measure of the vibronic strength in the $\tilde{A}$ state would provide a better benchmark for *ab initio* models of $NO_3$ and would offer valuable insight into the strength of the nonadiabatic effects of $NO_3$. Many of the previous studies focused on the JT activity along the $Q_4$ coordinate. The $\tilde{A}\,{}^2E'' \otimes \upsilon_4(e')$ manifold of the $\tilde{A}$ state is split into three vibronic levels: $a_1'' \oplus a_2'' \oplus e''$ (Fig. 3.4). The ordering and magnitude of the splitting are direct consequences of the strengths of vibronic interactions in $NO_3$. Only the $a_1''$ level has been examined via the $4^1_0$ band, as transitions to the $a_2''$ and $e''$ vibronic levels are forbidden from the ground state under HT selection rules. Access to the $e''$ level is allowed via the $4^1_1$ hot band, as the symmetry of the ground state is changed. Measurement of the $e''$-$a_1''$ splitting would provide the first quantitative gauge of the JT effect.

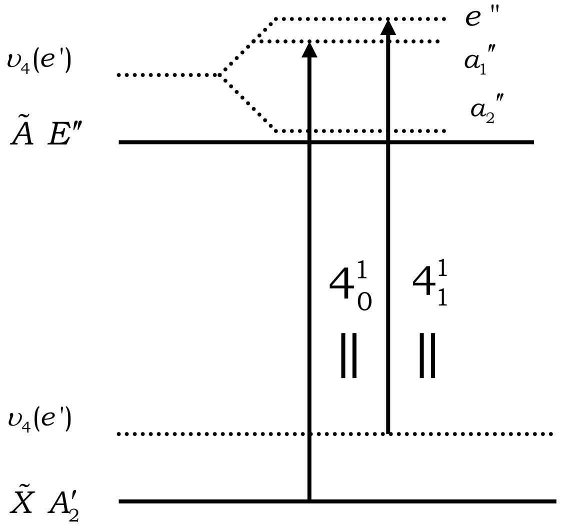

**Figure 3.4.** Schematic of the $\tilde{A}\,^2E'' \otimes \upsilon_4(e')$ manifold of the Ã state. To date, only the $a_1''$ level has been examined. We access the $e''$ level via the $4^1_1$ hot band.

In this work, we use the sensitivity of the pulsed CRDS apparatus to examine the origin and hot bands of the $\tilde{A} \leftarrow \tilde{X}$ transition of $NO_3$ in the 7000-7650 $cm^{-1}$ region and to measure directly the fundamental vibrational frequencies and JT strength of the $\tilde{A}$ state of $NO_3$.

## 3.3 Experimental conditions

Spectra of $NO_3$ were obtained in flow cells heated to > 40°C using the thermal decomposition of dinitrogen pentoxide ($N_2O_5$). The synthesis of $N_2O_5$ is described in Appendix 3.3. The pulsed CRDS apparatus was described in Chapter 2. The optical cavity consisted of a 50-cm long Pyrex cell wrapped in heating tape ($T$ = 40-160°C) with 13-cm purge volume couplers attached at each end to protect the CRD mirrors (LGR 1400 nm, $R$ = 99.995%). Scans were collected at 0.2 and 0.4 $cm^{-1}$ step size with helium/oxygen carrier gas (10-15 Torr) flowing through a $N_2O_5$ trap ($T$ = -12°C salt water/liquid nitrogen bath), with $P_{vapor,\ N2O5} \sim 1.5$ Torr. The chemical identity of the bands was verified using $N_2O_5$ photolysis at 193 nm.

In our previous CRDS study, we flowed ozone at room temperature over the $N_2O_5$ trap to produce $NO_3$ radicals. In this study, we observed a > 5-fold increase in the $NO_3$ concentration under heated conditions ($T$ = 40°C). The residual water in the cell was also reduced, minimizing formation of nitric acid:

$$H_2O + N_2O_5 \rightarrow 2\ HNO_3 \qquad (3.4)$$

Nitric acid absorption in the NIR is discussed in Appendix 3.4. Absolute concentrations of $NO_3$ were measured via single-pass direct absorption with a diode laser (Sanyo diode DL 6147-040, 662 nm). Typical $NO_3$ concentrations were $10^{14}$ molec $cm^{-3}$.

## 3.4 Observed Spectra

### 3.4.1 Assignments

We observed several vibronic bands in the CRD spectrum of $NO_3$ in the 7000-7650 cm$^{-1}$ region (Fig. 3.5). Assignments were aided by the distinct rotational contours of parallel and perpendicular bands of the $\tilde{A} \leftarrow \tilde{X}$ transition of $NO_3$. We modeled the contours using PGopher v. 5.3, developed by C. M. Western from the University of Bristol, to determine band origins of the observed bands (Appendix 3.5). The results have been summarized in Table 3.2, with schematics of the assigned bands shown in Figure 3.6.

*Hot bands*

Upon heating to 40°C, several absorption bands increased in intensity relative to the most intense band in the region, the $4_0^1$ band at 7602.8(2) cm$^{-1}$. We definitively assigned three of these to hot bands of the $\tilde{A} \leftarrow \tilde{X}$ transition arising from thermal population of the lowest vibrational excited state $4_1$: the $4_1^1$ $(||)$, $4_1^0 2_0^1$ $(\perp)$, and $4_1^0 1_0^1 (||)$ bands. Uncertainties in the band origins (1.0~3.0 cm$^{-1}$) were due to overlap of multiple hot bands. Other features that were observed but not assigned (* in Fig. 3.5), were attributed to hot bands of $NO_3$ based on their temperature dependence.

$4_1^0$ *hot band*

We collected CRD spectrum of the $4_1^0$ hot band of $NO_3$ in the 6650-6710 cm$^{-1}$ region. We compared the spectrum to a high resolution off-axis integrated cavity output spectrum (OA-ICOS) of the $4_1^0$ band that had been previously obtained by our group and found the two spectra matched (Fig. 3.7).[51] A brief summary of the OA-ICOS experiment is provided in Appendix 3.6. Analysis with an asymmetric top model led to assignment of the band origin to 6696.5(1.0) cm$^{-1}$. The band contour resembled the contours of the $4_0^n$ parallel bands, with a sharp R branch head and a gap near the origin.

| **Bandhead (cm$^{-1}$)** | **Intensity** | **Band origin (cm$^{-1}$)** | **Assignment** |
|---|---|---|---|
| 6703.906 | w | 6696.5(1.0) | $4_1^0$ |
| 7066.1, 7074.2 | v. w. | 7062.25(0.5) | $0_0^0$ |
| 7086.1 | v. v. w. | - | |
| 7243.1 | w. | 7235.5(1.5) | $4_1^1$ |
| 7375.8 | w. | 7370.0(3.0) | $4_1^0 2_0^1$ |
| 7434.7 | v. w. | - | |
| 7489.6 | v. w. | 7481.0(1.5) | $4_1^0 1_0^1$ |
| 7532.7 | v. w. | - | |
| 7610.6 | s. | 7602.8(2), **7602.5754(16)** | $4_0^1$ |
| 7745.5 | s. | 7740.9(3)*****, **7744** | $2_0^1$ |

**Bold**: Hirota and Kawaguchi high resolution studies
*****: observed in our previous CRD study
w = weak, v = very, s = strong

**Table 3.2**. Assignments of the observed $\tilde{A} \leftarrow \tilde{X}$ vibronic bands of $NO_3$

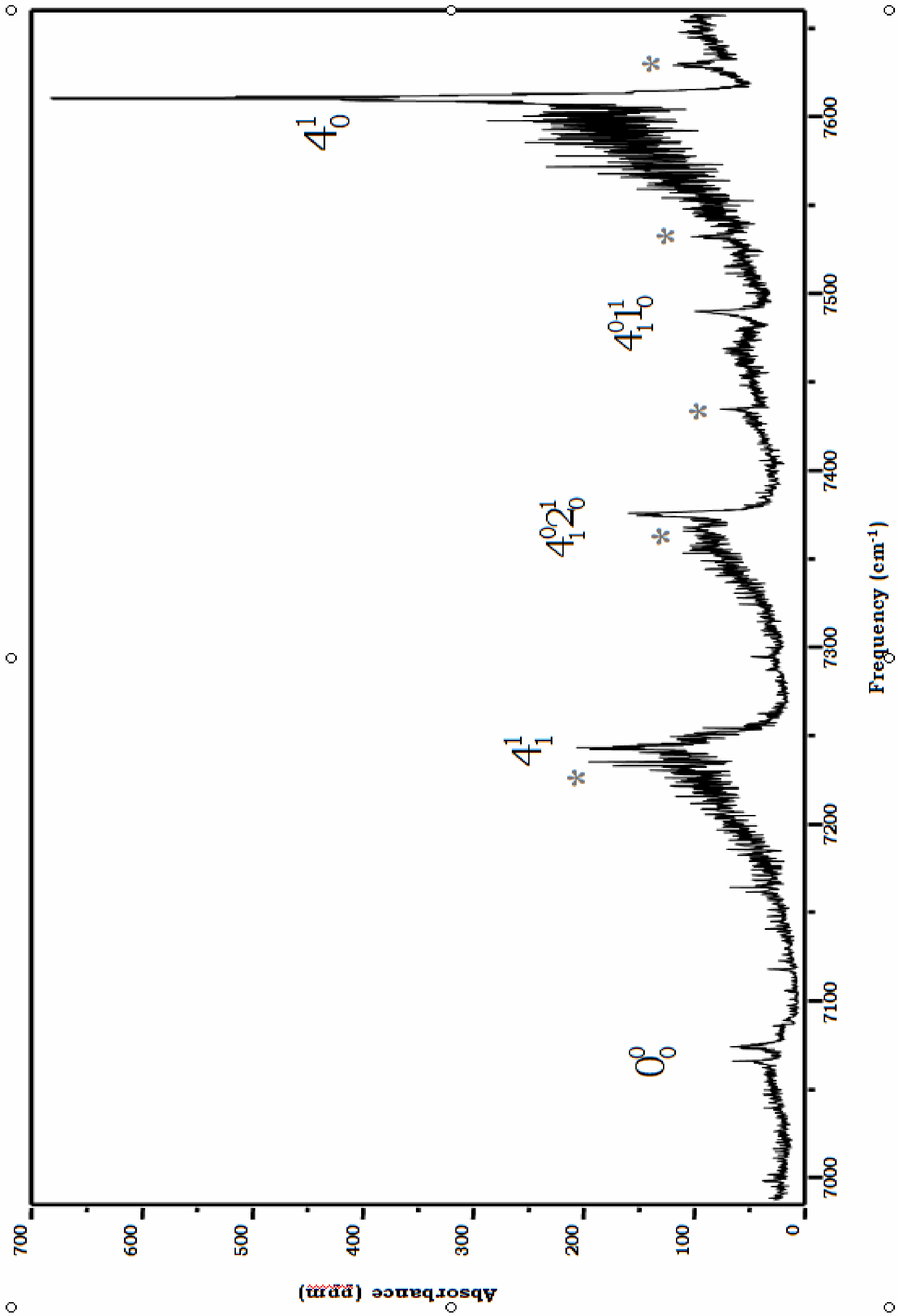

**Figure 3.5.** CRD spectrum of the $\tilde{A} \leftarrow \tilde{X}$ transitions of $NO_3$ in the 7000-7600 $cm^{-1}$ NIR region. * = observed but unassigned hot bands of $NO_3$.

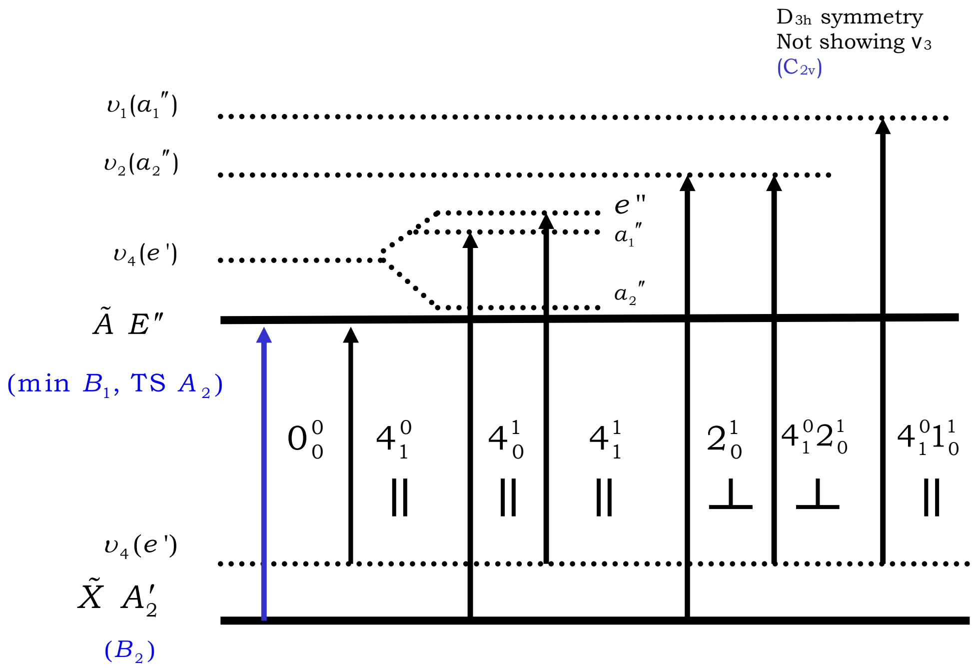

**Figure 3.6.** Diagram of the observed $\tilde{A} \leftarrow \tilde{X}$ vibronic bands of $NO_3$ in this work.

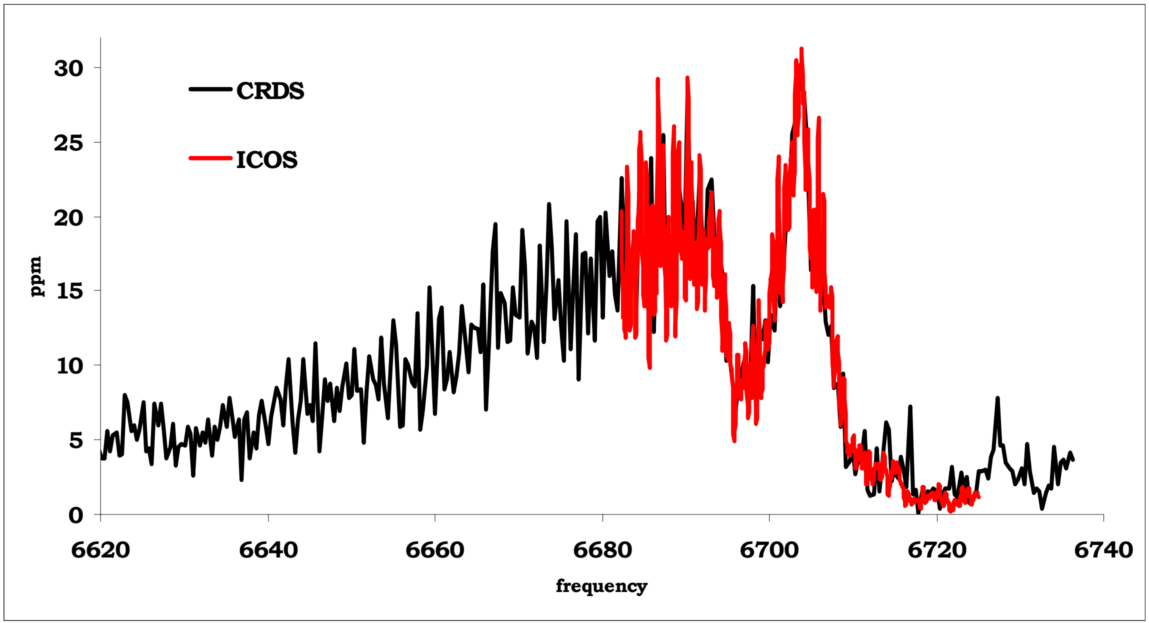

**Figure 3.7.** Comparison of the $4_1^0$ hot band obtained by CRDS apparatus and the ICOS apparatus. The ICOS data was convoluted to a lower resolution (0.1 $cm^{-1}$) for comparison.

*$0_0^0$ origin band*

We observed a weak spectrum in the 7000-7100 cm$^{-1}$, in the vicinity of the expected origin (Fig. 3.8). The feature comprised of a broad underlying absorption from 7020-7080 cm$^{-1}$ with two distinct Q-branch-like peaks at 7066.1 and 7074.2 cm$^{-1}$ and a sharp edge at 7090 cm$^{-1}$. The rise in the absorption below 7020 cm$^{-1}$ is due to the first overtone of the OH stretch of nitric acid impurities.

Variation of the intensity with temperature ($T$ = 40-160 °C) indicated that the main features were not due to hot bands, with exception of the sharp edge, which grew with temperature. We therefore believe some of the features can be assigned to the magnetic dipole allowed origin band $0_0^0$. We also scanned 700 cm$^{-1}$ to the blue of the band to observe the $1_0^1 0_0^0$ band for confirmation; however the observed absorption was very weak and inconclusive (Fig. 3.9).

Contour analysis of the absorption at 7000-7100 cm$^{-1}$ with magnetic dipole and electric quadrupole models could not fully reproduce all of the features, in particular the presence of two strong peaks. Simultaneous fits of the $0_0^0$ magnetic transition and $4_1^0$ vibronic transition bands led us to *tentatively* assign the first observed peak to the $0_0^0$ transition with band origin at 7062.25(0.5) cm$^{-1}$ and the second peak to an unidentified absorption by $NO_3$ or some contaminant with fortuitous absorption in the 7000-7100 cm$^{-1}$ region. We discuss the second peak further in section 3.5. Given our assignment of the origin band, we used the measured $NO_3$ concentration to calculate the integrated cross section for the origin band to be 1.3 × 10$^{-20}$ cm. We compared the integrated absorption cross sections of the $4_0^1$ and $0_0^0$ bands and found ratio = 25:1.

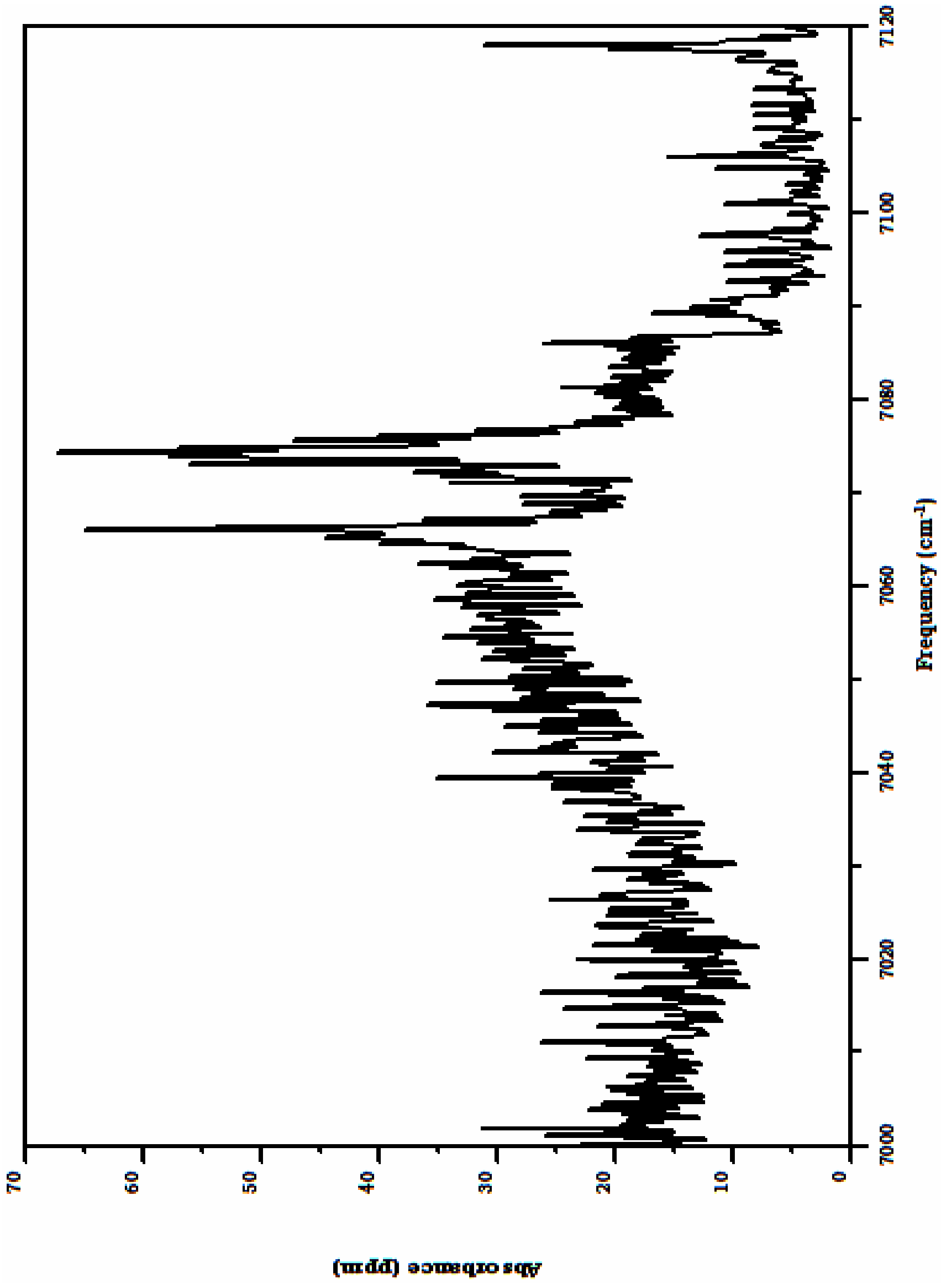

**Figure 3.8.** CRD spectrum of the origin of the $\tilde{A} \leftarrow \tilde{X}$ transition of $NO_3$.

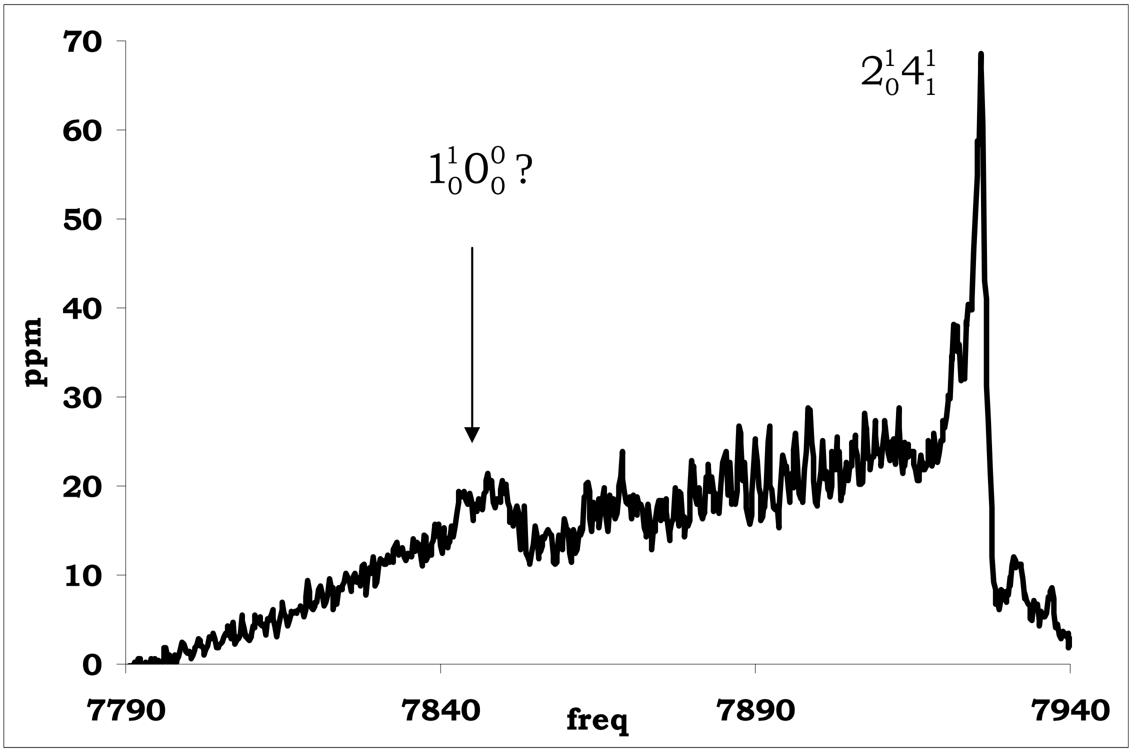

**Figure 3.9.** CRD spectrum of the 7790-7940 cm$^{-1}$ region of $NO_3$. A weak absorption is observed near 7850 cm$^{-1}$, approximately 800 cm$^{-1}$ (~$\upsilon_1$) to the blue of the observed origin band of the $\tilde{A} \leftarrow \tilde{X}$ transition of $NO_3$.

### $2^1_0 4^1_0$ *anomalous strong band*

In our previous CRDS study, we had tentatively assigned the anomalously strong band at 8287 cm$^{-1}$ to the $3^1_0$ band. We repeated the CRDS experiments at room and heated conditions (Fig. 3.10). We now reassign the band to $2^1_0 4^1_0$. The reassignment is discussed in detail in the discussion section.

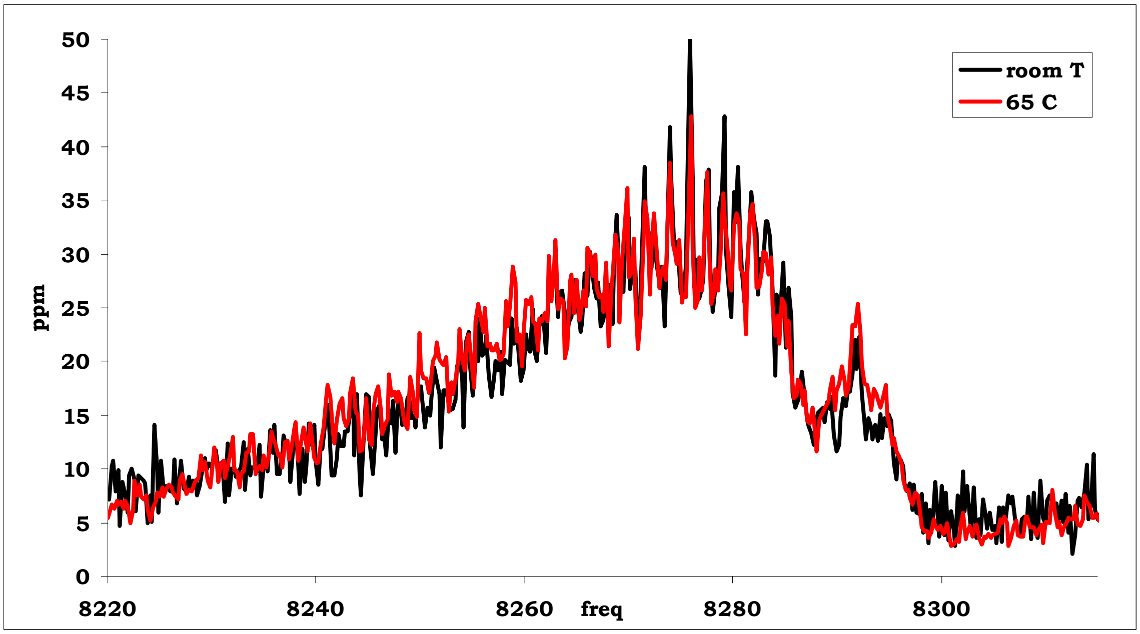

**Figure 3.10.** CRD spectra of $NO_3$ in the 8220-8350 $cm^{-1}$ region at room and T = 65˚C temperatures. The anomalously strong absorption at 8287 $cm^{-1}$ is reassigned to the $2_0^1 4_0^1$ band.

### 3.4.2 Fundamental vibrations

Many of the fundamental vibrations in both the ground and $\tilde{A}$ states of $NO_3$ can be calculated from the assigned bands. The frequencies of the fundamental vibrations are summarized in Table 3.3.

*Ground state* $\upsilon_4''$

The ground state $\upsilon_4''$ level has only been recently observed directly via absorption methods. Jacox *et al.* and Kawaguchi *et al.* reported $\upsilon_4''$ = 365.6 $cm^{-1}$ and $\upsilon_4''$ = 365.48419 $cm^{-1}$ in FTIR matrix and gas phase experiments, respectively.[36,52] Previous studies had involved LIF detection, with estimates of $\upsilon_4''$ varying from 360-380 $cm^{-1}$. From combination differences between $0_0^0 - 4_1^0$, we calculated $\upsilon_4''$ = 365.75(1.1) cm$^{-1}$.

**THE GROUND STATE VIBRATIONAL FREQUENCY**

| **Vibrational level** | **Expt. Freq. (cm$^{-1}$)** | **Method** | **Calc. Freq. (cm$^{-1}$)** | **Method** |
|---|---|---|---|---|
| $\upsilon_4$ (e') | 380 | LIF [18] | | |
| | 360/418 | LIF [19] | 272.9 | MR-SDCI [16] |
| | 368 | LIF [20] | 246 | EOMIP-CCSD [45] |
| | 365 | CRDS [24] | 249 | EOMIP-CCSD [45] |
| | 365.6 | Matrix FTIR [22] | 361 | LVC [13] |
| | 365.48419 | FTIR [52] | | |
| | **365.75(1.1)** | **CRDS** | | |

**THE Ã STATE VIBRATIONAL FREQUENCIES**

| **Vibrational level** | **Expt. Freq. (cm$^{-1}$)** | **Method** | **Calc. Freq.(cm$^{-1}$)** | **Method** |
|---|---|---|---|---|
| $\upsilon_1$ (a$_1$′) | 804(4) | Anion PES [32] | 820 | CCSD(T) [45] |
| | 785* | CRDS [24] | 905 | MR-SDCI [16] |
| | 783.1/782.5* | Matrix FTIR [36] | 801.8 | EOMIP-CCSD [45] |
| | **784.5(1.8)** | **CRDS** | | |
| $\upsilon_2$ (a$_2$″) | 683 | IR Diode [34] | 685 | CCSD(T) [45] |
| | 678 | CRDS [24] | 730.7 | MR-SDCI [16] |
| | 656/680.6 | Matrix FTIR [36] | 738 | EOMIP-CCSD [45] |
| | **678.65(58)** | **CRDS** | | |
| $\upsilon_3$ (e′) | 1223? | CRDS [24] | 1292/1569 | CCSD(T) [45] |
| | | | 1230/1595 | MR-SDCI [16] |
| | | | 1216.7/1754.8 | EOMIP-CCSD [45] |
| $\upsilon_4$ (e′) | 541(8) | Anion PES [32] | 566/567 | CCSD(T) [45] |
| | 519-547* | CRDS [24] | 373.7/270.9 | MR-SDCI [16] |
| | 514.2-558.3* | Matrix FTIR [36] | 681/588 | EOMIP-CCSD [45] |
| | **540.55(54)** | **CRDS** | | |

**Bold**: results from this work; * = assignment from combination band

**Table 3.3.** Comparison of the vibrational frequencies of NO$_3$ determined in this work with previous theoretical and experimental values.

### *Ã state* $\upsilon_1'$

Transitions to the $\upsilon_1'$ level from the ground state are forbidden by HT selection rules. We used the combination difference between the $4_1^0 1_0^1 - 4_1^0$ bands to calculate $\upsilon_1'$ = 784.5(1.8) cm$^{-1}$. Past absorption studies have relied on extricating the value of $\upsilon_1'$ from allowed transitions

$4_0^n 1_0^1$ and $2_0^1 1_0^1$. Combination differences between $4_0^n 1_0^1 - 4_0^{n-1}$ (n = 1, 2) bands were used by both Deev *et al.* and Jacox *et al.* to estimate $\upsilon_1'$ = 763-779 cm$^{-1}$ and $\upsilon_1'$ = 733.7-763.2 cm$^{-1}$ respectively, with the wide frequency range attributed to JT effects along the $Q_4$ coordinate.[24,36] The difference in the $2_0^1 1_0^1 - 2_0^1$ bands predicted a larger value for $\upsilon_1'$, $\upsilon_1'$ = 785 cm$^{-1}$ and $\upsilon_1'$ = 782.5-783.1 cm$^{-1}$, respectively. The latter estimates are more reliable as they involved non-JT active modes and agree with our assessment.

### *Ã state* $\upsilon_2'$

The fundamental frequency $\upsilon_2'$ was directly calculated from the $2_0^1$ and origin bands. We found $\upsilon_2'$ = 678.65(68) cm$^{-1}$, which is well within the experimental limits of previous studies.

To check our other band assignments, we calculated $\upsilon_2'$ and $\upsilon_4''$ from the combination differences between $4_1^0 2_0^1 - 4_1^0$ and $2_0^1 - 4_1^0 2_0^1$. We found $\upsilon_2'$ = 673.5(3.2) cm$^{-1}$ and $\upsilon_4''$ = 370.9(3.0) cm$^{-1}$, respectively. The $4_1^0 2_0^1$ hot band was difficult to simulate due to convolution of multiple hot bands. Interestingly, if the band origin for the $4_1^0 2_0^1$ band were shifted to the blue by 5 cm$^{-1}$, both calculated vibrational levels would be within errors of the frequency values calculated directly from the observed origin band $0_0^0$.

### *Ã state* $\upsilon_3'$

The $\upsilon_3'$ level was not observed in this study. More details can be found in the discussion section.

*Ã state* $\upsilon_4{}' = a_1{}''$

As a degenerate mode, the $\tilde{\mathrm{A}}{}^2\mathrm{E}''\otimes\upsilon_4(\mathrm{e}')$ manifold is split into three vibronic levels: $\mathrm{a}_1''\oplus\mathrm{a}_2''\oplus\mathrm{e}''$. HT selection rules only allow transitions to the *a₁"* level from the ground state. Current literature values for $\upsilon_4{}'$ all refer to the *a₁"* level. We thus calculated $\upsilon_4{}' = a_1{}''$ from $4_0^1 - 0_0^0$ to be 540.55(54) cm$^{-1}$. This is consistent with previous measurements.

### 3.4.3 Jahn Teller splitting in the $\upsilon_4{}' = 1$, $E''$ × $e'$ level

We used the $4_1^1$ band to probe the $e''$ level of the $\tilde{\mathrm{A}}{}^2\mathrm{E}''\otimes\upsilon_4(\mathrm{e}')$ manifold. Along with other measurements, we calculated the JT splitting *JT($a_1$" - e")* from the relation $(4_1^1 + \upsilon_4{}'') - 4_0^1$ to be -1.55(1.9) cm$^{-1}$. The relatively small magnitude of the splitting is consistent with previous observations of small to moderate JT coupling strength in the $Q_4$ coordinate.

### 3.5 Discussion

We observed the origin of the $\tilde{A} \leftarrow \tilde{X}$ transition of $NO_3$ for the first time in the gas phase. The band origin was assigned to $T_0(\tilde{A})$ = 7062.25(0.5) cm$^{-1}$, with integrated absorption cross section for the band ~1.3 × 10$^{-20}$ cm. From the assignment, we determined all the fundamental vibrational levels of the Ã state except $\upsilon_3{}'$. We also identified several $4_1^X$ hot bands in the 7000-7650 cm$^{-1}$ region. From the $4_1^1$ band, we calculated the splitting in the $\tilde{\mathrm{A}}{}^2\mathrm{E}''\otimes\upsilon_4(\mathrm{e}')$ manifold, *JT($a_1$" - e")* = -1.55(1.9) cm$^{-1}$. This was the first quantitative measurement of the JT activity along the $Q_4$ mode.

A comparison of our experimental vibrational frequencies to the calculated values was shown in Table 3.3. As MRCI calculations predict a large JT distortion for the $\tilde{A}$ state, vibrational frequencies were calculated for the $\tilde{A}$ state ($B_1$) assuming $C_{2v}$ symmetry. Table 3.3 shows that adiabatic models cannot quantitatively describe the $\tilde{A}$ state accurately, although CCSD(T) does surprisingly well. Non-adiabatic effects therefore must be included to model $NO_3$ correctly. Several groups have begun to use the LVC model to include PJT effects. The LVC model has already been used to calculate ground state vibrational frequencies of $NO_3$ with great quantitative success.[13] No one however has used the LVC model to directly study the origin band of the $\tilde{A} \leftarrow \tilde{X}$ transition of $NO_3$. In fact, no theoretical work has been done on the magnetic dipole transitions of $NO_3$.

The LVC model has been used by Faraji *et al.* to predict a small JT distortion along the $Q_4$ coordinate and a very strong JT distortion along the $Q_3$ coordinate for $NO_3$.[43] This could explain the difficulties in observing the $3_0^1$ band, as poor Franck-Condon overlap should lead to very weak absorption. In our previous CRD study, we had tentatively assigned the anomalously strong absorption at 8287 $cm^{-1}$ to the $3_0^1$ band (Fig. 3.10). The difference between the $3_0^1$ and $0_0^0$ band is approximately $\upsilon_2' \oplus \upsilon_4'$. If the anomalous band is reassigned to the $2_0^1 4_0^1$ band, the anomalous strong absorption could be explained by intensity borrowing from the "zero-frequency" electronic transition between the $\tilde{A}^2E''$ state components via strong quadratic PJT coupling between the $\tilde{A}$ and $\tilde{X}$ states (Fig. 3.11). The dipole moment between the $\tilde{A}^2E''$ state components is estimated to be quite strong (~1.2 Debeye).[53] Weak absorptions observed in the 8760 $cm^{-1}$ region in the previous CRD study would then be the best candidates for the $3^1_0$ band ($\upsilon_3'$~1697 cm$^{-1}$). The high density of bands in the region however makes definitive assignment difficult. Improved theoretical calculations of the vibrational frequencies in the Ã state would help us definitively assign the $3^1_0$ band.

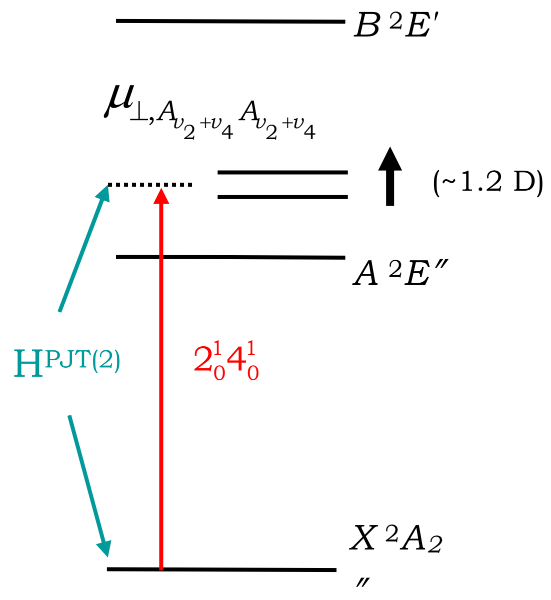

**Figure 3.11.** Schematic of intensity borrowing mechanism for the anomalous $2^1_0 4^1_0$ band. The "zero-frequency" transition can be compared to the first order Starks effect.

While we have provided many new benchmarks for *ab initio* models, open experimental questions on the $\tilde{A}$ state remain. The most obvious issue is the resolution of the two observed peaks in the origin region. Our assignment of the first peak to the origin band is consistent with other groups' estimates of the origin band: $T_0(\tilde{A})$ = 7000(110) cm$^{-1}$, 7061(8) cm$^{-1}$, 7064 cm$^{-1}$, and 7058.5 cm$^{-1}$, respectively.[24,32,33,36] The second peak is located only 8 cm$^{-1}$ to the blue of the first peak. As the second peak also grows relative to the concentration of $NO_3$, the peak appears to belong to $NO_3$. From our temperature experiments, we rule out the possibility that the second peak is a hot band. The feature is also too strong to be an electric quadrupole transition.

The second peak has a rotational contour similar to the parallel $4_0^1$ band. Of the $\tilde{A}\,^2E''\otimes\upsilon_4(e')=a_1''\oplus a_2''\oplus e''$ manifold, the $a_1''$ and $e''$ levels have been observed via the $4_0^1$ and $4_1^1$ bands, respectively. Only the $a_2''$ level has never been observed. Its energy level has been predicted to be ~10 cm$^{-1}$ above the zero point of the $\tilde{A}$ state.[53] This corresponds roughly to the observed shift in the second peak from the origin band.

Transitions from the ground state to the $a_2''$ level however are forbidden. This can be shown by examination of the symmetry of the total wavefunction $\Psi_{tot}$ for $NO_3$:

$$\Psi_{tot}=\Gamma_{elec}\times\Gamma_{vibr}\times\Gamma_{rot}\times\Gamma_{nuclr} \tag{3.5}$$

Assuming $D_{3h}$ symmetry (or subgroup $D_3$), $\Psi_{tot}$ should remain the same upon exchange of the oxygen atoms (bosons, with $I = 0$):

$$\hat{P}_{12}\Psi_{tot}=+\Psi_{tot}\,. \tag{3.6}$$

Then,

$$\begin{aligned}&A_1\in\Psi_{tot}=\Gamma_{elec}\times\Gamma_{vibr}\times\Gamma_{rot}\times\Gamma_{nuclr}\\&=\Gamma_{elec}\times\Gamma_{vibr}\times\Gamma_{rot}\otimes A_1\Rightarrow\Gamma_{elec}\times\Gamma_{vibr}\times\Gamma_{rot}=A_1\end{aligned}\,. \tag{3.7}$$

Assuming $\Gamma_{elec}=A_1$ and $\Gamma_{vibr}=A_1$, for $K = 0$, even $J$ levels have $A_1$ symmetry, while odd $J$ levels have $A_2$ symmetry. For $K = 3n$, the $J$ levels have both $A_1$ and $A_2$ symmetry, while for $K \neq 3n$, the $J$ levels have $E$ symmetry.[54]

The ground state of $NO_3$ has $A_2$ symmetry ($\Gamma_{elec} \otimes \Gamma_{vibr} = A_2$). Thus, from equation (3.7), only odd $J''$ levels of $K'' = 0$ and $J''$ levels of $K'' = 3n$ are allowed. The selection rules for a parallel band state that: $\Delta K = 0$, with $\Delta J = \pm 1$ for $K'' = 0$ and $\Delta J = 0, \pm 1$ for $K'' \neq 0$. Then for $K' = 0$, only even $J''$ levels ($A_1$) are allowed. In the $\tilde{A}^2E'' \otimes \upsilon_4(e')$ manifold, equation (3.7) implies that only the vibronic state with $A_1$ symmetry is allowed. A new mechanism is therefore needed to explain observation of the $a_2''$ level.

One possible mechanism is the inclusion of rotationally forbidden states. Oka *et al.* used this mechanism to explain the observation of the forbidden $\upsilon_1 \leftarrow 0$ ($A_1 \leftarrow A_1$) transition in $H_3^+$.[55] More explicitly, the rovibrational transition $\upsilon_1$, $J'$, $K+3 \leftarrow J''$, $K''$ borrows intensity from the allowed $\upsilon_2 \leftarrow 0$ ($A_2 \leftarrow A_1$) or $\upsilon_2$, $l = 1$, $J'$, $K+1 \leftarrow J''$, $K''$ transition in $H_3^+$. To better understand the mechanism, consider a simple basis set for a molecule, consisting of the product of vibrational and rotational wavefunctions:

$$\Gamma_{vibr} \otimes \Gamma_{rot} \Rightarrow \ |\upsilon\rangle \, |J \ K\rangle . \qquad (3.8\ \text{a})$$

The wavefunction of a specific energy level is described by the linear combination of the basis set (3.8 a). The symmetry of the individual components must retain the same symmetry as the overall wavefunction. Under this analysis, the $\upsilon_1$ and $\upsilon_2$ states of $H_3^+$ cannot interact:

$$|\upsilon_1\rangle + \lambda \, |\upsilon_2\rangle \Rightarrow A_1 + A_2 . \qquad (3.9\ \text{a})$$

If the vibronic basis set

$$\Gamma_{vibr} \otimes \Gamma_{rot} \Rightarrow \; |\upsilon \;\; J \;\; K\rangle \qquad (3.8\ \text{b})$$

is used, then the symmetries of the rotational levels can differ for each respective state to allow coupling:

$$|\upsilon_1 \;\; J \;\; K_1\rangle + \lambda\, |\upsilon_2 \;\; J \;\; K_2\rangle \Rightarrow (A_1 \otimes A_2) + (A_2 \otimes A_1) = A_2 + A_2 \qquad (3.9\ \text{b})$$

Thus, the forbidden $\upsilon_1 \leftarrow 0$ transition borrows intensity from the allowed $\upsilon_2 \leftarrow 0$ transition. A similar mechanism may be leading to the observation of the second peak in the $NO_3$ spectrum. More experimental and especially theoretical investigations however are needed.

This CRD study represents the only experimental work that has examined the $\tilde{A} \leftarrow \tilde{X}$ hot bands of $NO_3$. While we have focused primarily on the $\tilde{A}$ state, the hot bands can also shed light on the ground state of $NO_3$. We have already demonstrated this by determining the $\upsilon_4''$ level from the observed hot bands. There is current disagreement in the literature over the value of $\upsilon_3''$ (1492 $cm^{-1}$ vs. 1000 $cm^{-1}$). If we take the latter assignment for $\upsilon_3''$, many of the hot bands originating from the $\upsilon_3''$ state would lie in the * regions of Figure 3.5. There are however, many other possible combination bands that could have absorptions in the same region. More experiments are clearly needed.

## 3.6 Summary

This chapter highlighted the quantitative advances we have made in elucidating the non-adiabatic effects of the $\tilde{A}$ state of $NO_3$. We observed the $\tilde{A} \leftarrow \tilde{X}$ magnetic-dipole allowed origin transition, along with several vibronic hot bands, using the pulsed CRDS apparatus. From analysis, we assigned the fundamental vibrational levels of the $\tilde{A}$ state of $NO_3$ and calculated the JT splitting in the $\tilde{A}\,^2E'' \otimes \upsilon_4(e')$ manifold. As a small radical system with both JT and PJT effects, $NO_3$ is a benchmark system for many non-adiabatic models. Our work helped define areas in which theoretical models still need to be developed. Further experimental and theoretical collaborations are planned.

Now that we better understand the chemical physics of $NO_3$, we are ready to examine the role of $NO_3$ in our atmosphere. We are specifically interested in the oxidation of various volatile organic compounds by $NO_3$ at nighttime. We discuss these issues in the following chapter.

## 3.7 References

(1) Finlayson-Pitts, B. J.; Pitts, J. N. *Chemistry of the Upper and Lower Atmosphere: Theory, Experiments, and Applications*; Academic Press: San Diego, CA, 2000.

(2) Seinfeld, J. H.; Pandis, S. N. *Atmospheric Chemistry and Physics*; Wiley-Interscience, 1997.

(3) Wayne, R. P.; Barnes, I.; Biggs, P.; Burrows, J. P.; Canosamas, C. E.; Hjorth, J.; Lebras, G.; Moortgat, G. K.; Perner, D.; Poulet, G.; Restelli, G.; Sidebottom, H. *Atmospheric Environment Part a - General Topics* **1991**, *25*, 1.

(4) Chappuis, J. *Ann. d. l'' ecole Norm. Sup.* **1882**, *11*, 159.

(5) Walsh, A. D. *Journal of the Chemical Society* **1953**, 2301.

(6) Jahn, H. A.; Teller, E. *Proc. R. Soc. Lond. A - Math. Phys. Sci.* **1937**, *161*, 220.

(7) Longuethiggins, H. C.; Opik, U.; Pryce, M. H. L.; Sack, R. A. *Proc. R. Soc. Lond. A - Math. Phys. Sci.* **1958**, *244*, 1.

(8) Opik, U.; Pryce, M. H. L. *Proc. R. Soc. Lond. A - Math. Phys. Sci.* **1957**, *238*, 425.

(9) Applegate, B. E.; Barckholtz, T. A.; Miller, T. A. *Chemical Society Reviews* **2003**, *32*, 38.

(10) Barckholtz, T. A.; Miller, T. A. *International Reviews in Physical Chemistry* **1998**, *17*, 435.

(11) Kaldor, U. *Chemical Physics Letters* **1991**, *185*, 131.

(12) Eisfeld, W.; Morokuma, K. *Journal of Chemical Physics* **2000**, *113*, 5587.

(13) Stanton, J. F. *Journal of Chemical Physics* **2007**, *126.*

(14) Davy, R. D.; Schaefer, H. F. *Journal of Chemical Physics* **1989**, *91*, 4410.

(15) Crawford, T. D.; Stanton, J. F. *Journal of Chemical Physics* **2000**, *112*, 7873.

(16) Eisfeld, W.; Morokuma, K. *Journal of Chemical Physics* **2001**, *114*, 9430.

(17) Wladyslawski, M.; Nooijen, M.; Hoffmann, M. R., Dyall, K. G., Eds. 2002, p 65.

(18) Ishiwata, T.; Fujiwara, I.; Naruge, Y.; Obi, K.; Tanaka, I. *Journal of Physical Chemistry* **1983**, *87*, 1349.

(19) Nelson, H. H.; Pasternack, L.; McDonald, J. R. *Journal of Physical Chemistry* **1983**, *87*, 1286.

(20) Kim, B. S.; Hunter, P. L.; Johnston, H. S. *Journal of Chemical Physics* **1992**, *96*, 4057.

(21) Friedl, R. R.; Sander, S. P. *Journal of Physical Chemistry* **1987**, *91*, 2721.

(22) Jacox, M. E.; Thompson, W. E. *Journal of Chemical Physics* **2008**, *129*.

(23) Kawaguchi, K.; Hirota, E.; Ishiwata, T.; Tanaka, I. *Journal of Chemical Physics* **1990**, *93*, 951.

(24) Deev, A.; Sommar, J.; Okumura, M. *Journal of Chemical Physics* **2005**, *122*.

(25) Jones, E. J.; Wulf, O. R. *Journal of Chemical Physics* **1937**, *5*, 873.

(26) Matsumoto, J.; Imai, H.; Kosugi, N.; Kaji, Y. *Atmospheric Environment* **2005**, *39*, 6802.

(27) Matsumoto, J.; Imai, H.; Kosugi, N.; Kajii, Y. *Chemistry Letters* **2005**, *34*, 1214.

(28) Matsumoto, J.; Kosugi, N.; Imai, H.; Kajii, Y. *Review of Scientific Instruments* **2005**, *76*.

(29) Brown, S. S.; Osthoff, H. D.; Stark, H.; Dube, W. P.; Ryerson, T. B.; Warneke, C.; de Gouw, J. A.; Wollny, A. G.; Parrish, D. D.; Fehsenfeld, F. C.; Ravishankara, A. R. *Journal of Photochemistry and Photobiology a - Chemistry* **2005**, *176*, 270.

(30) Wood, E. C.; Wooldridge, P. J.; Freese, J. H.; Albrecht, T.; Cohen, R. C. *Environmental Science & Technology* **2003**, *37*, 5732.

(31) Carter, R. T.; Schmidt, K. F.; Bitto, H.; Huber, J. R. *Chemical Physics Letters* **1996**, *257*, 297.

(32) Weaver, A.; Arnold, D. W.; Bradforth, S. E.; Neumark, D. M. *Journal of Chemical Physics* **1991**, *94*, 1740.

(33) Hirota, E.; Ishiwata, T.; Kawaguchi, K.; Fujitake, M.; Ohashi, N.; Tanaka, I. *Journal of Chemical Physics* **1997**, *107*, 2829.

(34) Kawaguchi, K.; Ishiwata, T.; Hirota, E.; Tanaka, I. *Chemical Physics* **1998**, *231*, 193.

(35) Deev, A., *Ph. D. Thesis*, California Institute of Technology, 2004.

(36) Jacox, M. E.; Thompson, W. E. *Journal of Physical Chemistry A* **2009**.

(37) Liu, J. J.; Chen, M. W.; Melnik, D.; Yi, J. T.; Miller, T. A. *Journal of Chemical Physics* **2009**, *130*.

(38) Endo, Y.; Saito, S.; Hirota, E. *Journal of Chemical Physics* **1984**, *81*, 122.

(39) Momose, T.; Endo, Y.; Hirota, E.; Shida, T. *Journal of Chemical Physics* **1988**, *88*, 5338.

(40) Viel, A.; Eisfeld, W. *Journal of Chemical Physics* **2004**, *120*, 4603.

(41) Mahapatra, S.; Eisfeld, W.; Koppel, H. *Chemical Physics Letters* **2007**, *441*, 7.

(42) Koppel, H.; Domcke, W.; Cederbaum, L. S. *Advances in Chemical Physics* **1984**, *57*, 59.

(43) Faraji, S.; Koppel, H.; Eisfeld, W.; Mahapatra, S. *Chemical Physics* **2008**, *347*, 110.

(44) Stanton, J. F.; Okumura, M. *Physical Chemistry Chemical Physics* **2009**, *11*, 4742.

(45) Okumura, M.; Stanton, J. F.; Deev, A.; Sommar, J. 2006, p C64.

(46) Bernath, P. *Spectra of Atoms and Molecules*; 2nd ed.; Oxford University Press: New York, 2005.

(47) Callomon, J. H.; Innes, K. K. *Journal of Molecular Spectroscopy* **1963**, *10*, 166.

(48) Lombardi, J. R.; Freeman, D. E.; Klempere.W *Journal of Chemical Physics* **1967**, *46*, 2746.

(49) Van Vleck, J. H. *Astrophysical Journal* **1934**, *80*, 161.

(50) Havey, D. K.; Long, D. A.; Okumura, M.; Miller, C. E.; Hodges, J. T. *Chemical Physics Letters* **2009**, *483*, 49.

(51) Robichaud, D. J., *Ph. D. Thesis*, California Institute of Technology, 2008.

(52) Kawaguchi, K.; Shimizu, N.; Fujimori, R.; Tang, J.; Ishiwata, T.; Tanaka, I. *J. Molecular Spectroscopy* **2011 (submitted)**.

(53) Stanton, J. F., Private communication.

(54) Herzberg, G. *Molecular Spectra and Molecular Structure (3 volume set)*; Kriger Pub., 1992.

(55) Xu, L. W.; Rosslein, M.; Gabrys, C. M.; Oka, T. *Journal of Molecular Spectroscopy* **1992**, *153*, 726.

# Appendix for Chapter 3

## Appendix 3.1 Brief overview of the Jahn Teller (JT) effect

The original Jahn Teller (JT) theorem (1934) states that a *non-linear* molecule in a degenerate electronic orbital state distorts to a lower symmetry configuration to remove the degeneracy.[1] The theorem was extended to *linear* molecules for quadratic or second order vibronic coupling terms by Renner and Teller (Renner-Teller effect) and to molecules with near degenerate states by Öpik and Pryce (pseudo-JT effect).[2-4] Proof of the JT theorem involves perturbation theory, in which the corrections terms are the Taylor expanded vibronic coupling terms.

We define the Hamiltonian as the sum of the electronic potential ($H_{electr}$) for the system at its symmetric configuration (0 subscript in the formulas), the kinetic energy of the nuclei ($T_{nuclr}$), the electrostatic potential of the system ($V(r,Q)$) as a function of both nuclear ($Q$) and electronic ($r$) coordinates, and the spin-orbit Hamiltonian ($H_{SO}$):

$$H = H_{electr} + T_{nuclr} + V(r,Q) + H_{SO} \qquad \text{(A-3.1)}$$

with $$V(r,Q) - V(r,0) = \sum_i^N \left(\frac{\partial V}{\partial Q_i}\right)_0 Q_i + \frac{1}{2}\sum_{i,j}^N \left(\frac{\partial^2 V}{\partial Q_i \partial Q_j}\right)_0 Q_i Q_j + \ldots \qquad \text{(A-3.2)}$$

The $H_{SO}$ term is typically included, as JT systems necessarily involve open-shell systems. Both vibrational and spin angular momenta compete for the orbital angular momentum. In the case of $NO_3$, the spin-orbit coupling term is expected to be very small compared to the JT distortion. Thus, the $H_{SO}$ term is often ignored.

Analysis of $NO_3$ ($D_{3h}$) is parallel to Barckholtz and Miller's analysis of a $C_{3v}$ molecule in a $^2E$ state with degenerate JT active mode $Q_{i,\pm}(e)$. Using vibronic basis set $\{|\Lambda\rangle \prod |\upsilon_i, l_i\rangle\}$, the eigenvalues for the Hamiltonian are:[5]

$$\begin{aligned} U_{i,\pm} &= \frac{1}{2}\lambda_i\rho_i^2 \pm \rho_i k_i (1 + \frac{2g_{ii}\rho_i}{k_i}\cos(3\phi_i) + \frac{g_{ii}{}^2\rho_i{}^2}{k_i{}^2})^{\frac{1}{2}} \\ &\sim \frac{1}{2}\lambda_i\rho_i^2 \pm [k_i\rho_i + g_{ii}\rho_i{}^2\cos(3\phi_i)] \end{aligned} \tag{A-3.3}$$

with $\lambda_i$ = curvature of the potential energy surface at the symmetric configuration, $k_i$ = linear JT constant, and $g_{ii}$ = quadratic JT constant.

$$Q_{i,\pm} = \rho_i e^{\pm i\phi_i} \tag{A-3.4}$$

$$\lambda_i = \langle\Lambda|(\frac{\partial^2 V}{\partial Q_{i,+}\partial Q_{i,-}})_0|\Lambda\rangle \tag{A-3.5}$$

$$k_i = \langle\Lambda|(\frac{\partial V}{\partial Q_{i,\pm}})_0|-\Lambda\rangle \tag{A-3.6}$$

$$g_{ii} = \langle\Lambda|(\frac{\partial^2 V}{\partial Q_{i,\pm}{}^2})_0|-\Lambda\rangle\ . \tag{A-3.7}$$

The minimum and maximum energies at $\phi_{\min,i} = 0, \frac{2\pi}{3}, \frac{4\pi}{3}, \ldots$ and $\phi_{\max,i} = \frac{\pi}{3}, \pi, \ldots$ are:

$$E_{\min/\max,i} = -D_i\omega_{e,i}(1 \pm K_i)\ , \tag{A-3.8}$$

where $M_i$ = reduced mass of the JT active mode and

$$D_i = \frac{k_i^2}{2\hbar}\left(\frac{M_i}{\lambda_i^3}\right)^{\frac{1}{2}} \tag{A-3.9}$$

$$K_i = \frac{g_{ii}}{\lambda_i} \tag{A-3.10}$$

From equation A-3.8, distortion to lower symmetry occurs only when the linear JT or first order vibronic coupling term is non-zero ($D_i \neq 0$). The quadratic JT term ($K_i \neq 0$) removes the symmetry of the distortion. In literature, the JT stabilization energy is often reported as $\varepsilon = |E_{min/max,i}|$ with $K_i = 0$. The expression for the PJT effect is mathematically equivalent to the linear JT term. Both JT and PJT effects are needed to describe distortions in $NO_3$.

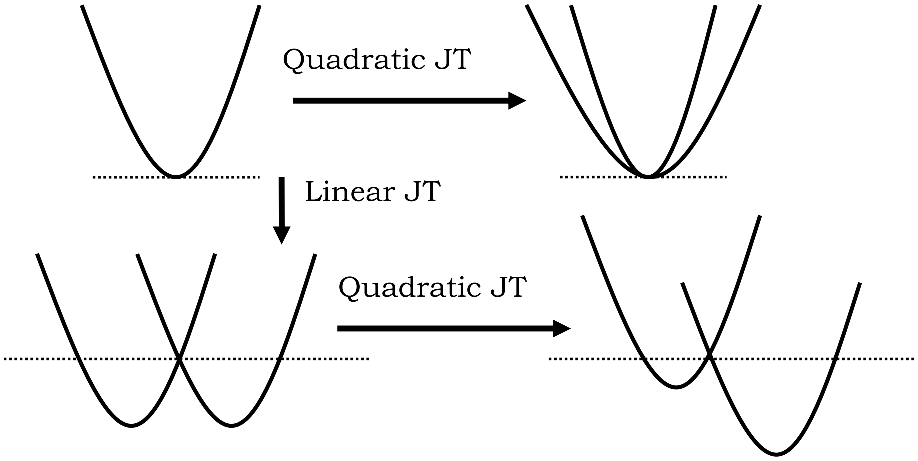

**Figure A-3.1.** Schematics of a two-dimensional slice of a potential energy surface with linear and quadratic JT effects. The linear JT effect must be non-zero for the system to undergo distortion.

## Appendix 3.2 Results from our previous CRDS study

In our previous CRDS study, we examined the Herzberg-Teller-allowed $\tilde{A} \leftarrow \tilde{X}$ transitions of $NO_3$ in the 5000-10000 $cm^{-1}$ region at room temperature.[6,7] The $D_{3h}$ and $C_{2v}$ character tables, along with a correlation table, are shown in Fig. A-3.2. Assuming $D_{3h}$ symmetry, we access all vibrational levels of the $\tilde{A}$ state, except the $\upsilon_1'$ level, from the ground state. Given the perpendicular and parallel electric dipole transition moments $\mu_\perp = E'$ and $\mu_\parallel = A_2''$, the transitions are the following:

$$\begin{aligned} &1_0^1 : a_1' \notin A_2' \otimes (E' \oplus A_2'') \otimes (E'' \otimes a_1') \\ &2_0^1 : a_1' \in A_2' \otimes (E') \otimes (E'' \otimes a_2'') \\ &3_0^1 : a_1' \in A_2' \otimes (A_2'') \otimes (E'' \otimes e') \\ &4_0^1 : a_1' \in A_2' \otimes (A_2'') \otimes (E'' \otimes e') \end{aligned} \tag{A-3.11}$$

The listed bands, along with multiple combination bands, were identified in the previous study. Assignments can be found in the original published papers.

| **$D_{3h}$** | $E$ | $2C_3$ | $3C_2$ | $\sigma_h$ | $2S_3$ | $3\sigma_v$ | | |
|---|---|---|---|---|---|---|---|---|
| $A_1'$ | 1 | 1 | 1 | 1 | 1 | 1 | | $x^2+y^2$, $z^2$ |
| $A_1'$ | 1 | 1 | -1 | 1 | 1 | -1 | $R_z$ | |
| $E'$ | 2 | -1 | 0 | 2 | -1 | 0 | $(x,y)$ | $(x^2-y^2, xy)$ |
| $A_1''$ | 1 | 1 | 1 | -1 | -1 | -1 | | |
| $A_2''$ | 1 | 1 | -1 | -1 | -1 | 1 | $z$ | |
| $E''$ | 2 | -1 | 0 | -2 | 1 | 0 | $(R_x, R_y)$ | $(xz, yz)$ |

| **$C_{2v}$** | E | $C_2$ | $\sigma_v(xz)$ | $\sigma_v'(yz)$ | | |
|---|---|---|---|---|---|---|
| $A_1$ | 1 | 1 | 1 | 1 | z | $x^2$, $y^2$, $z^2$ |
| $A_2$ | 1 | 1 | -1 | -1 | $R_z$ | xy |
| $B_1$ | 1 | -1 | 1 | -1 | x, $R_y$ | xz |
| $B_2$ | 1 | -1 | -1 | 1 | y, $R_x$ | yz |

| **$D_3$** | **$C_{2v}$** |
|---|---|
| $A_1'$ | $A_1$ |
| $A_1'$ | $B_2$ |
| E' | $A_1$+$B_2$ |
| $A_1''$ | $A_2$ |
| $A_2''$ | $B_1$ |
| | $A_2$ + $B_1$ |

**Figure A-3.2.** The $D_{3h}$ (top) and $C_{2v}$ [8] character tables. The correlation table is also included on the side.

The parallel $4_0^1$ and perpendicular $2_0^1$ bands are shown in Fig. A-3.3. While the rotational contours of the bands are distinct, the two bands have surprisingly similar intensities. The rotational contours are discussed in Appendix 3.5. We focus here on the intensities of the two bands. Examination of the intensity borrowing mechanisms reveals the importance of the PJT effect in $NO_3$. (Fig. A-3.4).[9]

For the $4_0^1$ band, the wavefunction describing the ground state of $NO_3$ has contributions from both the $\tilde{X}$ and $\tilde{B}$ states:

$$|\Psi,\tilde{X}\rangle = |\tilde{X}\rangle + \lambda_{PJT:BX}\,|\tilde{B},e'\rangle \tag{A-3.12 a}$$

where $\lambda_{PJT:BX}$ = PJT coupling between the $\tilde{X}$ and $\tilde{B}$ states. The transition dipole moment for the $4_0^1$ band is then:

$$\langle\Psi,\tilde{X}\,|\,\mu_{\parallel}\,|\,\tilde{A},e'\rangle = \langle\tilde{X}\,|\,\mu_{\parallel}\,|\,\tilde{A},e'\rangle + \lambda_{PJT:BX}\langle\tilde{B},e'\,|\,\mu_{\parallel}\,|\,\tilde{A},e'\rangle\,. \tag{A-3.12 b}$$

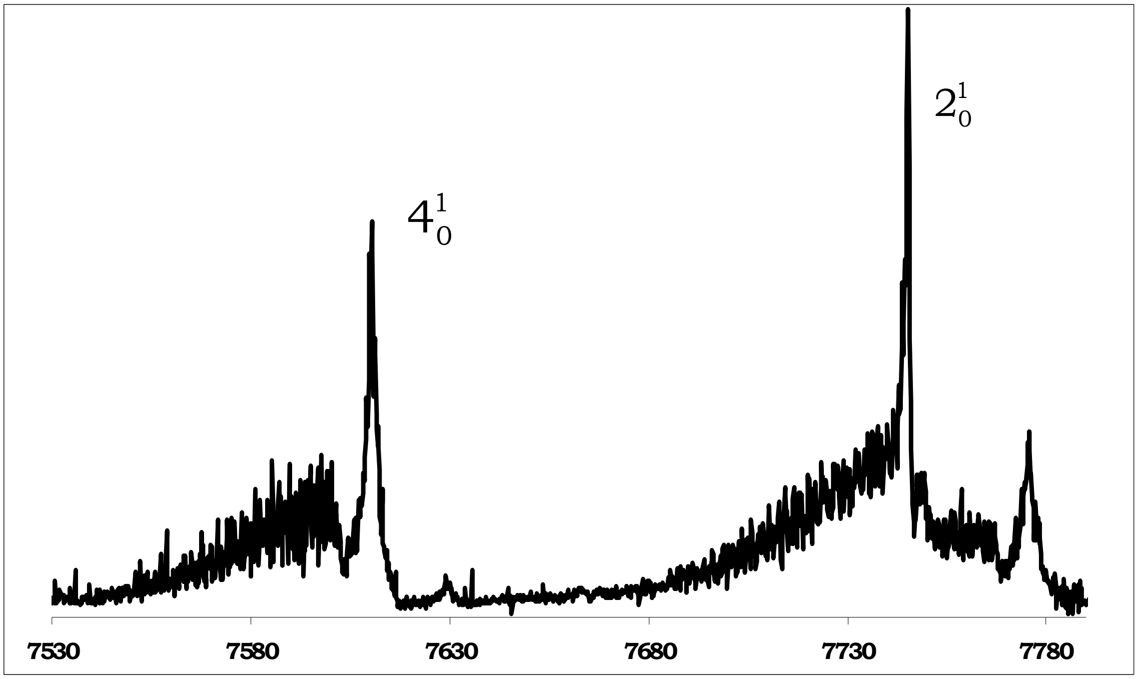

**Figure A-3.3.** CRD spectrum of the $4^1_0$ and $2^1_0$ bands in the 7530-7800 cm$^{-1}$ region.

For the $2^1_0$ band, the wavefunction describing the $\tilde{A}$ state has contributions from both the $\tilde{A}$ and $\tilde{B}$ states:

$$|\Psi,\tilde{A},a_2''\rangle = |\tilde{A},a_2''\rangle + \lambda_{PJT:AB}\,|\tilde{B}\rangle \qquad \text{(A-3.13 a)}$$

where $\lambda_{PJT:AB}$ = PJT coupling between the $\tilde{A}$ and $\tilde{B}$ states. The transition dipole moment for the band is then:

$$\langle\tilde{X}\,|\,\mu_\perp\,|\,\Psi,\tilde{A},a_2''\rangle = \langle\tilde{X}\,|\,\mu_\perp\,|\,\tilde{A},a_2''\rangle + \lambda_{PJT:AB}\langle\tilde{X}\,|\,\mu_\perp\,|\,\tilde{B}\rangle \qquad \text{(A-3.13 b)}$$

For the $4^1_0$ band, $\lambda_{PJT:BX}$ is expected to be very strong, while for the $2^1_0$ band, the $\tilde{B} \leftarrow \tilde{X}$ transition is known to be very strong. Thus, the $4^1_0$ and $2^1_0$ bands coincidentally have similar intensities. From our simulations of the experimental data, the intensity ratio of the bands $2^1_0 : 4^1_0$ was 1.76. Stanton modeled the intensities using a linear multimode vibronic coupling (LVC) model and found the ratio to be 1.36.[9]

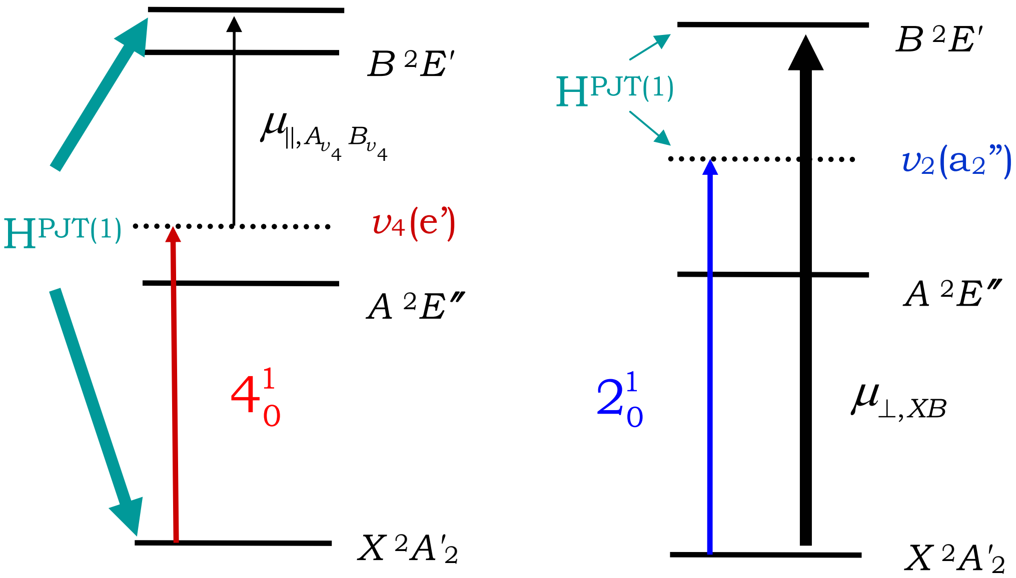

**Figure A-3.4.** Schematics of the intensity borrowing mechanisms for the parallel $4^1_0$ and perpendicular $2^1_0$ bands of $NO_3$. The parallel band borrows intensity from the weak $\tilde{B} \leftarrow \tilde{A}$ transition via strong PJT coupling between the $\tilde{B}$ and $\tilde{X}$ states. The perpendicular band borrows intensity from the strong $\tilde{B} \leftarrow \tilde{X}$ band via weak PJT coupling between the $\tilde{A}$ and $\tilde{B}$ states.

The analysis of the bands highlighted the importance of the PJT effect in $NO_3$. However, an interesting puzzle arose during the simulations. A symmetric top model was used to simulate the $4^1_0$ band; however an asymmetric top model had to be used to simulate the $2^1_0$ band. Asymmetry indicates JT distortion. What is then the symmetry or the extent of vibronic coupling in the $0^0$ level of the $\tilde{A}$ state?

Detection of the origin band $0_0^0$ would solve the puzzle. The $\tilde{A} \leftarrow \tilde{X}$ transition is electric dipole forbidden; however the origin band $0_0^0$ is magnetic-dipole and electric-quadrupole-allowed:

$D_{3h}$ :

magnetic $0_0^0 : a_1' \in A_2' \otimes (\cancel{a_2'} \oplus e'') \otimes E''$

electric quadrupole $0_0^0 : a_1' \in A_2' \otimes (\cancel{a_1'} \oplus \cancel{e'} \oplus e'') \otimes E''$

(A-3.14)

$C_{2v}$ :

magnetic $0_0^0 : a_1 \in B_2 \otimes (\cancel{b_1} \oplus \cancel{b_2} \oplus a_2) \otimes B_1$

electric quadrupole $0_0^0 : a_1 \in B_2 \otimes (\cancel{b_1} \oplus \cancel{b_2} \oplus \cancel{a_1} \oplus a_2) \otimes B_1$

The absorptions are expected to be very weak. A better $NO_3$ source would be necessary to increase the signal-to-noise of the spectra. Thus Chapter 3 built on the previous CRDS study by focusing on detection of the origin band and the hot bands in the 7000-7600 $cm^{-1}$ region.

## Appendix 3.3 $N_2O_5$ synthesis

Dinitrogen pentaoxide ($N_2O_5$) is synthesized in the hood by mixing gases, nitric oxide NO and ozone $O_3$, in a glass vessel (Fig A-3.5). The gas product $N_2O_5$ is collected in a bubbler in a dry ice/acetone bath. The product is a white powder or crystal. $N_2O_4$ impurities can easily be observed by a slight yellow tinge to the powder. To remove impurities, lift the bubbler out of the dry ice/acetone bath and run ozone through the bubbler until the yellow color disappears.

$N_2O_5$ crystals will form on any cold surface, including the inner tube of the bubbler. Before running experiments, warm the sample slowly by running either ozone or helium at room temperature through the bubler. Shake the bubbler gently to push all the $N_2O_5$ sample into the bottom of the bubbler. If extra $N_2O_5$ is synthesized, the bubbler can be put under high pressure helium and placed in liquid nitrogen for storage. Proper care should be taken when handling liquid nitrogen (Appendix 2.4).

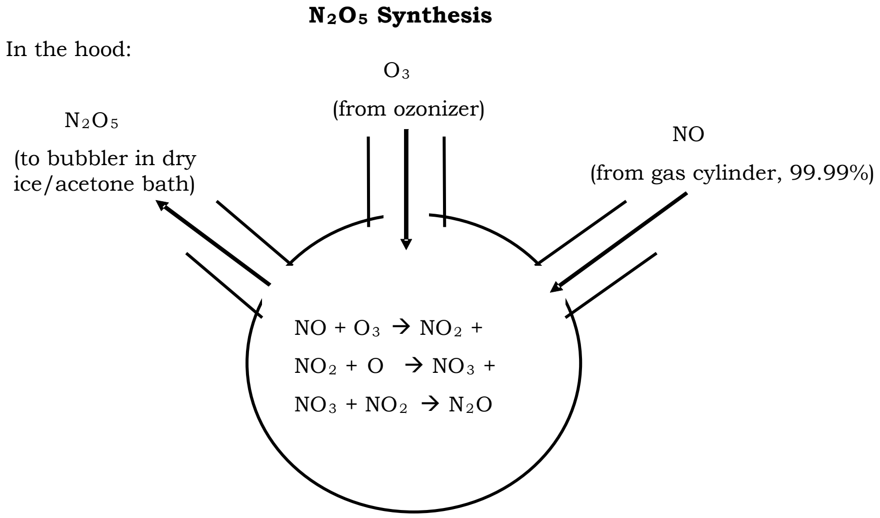

**Figure A-3.5**. Schematic of the synthesis of $N_2O_5$. All connections should be vacuum tight and made from stainless steel or Teflon, as ozone and nitric oxide destroy most o-rings.

## Appendix. 3.4 Nitric acid absorption in the NIR region

The overtone and combination bands of nitric acid ($HNO_3$) have been examined for potential contributions to the photochemistry of the atmosphere.[10,11] We further explored $HNO_3$ absorptions in the NIR region using the pulsed CRDS apparatus. Details of the pulsed CRDS apparatus has been provided in Chapter 2. The Nd:YAG was operated at 20 Hz for maximum data collection per second.

To minimize water absorptions in the NIR, we prepared a 3:1 solution of sulfuric acid (concentrated) and nitric acid (70% $HNO_3$) in a bubbler. The sample was freeze-pump-thawed before being placed in an ice bath. Helium (~20 Torr) was flowed slowly over the $HNO_3$ bubbler ($P_{vapor}$ ~ 1.5 Torr) and into a long residence time Pyrex ringdown cell. The ringdown cell was wrapped with thermal tape for temperature experiments.

Preliminary spectra were collected from 7200-7600 $cm^{-1}$ and 7900-8300 $cm^{-1}$ at 0.2 $cm^{-1}$ step size at both $T = 25^{\circ}C$ and $T = 60^{\circ}C$. The absorption features were identical at both temperatures, thus only the preliminary spectra of nitric acid at room temperature are shown in Fig. A-3.6 (a-b).

The $HNO_3$ bands are surprisingly structured in the region. Calculated intensities of the bands have been plotted in Fig. A-3.6 (a).[12] The experimental and theoretical data match very well. The strong OH overtone at ~6940 $cm^{-1}$ has been well-studied, with measured absorption cross section $\sigma < 6.9 \times 10^{-19}$ $cm^2$ $cm^{-1}$ $molec^{-1}$.[12,13] CRDS, however, cannot quantitatively measure strong absorptions (Chapter 2). We therefore are currently in the process of diluting $HNO_3$ concentrations such that spectra of both the OH overtone and combination bands can be obtained simultaneously. The integrated intensities of the bands can then be directly compared.

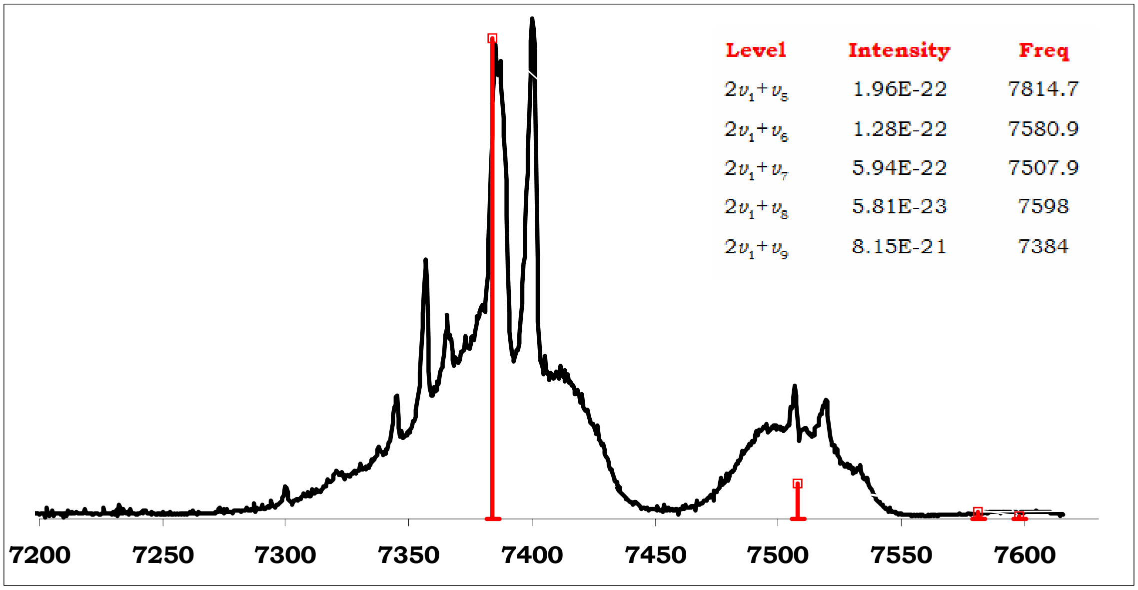

**Figure A-3.6 (a).** CRD spectrum of nitric acid in the 7200-7650 cm$^{-1}$ NIR region. The red lines are from VPT2 calculations from ref [11].

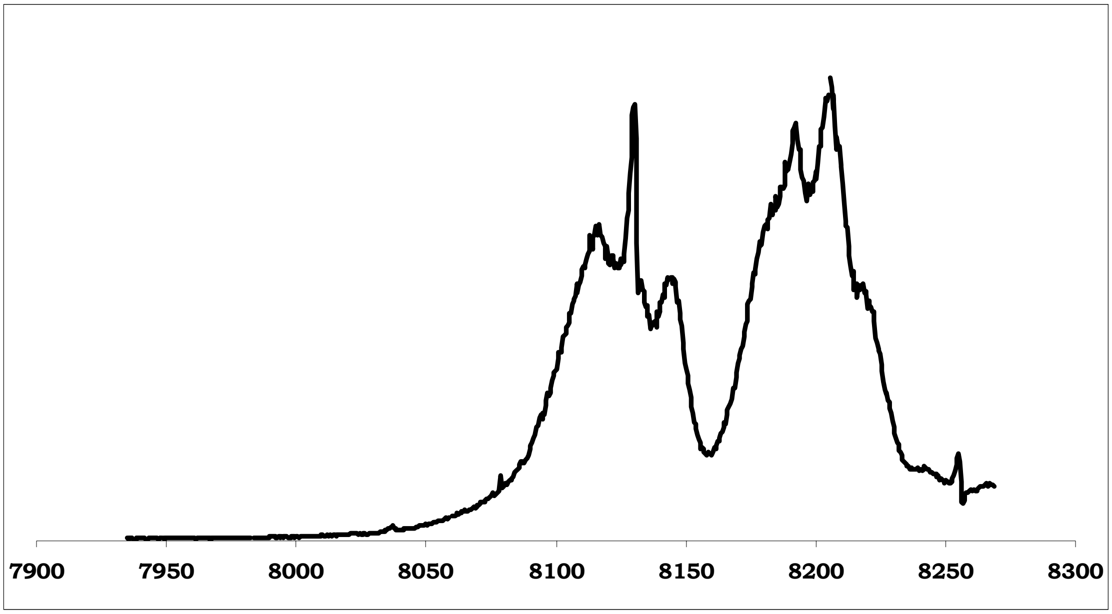

**Figure A-3.6 (b).** CRD spectrum of nitric acid in the 7900-8500 cm$^{-1}$ NIR region.

## Appendix 3.5 Calculations and simulations of $NO_3$

### A-3.5.1. PGopher simulations

We simulated the rotational contours of the $NO_3$ bands using PGopher v. 5.3. In Appendix 3.2, we compared the intensities of the parallel $4_0^1$ and perpendicular $2_0^1$ bands. We began simulations with these bands (Fig. A-3.7 and Fig. A-3.8). A comparison of the contours shows that the $4_0^1$ band has a small gap, caused by shifting of the Q-branch to the blue of the bandhead. The distinct contours for perpendicular and parallel bands are useful for band assignments in $NO_3$.

We next simulated the observed hot bands in the 7000-7600 cm$^{-1}$ region. In a recent study, Kawaguchi, *et al.* fit the $\upsilon_3 + \upsilon_4 \leftarrow \upsilon_4$ and $\upsilon_3 + 2\upsilon_4 \leftarrow \upsilon_4$ bands in the ground state to determine the rotational constants of the $4_1$ level.[14] We used these values to model the transitions; however, simulations were still difficult, as the observed bands consisted of a convolution of multiple hot bands in some absorption regions.

In the 7300-7400 cm$^{-1}$ region, we used the upper rotational constants of the $2_0^1$ band to simulate the $4_1^0 2_0^1$ band (Fig. A-3.9). There may be a second peak at 7360 cm$^{-1}$. If we adjust C′, however, the simulation matches the rotational contour of the hot band. Thus, we assigned the band origin of the $4_1^0 2_0^1$ band with large error bars to 7370.0(3.0) cm$^{-1}$. We analyzed the hot bands in the 7200-7270 cm$^{-1}$ and 7450-7500 cm$^{-1}$ regions similarly and assigned the peaks to $4_1^1$ at 7235.5(1.5) cm$^{-1}$ and $4_1^0 1_0^1$ at 7481.0(1.0) cm$^{-1}$, respectively (Fig. A-3.10 and A-3.11).

Simulation of the $0_0^0$ origin band was the most difficult (Fig. A-3.12). We could not re-create the two peaks with a magnetic dipole model. We therefore fit the first peak to the magnetic dipole transition and simulated perpendicular and parallel bands to take into account the other absorption features in the 7000-7100 cm$^{-1}$ region. In order to check whether the rotational constants for the $0^0$ level were reasonable, we used the same rotational constants to fit the $4_1^0$ band (Fig. A-3.13). The simulated contour was in good agreement with the experimental $4_1^0$ band.

We also tried using an electric quadrupole model to fit the absorption peaks (Fig. A-3.14), but this model also could not recreate the two absorption features. Electric quadrupole transitions are much weaker than magnetic dipole transitions; thus we maintain that the observed features resulted from the $0_0^0$ magnetic dipole transition. Determination of $\upsilon_4''$ = 365.75(1.1) cm$^{-1}$ from $0_0^0 - 4_1^0$ are very consistent with previous measurements of the $\upsilon_4''$ level ($\upsilon_4''$ = 365.6 cm$^{-1}$ and 365.48419 cm$^{-1}$).[14,15] Thus, we used the magnetic dipole PGopher simulation of the $0_0^0$ band to calculate the integrated absorption cross section in the study.

**File for PGopher v5.3: A X 4_7600band_symmetric.pgo**

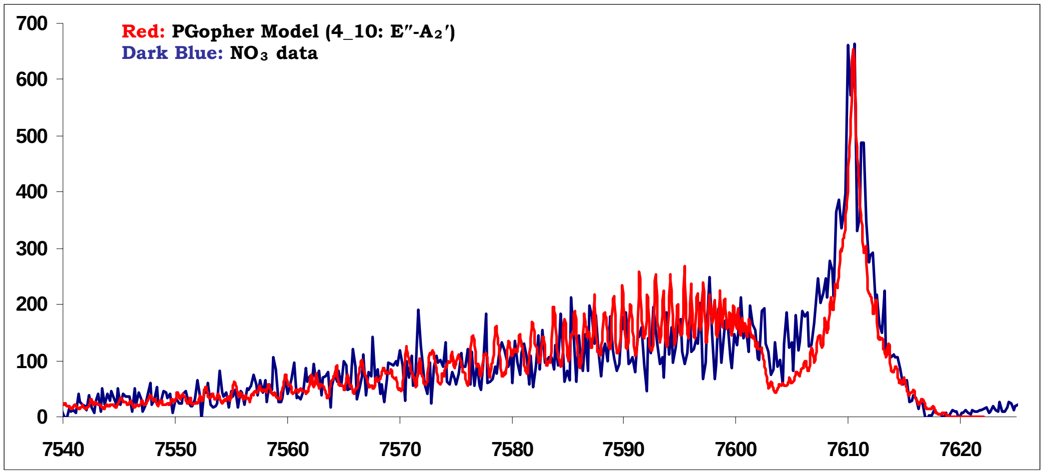

**$D_{3h}$ model:**

Ground State:
B = 0.458575
C = 0.229288

Excited Ã State:
B = 0.4325
C = 0.2155
$T_o$ = 7602.8 cm$^{-1}$

**$4^1_0$ 7602.8 ± 0.2 cm$^{-1}$**

**Figure. A-3.7.** PGopher simulation of the $4^1_0$ band using a symmetric top model.

**File for PGopher v5.3: mod_NO3 A-X 2 and 4 7660-7750.pgo**

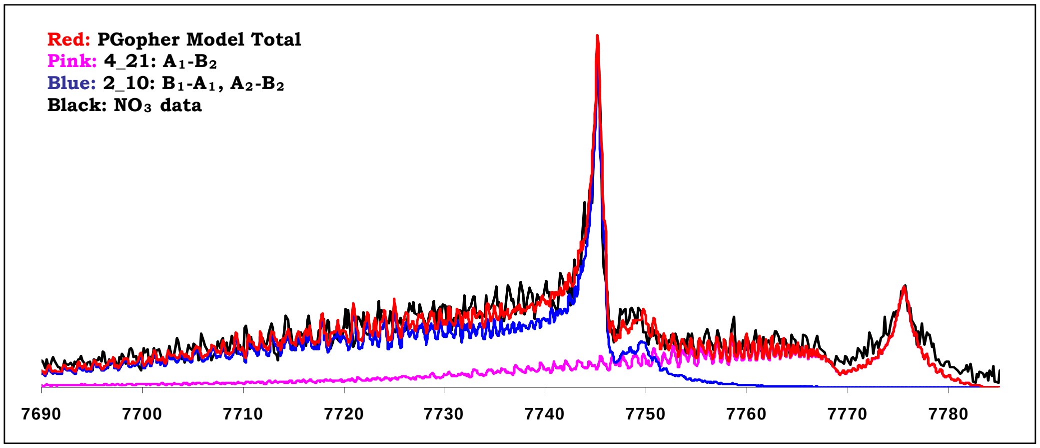

**$C_{2v}$ model:**

Ground State:
A = B = 0.458575
C = 0.229288

**$2^1_0$**

Excited Ã State:
A = 0.4395
B = 0.42
C = 0.22
$T_o$ = 7740.9 cm$^{-1}$

**7740.9 ± 0.3 cm$^{-1}$**

Ground State:
A = B =
0.4592222
C = 0.2278233

**$4^2_1$**

Excited Ã State:
A = 0.434
B = 0.425
C = 0.215
$T_o$ = 7768.85 cm$^{-1}$

**7768.9 ± 0.5 cm$^{-1}$**

**Figure A-3.8.** PGopher simulation of the $2^1_0$ band using a symmetric top model.

**File for PGopher v5.3: NO3 7300-7400.pgo**

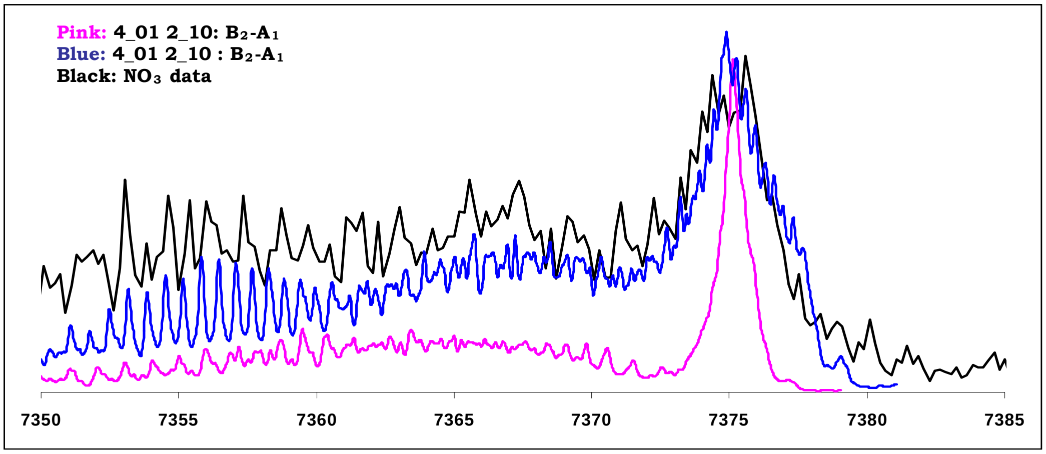

**C$_{2v}$ model:**

Ground State:
A = B = 0.458575
C = 0.229288

Excited Ã State:
A = 0.4395
B = 0.42
C = 0.22
T$_o$ = 7370.7 cm$^{-1}$
**Take values from 2_10**

$\mathbf{4^0_1 2^1_0}$

**7370 ± 3 cm$^{-}$**

Ground State:
A = B =
0.4592222
C = 0.2278233

Excited Ã State:
A = 0.434
B = 0.425
**C = 0.205**
T$_o$ = 7372.7 cm$^{-1}$
**Change C constant**

**Figure A-3.9.** PGopher simulation of the $4^0_1 2^1_0$ band using an asymmetric top model.

**File for PGopher v5.3: NO3 7100-7300.pgo**

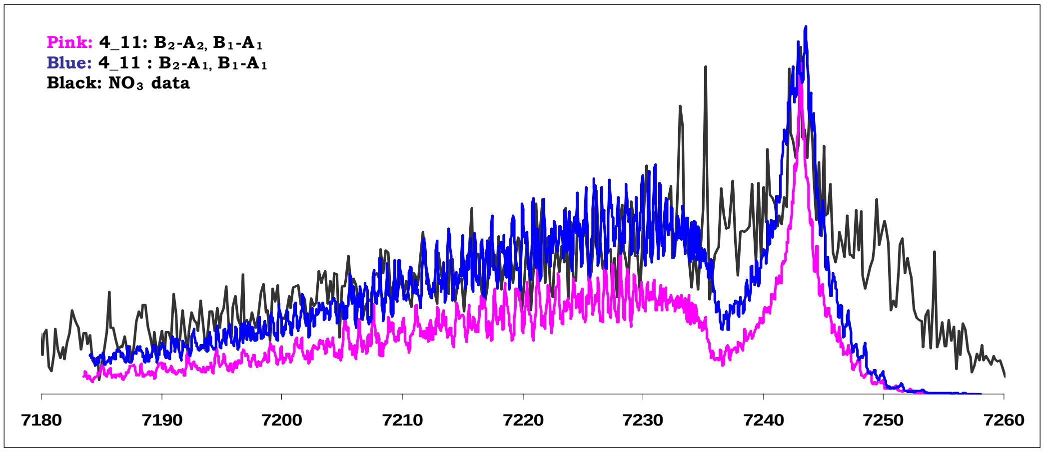

**C$_{2v}$ model:**

Ground State:
A = B =
0.4592222
C = 0.2278233
Excited Ã State:
A = 0.4325
B = 0.4325
C = 0.2175
T$_o$ = 7235.7 cm$^{-1}$
**Take values from 4_10**

$\mathbf{4^1_1}$

**7235.5 ± 1.5 cm$^{-1}$**

Ground State:
A = B =
0.4592222
C = 0.2278233
Excited Ã State:
A = 0.4325
**B = 0.4225**
C = 0.2175
T$_o$ = 7236.7 cm$^{-1}$
**Change B constant**

**Figure A-3.10.** PGopher simulation of the $4^1_1$ band using an asymmetric top model.

**File for PGopher v5.3: NO3 7440-7500.pgo**

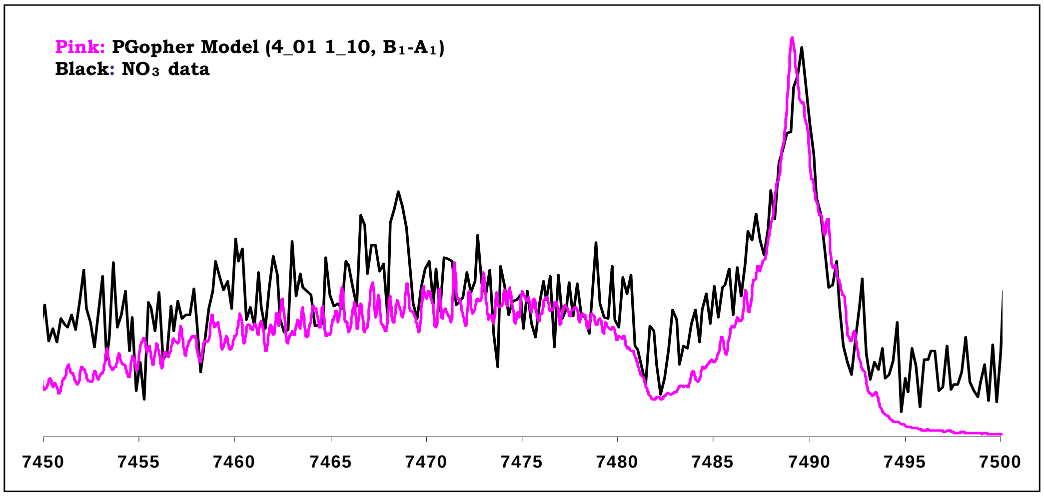

**$C_{2v}$ model:**

Ground State:
A = 0.4592222
B = 0.4592222
C = 0.2278233

Excited Ã State:
A = 0.44
B = 0.43
C = 0.215
$T_o$ = 7480.8 $cm^{-1}$

**$4^0_1 1^1_0$** **7481 ± 1.5 $cm^{-1}$**

**Figure A-3.11.** PGopher simulation of the $4^0_1 1^1_0$ band using an asymmetric top model.

**File for PGopher v5.3: NO3_origin_magdipole_allthree.pgo**

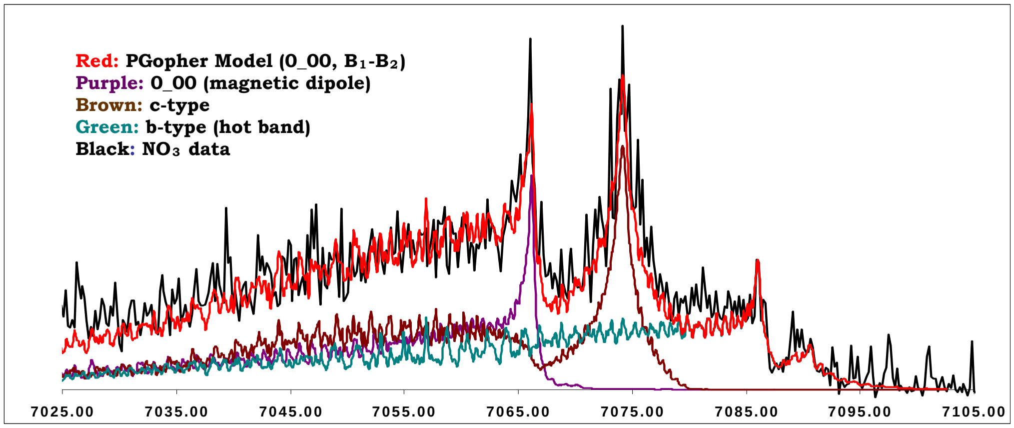

**$C_{2v}$ model:**

Ground State:
A = 0.458575
B = 0.458675
C = 0.229288

Excited Ã State:
A = 0.445
B = 0.4125
C = 0.2175
$T_o$ = 7062.25 $cm^{-1}$

**$0^0_0$**

**7062.25 ± 0.5 cm-**

**c-type (parallel)**
Excited Ã State:
A = 0.435
B = 0.43
C = 0.215
$T_o$ = 7066.46 $cm^{-1}$

**b-type (perpendicular)**
Excited Ã State:
A = 0.435
B = 0.41
C = 0.21
$T_o$ = 7083.5 $cm^{-1}$

**Figure A-3.12.** PGopher simulation of the $0^0_0$ band using a magnetic dipole $C_{2v}$ model.

**File for PGopher v5.3: 4_01_6700_ICOSband.pgo**

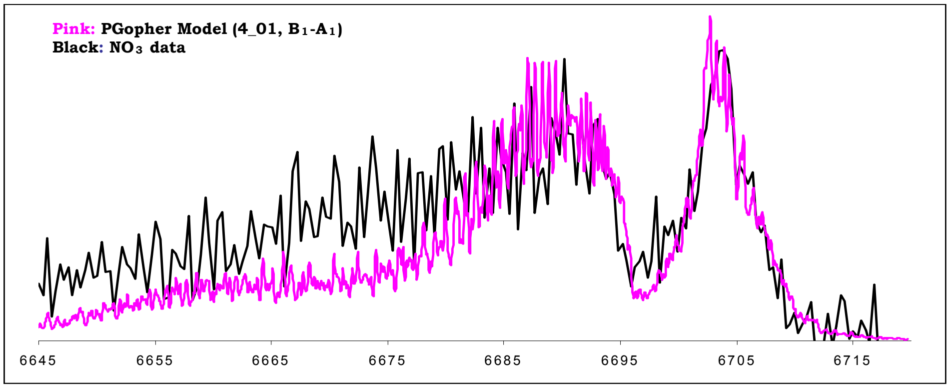

**$C_{2v}$ model:**

| Ground State: | Excited Ã State: |
|---|---|
| A = 0.4592222 | A = 0.445 |
| B = 0.4592222 | B = 0.4125 |
| C = 0.2278233 | C = 0.2175 |
| | $T_o$ = 6696.5 cm$^{-1}$ |

**$4^0_1$** **6696.5 ± 1.0 cm$^{-1}$**

**Take values from 0_00**

**Figure A-3.13.** PGopher simulation of the $4^0_1$ band using an asymmetric top model.

## Electric quadrupole model

In PGopher, simulate an electric quadrupole transition by using a spherical transition moment and choosing rank 2. Components (-2, 0, 2) resulted in spectra, although all component may not be allowed in NO$_3$.

**File for PGopher v5.3: quadrupole.pgo**

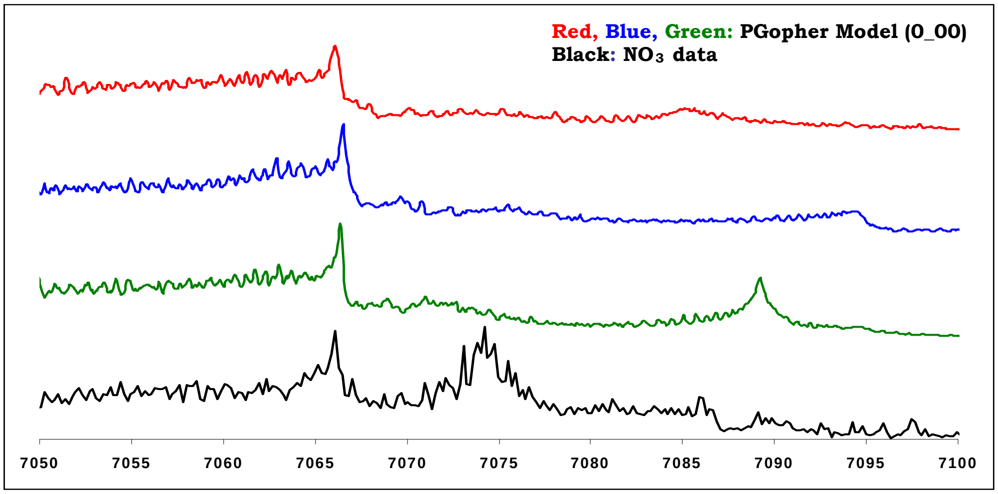

**$C_{2v}$ model:** **From earlier 0_00 fit**

| Ground State: | Excited Ã State: | Excited Ã State: | Excited Ã State: |
|---|---|---|---|
| A = 0.458575 | A = 0.445 | A = 0.445 | **A = 0.435** |
| B = 0.458675 | B = 0.4125 | **B = 0.43** | **B = 0.43** |
| C = 0.229288 | C = 0.2175 | C = 0.2175 | C = 0.2175 |
| | $T_o$ = 7062.25 cm$^{-1}$ | $T_o$ = 7062.25 cm$^{-1}$ | $T_o$ = 7062.25 cm$^{-1}$ |

**Figure A-3.14.** PGopher simulation of the $0^0_0$ band using an electric quadrupole $C_{2v}$ model.

### A-3.5.2 Rotational constants

Most theoretical papers publish the structural parameters of the chemical system, rather than the rotational constants. For $NO_3$, the most three important parameters are *d* and *r*, the length of the NO bonds in Å units, and *θ*, the angle between the z-axis and NO bond. To calculate the rotational constants from these parameters, $NO_3$ is drawn on a yz-graph with the origin of the axes at the center of mass of $NO_3$ (Fig. A-3.15). The planarity of the radical simplifies the calculations. The moments of the inertia tensor are determined from the coordinates and masses (amu) of the atoms:

$$
\begin{aligned}
I_{xx} &= \sum (m_i y_i^2 + m_i z_i^2) = I_y + I_z \\
I_{yy} &= \sum (m_i x_i^2 + m_i z_i^2) = \sum m_i z_i^2 \\
I_{zz} &= \sum (m_i x_i^2 + m_i y_i^2) = \sum m_i y_i^2 \\
I_{xy} &= -\sum m_i x_i y_i = 0 \\
I_{xz} &= 0;\ I_{yz} = 0
\end{aligned}
\tag{A-3.15}
$$

The rotational constants (A < B < C) are then:[16]

$$\text{Rotational constant } (A, B, C) = \frac{16.8576314}{\text{Inertia } (I_{xx},\ I_{yy},\ I_{zz})} \tag{A-3.16}$$

The z-axis is generally chosen as the axis of the symmetry. The coordinate system in Fig. A-3.15 was chosen assuming $C_{2v}$ symmetry for $NO_3$. If $NO_3$ has $D_{3h}$ symmetry, the coordinate system should be rewritten such that the z-axis is coming out of the plane. The calculations simplify even further as A = B for an oblate symmetric top.

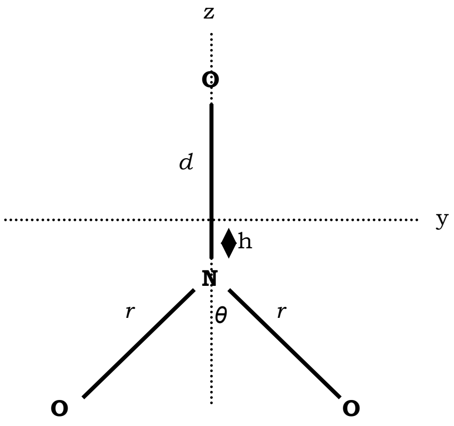

**Figure A-3.15.** The structural parameters of $NO_3$

A program was written in Mathematica to simplify the calculations. A copy of the code is provided below. Comments have been written in red to guide the reader through the program.

```
Clear[h]
mN = 14; amu
mO = 16; amu
r=1.28; angstroms
d=1.24; angstroms
θ=(120/2)*π/180; radians
Solve[mN*{0,0,-h}+mO*{0,0,d-h}
    +mO*{0,-r*Sin[θ],-h-r*Cos[θ]}+mO*{0,r*Sin[θ],-h-
r*Cos[θ]}==0,h]; solve for the center of mass of the
coordinate system i.e. h.
Ixx = mN*h^2+mO*(d-h)^2+2*mO*((-r*Sin[θ])^2+(-h-
r*Cos[θ])^2)/.Solve[mN*{0,0,-h}+mO*{0,0,d-h}
      +mO*{0,-r*Sin[θ],-h-r*Cos[θ]}+mO*{0,r*Sin[θ],-h-
r*Cos[θ]}==0,h];
Ixy=0;
Iyy=mN*h^2+mO*(d-h)^2+2*mO*(-h-r*Cos[θ])^2/.Solve[mN*{0,0,-
h}+mO*{0,0,d-h}
      +mO*{0,-r*Sin[θ],-h-r*Cos[θ]}+mO*{0,r*Sin[θ],-h-
r*Cos[θ]}==0,h];
Iyz=0;
Izz=2*mO*(r*Sin[θ])^2/.Solve[mN*{0,0,-h}+mO*{0,0,d-h}
      +mO*{0,-r*Sin[θ],-h-r*Cos[θ]}+mO*{0,r*Sin[θ],-h-
r*Cos[θ]}==0,h];
Inertia={Ixx,Iyy,Izz}
{A,B,c}=Reverse[Sort[16.8576314/Inertia]] A < B < C
```

Unfortunately, the structural parameters cannot be directly determined from the rotational constants. We can however use the relationship between the constants to evaluate the asymmetry and non-planarity of the chemical system. For asymmetry,

$$\kappa = \frac{2B - A - C}{A - C} \tag{A-3.17}$$

Deviations from $\kappa$ = 1 (oblate symmetric top) and $\kappa$ = -1 (prolate symmetric top) indicate the degree of asymmetry. For non-planarity,

$$\Delta_0 = 16.8576314 \times (\frac{1}{C} - \frac{1}{A} - \frac{1}{B}) \tag{A-3.18}$$

Deviations from $\Delta_0$ = 0 (planar) indicate non-planarity.

### A-3.5.3 Simulation of the bands in Mathematica

If the Hamiltonian is well-defined, the $NO_3$ bands can be simulated in Mathematica. We wrote a Mathematica simulation for the $4_0^1$ band using the symmetric top Hamiltonian from the high resolution diode study of the $4_0^1$ band.[17] While the code is too long to include in the thesis, we outline here the ideas behind the program.

A set of quantum numbers is first chosen to describe the energy levels of the molecular system. In general, the quantum labels include $J$ = the total angular momentum of the molecule $K$ = the projection of $J$ along the molecular z-axis, and $M$ = the projection of $J$ along a laboratory z-axis. It is convenient to first generate the lower and upper state energy levels separately using the Hamiltonian. The Hamiltonian is also a function of the quantum numbers and has been well-defined for symmetric tops:[16]

$$E(J,K) = BJ(J+1) - D_J(J(J+1))^2 + (A-B)K^2 - D_K K^4 - D_{JK}J(J+1)K^2$$

(A-

3.19)

where $D_J$, $D_K$, $D_{JK}$ are the centrifugal distortion constants.

The energy levels are organized by *K*-stacks, i.e., for every *K*, the *J*-dependent energy levels ($J \geq K$) for that value of *K* is calculated. Not all *J*-levels are however allowed. Thus, the symmetry of the *J*-levels must be investigated, along with the overall symmetry of the wave function describing the molecule (Chapter 3).[18]. Once the energy levels have been well-defined, for symmetric tops, the selection rules for the transition are very simple: $\Delta K = 0$, with $\Delta J = \pm 1$ for $K = 0$ and $\Delta J = 0, \pm 1$ for $K \neq 0$. A program can be written to calculate the energy differences between corresponding upper and lower energy levels from the selection rule.

A similar approach can be used for asymmetric tops. Finding good quantum numbers can be more difficult. Often the coordinate system is chosen such that the asymmetric top behaves as a near oblate or prolate symmetric top. The selection rules change according to the chosen coordinate system. Thus, great care should be taken to check that the correct selection rules are being used and the symmetry of the involved energy levels is correct within the chosen coordinate system.

The line positions are easily calculated once the Hamiltonian is well-defined. Simulating the line intensities of the bands can be more difficult. There may be some subtleties in weighing the energy levels, but to first approximation, the line intensity is a product of the square of the transition dipole moment and the Hönl-London factors. The Hönl-London factors are:[18]

For ΔK = 1,

$$\begin{aligned} &P(J''): \frac{(J''-1-K'')(J''-K'')}{J''} \\ &Q(J''): \frac{(J''+1+K'')(J''-K'')(2J''+1)}{4J''(J''+1)} \\ &R(J''): \frac{(J''+2+K'')(J''+1+K'')}{4(J''+1)} \end{aligned} \tag{A-3.20 a}$$

where P, Q, and R refer to ΔJ = -1, 0, and 1 respectively.

For ΔK = 0,

$$\begin{aligned} &P(J''): \frac{(J''+K'')(J''-K'')}{J''} \\ &Q(J''): \frac{2(J''+1)K''^2}{J''(J''+1)} \\ &R(J''): \frac{(J''+1+K'')(J''+1-K'')}{(J''+1)} \end{aligned} \tag{A-3.20 b}$$

For ΔK = -1,

$$\begin{aligned} &P(J''): \frac{(J''+1-K'')(J''+K'')(2J''+1)}{4J''(J''+1)} \\ &Q(J''): \frac{(J''-1+K'')(J''+K'')}{4J''} \\ &R(J''): \frac{(J''+2-K'')(J''+1-K'')}{4(J''+1)} \end{aligned} \tag{A-3.20 c}$$

For symmetric tops, only equations A-3.20 (b) are utilized. The transition dipole moment involves *ab initio* calculations that are beyond the scope of this discussion. However for relative line intensities within the same transition, only the Hönl-London factors are needed.

## Appendix 3.6 Off-axis integrated cavity output spectroscopy

The methodology of CRDS was discussed in Chapter 2. Improvements to CRDS and related cavity enhanced methods have focused on increasing the *Q*-factor of the cavity by efficiently coupling the laser to the cavity modes. In integrated cavity output spectroscopy (ICOS), the difference between the integrated light output from a cavity with and without an absorber is measured. Ideally, the spacing between the cavity modes is narrower than the laser line width such that the laser is always in resonance with the cavity.

The free spectral range (FSR) of a cavity (*L*) is defined as the frequency spacing between two successive resonant modes:

$$FSR = \Delta\upsilon_{longitudinal} = \frac{c}{2L} \tag{A-3.21}$$

In off-axis (OA)-ICOS, the laser is aligned off-axis to the optical cavity axis such that the transverse modes are activated. The mode density of the cavity is therefore significantly increased (Fig. A-3.16).[19,20] In many cases, however, the mode spacing remains large with respect to the laser line width. Thus, either the laser or the cavity modes are modulated to randomize interaction between the laser and cavity. This can be achieved by either sweeping the laser frequencies rapidly or jittering the length of the optical cavity.

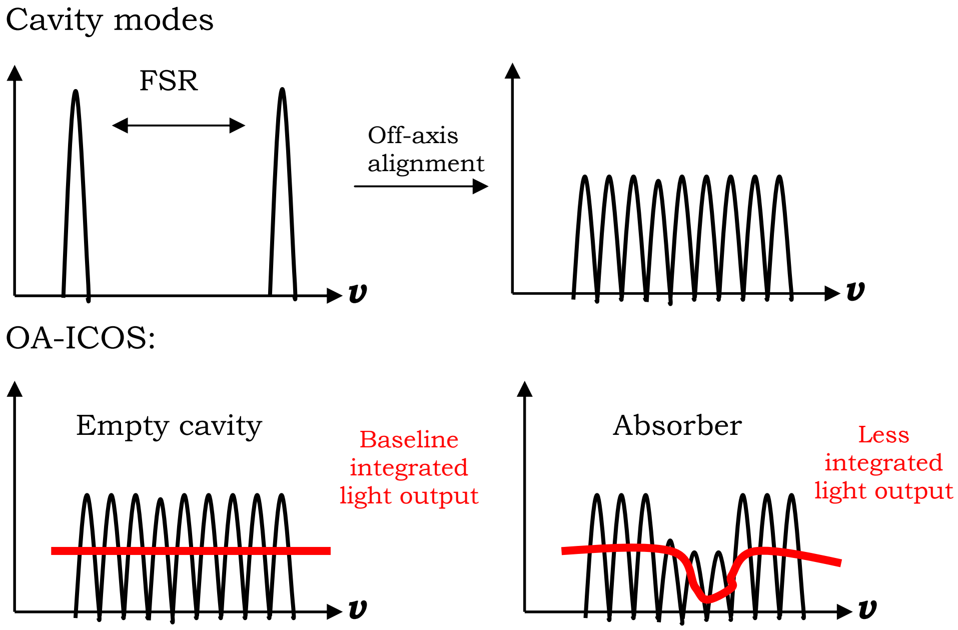

**Figure A-3.16.** Schematics of OA-ICOS. The integrated light output from the cavity is measured with and without an absorber. The high density of cavity modes increases the sensitivity of the method, as the baseline is better averaged.

A brief schematic of the OA-ICOS apparatus is shown in Fig. A-3.17. Output from an external cavity diode laser (New Focus TLB-6323, Γ = 100 kHz, 1407-1545 nm) with a 40-dB isolator is divided among the optical cavity, 1-m reference gas cell, and a 5-cm ultra-low expansion (ULE) quartz etalon (FSR ~ 2 GHz). A New Focus 2011 InGaAs detector (gain $10^4$, BW = 50 kHz) with voltage amplifier SRS560 (30 kHz low pass filter, gain 5) and two New Focus IR 1623 detectors (BW = 50 kHz) are used for detection along their respective paths. All signals are collected using an analog-to-digital converter (Keithley Instruments, KPCI-3108) and recorded in Labview simultaneously.

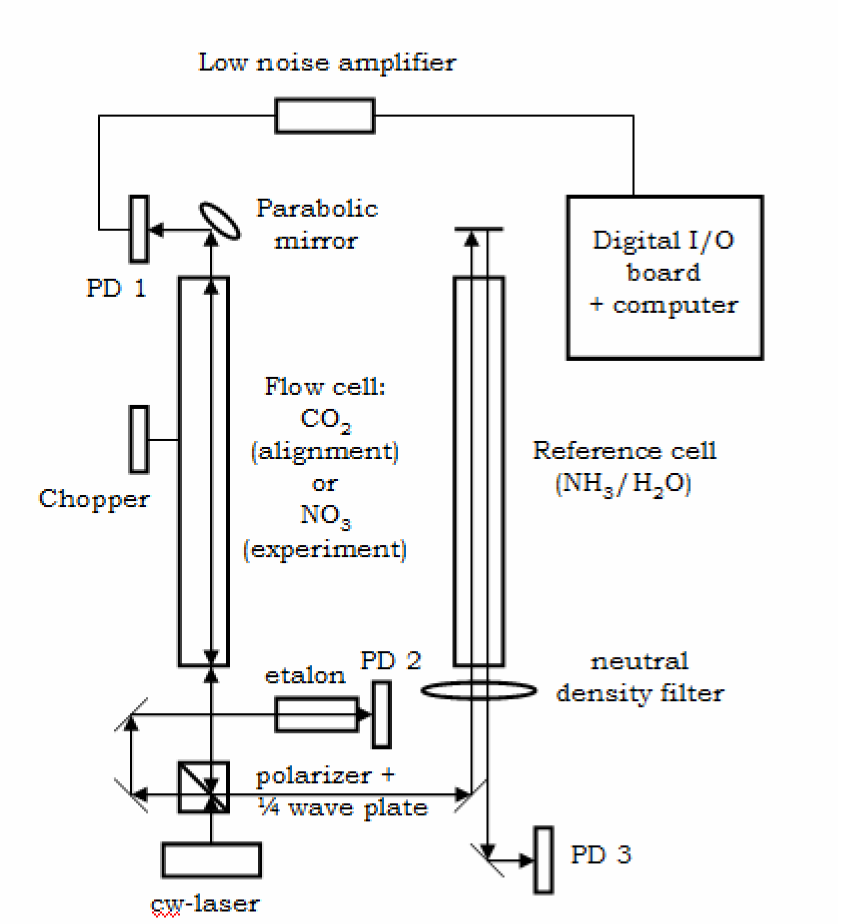

**Figure A-3.17.** Schematic of the OA-ICOS apparatus. The sensitivity of the apparatus is 2.5 x $10^{-8}$ per pass.

The optical cavity consists of two highly reflective mirrors (Newport 1500, R = 99.98%) spaced 85-cm apart (FSR ~ 176 mHz). The cavity is first aligned on-axis, before the laser is translated horizontally ~0.25 cm and tilted vertically for OA-ICOS experiments. Minor adjustments can be made while maximizing carbon dioxide signal. Mechanical jittering of the optical cavity by a chopper wheel increases the sensitivity of the apparatus to 2.5 x $10^{-8}$ per pass.

For the OA-ICOS experiments, the chemistry was very similar to that used in the pulsed CRDS experiment. In order to take a scan, the piezoelectric transducer (PZT) of the laser was modulated with a 50 Hz sawtooth function to span ~1.5 cm$^{-1}$. The stepper motor was used to coarsely tune the wavelength of the laser such that successive PZT scans could be collected and overlapped for a global spectrum of the $4^0_1$ band of NO$_3$. The effective resolution of the apparatus was 75 MHz or 0.002 cm$^{-1}$:

$$\begin{aligned}&\text{resolution} = \text{laser frequency span} \times \frac{\text{ramp frequency}}{\text{detector bandwidth}} \\ &= 45\ \text{GHz} \times \frac{50\ \text{Hz}}{30\ \text{kHz}} = 75\ \text{MHz}\ (0.002\ \text{cm}^{-1})\end{aligned} \tag{A-3.22}$$

The resolution is sufficiently below the Doppler width of NO$_3$ (0.01 cm$^{-1}$). The reference cell was filled with either ammonia or water to provide frequency calibration, while the ULE was used to calibrate the relative spacing between the cavity modes.

The raw data is shown in Fig. A-3.18. We found however that the NO$_3$ concentrations were not stable for the experimental run. Thus, we analyzed only the excerpt of the NO$_3$ data about the $4^0_1$ band head. To compare our data to the CRD spectrum, we convoluted the OA-ICOS spectrum with a 0.1 cm$^{-1}$ Gaussian line shape. The two spectra matched very well (Fig. 3.7).

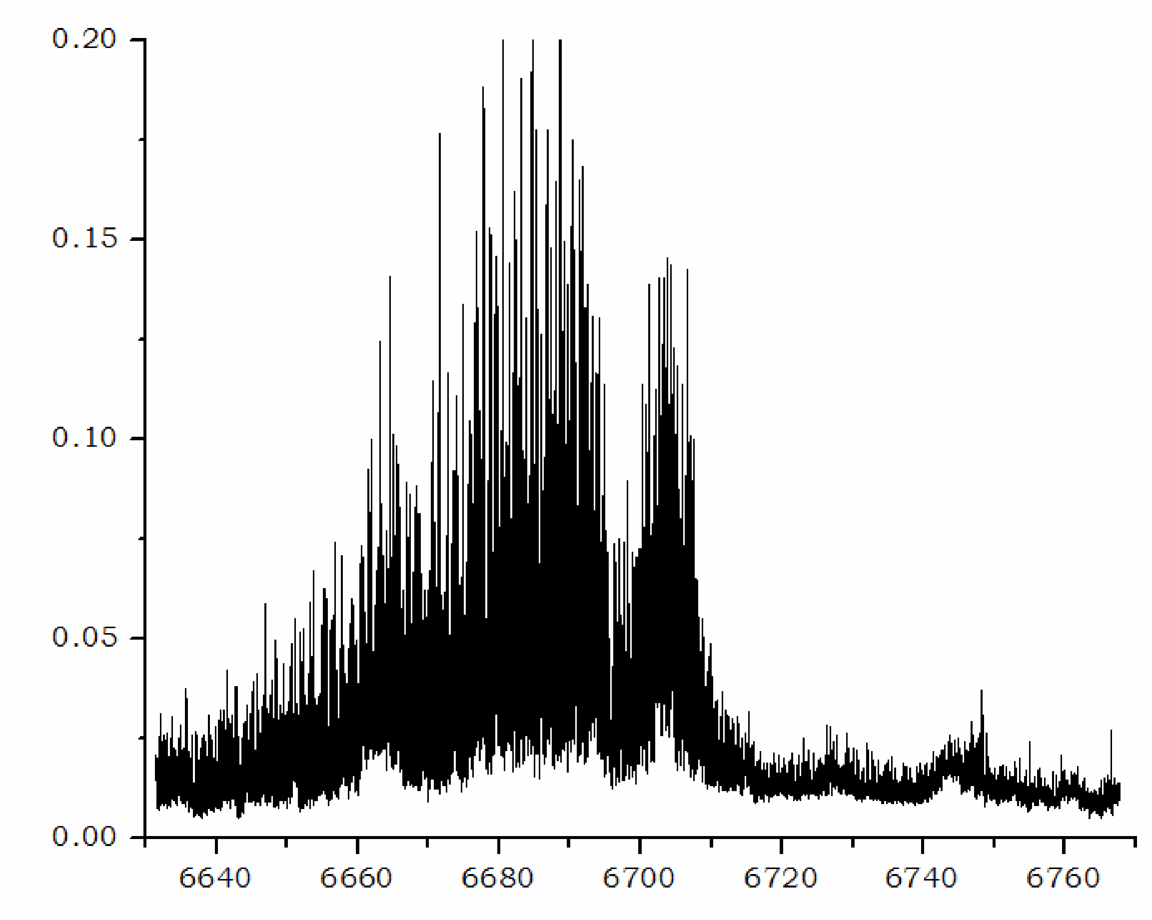

**Figure A-3.18.** Raw data from the OA-ICOS experiment (0.002 cm$^{-1}$). The bump at 6660 cm$^{-1}$ is due to fluctuations in the $NO_3$ concentrations. For analysis, we therefore used only the 6680-6720 cm$^{-1}$ region.

## Appendix 3.7 References

(1) Jahn, H. A.; Teller, E. *Proc. R. Soc. Lond. A - Math. Phys. Sci.* **1937**, *161*, 220.

(2) Renner, R. *Z. Phys.* **1934**, *92*.

(3) Longuethiggins, H. C.; Opik, U.; Pryce, M. H. L.; Sack, R. A. *Proc. R. Soc. Lond. A - Math. Phys. Sci.* **1958**, *244*, 1.

(4) Opik, U.; Pryce, M. H. L. *Proc. R. Soc. Lond. A-Math. Phys. Sci.* **1957**, *238*, 425.

(5) Barckholtz, T. A.; Miller, T. A. *International Reviews in Physical Chemistry* **1998**, *17*, 435.

(6) Deev, A., *Ph. D. Thesis,* California Institute of Technology, 2004.

(7) Deev, A.; Sommar, J.; Okumura, M. *Journal of Chemical Physics* **2005**, *122*.

(8) Wayne, R. P.; Barnes, I.; Biggs, P.; Burrows, J. P.; Canosamas, C. E.; Hjorth, J.; Lebras, G.; Moortgat, G. K.; Perner, D.; Poulet, G.; Restelli, G.; Sidebottom, H. *Atmospheric Environment Part a - General Topics* **1991**, *25*, 1.

(9) Stanton, J. F.; Okumura, M. *Physical Chemistry Chemical Physics* **2009**, *11*, 4742.

(10) Donaldson, D. J.; Tuck, A. F.; Vaida, V. *Chemical Reviews* **2003**, *103*, 4717.

(11) Vaida, V. *Journal of Physical Chemistry A* **2009**, *113*, 5.

(12) Feierabend, K. J.; Havey, D. K.; Varner, M. E.; Stanton, J. F.; Vaida, V. *Journal of Chemical Physics* **2006**, *124*.

(13) Feierabend, K. J.; Havey, D. K.; Vaida, V. *Spectroc. Acta Pt. A - Molec. Biomolec. Spectr.* **2004**, *60*, 2775.

(14) Kawaguchi, K.; Shimizu, N.; Fujimori, R.; Tang, J.; Ishiwata, T.; Tanaka, I. *J. Molecular Spectroscopy* **2011 (submitted)**.

(15) Jacox, M. E.; Thompson, W. E. *Journal of Physical Chemistry A* **2009**, accepted.

(16) Bernath, P. *Spectra of Atoms and Molecules*; 2nd ed.; Oxford University Press: New York, 2005.

(17) Hirota, E.; Ishiwata, T.; Kawaguchi, K.; Fujitake, M.; Ohashi, N.; Tanaka, I. *Journal of Chemical Physics* **1997**, *107*, 2829.

(18) Herzberg, G. *Molecular Spectra and Molecular Structure (3 volume set)*; Krieger Pub., 1992.

(19) O'Keefe, A. *Chemical Physics Letters* **1998**, *293*, 331.

(20) Paul, J. B.; Lapson, L.; Anderson, J. G. *Applied Optics* **2001**, *40*, 4904.

## Chapter 4

# DETECTION OF THE PEROXY INTERMEDIATE IN THE OXIDATION OF 2-BUTENE BY THE NITRATE RADICAL ($NO_3$)

## 4.1 Introduction to $NO_3$ as a tropospheric oxidant

The free radical oxidation of volatile organic compounds (VOCs) drives the chemistry of the Earth's atmosphere. While most radicals are produced photochemically, the nitrate radical ($NO_3$) is formed by reaction:

$$NO_2 + O_3 \rightarrow NO_3 + O_2 \qquad (4.1)$$

During the daytime, $NO_3$ is destroyed by sunlight:[1]

$$NO_3 + h\upsilon \rightarrow NO + O_2 \qquad (4.2\ a)$$

$$+ h\upsilon \rightarrow NO_2 + O(^3P) \qquad (4.2\ b)$$

At nighttime, however, $NO_3$ is the main oxidant in the troposphere (~50 ppt), with various roles in gas phase chemistry reactions and secondary organic aerosol (SOA) formation.[2-20]

The oxidation of VOCs by $NO_3$ is directly related to the formation of peroxy radicals in the atmosphere. For alkanes (RH), hydrogen abstraction is the main reaction mechanism:

$$RH + NO_3 \rightarrow R + HNO_3 \qquad (4.3)$$

$$R + O_2 \rightarrow RO_2 \text{ (peroxy radical)} \qquad (4.4)$$

The peroxy radicals play key roles in pollutant and ozone formation. The different reaction pathways and the relationship of the radicals to other atmospheric networks have been discussed in Chapter 1. Significant research has been focused on characterizing the peroxy radicals and measuring their rates of reaction with atmospheric gas species.[3,21-26]

Less research has been devoted to the oxidation of alkenes by $NO_3$. Observations of products from $NO_3$-initiated oxidation of isoprene in SOAs however have sparked interest in the oxidation of alkenes.[6,7,9-12,14,18,19] Isoprene is the most abundant non-methane VOC in the atmosphere, with global emissions of ~500 Tg (C) $yr^{-1}$.[5] As isoprene is released mainly from deciduous trees during the day, its reaction with the $NO_3$ was long believed to be insignificant. The new studies however show that under cloudy conditions or near dusk, both $NO_3$ and isoprene levels are sufficiently high to be of atmospheric relevance.

$NO_3$ addition to the double bond of alkenes (R=R′) leads to competing pathways of epoxide and $NO_3$-substituted peroxy radical formation:

$$R{=}R' + NO_3 \rightarrow R\text{-}R'(NO_3) \qquad (4.5)$$

$$R\text{-}R'(NO_3) \rightarrow ROR' \text{ (epoxide)} + NO_2 \qquad (4.6\ a)$$

$$+\ O_2 \rightarrow R\text{-}R'(NO_3)O_2 \text{ (nitrooxyalkyl peroxy radical)} \qquad (4.6\ b)$$

At low pressures, the epoxide channel (4.6 a) dominates, while at high pressures, the $NO_3$-peroxy radical channel (4.6 b) dominates.[13,27-41] $NO_3$-peroxy radicals undergo similar reaction pathways as the unsubstituted peroxy radicals; however, the reaction rates are not well-characterized. To date, only one theoretical paper has investigated the potential energy surface (PES) of isoprene oxidation by $NO_3$ and the different branching ratios of $NO_3$-peroxy radical formation.[42] No experiment has ever detected for any alkene oxidation system the $NO_3$-peroxy radical intermediate in the gas phase.

While much attention has been given to the formation of peroxy radicals, the epoxide channel is also of atmospheric interest, especially with respect to SOA formation.[43-46] Epoxide rings can open in acidic mediums to produce volatile diol, sulfate ester, and polymer products. These products have all been observed in SOA field samples. The Intergovernmental Panel on Climate Change recently highlighted aerosols as one of the greatest uncertainties in the Earth's radiation budget.[47] The radiation budget plays a significant factor in global warming and climate modeling predictions. All atmospheric sources of epoxides must be taken into account.

The quantitative yields of the competing pathways of $NO_3$-initiated oxidation of alkene systems are highly debated. In the simple $NO_3$ + 2-butene system, estimates of the epoxide yields range from <1% to 20%.[4,27,29] The majority of these measurements were made in aerosol chambers, in which the final end products were analyzed hours after initiation of the reactions. Early intermediate and product detection could resolve some of the observed disparities. In particular, *in situ* detection of the $NO_3$-peroxy radicals would be useful.

In this work, we use the pulsed CRDS apparatus to detect the 2-$NO_3$-butyl peroxy radical in the oxidation of 2-butene by $NO_3$. We discuss in the next section why this reaction system was chosen and how we propose to detect the radical in the gas phase.

## 4.2 Detection of the 2-$NO_3$-butyl peroxy radical

### 4.2.1 The $NO_3$ + 2-butene system

The reaction rate constants of $NO_3$ with various alkenes have recently been reviewed.[4] While the $NO_3$-ethyl peroxy radical is the simplest and therefore prototype of the substituted $NO_3$ peroxy radicals, the measured rate constant for $NO_3$ addition to ethene is considerably slower than $NO_3$ addition to 2-butene and isoprene:

$k_{298\,K}$ (ethene + $NO_3$) = $2.05 \times 10^{-16}$ cm$^3$ molec$^{-1}$ s$^{-1}$
$k_{298\,K}$ (*cis/trans*-2-butene + $NO_3$) = $3.52/3.90 \times 10^{-13}$ cm$^3$ molec$^{-1}$ s$^{-1}$
$k_{298\,K}$ (isoprene + $NO_3$) = $2.05 \times 10^{-13}$ cm$^3$ molec$^{-1}$ s$^{-1}$. (4.7 a-c)

The potential energy surfaces (PES) of $NO_3$ addition to ethene and 2-butene have been investigated to explain the difference between the two rate constants.[48-52] The PES barrier for the $NO_3$-ethene adduct to dissociate back to the reactants is much lower than the barrier for the $NO_3$-2-butene adduct. None of the PES calculations however take into consideration the presence of oxygen. More theoretical work is needed on $NO_3$-initiated oxidation of alkenes under atmospheric conditions.

For this work, we chose $NO_3$ + 2-butene as the prototype alkene oxidation system. While other large alkenes have similar rates of reaction with $NO_3$, the inherent symmetry of 2-butene simplifies the detection problem to only one $NO_3$-peroxy radical. The chemical pathways of $NO_3$ + 2-butene and the associated peroxy radical reactions are shown in Fig. 4.1. For simplicity, reactions with other common peroxy radical species such as the hydroperoxy species ($HO_2$) have not been included. Of the reactions shown, only the rate of $NO_3$ addition to 2-butene has been well-measured.

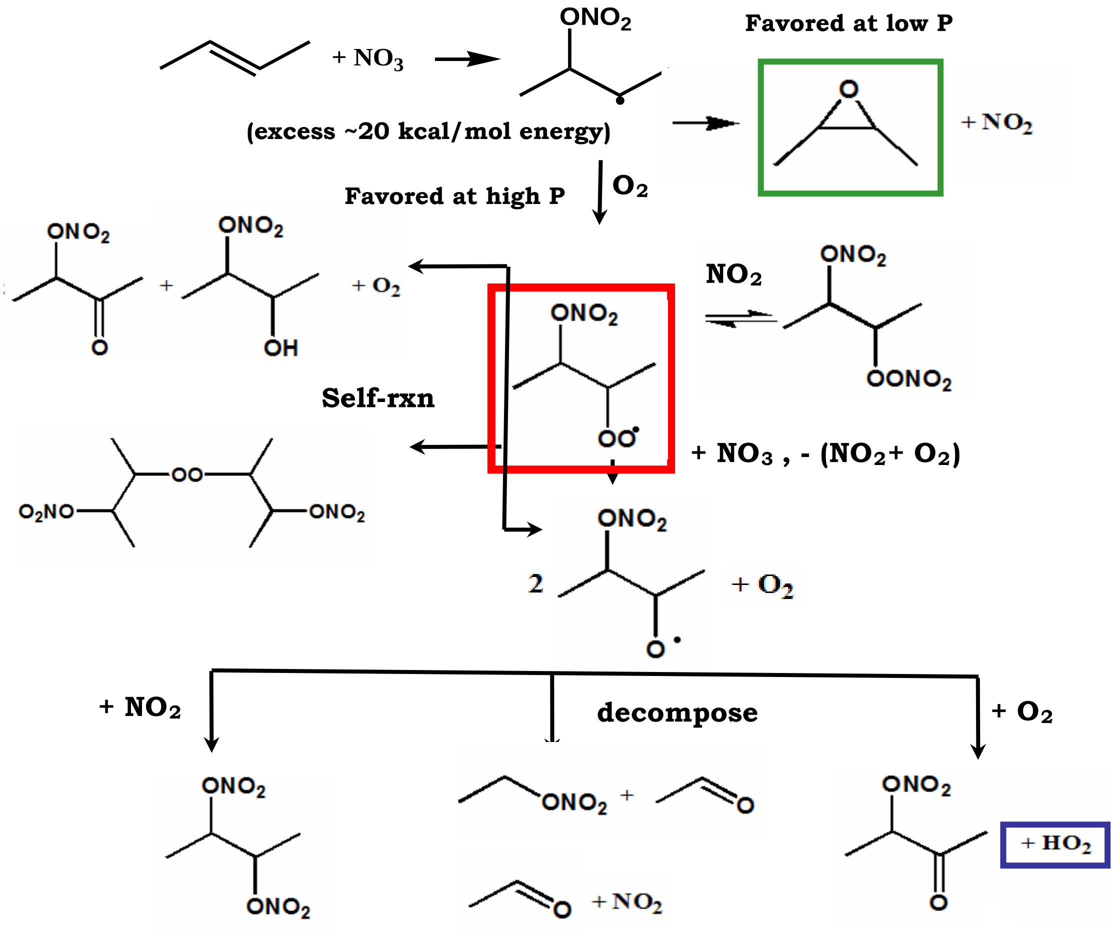

**Figure 4.1.** Schematics of the various chemical pathways of 2-butene oxidation by $NO_3$.. The red and green boxes signify major products of the competing oxidation pathways, the 2-$NO_3$-butyl peroxy radical (red) and the epoxide product, oxirane (green). Although the reactive hydroperoxy radical $HO_2$ (blue box) is formed downstream, reactions with unsubstituted peroxy radicals have not been included in the reaction scheme for simplicity.

### 4.2.2 Detection of peroxy radicals

Peroxy radicals have generally been detected spectroscopically via the $\tilde{B} \leftarrow \tilde{X}$ transition in the ultraviolet (UV) region.[3,21-26] While absorption cross sections are quite large ($\sigma_{UV}(RO_2) = 10^{-16} \sim 10^{-18}$ cm$^2$),[1] the spectral features tend to be broad and structure-less, as the PES for the upper $\tilde{B}$ state is a repulsive surface. Many peroxy radicals therefore have overlapping UV absorptions, complicating individual identification and quantification of the radicals (Fig. 4.2). In this work, we explore an alternate method to detect the peroxy radical.

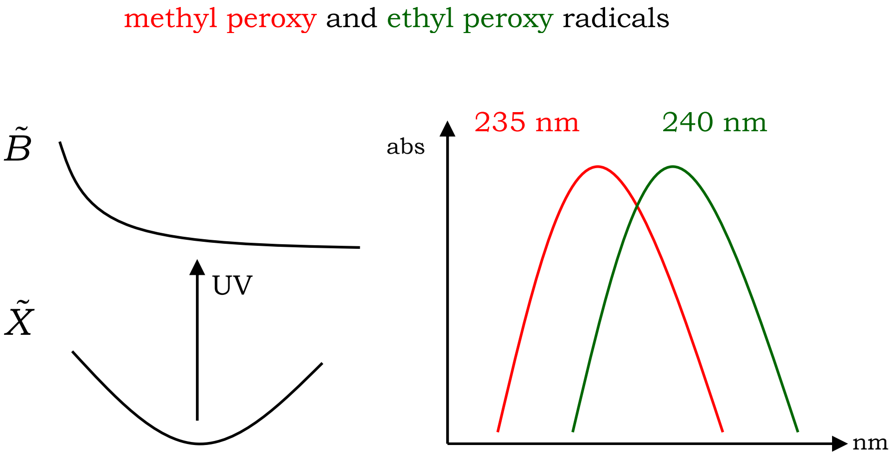

**Figure 4.2.** A cartoon representation of the UV transition from the bound ground $\tilde{X}$ state to the repulsive excited $\tilde{B}$ state surface (left). The resulting spectra for methyl and ethyl peroxy radicals are shown on the same plot (right). Overlap of the broad and non-distinctive absorptions complicates identification and quantification of the species.

Recent efforts have focused on detection of the peroxy radicals via the $\tilde{A} \leftarrow \tilde{X}$ transition in the near infrared (NIR) region.[53-61] Absorption cross sections are much weaker ($\sigma_{NIR}(RO_2) = 10^{-20} \sim 10^{-21}$ cm$^2$); yet transitions to the bound $\tilde{A}$ state result in more structured spectral features. In a systematic study of alkyl peroxy radicals, the Miller group demonstrated that not only the isomers but also the different conformers of the same structural peroxy radical isomer could be distinguished in the NIR spectra (7000-8000 $cm^{-1}$).[61] Each peroxy radical has a distinct $\tilde{A} \leftarrow \tilde{X}$ origin band and COO bend and COO stretch absorptions ~500 $cm^{-1}$ and ~1000 $cm^{-1}$ to the blue of the origin, respectively. The spectra of the smaller alkyl peroxy radicals showed narrow structured bands, while the spectra of the larger alkyl peroxy radicals contained broad absorptions (width ~500 $cm^{-1}$) with multiple bumps arising from overlap of the various conformers. *Ab initio* methods, including density functional theory (e.g., B3LYP) and Gaussian 2 Møller–Plesset 2 (G2MP2), were used with high quantitative accuracy to predict the origins of the $\tilde{A} \leftarrow \tilde{X}$ transitions of the alkyl peroxy radicals.

This spectroscopic approach has been extended to study the substituted peroxy radicals.[62-64] The origin of the $\tilde{A} \leftarrow \tilde{X}$ transition should shift to the red or blue of the parent peroxy radical depending on the electron-withdrawing or contributing nature of the substituent with respect to the OO moiety of the peroxy radical. The overall shape of the band should remain the same. In the extreme case of fluorinated methyl peroxy radical ($CF_3O_2$), the origin of the $\tilde{A} \leftarrow \tilde{X}$ transition shifted 727 $cm^{-1}$ to the red of the origin of the methyl peroxy radical ($CH_3O_2$); the rotational contour of the band remained very similar.[63]

Our group has systematically studied the $\tilde{A} \leftarrow \tilde{X}$ transitions of Cl-alkyl peroxy radicals.[64] The origin bands were shifted slightly to the red of the origins of the respective unsubstituted alkyl peroxy radicals. B3LYP calculations were done in *Gaussian98* to predict the origins of the $\tilde{A} \leftarrow \tilde{X}$ transitions of the Cl-alkyl peroxy radicals.[65] Specifc details are provided in the thesis of a senior lab member.[64] Briefly, C-C-Cl and C-O-O dihedral angles were systematically varied, with geometry and energy optimizations done at each scan point. At each minimum, the highest occupied alpha or beta orbital was manually adjusted in the Gaussian input file such that the overall symmetry of the radical was that of the excited state. The energy was then re-calculated and compared to the "ground state" energy value for determination of the origin band frequency. Theoretical results were consistent with experimental values, demonstrating that density functional theory could be applied to substituted peroxy radicals.

In the case of $NO_3$ addition to 2-butene, the number of electrons is too large for *ab initio* calculations. We instead use the previously published spectrum of the $\tilde{A} \leftarrow \tilde{X}$ transition of *sec*-butyl peroxy radical to predict the frequency of the origin band for the $\tilde{A} \leftarrow \tilde{X}$ transition of 2-$NO_3$-butyl peroxy radical.[54] The NIR spectrum of the *sec*-butyl peroxy radical shows a relatively broad absorption between 7350 $cm^{-1}$ and 7750 $cm^{-1}$, with two distinct bumps at 7560 $cm^{-1}$ and 7605 $cm^{-1}$ for conformers A and B. Weak absorptions corresponding to the torsional motions are observed at 8051 $cm^{-1}$ and 8507 $cm^{-1}$. We expect the origin band for 2-$NO_3$-butyl peroxy radical to be slightly red-shifted. We therefore conduct the pulsed CRDS experiments in the 7200-8600 $cm^{-1}$ region.

## 4.3 Experimental conditions

### 4.3.1 The chemistry

Our goal is to detect the substituted $NO_3$-peroxy radical *in situ*. Typical $NO_3$ sources include discharge of fluorine in the presence of nitric acid ($HNO_3$), photolysis of chlorine nitrate ($ClONO_2$), and thermal decomposition of dinitrogen pentoxide ($N_2O_5$):

$$F + HNO_3 \rightarrow HF + NO_3 \tag{4.8}$$

$$ClONO_2 \rightarrow Cl + NO_3 \tag{4.9}$$

$$N_2O_5 + \Delta(\text{heat}) \rightarrow NO_2 + NO_3 \tag{4.10 a}$$

In the first two methods, the F and Cl atom preferentially attack the alkene. Nitric acid concentrations cannot be increased significantly in to scavenge the F atoms in reaction 4.8, as nitric acid absorbs in the NIR region (Appendix 3.4). The third method is more plausible. The thermal decomposition of $N_2O_5$ was used as the $NO_3$ source for our study of the $\tilde{A}$ state of $NO_3$ (Chapter 3). Given our previous flow conditions, however, the residence time of the flow cell experiments is very long (~150 ms to 1 s). The lifetime of peroxy radicals is on the millisecond timescale such that secondary chemistry would complicate spectral detection (Appendix 4.1).

We therefore explored photolytic precursors of $NO_3$, as the NIR probe laser could be delayed on the microsecond timescale with respect to the excimer fire or chemical initiation. We searched for methods in which byproducts of the photolysis would not react with the alkene and found that the photolysis of (room temperature) $N_2O_5$ at 193 nm and 248 nm showed the greatest potential. We tried both wavelengths in the laboratory and observed identical $NO_3$ spectra (Fig 4.3). We however observed major differences when the excimer was fired with only the reactant, 2-butene, in the flow cell. At 193 nm, we observed formation of large amounts of methyl peroxy radical; at 248 nm, we observed no change in the spectrum. We therefore conducted the photolysis experiments at 248 nm ($\sigma_{248\ nm}(N_2O_5) = 4.19 \times 10^{-19}$ cm$^2$).[1]

$N_2O_5$ photolysis however also leads to production of nitrogen dioxide ($NO_2$). $NO_2$ can react with both $NO_3$ and the target species, the 2-$NO_3$-butyl peroxy radical, to complicate the detection process:[1]

$$NO_2 + NO_3 \rightarrow N_2O_5 \qquad (4.10\ \text{b-d})$$

with $K_{eq}(298\ K) = 2.9 \times 10^{-11}\ \text{cm}^3\ \text{molec}^{-1}$

$k_{298\ K}(NO_2 + NO_3 + M) = 7.4 \times 10^{-13}\ \text{cm}^3\ \text{molec}^{-1}\ \text{s}^{-1}$ at P = 80 Torr

$$CH_3CH(NO_3)CH(OO)CH_3 + NO_2 \leftrightarrow CH_3CH(NO_3)CH(OONO_2)CH_3 \qquad (4.11)$$

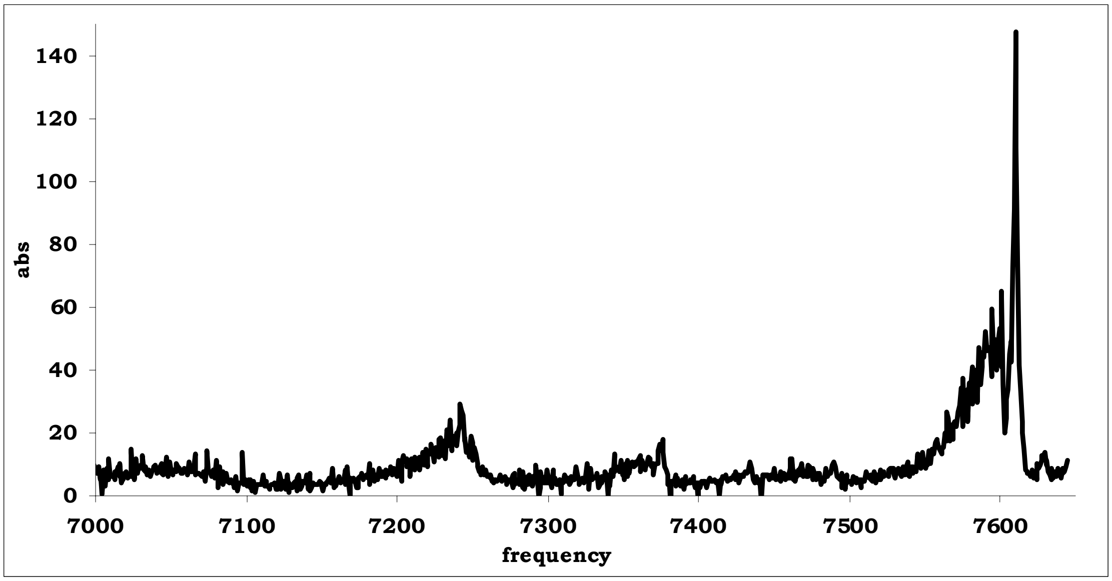

**Figure 4.3.** CRD spectrum of $NO_3$ from photolysis of $N_2O_5$ at 193 nm. Concentrations varied, depending on the vapor pressure of $N_2O_5$: $[NO_3] = 1\text{-}10 \times 10^{13}$ molec cm$^{-3}$. The CRD spectrum of $NO_3$ from photolysis of $N_2O_5$ at 248 nm showed slightly lower absorptions; however the scaled features were identical to the spectrum shown here.

To estimate $NO_2$ yields, we collected time-resolved CRD spectra of the $4_0^1$ band of $NO_3$ at 7602 cm$^{-1}$ and plotted the intensity of the band relative to the time delay of the NIR probe. If we assume that the rate of $NO_3$ signal decay is from reaction with $NO_2$ alone, we calculate $NO_2$ concentrations

~1-10 × $10^{14}$ molec $cm^{-3}$. The values are slightly higher than initial $NO_3$ concentrations, as $NO_3$ can recombine to form $NO_2$:[1]

$$NO_3 + NO_3 \rightarrow 2\ NO_2 + O_2 \qquad (4.12\ a\text{-}b)$$

$$k_{298\ K}\ (NO_3 + NO_3) = 2.3 \times 10^{-16}\ cm^3\ molec^{-1}$$

Until we quantitatively characterize the reaction rate between $NO_2$ and the peroxy radical, we will be unable to do any kinetic experiments using this chemical approach. Direct observation and characterization of the 2-$NO_3$-butyl peroxy radical however should still be possible and would be a major step in unraveling the complex oxidation scheme.

### 4.3.2 Apparatus and scan details

The pulsed CRDS apparatus has been described in Chapter 2. We operated the NIR probe and 248-nm excimer lasers at 5 Hz (250 ms residence time) to insure that all gas products were flushed from the cell before excimer fire. To cover the wide NIR wavelength range (7200-8300 $cm^{-1}$), we used a variety of laser dyes (DCM, Rh 640, Rh 640+610, Rh 610). The optical cavity consisted of a stainless steel photolysis cell with quartz windows, either the 30.5-cm cell with the 17.8-cm × 0.95-cm window or the 24.1-cm cell with the 12.7-cm × 0.95-cm window. 13-cm purge volume couplers were attached at each end of the ringdown cell to protect the CRD mirrors. We used multiple CRD mirrors to cover the NIR range: LGR 1200-nm (R = 99.99%), LGR 1315-nm (R = 99.99%) and Layertec 1390-nm (R = 99.99%) mirrors.

The gas conditions are provided in Fig. 4.4. As the experiment was conducted in smaller segment scans, mass flow meters were placed on each gas inlet for reproducibility. The main valve of the vacuum port was adjusted to determine the total pressure of the cell. A needle valve was added to the port for additional fine control, as the pump conditions fluctuated during the course of the experiment.

The probe laser was generally delayed 100 μs after excimer fire or chemical initiation. Scans were collected at 0.4 $cm^{-1}$ step size with the excimer on and off for $N_2O_5$ and $N_2O_5$/2-butene gas mixtures separately. Preparation of $N_2O_5$ and 2-butene gas was described in Appendix 3.3 and Appendix 2.4 respectively. Experiments were run at total pressure 80 Torr, with $N_2O_5$ ~1.5 Torr, 2-butene/$N_2$ mixture (15%) ~10 Torr, zero grade air ~60 Torr, and $N_2$ purge ~10 Torr. To confirm that the observed bands were not from 2-butene, we also obtained scans of 2-butene and zero grade air (background) in the 7000-7400 $cm^{-1}$ region. For peroxy verification experiments, we added a nitric oxide (NO, 1% in $N_2$ from Matheson) port to the ringdown cell.

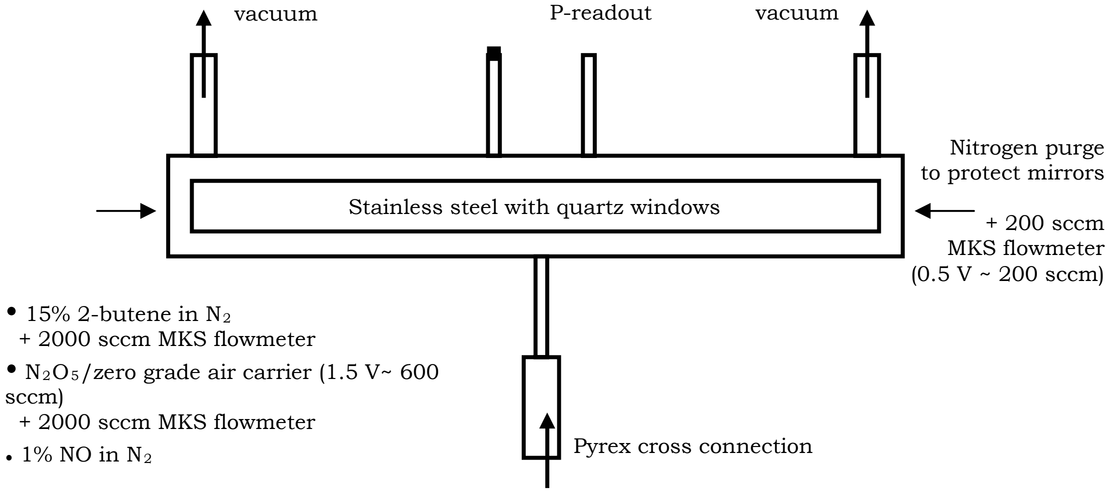

**Figure 4.4.** Schematic of the photolysis cell for the $NO_3$ + 2-butene experiment. Details of the gas flow conditions are also provided in the figure. The detection limit of the pulsed CRDS apparatus for the $NO_3$-peroxy radical is ~ $10^{12}$ molec $cm^{-3}$.

## 4.4 Results and discussion

### 4.4.1 Observed spectra

CRD spectra of "$NO_3$ + 2-butene" were obtained from differences between the $N_2O_5$/2-butene scans with the excimer on and off (Fig. 4.5 a). As $NO_3$ concentrations determine the final concentrations of 2-$NO_3$-butyl peroxy radicals, CRD spectra of $NO_3$ were also collected from differences between $N_2O_5$ scans with the excimer on and off (Fig. 4.5 b). $NO_3$ concentrations varied from successive scanning segments. We therefore used $NO_3$ absorption features to scale overlapping spectra. The same scaling factors were used to overlap the "$NO_3$ + 2-butene" spectra.

Given the relatively slow reaction rate constant between $NO_3$ and 2-butene, not all of the $NO_3$ reactant was consumed during the flow cell experiment. The concentration of 2-butene could not be further increased, as 2-butene has absorptions in the NIR region (Fig. 4.6). While contributions from 2-butene absorption is efficiently removed by subtraction, absorptions from $NO_3$ have to be manually subtracted from the "$NO_3$+2-butene" spectra. Analysis of each scanning segment showed that ~60 % of $NO_3$ was consumed by 2-butene. The corrected spectra were then combined into one spectrum. As the observed absorptions were broad with respect to the step size of the scan (0.4 $cm^{-1}$), we averaged every five data points for the plot.

The combined CRD spectrum of 2-$NO_3$-butyl peroxy radical is shown in Fig. 4.5 c. The most intense and broad absorption in the 7250 $cm^{-1}$ - 7800 $cm^{-1}$ region is assigned to the origin band of the $\tilde{A} \leftarrow \tilde{X}$ transition. The small bumps in the absorption belong to different conformers of the 2-$NO_3$-butyl peroxy radical. We mentioned beforehand that peroxy radicals have distinct torsional absorptions 500 $cm^{-1}$ and 1000 $cm^{-1}$ to the blue of the origin band. We observe small absorption at 8000 $cm^{-1}$ and 8516 $cm^{-1}$ that are assigned to the COO bend and OO stretch respectively.

The experiments were repeated at low pressure (~40 Torr) and higher 2-butene concentrations (×2). No change in the relative shape or intensities of the bands was observed in the spectra. A weak but sharp absorption was observed at 7383 $cm^{-1}$ and attributed to methyl peroxy radical, $CH_3O_2$.[55] The absorption was observed as early as 15 μs after the excimer fire, so it cannot be arising from secondary chemistry. Earlier tests on the photolysis of 2-butene at 248 nm did not report any $CH_3O_2$ production; it maybe that the sensitivity of the CRDS alignment was improved for the $NO_3$ + 2-butene scans. Some of the $NO_3$-peroxy radicals may also have enough internal energy to break apart into smaller fragments. Regardless, the $CH_3O_2$ yield was negligible and did not interfere with the spectral analysis.

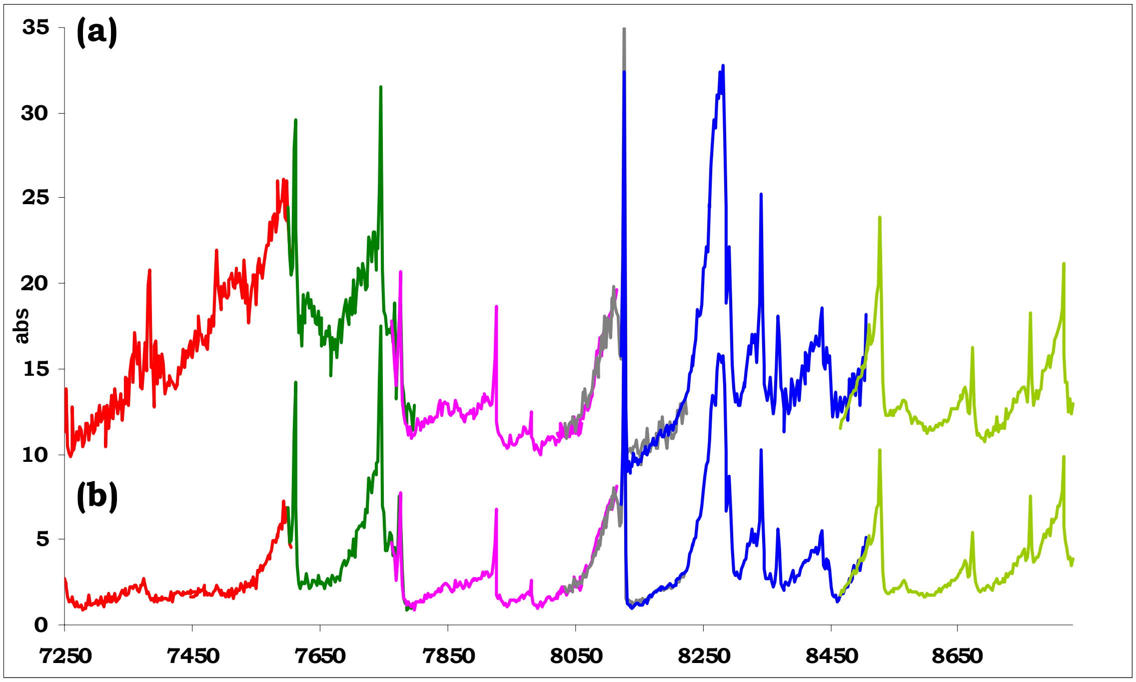

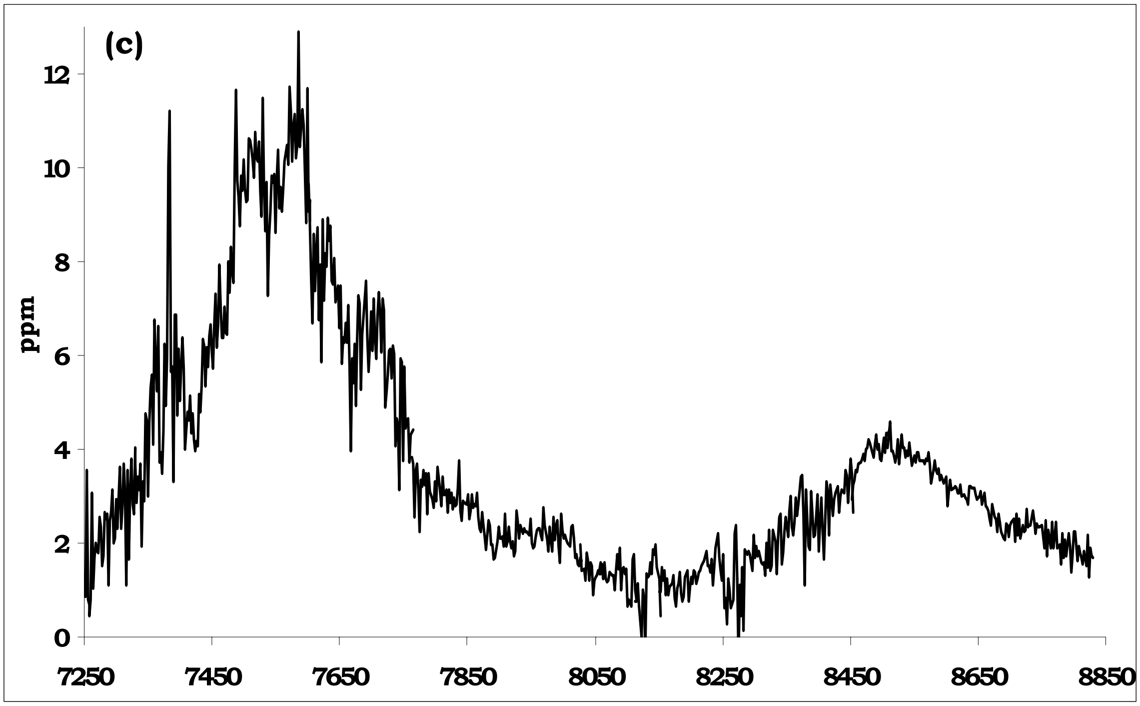

**Figure 4.5.** CRD spectra of (a) $NO_3$+2-butene (difference between the $N_2O_5$/2-butene scans with the excimer on and off) with a 10 ppm offset (b) $NO_3$ (difference between $N_2O_5$ scans with the excimer on and off), and (c) 2-$NO_3$-butyl peroxy radical (spectrum b - spectrum a). The colors indicate the different scanning segments. All spectra shown in the figure have been 5-point averaged.

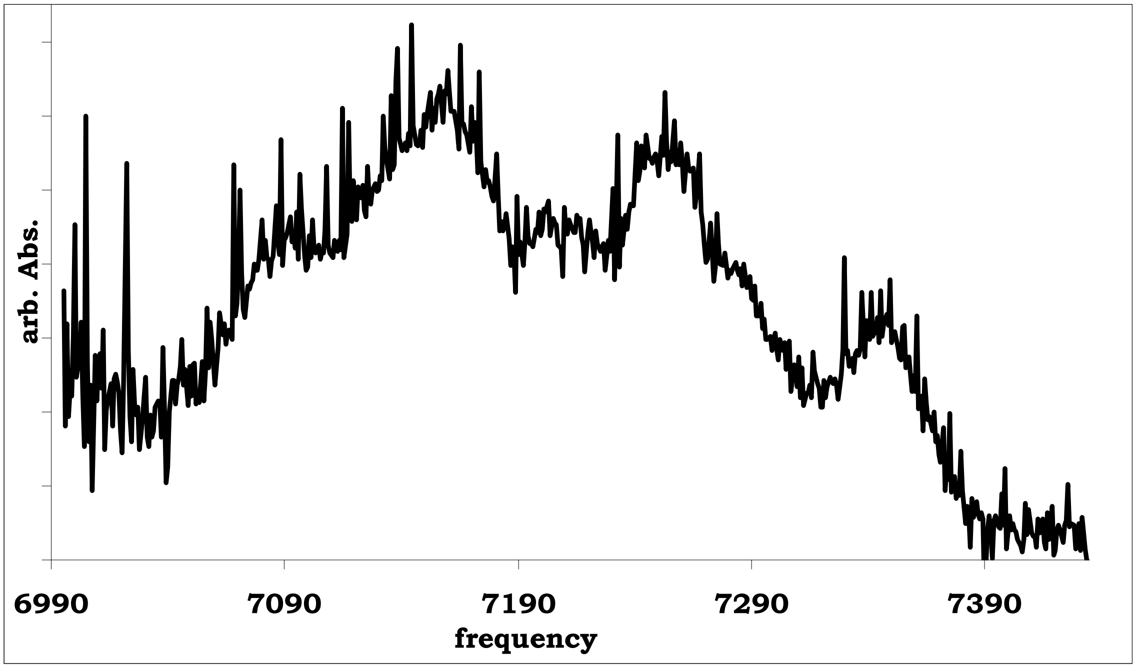

**Figure 4.6.** CRD spectrum of 2-butene in the 7000 - 7400 $cm^{-1}$ region. The absorption features are flat after 7390 $cm^{-1}$.

### 4.4.2 Verification of the peroxy radical spectrum

Observation of the torsional features, in addition to the origin band, is a strong indicator that the spectral absorptions belong to the 2-$NO_3$-butyl peroxy radical. The shape and absorption frequencies are similar to the spectral features of *sec*-butyl peroxy radical. As $NO_3$ concentrations determine the amount of peroxy radical generated in the experiment, we can also compare the two concentrations to check whether the values are consistent to first order. While the observation of multiple bumps in the 7250-7600 $cm^{-1}$ region suggest multiple conformers of the 2-$NO_3$-butyl peroxy radical were formed, they all should have similar absorption cross sections. Thus, we estimate the total concentration of peroxy radical from the observed peak signal at ~10 ppm. The absorption cross section for perxoy radicals in the NIR region has only been measured for ethyl perxoy radical ($CH_3CH_2O_2$), $\sigma_{7596\ cm^{-1}}(CH_3CH_2O_2) = 5.29 \times 10^{-21}\ cm^2$.[57] We estimate the cross section for 2-$NO_3$-butyl peroxy radical to be $\sigma_{NIR}$ ~

$10^{-20}$ ~ $10^{-21}$ $cm^2$. Assuming $L_R$ = 17.8-cm (our long photolysis cell), we calculate:

$$[\text{2-NO}_3\text{-butyl peroxy radical}] \sim \frac{10\times10^{-6}}{5\times10^{-21}\times17.8} \approx 10^{14}\,\frac{\text{molec}}{\text{cm}^3} \tag{4.13}$$

This is consistent with the amount of $NO_3$ generated during photolysis.

Additional experiments were also conducted to verify the spectral assignment. The lifetime for peroxy radicals is typically on the millisecond timescale. The presence of $NO_2$ will cause the peroxy radical concentration to decrease more quickly (rxn 4.10). We collected time-resolved spectra of the 7250 $cm^{-1}$ - 7650 $cm^{-1}$ region from 100 μs to 10 ms after chemical initiation. As expected, the peroxy radical signal decayed over time and disappeared by >5 ms.

We also injected NO into the system, as NO should react with the peroxy radical rapidly:[1,66]

$$RO_2 + NO \rightarrow RO + NO_2 \tag{4.14}$$

$k_{298\,K}(RO_2 + NO) \sim 1 \times 10^{-11}\ cm^3\ molec^{-1}$

The peroxy radical signal disappeared accordingly. All tests therefore indicated that the absorptions observed in the CRD spectrum belonged to the 2-$NO_3$-butyl peroxy radical.

## 4.5 Summary

We observed 2-$NO_3$-butyl peroxy radical in the gas phase for the first time using pulsed CRDS. We were able to observe the radical *in situ* via the $\tilde{A} \leftarrow \tilde{X}$ transition in the NIR region. Although the absorption is much weaker in the NIR than in the UV region, the spectrum has very distinctive structural features. Identification is also easier, as there is less spectral interference from other atmospheric species.

This was the first work to observe $NO_3$-substituted peroxy radical in any wavelength region or from any alkene oxidation system. Due to the atmospheric importance of $NO_3$-alkene oxidation, we plan to build on this work by examining larger $NO_3$-peroxy radicals. We are currently in the process of looking at the $NO_3$-initiated oxidation of 2-methyl-2-butene and isoprene. 2-methyl-2-butene is structurally similar to 2-butene, with only an extra methyl group on the double bond. As the symmetry is now broken, we should now observe two distinct isomers in the spectra. Studying the $NO_3$ oxidation of isoprene will be more difficult, as multiple isomers are formed. In the future, we plan to further elucidate the $NO_3$ oxidation mechanism by coupling the pulsed CRDS apparatus with a chemical ionization mass spectrometer that is equipped to detect multiple products, including the epoxide channel. Thus, we will be able to study the competing pathways of $NO_3$-initiated oxidation of alkenes simultaneously.

We build on this work in the next chapter, by studying another important subset of substituted peroxy radicals in the atmosphere, Cl-peroxy radicals. We outline preliminary work on both the detection and kinetics of Cl-peroxy radical intermediates to elucidate the mechanism of Cl-initiated oxidation of alkenes.

## 4.6 References

(1) Sander, S. P.; Friedl, R. R.; Golden, D. M.; Kurylo, M.; Moortgat, G. K.; Wine, P. H.; Ravishankara, A. R.; Kolb, C. E.; Molina, M. J.; Finlayson-Pitts, B. J.; Huie, R. E.; Orkin, V. L. 2006.

(2) Atkinson, R. *Journal of Physical and Chemical Reference Data* **1991**, *20*, 459.

(3) Atkinson, R. *Atmospheric Environment* **2000**, *34*, 2063.

(4) Atkinson, R.; Arey, J. *Chemical Reviews* **2003**, *103*, 4605.

(5) Finlayson-Pitts, B. J.; Pitts, J. N. *Chemistry of the Upper and Lower Atmosphere: Theory, Experiments, and Applications*; Academic Press, 1999.

(6) Ng, N. L.; Kwan, A. J.; Surratt, J. D.; Chan, A. W. H.; Chhabra, P. S.; Sorooshian, A.; Pye, H. O. T.; Crounse, J. D.; Wennberg, P. O.; Flagan, R. C.; Seinfeld, J. H. *Atmospheric Chemistry and Physics* **2008**, *8*, 4117.

(7) Seinfeld, J. H.; Pandis, S. N. *Atmospheric Chemistry and Physics*; Wiley-Interscience, 1997.

(8) Wayne, R. P.; Barnes, I.; Biggs, P.; Burrows, J. P.; Canosamas, C. E.; Hjorth, J.; Lebras, G.; Moortgat, G. K.; Perner, D.; Poulet, G.; Restelli, G.; Sidebottom, H. *Atmospheric Environment Part a-General Topics* **1991**, *25*, 1.

(9) Brown, S. S.; Degouw, J. A.; Warneke, C.; Ryerson, T. B.; Dube, W. P.; Atlas, E.; Weber, R. J.; Peltier, R. E.; Neuman, J. A.; Roberts, J. M.; Swanson, A.; Flocke, F.; McKeen, S. A.; Brioude, J.; Sommariva, R.; Trainer, M.; Fehsenfeld, F. C.; Ravishankara, A. R. *Atmospheric Chemistry and Physics* **2009**, *9*, 3027.

(10) Brown, S. S.; Dube, W. P.; Osthoff, H. D.; Stutz, J.; Ryerson, T. B.; Wollny, A. G.; Brock, C. A.; Warneke, C.; De Gouw, J. A.; Atlas, E.; Neuman, J. A.; Holloway, J. S.; Lerner, B. M.; Williams, E. J.; Kuster, W. C.; Goldan, P. D.; Angevine, W. M.; Trainer, M.; Fehsenfeld, F. C.; Ravishankara, A. R. *Journal of Geophysical Research-Atmospheres* **2007**, *112*.

(11) Brown, S. S.; Neuman, J. A.; Ryerson, T. B.; Trainer, M.; Dube, W. P.; Holloway, J. S.; Warneke, C.; de Gouw, J. A.; Donnelly, S. G.; Atlas, E.; Matthew, B.; Middlebrook, A. M.; Peltier, R.; Weber, R. J.; Stohl, A.; Meagher, J. F.; Fehsenfeld, F. C.; Ravishankara, A. R. *Geophysical Research Letters* **2006**, *33*.

(12) Fry, J. L.; Kiendler-Scharr, A.; Rollins, A. W.; Wooldridge, P. J.; Brown, S. S.; Fuchs, H.; Dube, W.; Mensah, A.; dal Maso, M.; Tillmann, R.; Dorn, H. P.; Brauers, T.; Cohen, R. C. *Atmospheric Chemistry and Physics* **2009**, *9*, 1431.

(13) Spittler, M.; Barnes, I.; Bejan, I.; Brockmann, K. J.; Benter, T.; Wirtz, K. *Atmospheric Environment* **2006**, *40*, S116.

(14) Yang, B.; Meng, J. W.; Zhang, Y.; Liu, C. G.; Gan, J.; Shu, J. N. *Atmospheric Environment* **2011**, *45*, 2074.

(15) Gong, H. M.; Matsunaga, A.; Ziemann, P. J. *Journal of Physical Chemistry A* **2005**, *109*, 4312.

(16) Lim, Y. B.; Ziemann, P. J. *Environmental Science & Technology* **2005**, *39*, 9229.

(17) Bruns, E. A.; Perraud, V.; Zelenyuk, A.; Ezell, M. J.; Johnson, S. N.; Yu, Y.; Imre, D.; Finlayson-Pitts, B. J.; Alexander, M. L. *Environmental Science & Technology* **2010**, *44*, 1056.

(18) Rollins, A. W.; Kiendler-Scharr, A.; Fry, J. L.; Brauers, T.; Brown, S. S.; Dorn, H. P.; Dube, W. P.; Fuchs, H.; Mensah, A.; Mentel, T. F.; Rohrer, F.; Tillmann, R.; Wegener, R.; Wooldridge, P. J.; Cohen, R. C. *Atmospheric Chemistry and Physics* **2009**, *9*, 6685.

(19) Pye, H. O. T.; Chan, A. W. H.; Barkley, M. P.; Seinfeld, J. H. *Atmospheric Chemistry and Physics* **2010**, *10*, 11261.

(20) Fuchs, H.; Dube, W. P.; Cicioira, S. J.; Brown, S. S. *Analytical Chemistry* **2008**, *80*, 6010.

(21) Ingold, K. U. *Accounts of Chemical Research* **1969**, *2*, 1.

(22) Wallington, T. J.; Dagaut, P.; Kurylo, M. J. *Chemical Reviews* **1992**, *92*, 667.

(23) Monks, P. S. *Chemical Society Reviews* **2005**, *34*, 376.

(24) Batt, L. *International Reviews in Physical Chemistry* **1987**, *6*, 53.

(25) Tyndall, G. S.; Cox, R. A.; Granier, C.; Lesclaux, R.; Moortgat, G. K.; Pilling, M. J.; Ravishankara, A. R.; Wallington, T. J. *Journal of Geophysical Research-Atmospheres* **2001**, *106*, 12157.

(26) Lightfoot, P. D.; Cox, R. A.; Crowley, J. N.; Destriau, M.; Hayman, G. D.; Jenkin, M. E.; Moortgat, G. K.; Zabel, F. *Atmospheric Environment Part a - General Topics* **1992**, *26*, 1805.

(27) Benter, T.; Liesner, M.; Schindler, R. N.; Skov, H.; Hjorth, J.; Restelli, G. *Journal of Physical Chemistry* **1994**, *98*, 10492.

(28) Olzmann, M.; Benter, T.; Liesner, M.; Schindler, R. N. *Atmos. Environ.* **1994**, *28*, 2677.

(29) Skov, H.; Benter, T.; Schindler, R. N.; Hjorth, J.; Restelli, G. *Atmos. Environ.* **1994**, *28*, 1583.

(30) Bukhtiyarov, V. I.; Nizovskii, A. I.; Bluhm, H.; Haevecker, M.; Kleimenov, E.; Knop-Gericke, A.; Schloegl, R. *Journal of Catalysis* **2006**, *238*, 260.

(31) Hjorth, J.; Jensen, N. R.; Skov, H.; Capellani, F.; Restelli, G. *Transport and Chemical Transformation of Pollutants in the Troposphere* **1997**, *3*, 113.

(32) Hjorth, J.; Lohse, C.; Nielsen, C. J.; Skov, H.; Restelli, G. *Journal of Physical Chemistry* **1990**, *94*, 7494.

(33) Kholdeeva, O. A.; Khavrutskii, I. V.; Romannikov, V. N.; Tkachev, A. V.; Zamaraev, K. I. *Studies in Surface Science and Catalysis* **1997**, *110*, 947.

(34) Skov, H.; Hjorth, J.; Lohse, C.; Jensen, N. R.; Restelli, G. *Atmospheric Environment, Part A: General Topics* **1992**, *26A*, 2771.

(35) Dlugokencky, E. J.; Howard, C. J. *Journal of Physical Chemistry* **1989**, *93*, 1091.

(36) Berndt, T. *Preprints - American Chemical Society, Division of Petroleum Chemistry* **2007**, *52*, 271.

(37) Berndt, T.; Boege, O. *Berichte der Bunsen-Gesellschaft* **1994**, *98*, 869.

(38) Berndt, T.; Boege, O. *Journal of Atmospheric Chemistry* **1995**, *21*, 275.

(39) Berndt, T.; Boege, O.; Rolle, W. *Environmental Science and Technology* **1997**, *31*, 1157.

(40) Berndt, T.; Boge, O. *International Journal of Chemical Kinetics* **1997**, *29*, 755.

(41) Berndt, T.; Boge, O. *Journal of the Chemical Society, Faraday Transactions* **1997**, *93*, 3021.

(42) Zhao, J.; Zhang, R. *Atmos. Environ.* **2008**, *42*, 5849.

(43) Cole-Filipiak, N. C.; O'Connor, A. E.; Elrod, M. J. *Environmental Science & Technology* **2010**, *44*, 6718.

(44) Minerath, E. C.; Elrod, M. J. *Environmental Science & Technology* **2009**, *43*, 1386.

(45) Herrick, R. F.; Smith, T. J.; Ellenbecker, M. J. *American Industrial Hygiene Association Journal* **1987**, *48*, 773.

(46) Paulot, F.; Crounse, J. D.; Kjaergaard, H. G.; Kurten, A.; St Clair, J. M.; Seinfeld, J. H.; Wennberg, P. O. *Science* **2009**, *325*, 730.

(47) IPCC *Climate Change 2007: Synthesis Report. Contribution of Working Groups I, II, and III to the Fourth Assessment, Report of the Intergovernmental Panel on Climate Change, Geneva, Switzerland*, 2007.

(48) Perez-Casany, M. P.; Nebot-Gil, I.; Sanchez-Marin, J.; Tomas-Vert, F.; Martinez-Ataz, E.; Cabanas-Galan, B.;

Aranda-Rubio, A. *Journal of Organic Chemistry* **1998**, *63*, 6978.

(49) Perez-Casany, M. P.; Nebot-Gil, I.; Sanchez-Marin, J. *J. Phys. Chem. A* **2000**, *104*, 10721.

(50) Cartas-Rosado, R.; Raul Alvarez-Idaboy, J.; Galano-Jimenez, A.; Vivier-Bunge, A. *Theochem* **2004**, *684*, 51.

(51) Cartas-Rosado, R.; Santoyo, M. E. R.; Alvarez-Idaboy, J. R.; Vivier-Bunge, A. *J. Phys. Chem. A* **2001**, *105*, 9222.

(52) Nguyen, T. L.; Park, J.; Lee, K.; Song, K.; Barker, J. R. *The Journal of Physical Chemistry A* **2011**, null.

(53) Chung, C.-Y.; Cheng, C.-W.; Lee, Y.-P.; Liao, H.-Y.; Sharp, E. N.; Rupper, P.; Miller, T. A. *Journal of Chemical Physics* **2007**, *127*, 044311/1.

(54) Glover, B. G.; Miller, T. A. *J. Phys. Chem. A* **2005**, *109*, 11191.

(55) Just, G. M. P.; McCoy, A. B.; Miller, T. A. *Journal of Chemical Physics* **2007**, *127*, 044310/1.

(56) Just, G. M. P.; Sharp, E. N.; Zalyubovsky, S.; Miller, T. A. *Abstracts of Papers, 231st ACS National Meeting, Atlanta, GA, United States, March 26-30, 2006* **2006**, PHYS.

(57) Melnik, D.; Chhantyal-Pun, R.; Miller, T. A. *Journal of Physical Chemistry A* **2010**, *114*, 11583.

(58) Pushkarsky, M. B.; Zalyubovsky, S. J.; Miller, T. A. *Journal of Chemical Physics* **2000**, *112*, 10695.

(59) Rupper, P.; Sharp, E. N.; Tarczay, G.; Miller, T. A. *J. Phys. Chem. A* **2007**, *111*, 832.

(60) Sharp, E., N.; Rupper, P.; Miller, T., A. *The journal of physical chemistry. A* **2008**, *112*, 1445.

(61) Sharp, E. N.; Rupper, P.; Miller, T. A. *Physical Chemistry Chemical Physics* **2008**, *10*, 3955.

(62) Chhantyal-Pun, R.; Kline, N. D.; Thomas, P. S.; Miller, T. A. *Journal of Physical Chemistry Letters* **2010**, *1*, 1846.

(63) Zalyubovsky, S. J.; Wang, D.; Miller, T. A. *Chemical Physics Letters* **2001**, *335*, 298.

(64) Deev, A., *Ph. D. Thesis*, California Institute of Technology, 2005.

(65) M. J. Frisch, G. W. T., H. B. Schlegel, G. E. Scuseria, M. A. Robb, J. R. Cheeseman, V. G. Zakrzewski, J. A. Montgomery, Jr., R. E. Stratmann, J. C. Burant, S. Dapprich, J. M. Millam, A. D. Daniels, K. N. Kudin, M. C. Strain, O. Farkas, J. Tomasi, V. Barone, M. Cossi, R. Cammi, B. Mennucci, C. Pomelli, C. Adamo, S. Clifford, J. Ochterski, G. A. Petersson, P. Y. Ayala, Q. Cui, K. Morokuma, D. K. Malick, A. D. Rabuck, K. Raghavachari, J. B. Foresman, J. Cioslowski, J. V. Ortiz, B. B. Stefanov, G. Liu, A. Liashenko, P. Piskorz, I.

Komaromi, R. Gomperts, R. L. Martin, D. J. Fox, T. Keith, M. A. Al-Laham, C. Y. Peng, A. Nanayakkara, C. Gonzalez, M. Challacombe, P. M. W. Gill, B. Johnson, W. Chen, M. W. Wong, J. L. Andres, C. Gonzalez, M. Head-Gordon, E. S. Replogle, and J. A. Pople, *Gaussian 98*, Gaussian, Inc.: Pittsburgh, PA, 1998.

(66) Atkinson, R.; Baulch, D. L.; Cox, R. A.; Crowley, J. N.; Hampson, R. F.; Hynes, R. G.; Jenkin, M. E.; Rossi, M. J.; Troe, J. *Atmos. Chem. Phys.* **2006**, *6*, 3625.

# Appendix for Chapter 4

## Appendix 4.1 Long residence time experiments

### A-4.1.1 $NO_3$+2-butene

The long residence time CRDS experiments on the $NO_3$ oxidation of 2-butene utilized thermal decomposition of $N_2O_5$ as the $NO_3$ source. The optical cavity was identical to that used in the $NO_3$ study (Chapter 3). An oxygen carrier gas was flowed over a $N_2O_5$ trap ($P_{vapor}$ = 1.5 Torr) and into a heated (T = 40°C) Pyrex ringdown cell. 2-butene (10 Torr of a 15% 2-butene/$N_2$ mixture) was slowly injected into the system. Residence times ranged from 500 milliseconds to 1 second. On this timescale, products from secondary chemistry were collected in the cell.

In Fig. 4.1, we showed that the different reaction pathways of the $NO_3$-peroxy radical lead to alcohol and carbonyl compound production. Hydroxyl (OH) overtones and alkyl (CH) stretches have absorptions in the NIR region, which can be observed using the pulsed CRDS apparatus. The hydroxyl peroxy radical ($HO_2$) is also formed in the oxidation scheme (blue box in Fig. 4.1). $HO_2$ reacts not only with the $NO_3$-peroxy radical, but with $NO_3$ itself to form the hydroxyl radical (OH):[1]

$$HO_2 + NO_3 \rightarrow OH + NO_2 + O_2 \qquad \text{(A-4.1 a)}$$

$$\rightarrow HNO_3 + O_2 \qquad \text{(A-4.1 b)}$$

$$k_{298K}\,(HO_2 + NO_3) < 3.5 \times 10^{-12}\ \text{cm}^3\ \text{molec}^{-1}\ \text{s}^{-1} \qquad \text{(A-4.1 c)}$$

OH is very reactive and attacks 2-butene to initiate its own complex oxidation scheme:

$OH + R{=}R' + O_2 \rightarrow R\text{-}R'(OH)OO$ (OH-peroxy radical) (A-4.2)

The CRD spectrum of the long residence experiments is shown in Fig. A-4.1. The observed products are red shifted from the observed peroxy radical absorptions. Spectral identification is difficult without more chemical information. We mentioned at the end of Chapter 4 that we plan to couple a chemical ionization mass spectrometer to the CRDS apparatus. It will be interesting to repeat the long residence experiments in the extended apparatus.

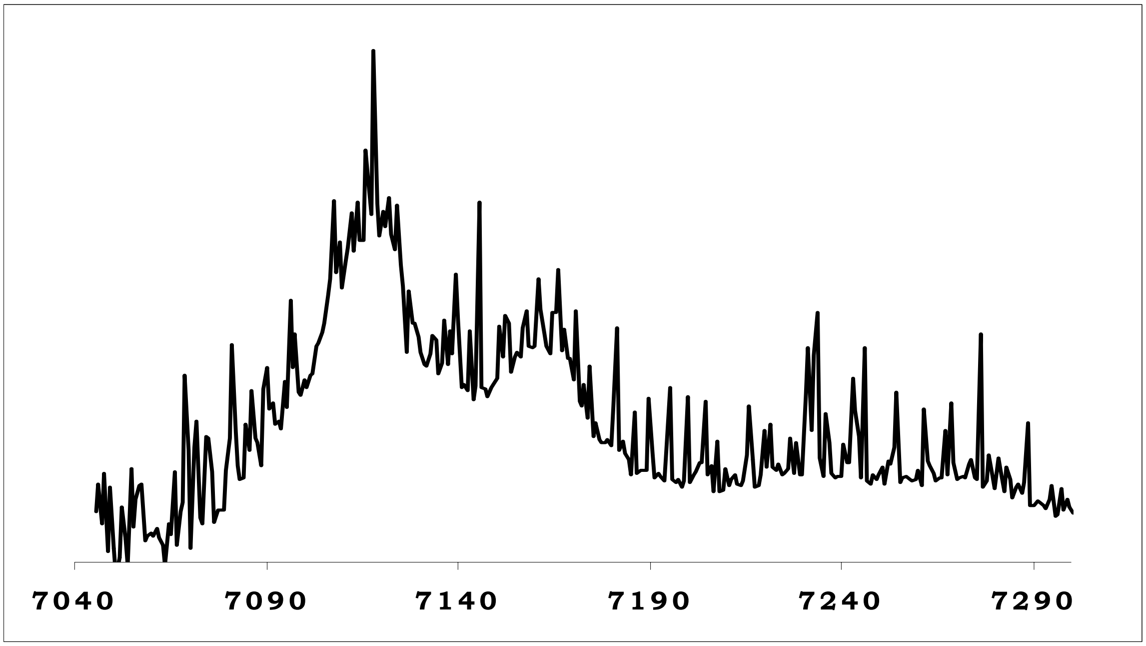

**Figure A-4.1.** CRD spectrum from long residence cell experiments with $NO_3$ + 2-butene.

### A-4.1.2 $O_3$+2-butene

The oxidation of 2-butene by ozone ($O_3$) has been studied by many groups:[2-11]

$O_3 + CH_3HC{=}CHCH_3 \rightarrow CH_3C(O)H + CH_3CHOO$ (A-4.3)

The latter product $CH_3CHOO$ is called the Criegee intermediate and is both a biradical and zwitterion (Fig. A-4.2). The fate of the Criegee intermediate is of strong interest to the atmospheric community, as it has been predicted to be a possible OH and epoxide source:

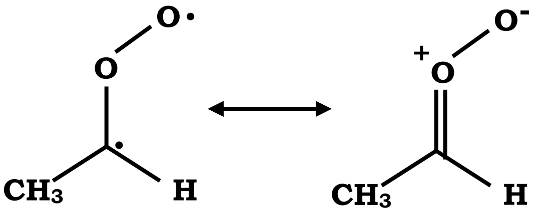

**Figure A-4.2.** The Criegee intermediate, drawn as a biradical (left) and zwitterion (right).

$CH_3CHOO \rightarrow CH_3HCOO$ (dioxirane) (A-4.4 a)

$\rightarrow [H_2C{=}CH(OOH)]^*$ (hydroperoxide) (A-4.4 b)

$[H_2C{=}CH(OOH)]^* \rightarrow HCOCH_2 + OH$ (A-4.4 c)

We examined the oxidation products using the same long residence time CRDS apparatus as above. Oxygen was flowed through an ozonizer before interacting with the 2-butene at room temperature in the flow cell. Similarities in the observed CRD spectra (Fig. A-4.1 and Fig. A-4.3) suggest parallel reaction pathways for $NO_3$ and $O_3$ oxidation of 2-butene.

CRD spectra were also collected to the blue, in the 7720-7850 $cm^{-1}$ region, for both $NO_3$ and $O_3$-initiated oxidation of 2-butene. We observed identical spectra for the two experiments. (Fig. A-4.4). The structure of the spectra indicated a small compound. We first thought that the absorption belonged to $HO_2$; however the absorption did not match the published spectrum of the $\tilde{A} \leftarrow \tilde{X}$ transition of $HO_2$.[12] It could be that the products in the spectra are from OH oxidation of alkenes. Further research is clearly needed.

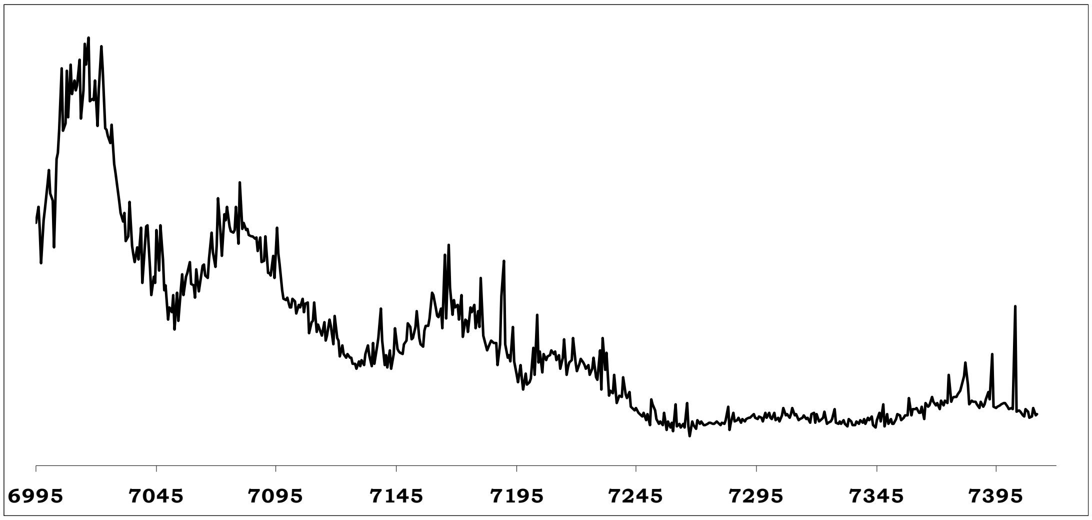

**Figure A-4.3.** CRD spectrum from a long residence cell experiment with $O_3$ + 2-butene.

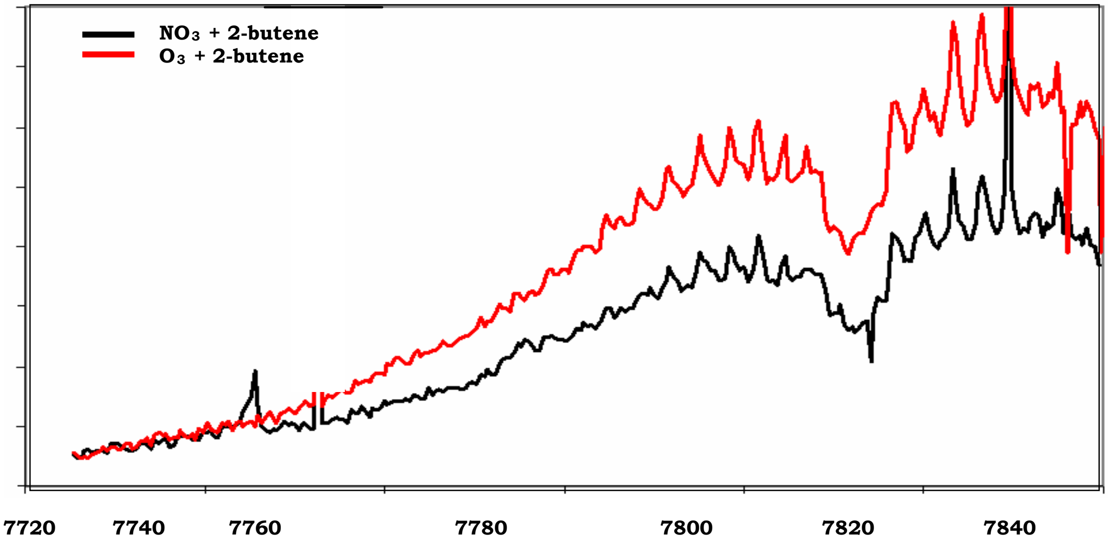

**Figure A-4.4.** CRD spectra from long residence cell experiments with $NO_3$ + 2-butene and $O_3$ + 2-butene.

## Appendix 4.2 References

(1) Sander, S. P.; Friedl, R. R.; Golden, D. M.; Kurylo, M.; Moortgat, G. K.; Wine, P. H.; Ravishankara, A. R.; Kolb, C. E.; Molina, M. J.; Finlayson-Pitts, B. J.; Huie, R. E.; Orkin, V. L. *Chemical Kinetics and Photochemical Data for Use in Atmospheric Studies, Evaluation No. 15,* 2006.

(2) Hasson, A. S.; Orzechowska, G.; Paulson, S. E. *Journal of Geophysical Research-Atmospheres* **2001**, *106*, 34131.

(3) Orzechowska, G. E.; Paulson, S. E. *Journal of Physical Chemistry A* **2005**, *109*, 5358.

(4) Grosjean, D.; Grosjean, E.; Williams, E. L. *Environmental Science & Technology* **1994**, *28*, 186.

(5) Horie, O.; Moortgat, G. K. *Atmospheric Environment Part a - General Topics* **1991**, *25*, 1881.

(6) Rickard, A. R.; Johnson, D.; McGill, C. D.; Marston, G. *Journal of Physical Chemistry A* **1999**, *103*, 7656.

(7) Donahue, N. M.; Kroll, J. H.; Anderson, J. G.; Demerjian, K. L. *Geophysical Research Letters* **1998**, *25*, 59.

(8) Drozd, G. T.; Kroll, J.; Donahue, N. M. *Journal of Physical Chemistry A* **2011**, *115*, 161.

(9) Lambe, A. T.; Zhang, J. Y.; Sage, A. M.; Donahue, N. M. *Environmental Science & Technology* **2007**, *41*, 2357.

(10) Chew, A. A.; Atkinson, R. *Journal of Geophysical Research - Atmospheres* **1996**, *101*, 28649.

(11) Gutbrod, R.; Kraka, E.; Schindler, R. N.; Cremer, D. *Journal of the American Chemical Society* **1997**, *119*, 7330.

(12) Fink, E. H.; Ramsay, D. A. *J. Mol. Spectrosc.* **2002**, *216*, 322.

### Chapter 5

# DETECTION OF PEROXY INTERMEDIATES IN THE OXIDATION OF VOLATILE ORGANIC COMPOUNDS BY CHLORINE ATOMS

## 5.1 Introduction to chlorine atoms in the troposphere

Chlorine atoms (Cl) are extremely reactive species, oxidizing volatile organic compounds (VOCs) in the atmosphere at kinetic rates comparable to hydroxyl radicals (OH) and faster than ozone ($O_3$) and nitrate radicals ($NO_3$). Cl atoms, however, are lower in concentration ($10^4$ $cm^{-3}$) than other oxidants: [OH] = $10^6$ $cm^{-3}$, [$O_3$] = 100 ppb, and [$NO_3$] = 50 ppt.[1] The impact of Cl atoms has therefore largely been restricted to coastal or marine regions. Sodium chloride (NaCl) from sea salt sprays react with the gas species dinitrogen pentaoxide ($N_2O_5$) and chlorine nitrate ($ClONO_2$) to form Cl photolytic precursors, nitryl chloride ($ClNO_2$) and chlorine ($Cl_2$):[2-7]

$$N_2O_5\ (g) + NaCl\ (s/aq) \rightarrow ClNO_2\ (g) + NaNO_3\ (s/aq) \qquad (5.1\ a)$$

$$ClNO_2\ (g) + h\nu \rightarrow Cl + NO_2 \qquad (5.1\ b)$$

$$ClONO_2\ (g) + NaCl\ (s/aq) \rightarrow Cl_2\ (g) + NaNO_3\ (s/aq) \qquad (5.2\ a)$$

$$Cl_2\ (g) + h\nu \rightarrow 2Cl \qquad (5.2\ b)$$

The heterogeneous chemistry of the reactions is not well-understood.[8-14] Models of the effect of $ClNO_2$ and Cl on the chemistry of coastal urban regions show increased ozone concentrations from rapid oxidant cycling.[15,16]

Recent studies indicate that chlorine levels may also be sufficiently high at mid-continental regions to impact local atmospheric chemistry.[17,18] Thornton, *et al.* observed $ClNO_2$ production in field studies at Boulder, Colorado (USA), 1400 km away from the nearest coastline.[17] From their models, they estimated 3.2-8.2 Tg $yr^{-1}$ $ClNO_2$ production or 1.4-3.6 Tg $yr^{-1}$ Cl atom formation from contiguous US regions. These estimates are comparable to global coastal and marine sources of $ClNO_2$ ~3.2 Tg $yr^{-1}$.[16]

A significant fraction of inland $ClNO_2$ production results from anthropogenic sources of Cl ions reacting with $N_2O_5$:[12,17-20]

$$N_2O_5\ (g) + Cl^-\ (aq) \rightarrow ClNO_2\ (g) + NO_3^-\ (aq) \qquad (5.1\ c)$$

Sources include emissions of chlorinated hydrocarbons such as trichloroethene ($C_2HCl_3$), tetrachloroethene ($C_2Cl_4$), dichloromethane ($CH_2Cl_2$), and trichloromethane ($CHCl_3$) from water treatment and paper facilities.[21-26] Chlorinated hydrocarbons can also be directly attacked by other atmospheric radicals to release Cl atoms.[1,27]

With prevalent Cl concentrations, the oxidation of VOCs by Cl atoms need to be better characterized. Similar to the oxidation of alkenes by $NO_3$, Cl addition to alkenes in the presence of oxygen leads to formation of substituted peroxy radicals:

$$R{=}R' + Cl \rightarrow R\text{-}R'(Cl) \qquad (5.3)$$

$$R\text{-}R'(Cl) + O_2 \rightarrow R\text{-}R'(Cl)O_2 \text{ (chloroalkenyl peroxy radical)} \qquad (5.4)$$

The addition of Cl to various alkenes has been studied.[28-48] Most works have focused on Cl addition to isoprene.[28,29,32,36,39,41-48] Isoprene has multiple sites of attack, resulting in formation of six Cl-isoprenyl peroxy radicals, three β-Cl-isoprenyl peroxy radicals and three δ-Cl-isoprenyl peroxy radicals (Fig. 5.1). Several experimental groups have measured the rate of Cl addition to isoprene ($k_{298K}$(isoprene + Cl) = 3-4 × $10^{-10}$ $cm^3$ $molec^{-1}$ $s^{-1}$) and have estimated branching ratios from end product analyses. One product, 1-chloro-3-methyl-3-buten-2-one (CMBO), in particular, has been cited as a possible tracer for chlorine chemistry in the atmosphere.[49]

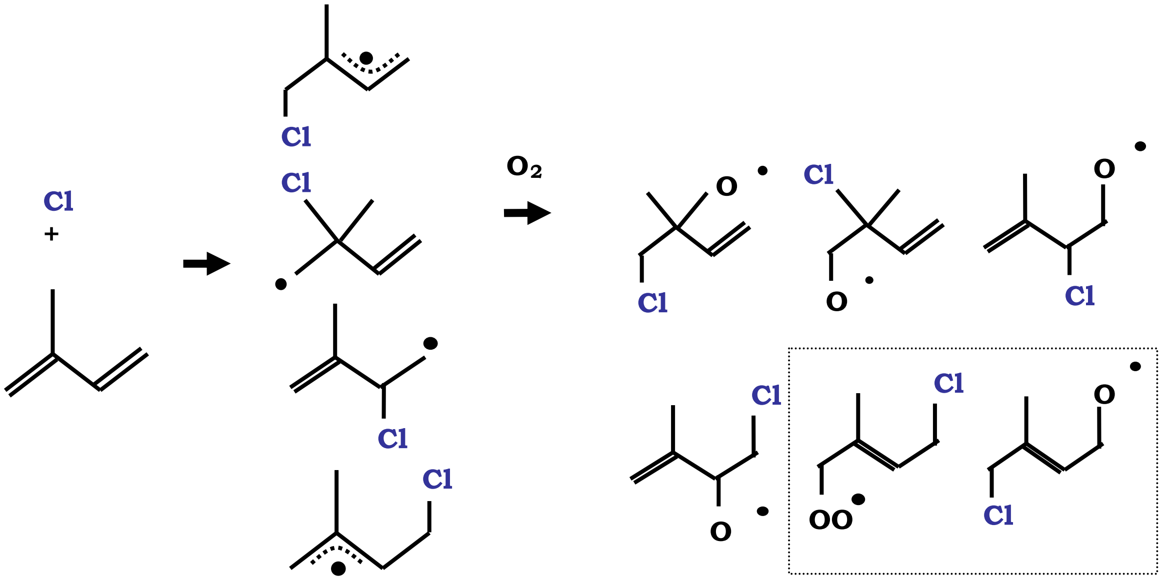

**Figure 5.1.** Schematics of Cl addition to isoprene in the presence of oxygen. Six structurally different Cl-isoprenyl peroxy radicals are formed. Four result from Cl addition to the β-C position, and two result from Cl addition to the δ-C position (dotted rectangle).

Molina *et al.* have done theoretical calculations on the formation of Cl-isopreny peroxy radicals and predict large yields for the δ-chloroisoprenyl peroxy radicals.[29] Unfortunately, there are no direct experimental studies on the branching ratios of the peroxy radicals. Hsin and Elrod have detected Cl-isoprenyl peroxy radicals with chemical ionization mass spectrometry (CIMS) in their laboratory;[40] they were, however, unable to distinguish the different structural isomers. A method still needs to be developed to directly detect the Cl-isoprenyl peroxy radicals in the gas phase with a high degree of specificity.

Other biogenic VOCs contribute to the global atmospheric chemistry.[39,50,51] 2-methyl-3-buten-2-ol (MBO232) is emitted in large quantities from pine trees.[52-54] Addition of Cl to MBO232 leads to a peroxy radical with both Cl and OH substituents:

$$\mathrm{Cl + CH_2{=}CHC(CH_3)_2OH + O_2 \rightarrow CH_2(Cl)\text{-}CH(OO)C(CH_3)_2OH} \qquad (5.5\ a)$$

$$\rightarrow \mathrm{CH_2(OO)\text{-}CH(Cl)C(CH_3)_2OH} \qquad (5.5\ b)$$

While there have been kinetic studies on the Cl-oxidation of MBO232,[45,55-57] the double substituted peroxy radicals have never been directly observed. Thus, we outline in the next section our efforts to directly detect both the Cl-isoprenyl and Cl-MBO232 peroxy radicals in the gas phase.

## 5.2 Cl-peroxy radical detection

### 5.2.1 Background

Small chlorinated alkyl peroxy radicals have been detected in the ultraviolet (UV) region via the $\tilde{B} \leftarrow \tilde{X}$ transition by absorption methods. Samples include $CH_2ClO_2$, $CHCl_2O_2$, $ClCH_2CH_2O_2$, $CHCl_2CHClO_2$, $CHCl_2CCl_2O_2$, and $CCl_3CCl_2O_2$.[58-61] Larger chlorinated peroxy radicals, derivatives of methacrolein (MACR), methyl vinyl ketone (MVK), and alkenes have been detected with CIMS.[40,41] While both methods have provided insight into the Cl-VOC oxidation chemistry, there are some limitations. With respect to UV studies, the observed spectra reveal strong and broad absorptions. Identification of the species is possible when the chemistry is limited to individual synthesis; however, it becomes difficult to distinguish the substituted peroxy radicals when multiple species are present. The CIMS studies also cannot distinguish between different structural isomers of the peroxy radical.

In the previous chapter, we detected substituted $NO_3$-peroxy radicals in the near-infrared (NIR) region via the $\tilde{A} \leftarrow \tilde{X}$ transition. Different structural isomers and conformers of the substituted peroxy radicals could be distinguished in the NIR spectra. Our group has already used this approach to detect Cl-alkyl peroxy radicals in the NIR region, including ethene, propene, butene, and butadiene derivatives.[62] We therefore use the same spectroscopic approach to directly detect the Cl-isoprenyl and Cl-MBO232 peroxy radicals in this work.

### 5.2.2 Preliminary scans of Cl-ethyl peroxy radical

The pulsed CRDS apparatus and optical cavity used in the study were identical to that described in the previous chapter for studies of the 2-$NO_3$-butyl peroxy radical. Only the chemistry or the gases used in the experiments differed. In our group's previous work on the Cl-alkyl peroxy radicals, we used photolysis of chlorine ($Cl_2$) at 308 nm as our Cl source. Chlorine molecules however react slowly with alkene species.

Oxalyl chloride (OxCl or $(ClC(O))_2$) has recently been demonstrated as a clean chlorine source:[63]

$$(ClC(O))_2 + h\nu \rightarrow 2\ Cl + 2\ CO \qquad (5.6)$$

As we had previously obtained a CRD spectrum of chloroethyl peroxy radical ($ClCH_2CH_2O_2$) in the NIR using $Cl_2$ photolysis, we conducted preliminary photolysis experiments with OxCl in the presence of ethene. Due to fragmentation of alkenes at 193 nm (Chapter 4), we conducted the photolysis experiments at 248 nm ($\sigma_{248\ nm}$(OxCl) = $2.7 \times 10^{-19}$ cm$^2$).

OxCl (Sigma Aldrich) is a liquid at room temperature and solid at T < -5°C. We utilized methanol in a Neslab ULT 80 Chiller at T = -10°C for our bath instead of the standard salt water/liquid nitrogen bath, as OxCl reacts violently with water. In fact, excess OxCl from experiments was disposed in the hood by slow addition of water droplets. Under regular flow conditions, the vapor pressure of solid OxCl was ~1.5 Torr. Photolysis experiments with only OxCl in the ringdown cell showed no absorption in the 7000-7600 cm$^{-1}$ region.

Experiments were run at total pressure 40 Torr, with OxCl at 1.5 Torr, ethene (Matheson) at 1.5 Torr, zero grade air at 30 Torr, and $N_2$ purge for the CRD mirrors at 7 Torr. The excimer was operated at 5 Hz to insure the gases had time to flush the cell between each excimer fire. Unlike $NO_3$-ethene oxidation, Cl attacks ethene rapidly. Within 10 μs, all the Cl atoms are consumed. We therefore delayed our NIR laser by 10-50 μs for peroxy radical detection.

The preliminary CRD spectrum of photolysis of OxCl in the presence of ethene at 248 nm is shown in Fig. 5.2, along with our previously observed spectrum of Cl-ethyl peroxy radical from the photolysis experiments of $Cl_2$ at 308 nm. The two spectra are identical. Similarly to how we checked the consistency of the $NO_3$-peroxy radical concentrations with the limiting reactant $NO_3$ concentrations (Chapter 4), we compare here the concentration of Cl-ethyl peroxy radical with Cl atom concentrations.

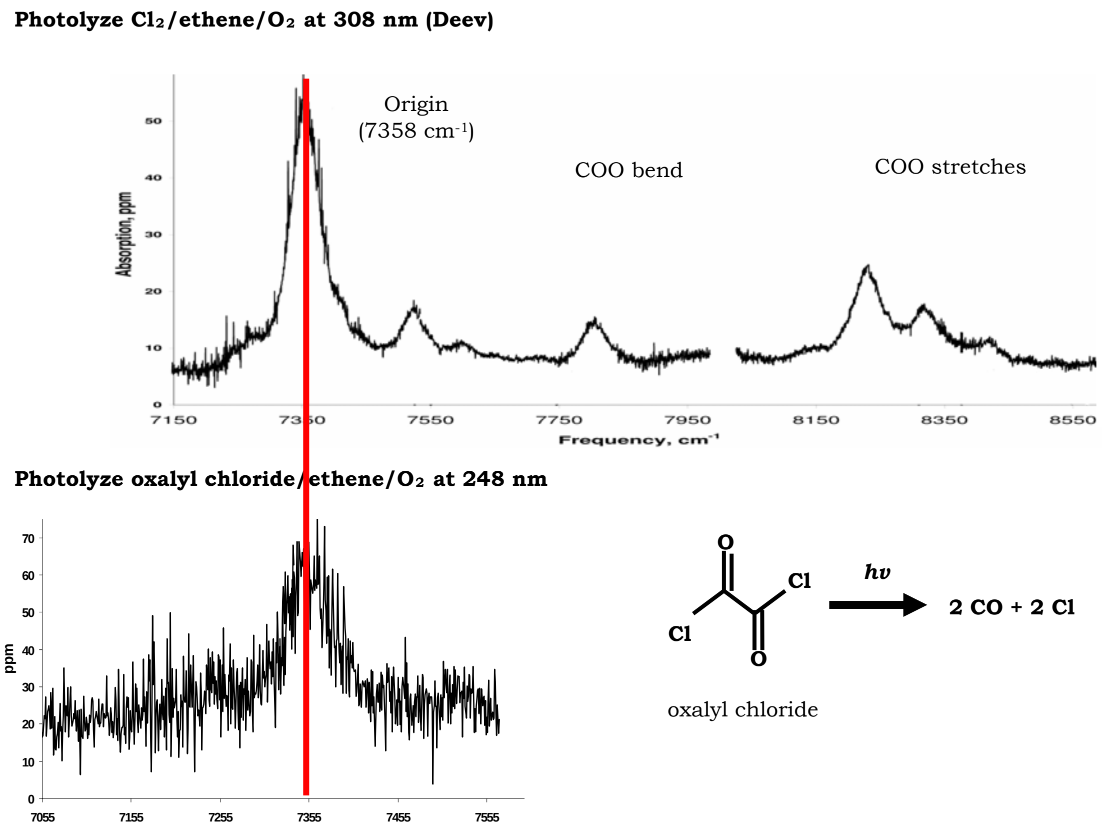

**Figure 5.2** Preliminary CRD spectrum of the $\tilde{A} \leftarrow \tilde{X}$ transition of Cl-ethyl peroxy radical in the NIR region (bottom). The spectrum was obtained from photolysis of oxalyl chloride at 248 nm in the presence of ethene and oxygen. We compared the spectrum to the CRD spectrum of Cl-ethyl peroxy radcial obtained from photolysis of chlorine at 308 nm in the presence of ethene and oxygen (top). The two spectra are identical.

Given $\sigma_{NIR}$ $(ClCH_2CH_2O_2)\sim10^{-20}$ $cm^2$ and the parameters of our medium-sized photolysis cell, from the observed peak Cl-ethyl peroxy radical absorption (~45 ppm), we estimate $[ClCH_2CH_2O_2]\sim3 \times 10^{14}$ molec $cm^{-3}$. At excimer powers of 100 mJ/pulse at 248 nm, we generate chlorine concentrations:

$$
\begin{aligned}
[Cl] &= [OxCl] \times \sigma_{248nm}(OxCl) \times \frac{\#\,photons\,/\,pulse}{area} \times 2 \\
&= (1.5 \times 3 \times 10^{16}) \times (2.7 \times 10^{-19}) \times \frac{10^{18} * 0.1}{12.7 \times 0.5} \times 2 \qquad (5.7) \\
&= 3.8 \times 10^{14} \text{ molec cm}^{-3}
\end{aligned}
$$

The consistency of the two values indicates that OxCl photolysis in the presence of alkene directly leads to Cl-peroxy radical formation. The signal-to-noise (S/N) of our spectrum could be further improved by optimizing the excimer and optical cavity alignment. The experiment confirmed that we could use OxCl as our Cl source for the remaining Cl-peroxy radical experiments.

### 5.2.3 Cl-isoprenyl peroxy radical detection

*Preliminary results*

Due to the atmospheric significance of isoprene, we began our studies with detection of Cl-isoprenyl peroxy radicals. Isoprene (Sigma Aldrich) is a liquid at very low temperatures. It is also very sensitive to light. We therefore put 5 mL of isoprene in a bubbler and wrapped the container with aluminum foil. The wrapped bubbler was then placed in a dry ice acetone bath (T = -60 °C) and covered with a black blanket. Zero grade air was passed through a molecular sieve before being used as carrier gases for both the isoprene and oxalyl chloride samples in the experiments. As the peroxy radical scan will eventually cover a large wavelength region (>1000 $cm^{-1}$ using multiple laser dyes), we recorded for reproducibility the flow rates and pressures for each reactant gas (Fig. 5.3). Experiments were run at total pressure 40 Torr, with zero grade air carrier for OxCl at 15 Torr, OxCl at 1.5 Torr, zero grade air carrier for isoprene at 15 Torr, isoprene at 1.5 Torr, and $N_2$ purge at 10 Torr.

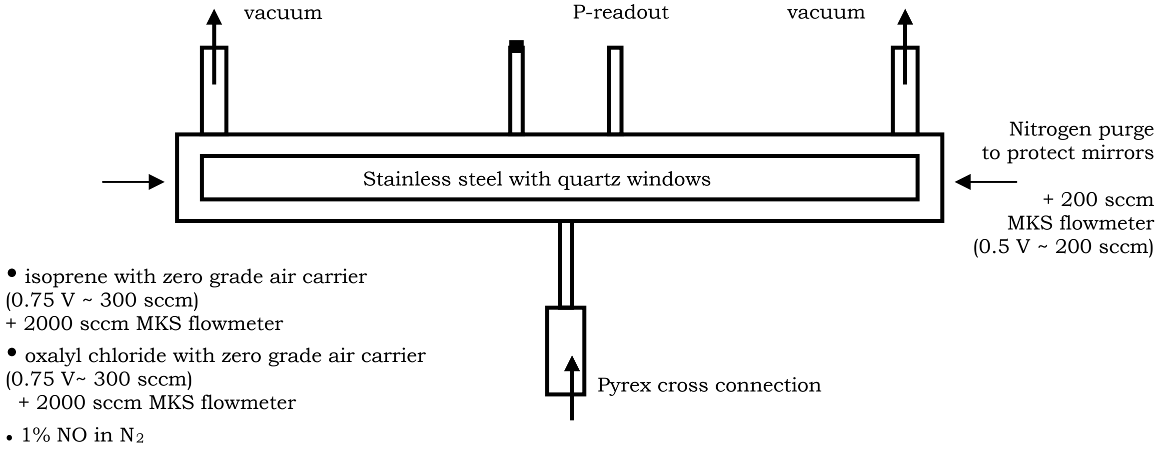

**Figure 5.3.** Schematic of ringdown cell for isoprene+ OxCl experiments. The gas flow conditions are provided in the figure.

Neither the isoprenyl nor other substituted isoprenyl peroxy radicals have been observed in the NIR region, and *ab inito* calculations on the origin band frequency have not been done for such a large peroxy radical system. We therefore relied on our group's previous CRD study on the $\tilde{A} \leftarrow \tilde{X}$ transitions of resultant peroxy radicals from oxidation of 1,3-butadiene by Cl to estimate the scanning region for the Cl-isoprene oxidation study. The observed origin band is a broad absorption from 7200-7600 $cm^{-1}$ with two major bumps at 7500 and 7600 $cm^{-1}$ for different isomers of the radical. We therefore conducted preliminary experiments in the 7200-7600 $cm^{-1}$ region using the DCM dye and Layertec 1390 nm mirrors. Scans were collected at 0.4 $cm^{-1}$ step size for the excimer on and off with isoprene/OxCl or isoprene alone in the ringdown cell. Due to fast Cl kinetics, we primarily collected spectra 10 μs after excimer fire.

The preliminary CRD spectrum of Cl-isoprenyl peroxy radical was obtained by subtraction of the isoprene/OxCl scans with the excimer on and off (Fig. 5.4). The absorptions in the spectrum resemble that of Cl-butadienyl peroxy radical, with a strong broad absorption between 7250-

7700 cm$^{-1}$ and multiple bumps at 7450 cm$^{-1}$ and 7650 cm$^{-1}$. The difference between the isoprene scans with the excimer on and off showed a flat line, indicating that the absorptions observed in Fig. 5.4 were not from photolysis of isoprene. The absorptions were also not from isoprene itself, which has C-H overtone absorptions in the NIR region (Fig. 5.5).

We conducted additional experiments to confirm whether the absorptions belonged to the Cl-isoprenyl peroxy radical. As the lifetime of peroxy radicals is on the order of milliseconds, we delayed our NIR probe with respect to the excimer fire and observed the absorptions decay over time. The absorptions could be scaled such that they were identical, indicating that all absorptions belonged to the same species. We also injected nitric oxide (NO) into the cell, along with isoprene and OxCl, during the photolysis experiment, as NO should react with the peroxy radicals rapidly. We consequently observed rapid decay of the absorptions in the time-resolved spectra.

The preliminary experiments suggest that the observed absorptions can be assigned to the $\tilde{A} \leftarrow \tilde{X}$ transition of Cl-isoprenyl peroxy radical. In the last chapter, we discussed how peroxy radicals have signature torsional absorptions 500 cm$^{-1}$ and 1000 cm$^{-1}$ to the blue of the origin, corresponding to the COO bend and OO stretch, respectively. We therefore plan to scan 1000 cm$^{-1}$ to the blue of the current spectral range for spectroscopic confirmation of the peroxy radical assignment.

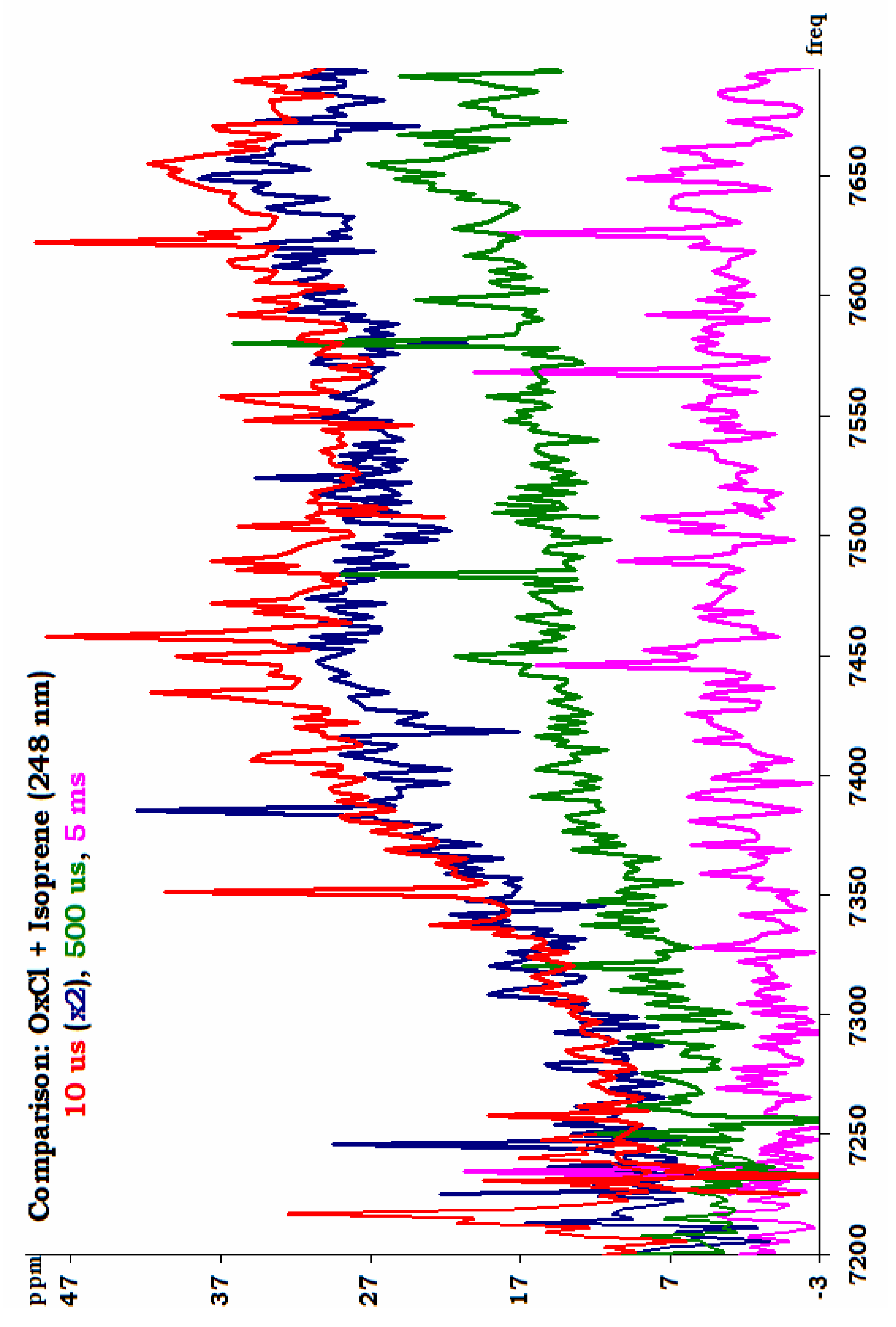

**Figure 5.4.** Preliminary CRD spectra of Cl-isoprenyl peroxy radical in the 7200-7700 cm$^{-1}$ region, collected at various delay times after excimer fire (t = 10 μs, 500 μs, and 5 ms). The absorption signal decays, as the peroxy radicals self-react.

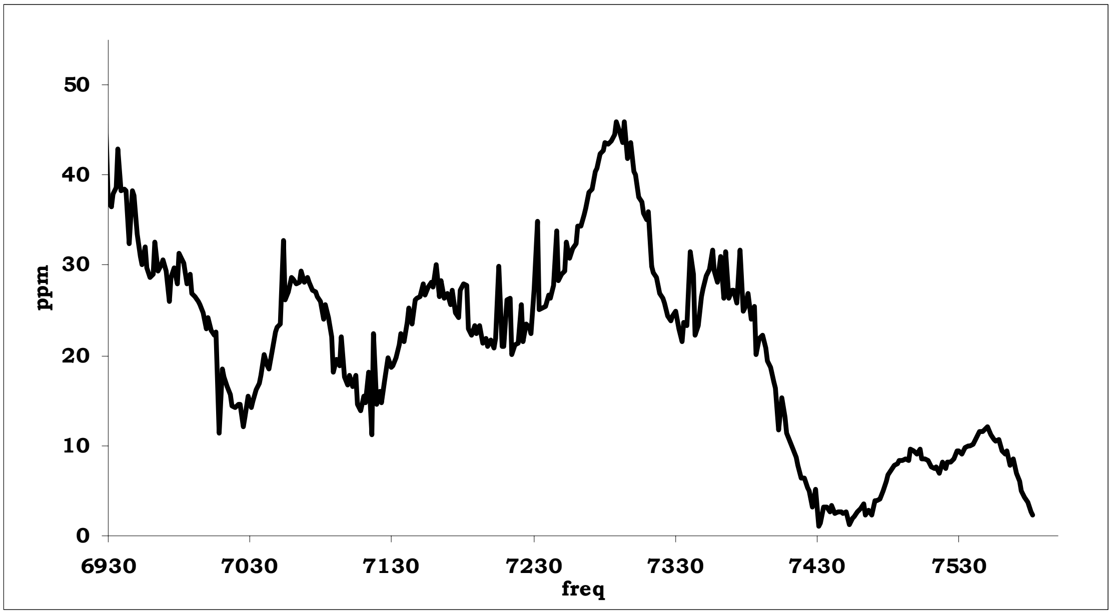

**Figure 5.5.** CRD spectrum of isoprene in the 6930-7550 $cm^{-1}$ region. We subtracted a 10 ppm offset in the figure. There are several strong peaks in the 7030-7430 $cm^{-1}$ region. These spectral features were not observed in the photolysis experiment with OxCl and isoprene, confirming that absorption contributions from isoprene were effectively removed during subtraction of the excimer on/off for CRD experiments (Fig. 5.4).

### *Large scan for Cl-peroxy radical*

We divide the large scan (7200-8700 $cm^{-1}$) into smaller segments, as we are limited by the wavelength range of the laser dyes (Chapter 2). Successive spectra must be scaled appropriately such that spectral intensities can be directly compared. One option is to use absorption features in overlapping spectral regions to scale the spectra. Ideally, the spectra should be scaled by the concentration of Cl-isoprenyl peroxy radical generated in each experiment. In our study of the oxidation of 2-butene by $NO_3$, the concentration of $NO_3$ was the limiting reactant for 2-$NO_3$-butyl peroxy radical formation. Thus, we used CRD spectra of $NO_3$ to scale all collected spectra. We could similarly use the measurement of Cl atoms to directly estimate the concentration of Cl-isoprenyl peroxy radical formation.

Neither OxCl nor the Cl atom have absorptions in the NIR region. We could measure the excimer power and estimate the concentration of Cl atom formation from the vapor pressure of OxCl and absorption cross section of OxCl at 248 nm. A more accurate measurement would be spectroscopic quantification of a species related directly to Cl atom concentrations under similar gas flow conditions as the Cl-isoprene oxidation experiments. We therefore propose to use formation of ethyl peroxy radicals as a means to measure the Cl concentrations in the experiment.

The oxidation of alkanes by radicals proceeds by hydrogen abstraction and forms peroxy radicals in the presence of oxygen. For the simplest alkanes:[64]

$Cl + CH_4 \rightarrow CH_3 + HCl$ (5.8 a)
$k_{298\,K}$ $(Cl + CH_4) = 1.0 \times 10^{-13}$ cm$^3$ molec$^{-1}$ s$^{-1}$ (5.8 b)
$CH_3 + O_2 \rightarrow CH_3O_2$ (methyl peroxy radical) (5.9)

$Cl + C_2H_6 \rightarrow CH_3CH_2 + HCl$ (5.10 a)
$k_{298\,K}$ $(Cl + C_2H_6) = 5.7 \times 10^{-11}$ cm$^3$ molec$^{-1}$ s$^{-1}$ (5.10 b)
$CH_3CH_2 + O_2 \rightarrow CH_3CH_2O_2$ (ethyl peroxy radical) (5.11)

Both methyl and ethyl peroxy radicals are produced 1:1 with respect to the Cl atoms. CRD spectra of the $\tilde{A} \leftarrow \tilde{X}$ transition of both peroxy radicals have been published and show distinct spectral features in the 7200-8700 cm$^{-1}$ region.[65-67] We chose to use ethyl peroxy radicals in this work, as Cl addition to ethane proceeds faster than addition to methane. The same chemical approach has been used to determine the absorption cross section of ethyl peroxy radical in the NIR region. Melnik, *et al.* used a dual wavelength CRD spectrometer to detect both the ethyl peroxy radical and HCl production simultaneously.[68] As the cross sections for HCl lines are well-known, they determined a peak absorption cross section for ethyl peroxy radical at 7596 cm$^{-1}$, $\sigma_{NIR}(CH_3CH_2O_2) = 5.29(20) \times 10^{-21}$ cm$^2$. Thus, we use the spectra of ethyl peroxy radical to not only scale the overlapping spectra for Cl-isoprene oxidation but to also determine the exact concentration of Cl-isoprenyl peroxy radicals observed in the experiments.

Preliminary experiments on the detection of ethyl peroxy radicals were conducted with the pulsed CRD apparatus. We maintained similar gas flow conditions as our Cl-isoprene oxidation experiments. The only major difference was the replacement of the isoprene source with ethane (Matheson). The excimer was operated at 5 Hz and the NIR probe laser was delayed 10-50 μs after the excimer fire. We collected scans of the OxCl/ethane mixture with the excimer on and off and obtained a CRD spectrum of the ethyl peroxy radical from the difference between the two scans (Fig. 5.6). The spectral features were consistent with previously published NIR spectra of the ethyl peroxy radical.

The gas lines for isoprene (or specifically the zero grade air carrier for isoprene) and ethane are interchangeable such that ethyl peroxy radical scans can be run before and after every Cl-isoprene oxidation experiment. Thus, we are now prepared to conduct our wide range scans on the Cl-isoprene oxidation system.

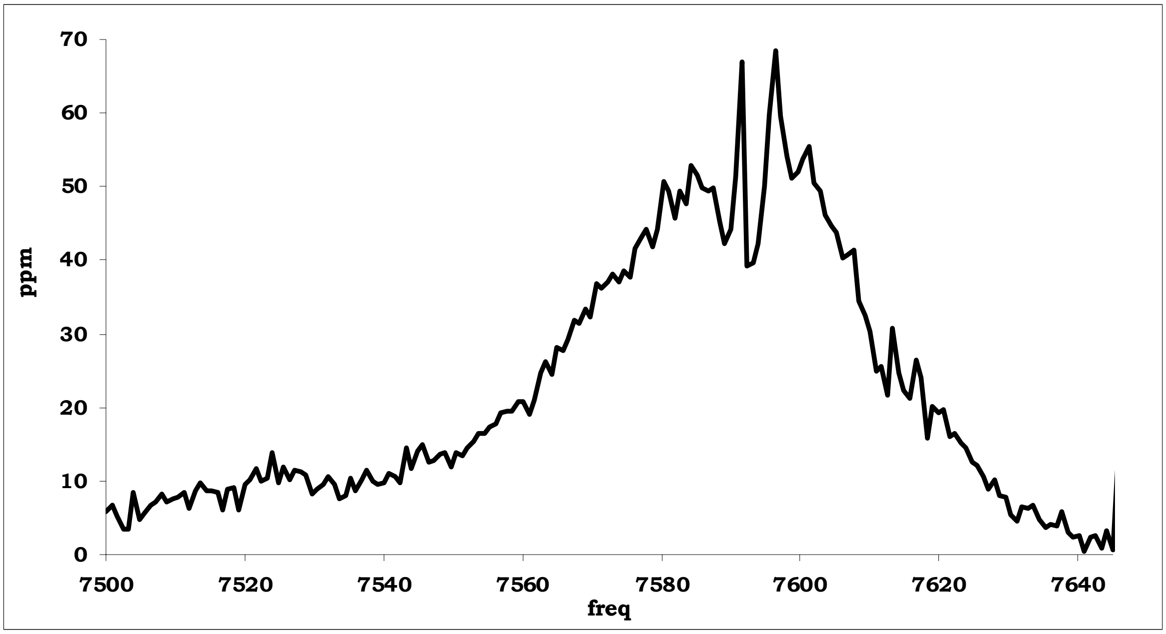

**Figure 5.6.** Preliminary spectrum of the $\tilde{A} \leftarrow \tilde{X}$ transition of ethyl peroxy radical in the 7500-7650 cm$^{-1}$ region. The concentration of ethyl peroxy radicals is related directly to the concentration of Cl atoms generated in the photolysis cell. The Cl atoms further determine the concentration of Cl-isoprenyl peroxy radicals formed during the oxidation experiments.

### 5.2.4 Cl-MBO232 peroxy radical detection

*Preliminary results*

In addition to the low-lying electronic transitions, OH vibrational overtones have absorptions in the NIR region. We expect to observe both the origin of the $\tilde{A} \leftarrow \tilde{X}$ transition and the OH overtone of Cl-MBO232 peroxy radical in the NIR region. We outline methods to distinguish the two transitions in the spectra.

With respect to the $\tilde{A} \leftarrow \tilde{X}$ transition, addition of Cl to MBO232 results in two structural isomers, I (rxn 5.5 a) and II (rxn 5.5 b) (Fig. 5.7). Peroxy isomer I resembles the 3-methyl-2-butyl peroxy radical, while peroxy isomer II resembles the 3-methylbutyl peroxy radical. NIR spectra of the $\tilde{A} \leftarrow \tilde{X}$ transitions for both methylbutyl peroxy radicals have been published.[69] For the 3-methyl-2-butyl peroxy radical, three different conformers were observed with origin bands at 7318 $cm^{-1}$, 7490 $cm^{-1}$, and 7549 $cm^{-1}$. The most intense absorption was located between 7500-7620 $cm^{-1}$ with two sharp bumps for two of the conformers. For the 3-methylbutyl peroxy radical, three conformers were observed with origin bands at 7361 $cm^{-1}$, 7551 $cm^{-1}$, and 7620 $cm^{-1}$. The most intense absorption was between 7200-7800 $cm^{-1}$, with a very sharp rise to the 7620 $cm^{-1}$ peak.

The addition of both Cl and OH substituents should shift the origins of the conformers to the red. The shape however should be very similar. We should be able to identify the absorptions arising from the Cl-MBO232 peroxy radical from spectral comparisons. We can then scan 500 $cm^{-1}$ and 1000 $cm^{-1}$ to the blue of the observed origin band frequencies to detect the signature torsional absorptions of peroxy radicals for spectroscopic confirmation of the assignments.

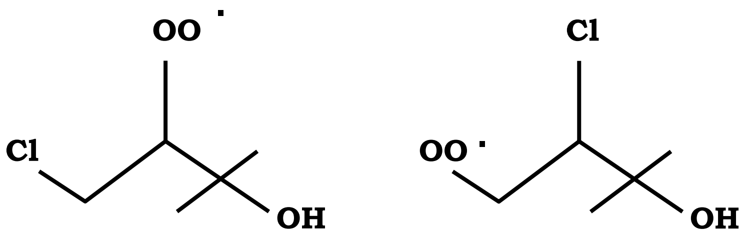

**Isomer I** **Isomer II**

**Figure 5.7.** The two structural isomers of Cl-MBO232 peroxy radical.

With respect to the OH overtone, most OH stretches are in the 3500 $cm^{-1}$ region with overtones in the 7000 $cm^{-1}$ region. The mid-IR and NIR spectra of ethanol and Cl-ethanol were compared and found to be very similar in band shape and position.[70] Thus, as long as the Cl substituent does not directly affect the OH stretch, the effect on the absorptions should be minimal. The parent compound MBO232 has an OH overtone absorption in the NIR region. The OH overtones for both isomers of Cl-MBO232 peroxy radicals should have very similar absorptions. Thus, we obtain a CRD spectrum of MBO232 as a reference. The OH absorption should be to the red of the $\tilde{A} \leftarrow \tilde{X}$ transitions of the peroxy radicals. We may not be able to observe the weak peroxy radical conformer absorption in the 7300 cm$^{-1}$ region, but we should be able to observe the conformer absorptions in the 7500-7700 cm$^{-1}$ region without much spectral interference.

Experiments on the Cl oxidation of MBO232 were conducted using the same pulsed CRDS apparatus and gas flow conditions as described in the previous section. Only the isoprene sample with replaced with MBO232 (Sigma Aldrich). MBO232 is a liquid at room temperature. We pipetted 5 mL of MBO232 into a bubbler and placed it in a methanol chiller bath (T ~ -10°C). Experiments were typically run with 1.5 Torr vapor pressure of MBO232. Scans were taken at 0.4 cm$^{-1}$ step size with the excimer operating at 5 Hz and the NIR probe delayed 10 μs after chemical initiation.

Preliminary CRD spectra of Cl-MBO232 peroxy radical were obtained in the 7150-7600 cm$^{-1}$ region from subtraction of scans collected with the excimer on and off for OxCl/MBO232 in the ringdown cell (Fig. 5.8). A CRD spectrum was also obtained for MBO232 (Fig. 5.9). The absorptions observed in the two spectra (Fig. 5.8 and Fig. 5.9) are very different, especially in the 7450-7600 cm$^{-1}$ region. While more experiments are needed to confirm that the absorptions in the latter region belong to the $\tilde{A} \leftarrow \tilde{X}$ transition of the peroxy radicals, the preliminary results look very promising. It may be worthwhile to extend the CRD studies to Cl-oxidation of 3-methyl-1-butene to examine the effect of the OH substituent on the origin frequency of $\tilde{A} \leftarrow \tilde{X}$ transition and better assign which bands belong to the OH overtone in the current spectra.

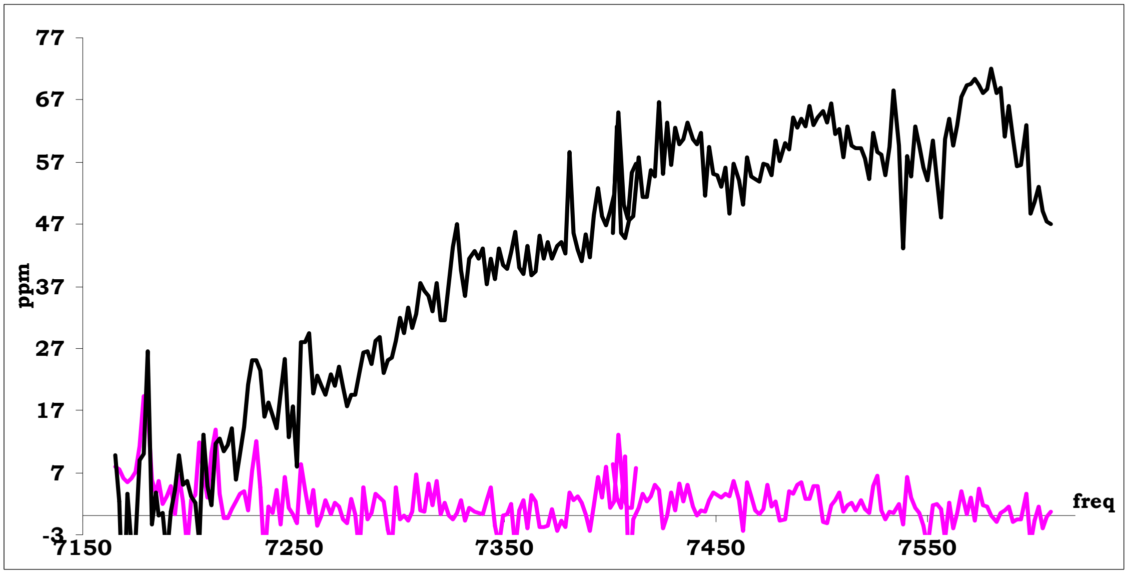

**Figure 5.8.** Preliminary CRD spectra of Cl-MBO232 peroxy radical in the 7150-7600 cm$^{-1}$ region. The scans were collected at $t$ =10 μs (black) and $t$ = 2 ms (pink) after the excimer fire. The peroxy radical disappeared over time from self-reaction.

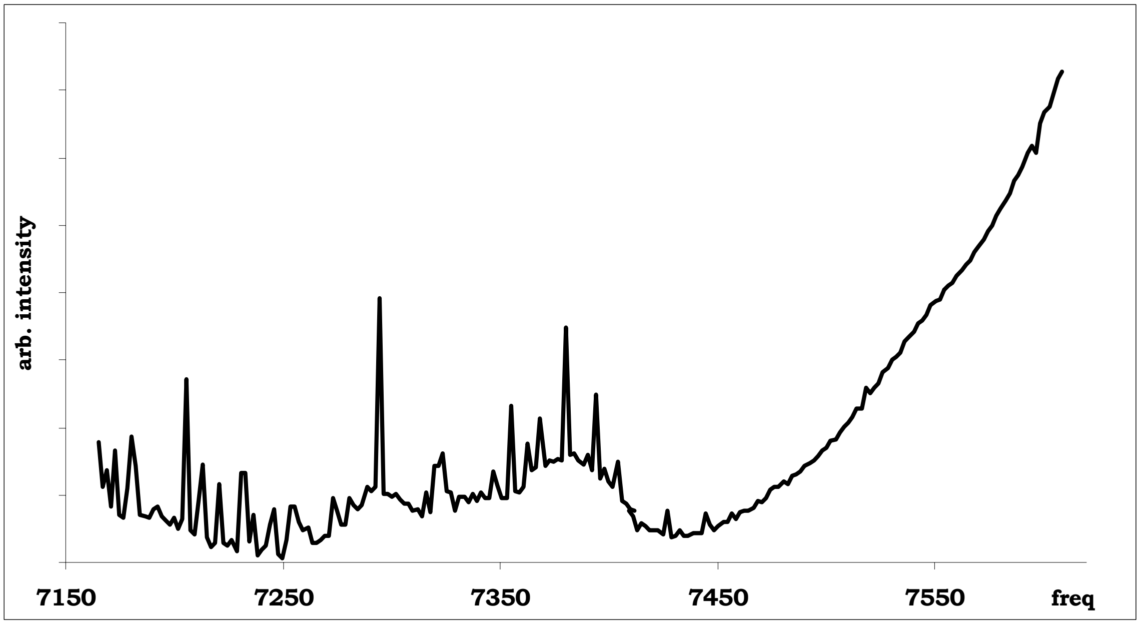

**Figure 5.9.** Preliminary CRD spectrum of MBO232 in the 7150-7600 cm$^{-1}$ region. The spectrum has not been background-subtracted. The spectral rise at 7450 cm$^{-1}$ is therefore from the reflectivity of the CRD mirrors. Problems with the laser power prevented scans to the red of 7150 cm$^{-1}$. The OH overtone should be around 7000 cm$^{-1}$.

## 5.3 Cl-peroxy radical kinetics

### 5.3.1 Background

We have thus far discussed the detection of substituted peroxy radicals. Detection of the radicals allows us to examine the kinetics of the substituted peroxy radicals. In Chapter 1, we outlined two different environments for peroxy radical kinetics: high and low $NO_x$ conditions. Under high $NO_x$ conditions, the reaction between the peroxy radicals and nitric oxide (NO) dominates. Under low $NO_x$ conditions, the reaction between the peroxy radicals with hydroperoxy radical $HO_2$ and other peroxy radicals dominates. For substituted peroxy radicals, most of these rates of reaction have never been measured.

For Cl-peroxy radicals, the self reaction rates for a few species have been measured using UV absorption spectroscopy: $CHCl_2CHClO_2$, $CHCl_2CCl_2O_2$, $CCl_3CCl_2O_2$, $CH_2ClO_2$, $CHCl_2O_2$, and $ClCH_2CH_2O_2$. Self reactions rates vary from from $k_{298K}$ ($ClRO_2$ + $ClRO_2$) = 3.6-8.6 × $10^{-12}$ $cm^3$ $molec^{-1}$ $s^{-1}$.[58,59,61] For comparison, self-reaction rates of methyl and ethyl peroxy radicals have been measured, $k_{298K}$ ($CH_3O_2$+$CH_3O_2$) = 3.5 × $10^{-13}$ $cm^3$ $molec^{-1}$ $s^{-1}$ and $k_{298K}$ ($CH_3CH_2O_2$+$CH_3CH_2O_2$) = 6.8 × $10^{-14}$ $cm^3$ $molec^{-1}$ $s^{-1}$, respectively.[64] Cl addition significantly increases the rate of self-reaction:

$ClRO_2 + ClRO_2 \rightarrow$ Products (5.12 a-b)

$k_{298K}$ ($ClRO_2$ + $ClRO_2$) = 3.6-8.6 × $10^{-12}$ $cm^3$ $molec^{-1}$ $s^{-1}$

$RO_2 + RO_2 \rightarrow$ Products (5.13 a-b)

$k_{298K}$ ($RO_2$ + $RO_2$) = 0.68-3.5 × $10^{-13}$ $cm^3$ $molec^{-1}$ $s^{-1}$

There has been one measurement for the reaction between the Cl-ethyl peroxy radical ($ClCH_2CH_2O_2$) and $HO_2$: $k_{298K}$ ($ClCH_2CH_2O_2$ + $HO_2$)= 1.4 × $10^{-11}$ $cm^3$ $molec^{-1}$ $s^{-1}$.[58] The reaction rate between the ethyl peroxy radical and $HO_2$ has been measured to be $k_{298K}$ ($CH_3CH_2O_2$ + $HO_2$) = 8 × $10^{-12}$ $cm^3$ $molec^{-1}$ $s^{-1}$.[64] The rate of reaction is again increased by Cl addition:

$ClCH_2CH_2O_2 + HO_2 \rightarrow$ Products (5.14 a-b)
$k_{298K}$ ($ClCH_2CH_2O_2$ + $HO_2$)= 1.4 × $10^{-11}$ $cm^3$ $molec^{-1}$ $s^{-1}$

$CH_3CH_2O_2 + HO_2 \rightarrow$ Products (5.15 a-b)
$k_{298K}$ ($CH_3CH_2O_2$ + $HO_2$) = 8 × $10^{-12}$ $cm^3$ $molec^{-1}$ $s^{-1}$

Finally, there have been CIMS studies by the Elrod group on the reaction rate between NO and Cl-alkenyl and Cl-MACR/MVK peroxy radicals.[40,41] Measured rates range from $k_{298K}$ ($ClRO_2$ + NO) = 0.84-1.17 × $10^{-11}$ $cm^3$ $molec^{-1}$ $s^{-1}$. Reaction rates for methyl and ethyl peroxy radicals with NO are $k_{298K}$ ($CH_3O_2$ + NO) = 7.7 × $10^{-12}$ $cm^3$ $molec^{-1}$ $s^{-1}$ and $k_{298K}$ ($CH_3CH_2O_2$ + NO) = 8.7 × $10^{-12}$ $cm^3$ $molec^{-1}$ $s^{-1}$, respectively.[64] Cl addition appears to have less effect on the reaction rates:

$ClRO_2 + NO \rightarrow$ Products (5.16 a-b)
$k_{298K}$ ($ClRO_2$ + NO) = 8.4-11.7 × $10^{-12}$ $cm^3$ $molec^{-1}$ $s^{-1}$

$RO_2 + NO \rightarrow$ Products (5.17 a-b)
$k_{298K}$ ($RO_2$ + NO) = 7.7-8.7 × $10^{-12}$ $cm^3$ $molec^{-1}$ $s^{-1}$

A handful of theoretical works have examined the effect of Cl addition on the reaction rates. King and Thompson examined singly occupied molecule orbitals (SOMO) of reactant species and determined that peroxy radicals derived from halogenated alkenes had faster rate constants for reaction with NO relative to reaction with $HO_2$.[71] There are not enough measurements of the reaction rate between Cl-peroxy radical and $HO_2$ to verify the theory. Kosmas, *et al.* performed *ab initio* and density functional calculations on the reaction between halogenated methyl peroxy radicals and NO and found that the increased attractive character of the potential energy surface, along with the increased exothermicity of the reactions, contributed to higher rates of reaction between halogenated methyl peroxy radical and NO than methyl peroxy radicals and NO.[72] The available experimental data, however, indicates that the rates of reaction between halogenated and non-halogenated species with NO are very similar. More experimental work is needed.

To date, despite the significance of isoprenyl peroxy radicals in the atmosphere, the previously mentioned CIMS study is the only direct measurement of the rate of reaction between Cl-isoprenyl peroxy radical and NO. There has been no direct measurements on the reaction rates between Cl-MBO232 peroxy radicals and other atmospheric species. We therefore propose to measure the following rates of reaction for the Cl-isoprenyl and MBO232 peroxy radicals: the rate of self-reaction, the rate of reaction with NO, and the rate of reaction with $HO_2$.

Reproducibility and fine experimental control are key factors in kinetic measurements. Before we begin the complicated kinetic measurements, we need to conduct control experiments to better characterize the apparatus. We chose to examine the kinetics of ethyl peroxy radical for this purpose.

### 5.3.2 Kinetics of the ethyl peroxy radical

The kinetics of ethyl peroxy radicals have been studied in great detail.[64,73] We generate ethyl peroxy radicals via H-abstraction by Cl atoms from ethane (Fig. 5.6). As the peak cross section for the ethyl peroxy radical has been measured in the NIR, we can measure absolute concentrations of ethyl peroxy radicals for the kinetic experiments. We use the kinetic modeling program Kintecus (version 4.0)[74] to model the ethyl peroxy radical chemistry under both high and low $NO_x$ conditions. The simulated decays of the ethyl peroxy radical can be directly compared to the measured signal decays of the ethyl peroxy radical from the pulsed CRDS experiments. We outline the CRD studies below.

*Testing wall reactions via self-reaction experiments*

A major concern for kinetic experiments is wall reactions. Products stick to the cell walls and react with the intermediates of interest. We have worked on coating the ringdown cell with halocarbon wax and Fluoropel to minimize heterogeneous reactions. To quantitatively test the conditions of the cell, we measure the rate of self-reaction for the ethyl peroxy radical:

$$2\ CH_3CH_2O_2 \rightarrow \text{products} \tag{5.18 a}$$

$$\begin{aligned} -\frac{\partial[CH_3CH_2O_2]}{\partial t} &= k[CH_3CH_2O_2]^2 \\ \Rightarrow \frac{1}{[CH_3CH_2O_2(t)]} - \frac{1}{[CH_3CH_2O_2(0)]} &= kt \end{aligned} \tag{5.18 b}$$

The Cl + ethane kinetics model is shown in Table 5.1. Simulations were run under experimental conditions: *T* = 298 K and *P* = 50 Torr, with $[C_2H_6]_0 = 3 \times 10^{16}$ molec $cm^{-3}$ (~1 Torr), $[Cl]_0 = 5 \times 10^{13}$ molec $cm^{-3}$, and $[O_2]_0 = 50 \times 3 \times 10^{16}$ molec $cm^{-3}$. The concentrations of the ethyl peroxy radical are plotted with respect to time in Fig. 5.10. When there is no external reactant, the concentration of the ethyl peroxy radical decreases only by 10% over a 10-ms timeframe. Deviations in the observed decay from the model would most likely be from wall loss.

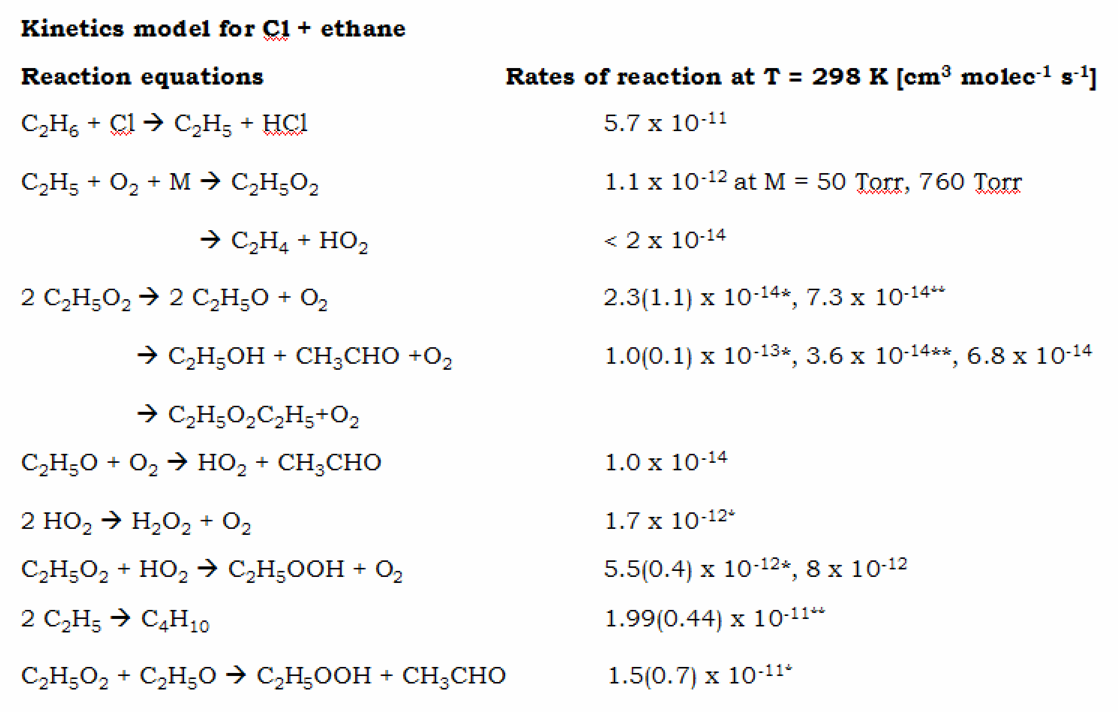

**Kinetics model for Cl + ethane**

| **Reaction equations** | **Rates of reaction at T = 298 K [$cm^3$ $molec^{-1}$ $s^{-1}$]** |
|---|---|
| $C_2H_6 + Cl \rightarrow C_2H_5 + HCl$ | $5.7 \times 10^{-11}$ |
| $C_2H_5 + O_2 + M \rightarrow C_2H_5O_2$ | $1.1 \times 10^{-12}$ at M = 50 Torr, 760 Torr |
| $\rightarrow C_2H_4 + HO_2$ | $< 2 \times 10^{-14}$ |
| $2\ C_2H_5O_2 \rightarrow 2\ C_2H_5O + O_2$ | $2.3(1.1) \times 10^{-14*}$, $7.3 \times 10^{-14**}$ |
| $\rightarrow C_2H_5OH + CH_3CHO + O_2$ | $1.0(0.1) \times 10^{-13*}$, $3.6 \times 10^{-14**}$, $6.8 \times 10^{-14}$ |
| $\rightarrow C_2H_5O_2C_2H_5 + O_2$ | |
| $C_2H_5O + O_2 \rightarrow HO_2 + CH_3CHO$ | $1.0 \times 10^{-14}$ |
| $2\ HO_2 \rightarrow H_2O_2 + O_2$ | $1.7 \times 10^{-12*}$ |
| $C_2H_5O_2 + HO_2 \rightarrow C_2H_5OOH + O_2$ | $5.5(0.4) \times 10^{-12*}$, $8 \times 10^{-12}$ |
| $2\ C_2H_5 \rightarrow C_4H_{10}$ | $1.99(0.44) \times 10^{-11**}$ |
| $C_2H_5O_2 + C_2H_5O \rightarrow C_2H_5OOH + CH_3CHO$ | $1.5(0.7) \times 10^{-11*}$ |

**Table 5.1.** Kinetics model for Cl + ethane. References for rates of reaction: unmarked = ref[64], * = ref[75], and ** = ref[76]

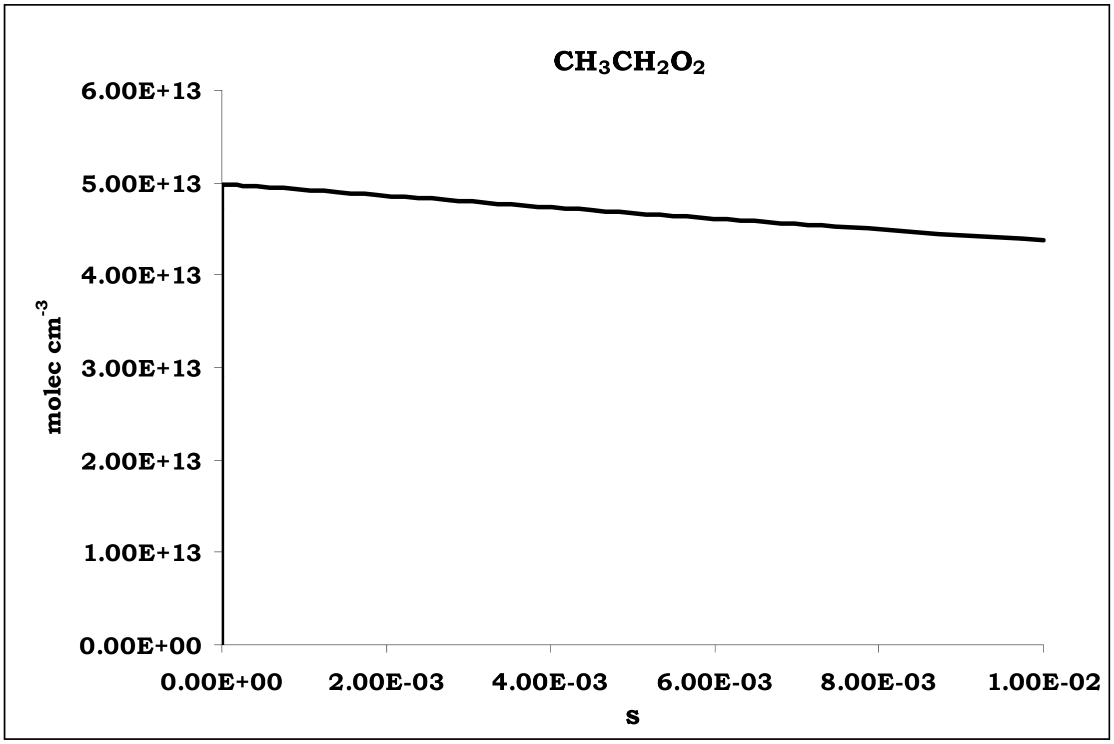

**Figure 5.10.** Concentrations of the ethyl peroxy radical using the kinetics model from Table 5.1. The initial reactant concentrations are: $[C_2H_6]_0$ = 3 × $10^{16}$ molec $cm^{-3}$ (1 Torr), $[Cl]_0$ = 5 × $10^{13}$ molec $cm^{-3}$, and $[O_2]_0$ = 50 × 3 × $10^{16}$ molec $cm^{-3}$.

*Kinetic experiments with NO*

A mass flow controller (Edwards, 100 sccm) is added to the NO (1% Matheson) line for fine control and reproducibility. The pressure readout is used to relate the flow rate with the concentration of NO added to the ringdown cell. Experiments are run under pseudo-first-order conditions, such that the concentrations of NO remain constant during the experiment, $[NO] = [NO]_0$.

$$CH_3CH_2O_2 + NO \rightarrow CH_3CH_2O + NO_2 \qquad (5.19\ a)$$

$$-\frac{\partial[CH_3CH_2O_2]}{\partial t} = k[NO][CH_3CH_2O_2] \simeq k_{obs}[CH_3CH_2O_2]$$
$$\Rightarrow [CH_3CH_2O_2(t)] = [CH_3CH_2O_2(0)] \times e^{-k_{obs}t} \qquad (5.19\ b)$$

where $k_{obs} = k[NO]_0$.

The reactions listed in Table 5.2 are added to the previous kinetics model for simulations. The concentration of the ethyl peroxy radical are re-plotted with respect to time (Fig. 5.11).

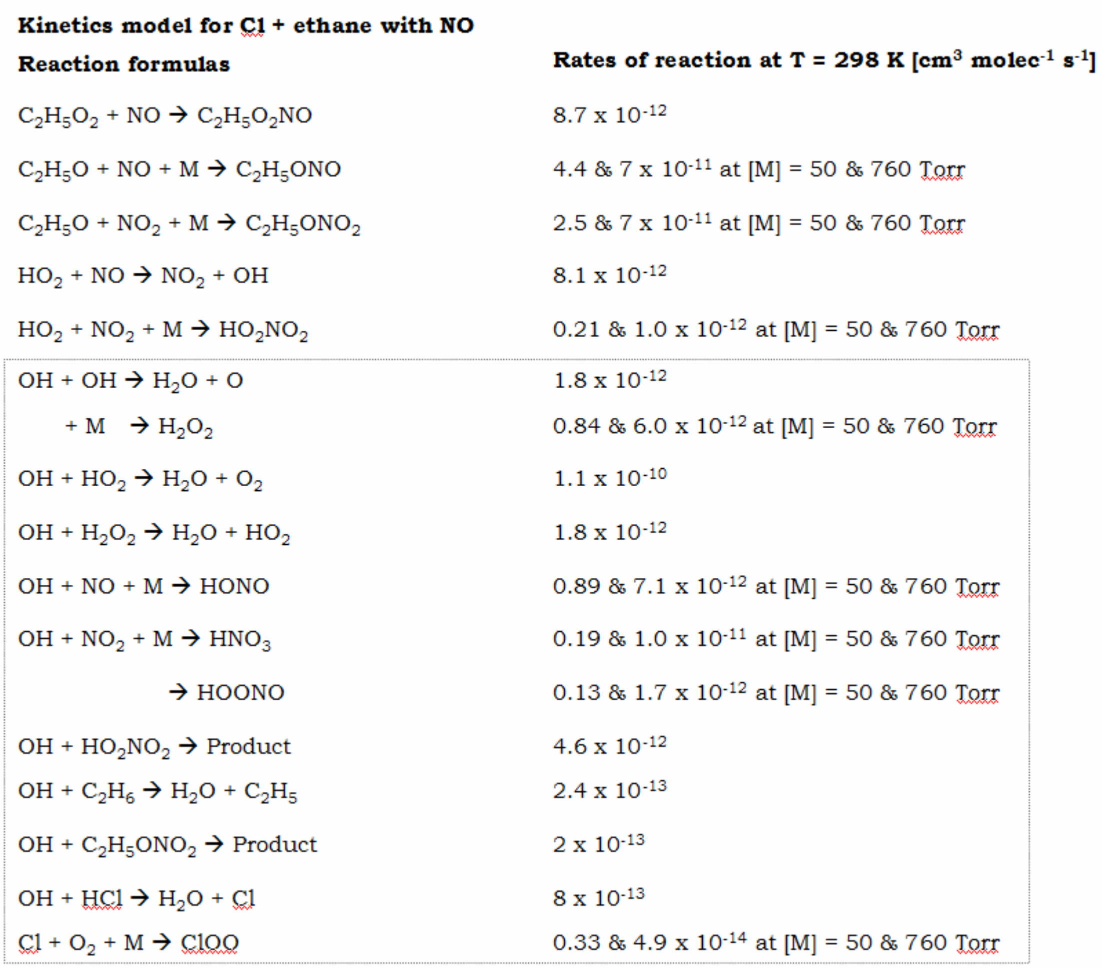

**Kinetics model for Cl + ethane with NO**

| **Reaction formulas** | **Rates of reaction at T = 298 K [$cm^3$ $molec^{-1}$ $s^{-1}$]** |
|---|---|
| $C_2H_5O_2 + NO \rightarrow C_2H_5O_2NO$ | $8.7 \times 10^{-12}$ |
| $C_2H_5O + NO + M \rightarrow C_2H_5ONO$ | $4.4$ & $7 \times 10^{-11}$ at [M] = 50 & 760 Torr |
| $C_2H_5O + NO_2 + M \rightarrow C_2H_5ONO_2$ | $2.5$ & $7 \times 10^{-11}$ at [M] = 50 & 760 Torr |
| $HO_2 + NO \rightarrow NO_2 + OH$ | $8.1 \times 10^{-12}$ |
| $HO_2 + NO_2 + M \rightarrow HO_2NO_2$ | $0.21$ & $1.0 \times 10^{-12}$ at [M] = 50 & 760 Torr |
| $OH + OH \rightarrow H_2O + O$ | $1.8 \times 10^{-12}$ |
| $+ M \rightarrow H_2O_2$ | $0.84$ & $6.0 \times 10^{-12}$ at [M] = 50 & 760 Torr |
| $OH + HO_2 \rightarrow H_2O + O_2$ | $1.1 \times 10^{-10}$ |
| $OH + H_2O_2 \rightarrow H_2O + HO_2$ | $1.8 \times 10^{-12}$ |
| $OH + NO + M \rightarrow HONO$ | $0.89$ & $7.1 \times 10^{-12}$ at [M] = 50 & 760 Torr |
| $OH + NO_2 + M \rightarrow HNO_3$ | $0.19$ & $1.0 \times 10^{-11}$ at [M] = 50 & 760 Torr |
| $\rightarrow HOONO$ | $0.13$ & $1.7 \times 10^{-12}$ at [M] = 50 & 760 Torr |
| $OH + HO_2NO_2 \rightarrow$ Product | $4.6 \times 10^{-12}$ |
| $OH + C_2H_6 \rightarrow H_2O + C_2H_5$ | $2.4 \times 10^{-13}$ |
| $OH + C_2H_5ONO_2 \rightarrow$ Product | $2 \times 10^{-13}$ |
| $OH + HCl \rightarrow H_2O + Cl$ | $8 \times 10^{-13}$ |
| $Cl + O_2 + M \rightarrow ClOO$ | $0.33$ & $4.9 \times 10^{-14}$ at [M] = 50 & 760 Torr |

**Table 5.2.** Kinetics model for Cl + ethane with NO. The model also includes all reactions from Table 5.1. OH is formed late in the reaction after $HO_2$ concentrations become relevant. While they are included in the model (in rectangle box), they are not expected to affect the ethyl peroxy radical yields significantly. Rates of reaction from ref [64].

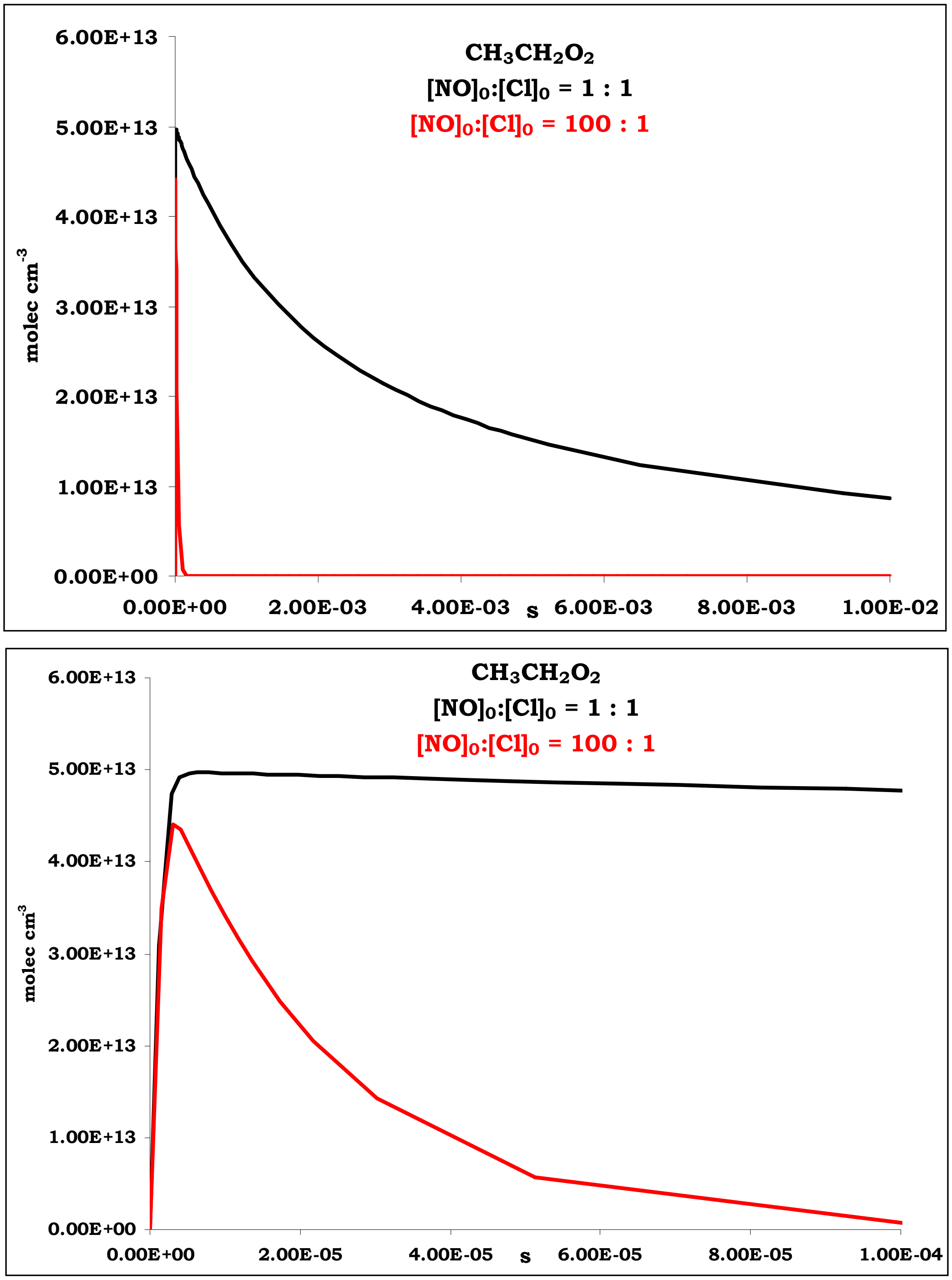

**Figure 5.11.** Concentrations of the ethyl peroxy radical using the kinetic model from Tables 5.2. The initial reactant concentrations are: $[C_2H_6]_0 = 3 \times 10^{16}$ molec cm$^{-3}$ (1 Torr), $[Cl]_0 = 5 \times 10^{13}$ molec cm$^{-3}$, and $[O_2]_0 = 50 \times 3 \times 10^{16}$ molec cm$^{-3}$. In black, $[NO]_0:[Cl]_0 = 1$, while in red, $[NO]_0:[Cl]_0 = 100$. The bottom plot looks at early times of the same simulation.

*Kinetic experiments with $HO_2$*

Determination of the rate of reaction between ethyl peroxy radical and $HO_2$ is more complex, as $HO_2$ has to be generated in the cell simultaneously. Three common methods for $HO_2$ production are:[64]

Source 1:

$Cl + CH_3OH \rightarrow CH_2OH + HCl$ (5.20 a)

$k_{298\,K}(Cl + CH_3OH) = 5.5 \times 10^{-11}$ cm$^3$ molec$^{-1}$ s$^{-1}$ (5.20 b)

$CH_2OH + O_2 \rightarrow CH_2O + HO_2$ (5.21 a)

$k_{298\,K}(HCO + O_2) = 9.1 \times 10^{-12}$ cm$^3$ molec$^{-1}$ s$^{-1}$ (5.21 b)

Source 2:

$Cl + H_2CO \rightarrow HCl + HCO$ (5.22 a)

$k_{298\,K}(Cl + H_2CO) = 7.3 \times 10^{-11}$ cm$^3$ molec$^{-1}$ s$^{-1}$ (5.22 b)

$HCO + O_2 \rightarrow CO + HO_2$ (5.23 a)

$k_{298\,K}(HCO + O_2) = 5.2 \times 10^{-12}$ cm$^3$ molec$^{-1}$ s$^{-1}$ (5.23 b)

Source 3:

$H_2O_2 + h\nu\,(248\text{ nm}) \rightarrow 2\,HO_2$ (5.24 a)

with $\sigma_{248\,nm}(H_2O_2) = 9 \times 10^{-20}$ cm$^2$ (5.24 b)

The first approach is the easiest to implement. The first overtone of the OH stretch of methanol ($CH_3OH$) is between 7000-7300 cm$^{-1}$ region;[70] thus, the absorption is to the red of origin transitions of large peroxy radical absorptions in the NIR. Methanol however competes with ethane for the chlorine atoms. Thus, experiments can no longer be run under pseudo-first-order conditions.

$CH_3CH_2O_2 + HO_2 \rightarrow$ products (5.25 a)

$$-\frac{\partial[CH_3CH_2O_2]}{\partial t} = k[HO_2][CH_3CH_2O_2] \quad (5.25\ b)$$

Reactions in Table 5.3 were added to the kinetics model. The concentrations of both ethyl peroxy radical and $HO_2$ are shown in Fig. 5.12 with initial concentrations of reactants, ethane and methanol, at 1:1, 100:1, and 1:100 ratios. Measuring the decays of ethyl peroxy radical under the different conditions would confirm our control of $HO_2$ concentrations from source 1. An interesting comparison would be to also measure the $HO_2$ decays. The origin of the $\tilde{A} \leftarrow \tilde{X}$ transition of $HO_2$ is located 7029.688 cm$^{-1}$,[77] within the scanning range of our pulsed CRDS apparatus. Contributions from methanol absorption should be effectively removed during subtraction of the photolysis scans (excimer on and off).

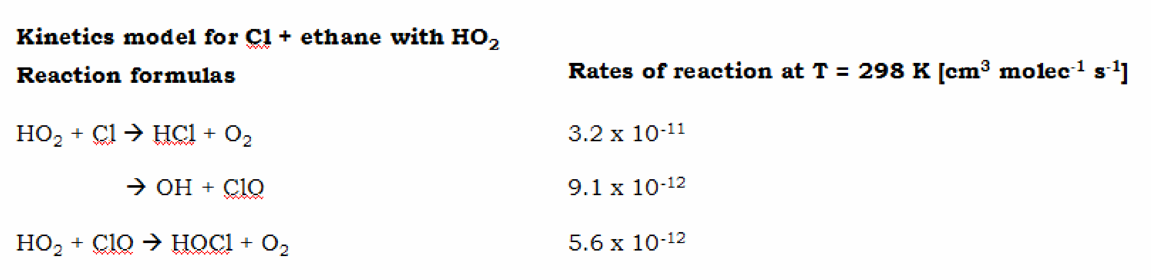

**Kinetics model for Cl + ethane with $HO_2$**

| **Reaction formulas** | **Rates of reaction at T = 298 K [cm$^3$ molec$^{-1}$ s$^{-1}$]** |
|---|---|
| $HO_2 + Cl \rightarrow HCl + O_2$ | $3.2 \times 10^{-11}$ |
| $\rightarrow OH + ClO$ | $9.1 \times 10^{-12}$ |
| $HO_2 + ClO \rightarrow HOCl + O_2$ | $5.6 \times 10^{-12}$ |

**Table 5.3.** Kinetics model for Cl + ethane with $HO_2$, in addition to the reactions included in Table 5.1 and Table 5.2. Rates of reaction from ref [64].

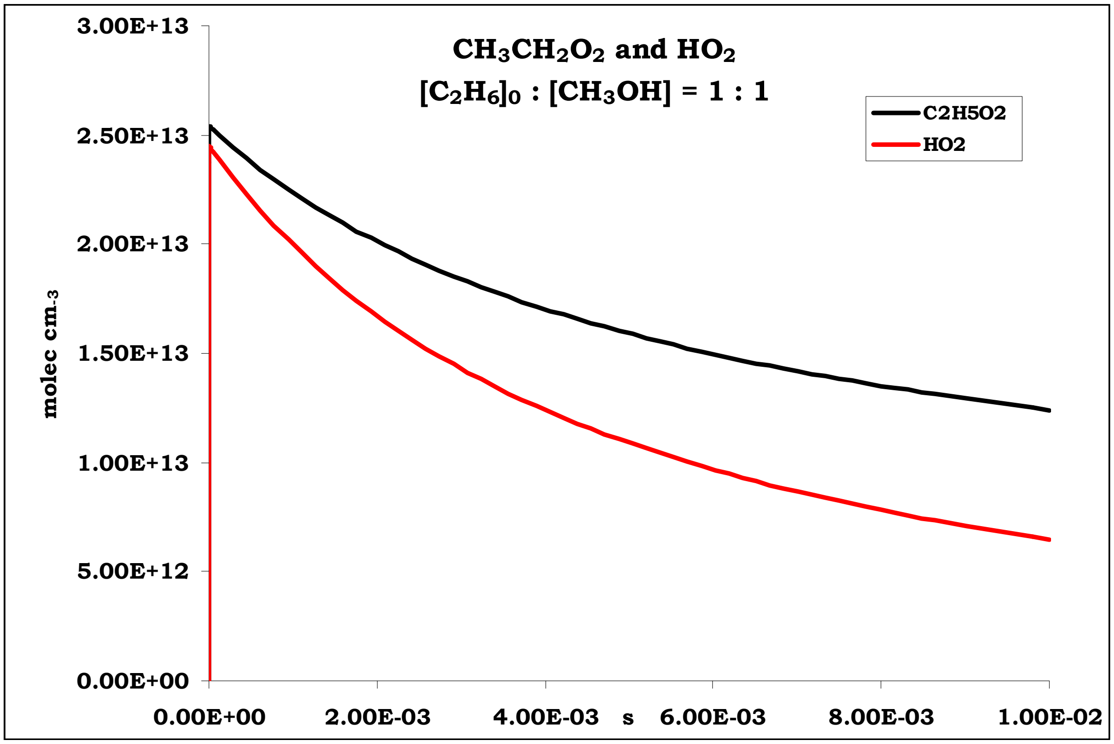
$CH_3CH_2O_2$ and $HO_2$
$[C_2H_6]_0 : [CH_3OH] = 1 : 1$
C2H5O2
HO2
molec cm-3
3.00E+13
2.50E+13
2.00E+13
1.50E+13
1.00E+13
5.00E+12
0.00E+00
0.00E+00
2.00E-03
4.00E-03
s
6.00E-03
8.00E-03
1.00E-02

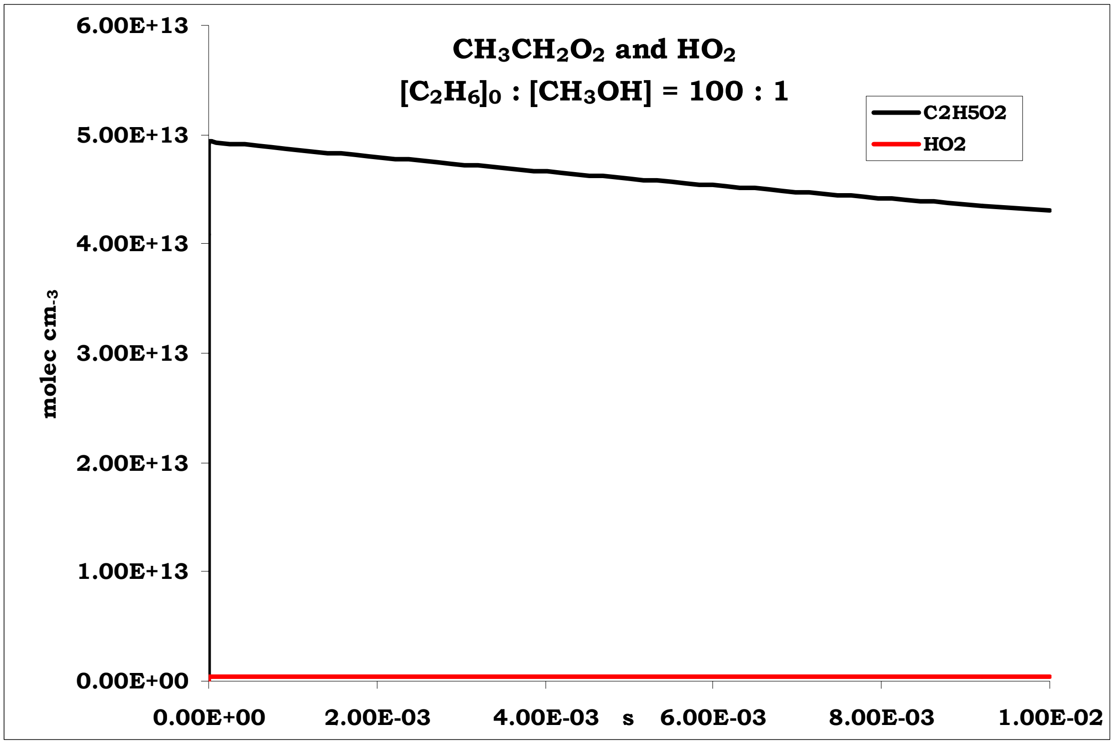
$CH_3CH_2O_2$ and $HO_2$
$[C_2H_6]_0 : [CH_3OH] = 100 : 1$
C2H5O2
HO2
molec cm-3
6.00E+13
5.00E+13
4.00E+13
3.00E+13
2.00E+13
1.00E+13
0.00E+00
0.00E+00
2.00E-03
4.00E-03
s
6.00E-03
8.00E-03
1.00E-02

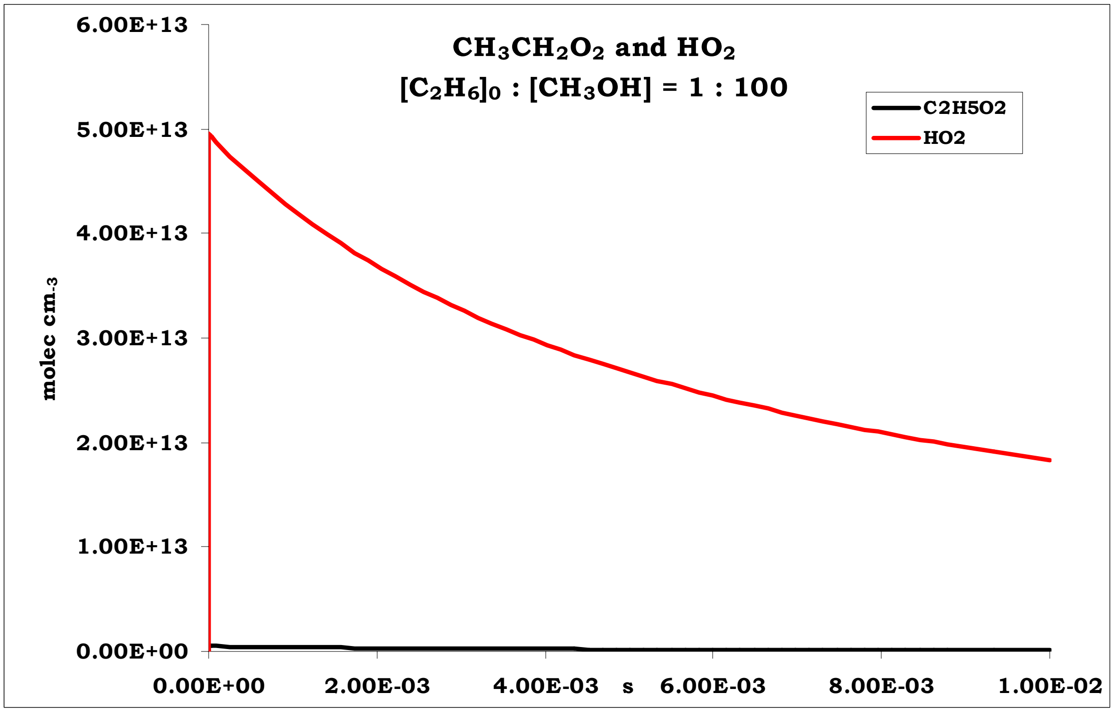

**Figure 5.12.** Concentrations of the ethyl peroxy radical and $HO_2$ using the kinetic model from Tables 5.3. The initial reactant concentrations are: $[C_2H_6]_0 = 3 \times 10^{16}$ molec $cm^{-3}$ (~1 Torr), $[Cl]_0 = 5 \times 10^{13}$ molec $cm^{-3}$, and $[O_2]_0 = 50 \times 3 \times 10^{16}$ molec $cm^{-3}$. The ratio of the ethane and methanol reactants were varied: $[C_2H_6]_0$:$[CH_3OH]_0$ = 1 (top, on previous page), $[C_2H_6]_0$:$[CH_3OH]_0$ = 100 (middle), and $[C_2H_6]_0$:$[CH_3OH]_0$ = 0.01 (bottom). Note: for these simulations, $[NO]_0 = 0$.

If the chemical approach is unable to be well-quantified, we will try the other $HO_2$ sources. Formaldehyde ($H_2CO$) is difficult to use, as paraformaldehyde must be warmed carefully in a separate vessel to avoid oligomerization. Our group has experience using formaldehyde in other experiments.[78] Hydrogen peroxide ($H_2O_2$) is often available commercially as a 30% mixture of $H_2O_2$ and water. Concentrated $H_2O_2$ is explosive. Water, however, causes both spectral and chemical interference. We are in the process of exploring methods to safely collect concentrated $H_2O_2$.

## 5.4 Summary

We collected preliminary CRD spectra of the $\tilde{A} \leftarrow \tilde{X}$ transitions of Cl-isoprenyl and Cl-MBO232 peroxy radicals in the 7200-7700 $\text{cm}^{-1}$ region. Neither species had ever been detected in the gas phase by absorption spectroscopy. The novel detection of the Cl-peroxy radicals provided groundwork for studies on the kinetics of Cl-peroxy radical species under high and low $NO_x$ conditions. We outlined preliminary control experiments on the kinetics of ethyl peroxy radicals to prepare the apparatus and gas lines for kinetic studies of the Cl-peroxy radicals. As many of the reactions rates between Cl-peroxy radicals and atmospheric species have never been measured, these experiments will be highly useful for atmospheric modeling.

## 5.5 Afterword

We began with an examination of the chemical physics of the nitrate radical ($NO_3$) (Chapter 3) before exploring its role in the oxidation of VOCs in the atmosphere (Chapter 4). On one level, the chlorine (Cl) chemistry discussed in this chapter was a simple extension of the study of substituted peroxy radicals. The reaction pathways of Cl and $NO_3$ oxidation of alkenes are indeed parallel. The connection however between chlorine and nitrate radical is more complex. For example, the same dinitrogen pentaoxide ($N_2O_5$) that decomposes to $NO_3$ at night also reacts with chlorine ions to produce nitryl chloride ($ClNO_2$), the photolytic precursors of Cl atoms. Thus, nighttime or daytime, coastal or inland, the atmospheric networks are deeply intertwined. Understanding the chemistry of our atmosphere is understanding all the individual components of the network.

We discussed only a few but important pieces of the atmospheric puzzle in this work. The quality of the air, the climate of the Earth, and the effects on public health are all issues that will only continue to grow in the next century. We have both a scientific and societal responsibility to learn more about our atmosphere. It is the author's hope that others continue the work presented in the thesis and enjoy the same journey of learning that she had over the past years. Cheers!

## 5.5 References

(1) Finlayson-Pitts, B. J.; Pitts, J. N. *Chemistry of the Upper and Lower Atmosphere: Theory, Experiments, and Applications*; Academic Press, 1999.
(2) Finlayson-Pitts, B. J. *Chemical Reviews* **2003**, *103*, 4801.
(3) Graedel, T. E.; Keene, W. C. *Global Biogeochemical Cycles* **1995**, *9*, 47.
(4) Keene, W. C.; Khalil, M. A. K.; Erickson, D. J.; McCulloch, A.; Graedel, T. E.; Lobert, J. M.; Aucott, M. L.; Gong, S. L.; Harper, D. B.; Kleiman, G.; Midgley, P.; Moore, R. M.; Seuzaret, C.; Sturges, W. T.; Benkovitz, C. M.; Koropalov, V.; Barrie, L. A.; Li, Y. F. *Journal of Geophysical Research-Atmospheres* **1999**, *104*, 8429.
(5) Moldanova, J.; Ljungstrom, E. *Journal of Geophysical Research - Atmospheres* **2001**, *106*, 1271.
(6) Thomas, J. L.; Jimenez-Aranda, A.; Finlayson-Pitts, B. J.; Dabdub, D. *Journal of Physical Chemistry A* **2006**,*110*, 1859.
(7) Pszenny, A. A. P.; Keene, W. C.; Jacob, D. J.; Fan, S.; Maben, J. R.; Zetwo, M. P.; Springeryoung, M.; Galloway, J. N. *Geophysical Research Letters* **1993**, *20*, 699.
(8) Ghosal, S.; Brown, M. A.; Bluhm, H.; Krisch, M. J.; Salmeron, M.; Jungwirth, P.; Hemminger, J. C. *Journal of Physical Chemistry A* **2008**, *112*, 12378.
(9) Hoffman, R. C.; Gebel, M. E.; Fox, B. S.; Finlayson-Pitts, B. J. *Physical Chemistry Chemical Physics* **2003**, *5*, 1780.
(10) Leu, M. T.; Timonen, R. S.; Keyser, L. F.; Yung, Y. L. *Journal of Physical Chemistry* **1995**, *99*, 13203.
(11) Roberts, J. M.; Osthoff, H. D.; Brown, S. S.; Ravishankara, A. R. *Science* **2008**, *321*, 1059.
(12) Thornton, J. A.; Abbatt, J. P. D. *Journal of Physical Chemistry A* **2005**, *109*, 10004.
(13) Wingen, L. M.; Moskun, A. C.; Johnson, S. N.; Thomas, J. L.; Roeselova, M.; Tobias, D. J.; Kleinman, M. T.; Finlayson-Pitts, B. J. *Physical Chemistry Chemical Physics* **2008**, *10*, 5668.
(14) Knipping, E. M.; Lakin, M. J.; Foster, K. L.; Jungwirth, P.; Tobias, D. J.; Gerber, R. B.; Dabdub, D.; Finlayson-Pitts, B. J. *Science* **2000**, *288*, 301.
(15) Knipping, E. M.; Dabdub, D. *Environmental Science & Technology* **2003**, *37*, 275.

(16) Osthoff, H. D.; Roberts, J. M.; Ravishankara, A. R.; Williams, E. J.; Lerner, B. M.; Sommariva, R.; Bates, T. S.; Coffman, D.; Quinn, P. K.; Dibb, J. E.; Stark, H.; Burkholder, J. B.; Talukdar, R. K.; Meagher, J.; Fehsenfeld, F. C.; Brown, S. S. *Nature Geoscience* **2008**, *1*, 324.

(17) Thornton, J. A.; Kercher, J. P.; Riedel, T. P.; Wagner, N. L.; Cozic, J.; Holloway, J. S.; Dube, W. P.; Wolfe, G. M.; Quinn, P. K.; Middlebrook, A. M.; Alexander, B.; Brown, S. S. *Nature* **2010**, *464*, 271.

(18) von Glasow, R. *Nature* **2010**, *464*, 168.

(19) Brown, S. S.; Dube, W. P.; Fuchs, H.; Ryerson, T. B.; Wollny, A. G.; Brock, C. A.; Bahreini, R.; Middlebrook, A. M.; Neuman, J. A.; Atlas, E.; Roberts, J. M.; Osthoff, H. D.; Trainer, M.; Fehsenfeld, F. C.; Ravishankara, A. R. *Journal of Geophysical Research - Atmospheres* **2009**, *114*.

(20) Kercher, J. P.; Riedel, T. P.; Thornton, J. A. *Atmospheric Measurement Techniques* **2009**, *2*, 193.

(21) Chang, S. Y.; McDonald-Buller, E.; Kimura, Y.; Yarwood, G.; Neece, J.; Russell, M.; Tanaka, P.; Allen, D. *Atmospheric Environment* **2002**, *36*, 4991.

(22) Tanaka, P. L.; Oldfield, S.; Neece, J. D.; Mullins, C. B.; Allen, D. T. *Environmental Science & Technology* **2000**, *34*, 4470.

(23) Tanaka, P. L.; Riemer, D. D.; Chang, S. H.; Yarwood, G.; McDonald-Buller, E. C.; Apel, E. C.; Orlando, J. J.; Silva, P. J.; Jimenez, J. L.; Canagaratna, M. R.; Neece, J. D.; Mullins, C. B.; Allen, D. T. *Atmospheric Environment* **2003**, *37*, 1393.

(24) Aucott, M. L.; McCulloch, A.; Graedel, T. E.; Kleiman, G.; Midgley, P.; Li, Y. F. *Journal of Geophysical Research - Atmospheres* **1999**, *104*, 8405.

(25) McCulloch, A.; Aucott, M. L.; Benkovitz, C. M.; Graedel, T. E.; Kleiman, G.; Midgley, P. M.; Li, Y. F. *Journal of Geophysical Research - Atmospheres* **1999**, *104*, 8391.

(26) McCulloch, A.; Aucott, M. L.; Graedel, T. E.; Kleiman, G.; Midgley, P. M.; Li, Y. F. *Journal of Geophysical Research - Atmospheres* **1999**, *104*, 8417.

(27) Seinfeld, J. H.; Pandis, S. N. *Atmospheric Chemistry and Physics*; Wiley-Interscience, 1997.

(28) Lei, W. F.; Zhang, D.; Zhang, R. Y.; Molina, L. T.; Molina, M. J. *Chemical Physics Letters* **2002**, *357*, 45.

(29) Lei, W. F.; Zhang, R. Y.; Molina, L. T.; Molina, M. J. *Journal of Physical Chemistry A* **2002**, *106*, 6415.

(30) Ezell, M. J.; Wang, W. H.; Ezell, A. A.; Soskin, G.; Finlayson-Pitts, B. J. *Physical Chemistry Chemical Physics* **2002**, *4*, 5813.

(31) Riemer, D. D.; Apel, E. C.; Orlando, J. J.; Tyndall, G. S.; Brune, W. H.; Williams, E. J.; Lonneman, W. A.; Neece, J. D. *Journal of Atmospheric Chemistry* **2008**, *61*, 227.

(32) Orlando, J. J.; Tyndall, G. S.; Apel, E. C.; Riemer, D. D.; Paulson, S. E. *International Journal of Chemical Kinetics* **2003**, *35*, 334.

(33) Ceacero-Vega, A. A.; Ballesteros, B.; Albaladejo, J.; Bejan, I.; Barnes, I. *Chemical Physics Letters* **2009**, *484*, 10.

(34) Iwasaki, E.; Chiba, H.; Nakayama, T.; Matsumi, Y.; Wallington, T. J. *Chemical Physics Letters* **2010**, *494*, 174.

(35) Kaiser, E. W.; Wallington, T. J. *Chemical Physics Letters* **2011**, *501*, 187.

(36) Xing, J. H.; Takahashi, K.; Hurley, M. D.; Wallington, T. J. *Chemical Physics Letters* **2009**, *472*, 39.

(37) Andersen, M. P. S.; Nilsson, E. J. K.; Nielsen, O. J.; Johnson, M. S.; Hurley, M. D.; Wallington, T. J. *Journal of Photochemistry and Photobiology a-Chemistry* **2008**, *199*, 92.

(38) Kaiser, E. W.; Donahue, C. J.; Pala, I. R.; Wallington, T. J.; Hurley, M. D. *Journal of Physical Chemistry A* **2007**, *111*, 1286.

(39) Finlayson-Pitts, B. J.; Keoshian, C. J.; Buehler, B.; Ezell, A. A. *International Journal of Chemical Kinetics* **1999**, *31*, 491.

(40) Hsin, H. Y.; Elrod, M. J. *Journal of Physical Chemistry A* **2007**, *111*, 613.

(41) Patchen, A. K.; Pennino, M. J.; Elrod, M. J. *Journal of Physical Chemistry A* **2005**, *109*, 5865.

(42) Ragains, M. L.; FinlaysonPitts, B. J. *Journal of Physical Chemistry A* **1997**, *101*, 1509.

(43) Fan, J. W.; Zhang, R. Y. *Environmental Chemistry* **2004**, *1*, 140.

(44) Canosa-Mas, C. E.; Hutton-Squire, H. R.; King, M. D.; Stewart, D. J.; Thompson, K. C.; Wayne, R. P. *Journal of Atmospheric Chemistry* **1999**, *34*, 163.

(45) Fantechi, G.; Jensen, N. R.; Saastad, O.; Hjorth, J.; Peeters, J. *Journal of Atmospheric Chemistry* **1998**, *31*, 247.

(46) Stutz, J.; Ezell, M. J.; Ezell, A. A.; Finlayson-Pitts, B. J. *Journal of Physical Chemistry A* **1998**, *102*, 8510.

(47) Suh, I.; Zhang, R. Y. *Journal of Physical Chemistry A* **2000**, *104*, 6590.

(48) Timerghazin, Q. K.; Ariya, P. A. *Physical Chemistry Chemical Physics* **2001**, *3*, 3981.

(49) Wang, W. H.; Finlayson-Pitts, B. J. *Journal of Geophysical Research-Atmospheres* **2001**, *106*, 4939.

(50) Kesselmeier, J.; Staudt, M. *Journal of Atmospheric Chemistry* **1999**, *33*, 23.

(51) Atkinson, R.; Arey, J. *Atmospheric Environment* **2003**, *37*, S197.

(52) Goldan, P. D.; Kuster, W. C.; Fehsenfeld, F. C.; Montzka, S. A. *Geophysical Research Letters* **1993**, *20*, 1039.

(53) Schade, G. W.; Goldstein, A. H.; Gray, D. W.; Lerdau, M. T. *Atmospheric Environment* **2000**, *34*, 3535.

(54) Tarvainen, V.; Hakola, H.; Hellen, H.; Back, J.; Hari, P.; Kulmala, M. *Atmospheric Chemistry and Physics* **2005**, *5*, 989.

(55) Takahashi, K.; Xing, J. H.; Hurley, M. D.; Wallington, T. J. *Journal of Physical Chemistry A* **2010**, *114*, 4224.

(56) Rodriguez, A.; Rodriguez, D.; Soto, A.; Notario, A.; Aranda, A.; Diaz-De-Mera, Y.; Bravo, I. *Atmospheric Environment* **2007**, *41*, 4693.

(57) Ferronato, C.; Orlando, J. J.; Tyndall, G. S. *Journal of Geophysical Research - Atmospheres* **1998**, *103*, 25579.

(58) Chakir, A.; Brion, J.; Ganne, J. P.; Daumont, D. *Physical Chemistry Chemical Physics* **2003**, *5*, 2573.

(59) Biggs, P.; Canosa-Mas, C. E.; Percival, C. J.; Shallcross, D. E.; Wayne, R. P. *International Journal of Chemical Kinetics* **1999**, *31*, 433.

(60) Le Crane, I. P.; Villenave, E. *International Journal of Chemical Kinetics* **2006**, *38*, 276.

(61) Villenave, E.; Morozov, I.; Lesclaux, R. *Journal of Physical Chemistry A* **2000**, *104*, 9933.

(62) Deev, A., California Institute of Technology, 2005.

(63) Baklanov, A. V.; Krasnoperov, L. N. *Journal of Physical Chemistry A* **2001**, *105*, 97.

(64) Sander, S. P.; Friedl, R. R.; Golden, D. M.; Kurylo, M.; Moortgat, G. K.; Wine, P. H.; Ravishankara, A. R.; Kolb, C. E.; Molina, M. J.; Finlayson-Pitts, B. J.; Huie, R. E.; Orkin, V. L. *Chemical Kinetics and Photochemical Data for Use in Atmospheric Studies, Evaluation No. 15,* 2006.

(65) Rupper, P.; Sharp, E. N.; Tarczay, G.; Miller, T. A. *J. Phys. Chem. A* **2007**, *111*, 832.

(66) Just, G. M. P.; McCoy, A. B.; Miller, T. A. *Journal of Chemical Physics* **2007**, *127*, 044310/1.

(67) Sharp, E. N.; Rupper, P.; Miller, T. A. *Phys. Chem. Chem. Phys.* **2008**, *10*, 3955.

(68) Melnik, D.; Chhantyal-Pun, R.; Miller, T. A. *Journal of Physical Chemistry A* **2010**, *114*, 11583.

(69) Sharp, E. N.; Rupper, P.; Miller, T. A. *Journal of Physical Chemistry A* **2008**, *112*, 1445.
(70) Sharpe, S. W.; Johnson, T. J.; Sams, R. L.; Chu, P. M.; Rhoderick, G. C.; Johnson, P. A. *Applied Spectroscopy* **2004**, *58*, 1452.
(71) King, M. D.; Thompson, K. C. *Atmospheric Environment* **2003**, *37*, 4517.
(72) Kosmas, A. M.; Salta, Z.; Lesar, A. *Journal of Physical Chemistry A* **2009**, *113*, 3545.
(73) Atkinson, R.; Baulch, D. L.; Cox, R. A.; Crowley, J. N.; Hampson, R. F.; Hynes, R. G.; Jenkin, M. E.; Rossi, M. J.; Troe, J. *Atmospheric Chemistry and Physics* **2004**, *4*, 1461.
(74) Ianni, J. C. 2011.
(75) Noell, A. C.; Alconcel, L. S.; Robichaud, D. J.; Okumura, M.; Sander, S. P. *Journal of Physical Chemistry A* **2010**, *114*, 6983.
(76) Atkinson, D. B.; Hudgens, J. W. *Journal of Physical Chemistry A* **1997**, *101*, 3901.
(77) Fink, E. H.; Ramsay, D. A. *Journal of Molecular Spectroscopy* **2002**, *216*, 322.
(78) Mollner, A., *Ph. D. Thesis,* California Institute of Technology, 2007.